Delft University of Technology

Investigation of Görtler vortices in hypersonic flow using Quantitative Infrared Thermography (QIRT) and Tomographic Particle Image Velocimetry (Tomo-PIV)

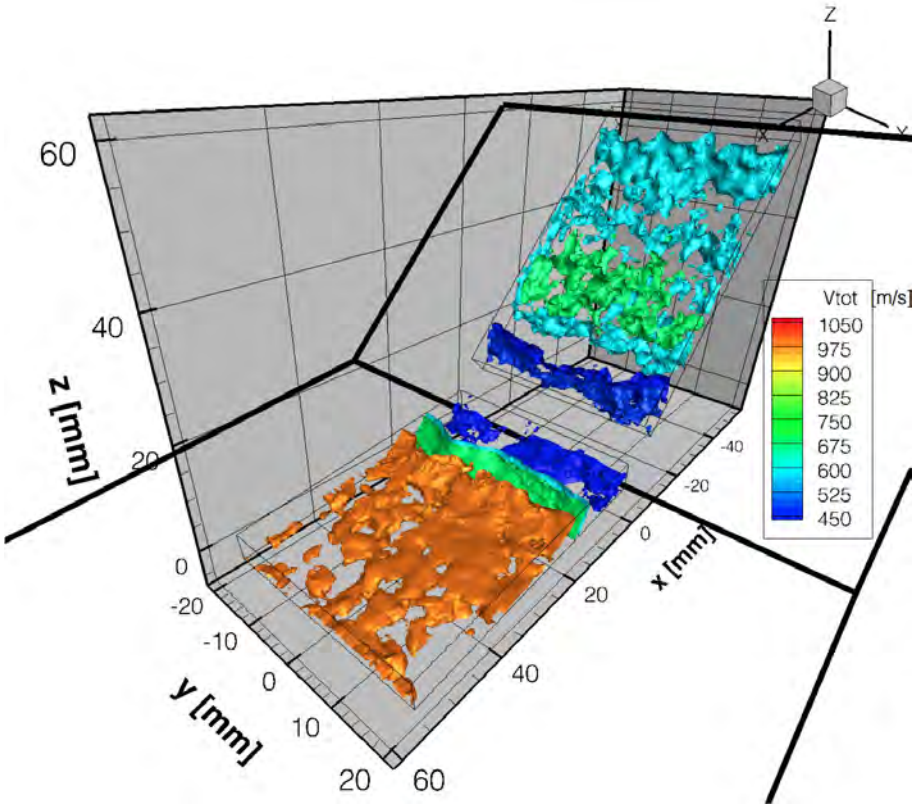

Author:
BSc. Dirk Ekelschot

Supervisor:
dr. ir. Ferry Schrijer

June 28, 2012

TU Delft Delft University of Technology

Challenge the future

Delft University of Technology

Copyright © Aerospace Engineering, Delft University of Technology
All rights reserved.

Delft University of Technology

Investigation of Görtler vortices in hypersonic flow using Quantitative Infrared Thermography (QIRT) and Tomographic Particle Image Velocimetry (Tomo-PIV)

For obtaining the degree of Master of Science in Aerospace Engineering
at Delft University of Technology

Dirk Ekelschot

June 28, 2012

DELFT UNIVERSITY OF TECHNOLOGY
DEPARTMENT OF AERODYNAMICS

The undersigned hereby certify that they have read and recommend to the Faculty of Aerospace Engineering for acceptance the thesis entitled **"Investigation of Görtler vortices in hypersonic flow using Quantitative Infrared Thermography (QIRT) and Tomographic Particle Image Velocimetry (Tomo-PIV)"** by **Dirk Ekelschot** in fulfillment of the requirements for the degree of **Master of Science**.

Supervisors:

dr. ir. F.F.J. Schrijer

prof. dr. F. Scarano

ir. W.J. Bannink

dr. ir. B.W. van Oudheusden

Preface

The following document presents the results of my master thesis project, which is the last examination in order to obtain the Master of Science degree (MSc) at the faculty of Aerospace Engineering at Delft University of Technology (DUT).

The main goal of this thesis project was to obtain a better understanding of the complex flow topology around flap shaped configurations in hypersonic flow. Experimental research was performed in the framework of hypersonic double compression ramp flow in the Hypersonic Test Facility Delft (HTFD).

This document is divided into three main parts: a general flow description of hypersonic double compression ramp flow where theory and measurement data is combined, a presentation of the results obtained by Quantitative Infrared Thermography (QIRT) and Tomographic Particle Image Velocimetry (Tomo-PIV) regarding Görtler vortices and the validation of the application of Tomographic Particle Image Velocimetry in the HTFD.

I would like to thank in particular my supervisor dr. ir. Ferry Schrijer for his guidance and insight. Also I would like to thank all the people who assisted me through the (tough) process of the measurement set-up phase of my thesis, Peter Duyndam, Nico van Beek, Frits Donker Duyvis and Ing. Eric de Keizer.

To my parents and Tatiana, many thanks for your support.

Dirk Ekelschot

Contents

Preface **i**

List of Symbols **viii**

Abstract **x**

1 Introduction **1**
1.1 Background . . . 1
1.2 Project statement . . . 3
1.3 Report outline . . . 4

2 Experimental apparatus **5**
2.1 Description HTFD . . . 5
2.1.1 Storage tube . . . 5
2.1.2 Tandem nozzle . . . 7
2.1.3 Operational envelope . . . 8
2.2 Wind tunnel model . . . 8
2.2.1 Measurability . . . 10
2.2.2 Undisturbed flow region . . . 11
2.2.3 Thermal properties . . . 11
2.2.4 Forces on the model . . . 12
2.2.5 Zig-Zag Vortex Generator . . . 13
2.2.6 Model coordinate system . . . 13
2.2.7 Model characteristics . . . 14

3 Flow measurement techniques **15**
3.1 Schlieren photography . . . 15
3.1.1 Refractive theory . . . 15
3.1.2 Measurement set-up . . . 15
3.1.3 Schlieren example . . . 17
3.2 QIRT . . . 17
3.2.1 Infrared theory . . . 17
3.2.2 QIRT application in the HTFD . . . 19
3.2.3 Data reduction technique . . . 21
3.3 PIV . . . 23
3.3.1 The tracer particles . . . 23
3.3.2 Particle imaging and illumination . . . 25
3.3.3 Image processing . . . 27
3.4 Tomo-PIV . . . 29
3.4.1 Calibration . . . 30
3.4.2 Multiplicative Algebraic Reconstruction Technique (MART) . . . 32

4 Hypersonic double ramp flow **36**
4.1 Flow topology . . . 38
4.1.1 Schlieren Photography . . . 38
4.1.2 General shock lay-out . . . 38
4.1.3 Influence of the VG on the shock lay-out . . . 38

4.1.4 Theoretical pressure distribution on the $5° - 45°$ ramp . . . 39
4.1.5 Particle Image Velocimetry (PIV) measurement campaign . . . 41
4.2 RTM . . . 46
4.2.1 Boundary layer thickness . . . 46
4.2.2 Streamwise heat transfer distribution . . . 47
4.3 VG flow topology . . . 50
4.4 Görtler instability . . . 54
4.5 Görtler vortices . . . 57

5 QIRT campaign **61**
5.1 Influence of the VG . . . 61
5.2 Influence of Reynolds number . . . 63
5.3 Growth rate . . . 66
5.3.1 Growth rate evaluation parallel to the 5° ramp . . . 67
5.3.2 Growth rate evaluation parallel to the 45° ramp . . . 71

6 Tomo-PIV campaign **74**
6.1 Camera set-up . . . 74
6.2 Laser set-up . . . 76
6.3 Refractive effect . . . 78
6.4 Self-calibration . . . 82
6.5 Interrogation volume size . . . 83
6.6 Spurious vector determination . . . 84
6.7 Accuracy estimation . . . 84
6.8 Reconstruction quality estimation . . . 87
6.9 General flow topology . . . 88
6.10 Flow topology 5° ramp . . . 89
6.11 Flow topology 45° ramp . . . 92

7 Conclusions **100**
7.1 Conclusions based on QIRT . . . 100
7.2 Conclusions Tomo-PIV application . . . 101
7.3 Conclusions based on Tomo-PIV . . . 102
7.4 Recommendations . . . 103

A The three separate FOV for 2C-PIV **105**

B Derivation of the entries $(L_{11}, L_{12}, L_{21}, L_{22})$ of the local stability eigenvalue problem **109**

C Heat transfer distribution mapped on the physical coordinates **111**

D Disparity map obtained during self calibration for both FOVs **117**

E Contour plot of the standard deviation in V_x parallel to the 5° ramp **118**

List of Figures

1 Sketch of the investigated windtunnel model and a sketch of the zig-zag Vortex Generator (VG) . . . x

1.1 Maneuverable space vehicles . . . 1
1.2 Examples of experimental space flight testbeds . . . 2
1.3 Double compression ramp models a flap-body control surface . . . 3

2.1 Overview of the HTFD . . . 5
2.2 Tamdem nozzle of the HTFD. Figure taken from Schrijer [2010a] . . . 7
2.3 The undisturbed flow region in the test section [Schrijer, 2010a, Schrijer and Bannink, 2008] 8
2.4 Double compression ramp designs . . . 9
2.5 Double compression ramp model located in the test section of the HTFD. Image taken from Caljouw [2007] . . . 10
2.6 Design plot of the boundary layer thickness against the wedge angle (θ) and the wedge length (L) [Ekelschot, 2012] . . . 11
2.7 Top view of the double compression ramp with Mach waves and the undisturbed region (grey) . . . 11
2.8 Forces and moment on the model . . . 12
2.9 Sketch of the zig-zag VG and the model with corresponding coordinate systems . . . 14
2.10 Determination of the radius of curvature and Görtler number . . . 14

3.1 Graphical representation of Snell's law . . . 16
3.2 Set-up of the Schlieren system in the HTFD. Figure taken from Schrijer [2010a] . . . 16
3.3 General working principle of Schlieren photography . . . 16
3.4 Example of one of the obtained Schlieren images for the case of a zigzag VG with $h = 1.15mm$ and a $Re_{unit} = 14.1 \times 10^6 m^{-1}$. . . . 17
3.5 Planck's law (blue lines) and Wien's law (red line) . . . 18
3.6 radiant thermal budget. Figure taken from Scarano [2007] . . . 18
3.7 The CEDIP camera . . . 20
3.8 The two FOVs for the test case $h_{zz} = 1.15\ mm$ and $Re_{unit} = 14.1 \times 10^6 [m^{-1}]$ . . . 20
3.9 The camera set-up with respect to the test section and the model during a QIRT experiment and the variation in directional emissivity for several electrical nonconductors [Scarano, 2007] . . . 21
3.10 The measured data at a local point in the measurement plane $(x_{pix}, y_{pix}) = (150, 150)$ . . . 21
3.11 Schematic representation of the working principle of a 2C-PIV experiment. Figure taken from Schrijer [2010a] . . . 23
3.12 Cyclone seeder. . . . 24
3.13 Particle velocity plotted together with the velocity of the fluid passing through a shock . . . 25
3.14 Scanning Electron Microscope (SEM) images of the TiO_2 50 nm particle tracers. Figures taken from Schrijer et al. [2005] . . . 25
3.15 The laser set-up . . . 26
3.16 2D cross correlation procedure . . . 27
3.17 graphical representation of window deformation . . . 28
3.18 Block diagram of the iterative image deformation interrogation method . . . 29
3.19 Schematic representation of the working principle of a Tomo-PIV experiment [Elsinga, 2008] 29
3.20 Plate calibration procedure . . . 30
3.21 Schematic representation of the triangulation error. Figure taken from Wieneke [2008]. . . . 31

3.22 Summed disparity map over 1 - 16 images [Wieneke, 2008] . . . 31
3.23 Ghost particles seen by the recording system [Novara et al., 2010] . . . 33
3.24 Quality factor plotted against *ppp* and viewing angle θ figures are all taken from Elsinga [2008] . . . 34

4.1 Flow topology for a single compression ramp. Figure taken from Arnal and Delery [2004] 36
4.2 Typical laminar boundary layer profile compared to a typical separated boundary layer profile . . . 37
4.3 Instantaneous schlieren image for the case $h_{zz} = 0mm$ and $Re = 8.47 \times 10^6 m^{-1}$ . . . 38
4.4 Instantaneous schlieren image for the case $h_{zz} = 1.15mm$ and $Re = 8.47 \times 10^6 m^{-1}$ . . . 39
4.5 Sketch of the $5° - 45°$ model . . . 40
4.6 Overview of the domain of interest during the PIV measurement campaign . . . 41
4.7 Converging mean of V_x at a local data point in the free stream . . . 42
4.8 Macroscopic flow overview by means of a contour map for V_{tot}. V_{tot} is given in m/s . . . 42
4.9 Leading edge shock and separation shock indicated by the colormap of the V_y. V_y is given in m/s . . . 43
4.10 Detailed colormap of the flow angle on the 45° ramp. Flow angle is given in degrees . . . 43
4.11 Detail of the separation bubble upstream of the hinge line of the model. V_{tot} is given in m/s 44
4.12 Recirculation bubble near the hinge line of the model. V_{tot} is given in m/s . . . 45
4.13 Detailed velocity field behind the bow shock on the 45° ramp. V_{tot} is given in m/s . . . 45
4.14 The boundary layer thickness plotted against the streamwise coordinate s . . . 47
4.15 Comparison between the measured c_h on the 5° ramp and c_h determined by the Reference Temperature Method . . . 48
4.16 Example of a streamwise Stanton number distribution for the case of $h_{zz} = 0$, $Re = 14.1 \times 10^6$ $[m^{-1}]$ . . . 49
4.17 The logarithm of the Stanton number (c_h) mapped on the surface coordinate system for the case $h_{zz} = 0mm$, $Re = 14.1 \times 10^6$ m^{-1} . . . 50
4.18 Expected flow topology behind a zig-zag VG . . . 50
4.19 Evolution of the secondary instability [Saric, 1994] . . . 51
4.20 The expected V_y and V_z distribution together with the expected surface heat flux . . . 52
4.21 Results regarding the flow topology around zig-zag in subsonic flow by Elsinga and Westerweel [2012] . . . 52
4.22 Results regarding the flow topology around zig-zag in subsonic flow by Schülein and Trofimov [2011] . . . 53
4.23 Instable flow situation causing the Görtler instability. Figure taken from Saric [1994] . . . 54
4.24 Sketch of Görtler vortices in a boundary layer and a sketch of the model with cylindrical coordinate system . . . 55
4.25 Stability plot [Ekelschot, 2012] . . . 56
4.26 PIV results obtained by Schrijer [2010a] . . . 57
4.27 Growth rate plotted against the Görtler number for three different wavelengths for the two configurations presently discussed [Schrijer, 2010b] . . . 58
4.28 Görtler number plotted against the wavelength parameter for the two configurations presently discused [Schrijer, 2010b] . . . 59
4.29 Test case presented in Luca de et al. [1993] . . . 59

5.1 The mapped heat transfer distributions for all the tested Reynolds numbers and $h_{zz} = 1.15mm$ . . . 62
5.2 Filtering procedure illustrated for $h_{zz} = 1.15$ mm and $Re_{unit} = 14.1 \times 10^6$ $[m^{-1}]$ . . . 62
5.3 The effect of the Reynolds number on the stream wise heat transfer distribution for all h_{zz}. 64
5.4 The effect of the Reynolds number on the spanwise heat transfer distribution at fixed x for all h_{zz} . . . 65
5.5 Noise level comparison . . . 67
5.6 Growth rate plotted in x direction for all h_{zz} . . . 68
5.7 Example of initial disturbance . . . 68
5.8 Examples of secondary disturbance amplification . . . 69
5.9 Example of obtaining the spanwise wavelength by means of autocorrelation . . . 70
5.10 Correlation analysis of the spanwise heat transfer fluctuations . . . 70
5.11 Growth rate plotted in x direction for all h_{zz} . . . 71

5.12 Comparison of the spanwise surface heat flux at three different locations for $h_{zz} = 0.20$ mm and $h_{zz} = 1.15$ mm 72

6.1 Sketch of the double compression ramp with the FOVs 74
6.2 Overview of the Tomo-PIV set-up in the HTFD for the first FOV 75
6.3 Camera orientation with respect to the measurement domain 76
6.4 Overview of the Tomo-PIV set-up in the HTFD for the first FOV 76
6.5 Laser sheet orientation for both measurements parallel to first and parallel to the 45° ramp 77
6.6 The mean Intensity plotted in z direction to check the sheet thickness 78
6.7 Graphical representation of the refractive effect 79
6.8 Three dimensional theoretical error estimation due to the refractive effect 80
6.9 Experimentally determined pixel shift for the three camera set-up used for FOV 1 80
6.10 Graphical representation of the pixel shift caused by a tilted refractive interface 81
6.11 Pixel shift induced by the tilting of the window 82
6.12 Determination of the *ppp* 83
6.13 Measurement accuracy assessment for FOV 1 85
6.14 Measurement accuracy assessment for FOV 2 86
6.15 Correlation factor in x, y, z based on the reconstructed particle distribution 87
6.16 General 3D flow overview 88
6.17 General 3D flow overview 89
6.18 Flow overview parallel to the 5° ramp. Velocity magnitude is given in m/s 90
6.19 Contour map V_x parallel to the 5° ramp 90
6.20 Contour map V_z parallel to the 5° ramp 90
6.21 The spanwise v'_y and v'_z distribution for four fixed x positions 91
6.22 Contour map of V_x with its corresponding contour map v'_y for four different fixed streamwise positions on the 5° ramp 93
6.23 Flow overview parallel to the 45° ramp. Velocity magnitude is given in m/s 94
6.24 The mean streamwise V_x velocity distribution parallel to the 45° ramp 94
6.25 The mean streamwise V_z velocity distribution parallel to the 45° ramp 95
6.26 Contour map for V_x and V_z for four fixed z positions parallel to the 45° ramp 96
6.27 Spanwise velocity perturbations v'_y and v'_z for four fixed x positions 97
6.28 Contour map of the velocity perturbations v'_y and v'_z for four fixed z positions 98

A.1 Sample of a raw PIV images and the corresponding mean velocity field for the first FOV . 106
A.2 Sample of a raw PIV images and the corresponding mean velocity field for the second FOV 107
A.3 Sample of a raw PIV images and the corresponding mean velocity field for the third FOV 108

C.1 The Stanton number (c_h) plotted on the physical model coordinates for the three Reynolds numbers and $h_{zz} = 0$ mm 112
C.2 The Stanton number (c_h) plotted on the physical model coordinates for the three Reynolds numbers and $h_{zz} = 0.20$ mm 113
C.3 The Stanton number (c_h) plotted on the physical model coordinates for the three Reynolds numbers and $h_{zz} = 0.40$ mm 114
C.4 The Stanton number (c_h) plotted on the physical model coordinates for the three Reynolds numbers and $h_{zz} = 0.75$ mm 115
C.5 The Stanton number (c_h) plotted on the physical model coordinates for the three Reynolds numbers and $h_{zz} = 1.15$ mm 116

D.1 Typical disparity map for the three different cameras 117

E.1 Contour map of V_x with its corresponding contour map std_{V_x} for four different fixed streamwise positions on the 5° ramp 119

List of Tables

2.1 Total quantities in the test section depending on the nozzle. The values are taken from Schrijer [2010a] . . . 9

3.1 Number of vectors in x and y direction during the performed 2C-PIV measurements in the HTFD . . . 28

4.1 Local Mach number for all domains . . . 40
4.2 Local Mach number for all domains . . . 46
4.3 Flow conditions behind the leading edge shock . . . 47
4.4 Dimensions of the two tested configurations test by Schrijer [2010b,a] . . . 57
4.5 Dimensions of the two tested configurations test by Luca de et al. [1993] . . . 58

5.1 Test matrix . . . 61

6.1 Geometrical characteristics of the measurement set-up parallel to the 5° ramp . . . 75
6.2 Geometrical characteristics of the measurement set-up parallel to the 45° ramp . . . 77
6.3 Pixel shift . . . 80
6.4 Geometrical characteristics of the measurement set-up parallel to the 5° ramp . . . 83
6.5 Number of vectors . . . 84
6.6 Standard deviation and mean for every velocity component in the (y_1, z_1) plane for the presented test case . . . 85
6.7 Standard deviation and mean for every velocity component in the (y, z) plane for the presented test case . . . 86

7.1 Standard deviation and mean for every velocity component in the (y, z) plane for the presented test case . . . 102
7.2 Standard deviation and mean for every velocity component in the (y, z) plane for the presented test case . . . 102

List of Symbols

x	Longitudinal coordinate $[mm]$	5
y	Spanwise coordinate $[mm]$	14
z	Normal coordinate $[mm]$	14
x_1	Streamwise coordinate tangent to the 5° ramp $[mm]$	14
y_1	Spanwise coordinate defined at the hinge line at the 5° ramp $[mm]$	14
z_1	Normal coordinate at the 5° ramp $[mm]$	14
x_2	Streamwise coordinate tangent to the 45° ramp $[mm]$	14
y_2	Spanwise coordinate defined at the hinge line at the 45° ramp $[mm]$	14
z_2	Normal coordinate at the 45° ramp $[mm]$	14
θ	Ramp angle [°]	14
t	Time $[s]$	5
a	Speed of sound $[m/s]$	6
γ	Specific heat ratio [-]	6
M	Mach number [-]	6
A	Cross sectional area $[mm^2]$	7
d	Diameter $[mm]$	7
p	Pressure $[Pa]$	7
p_t	Total pressure $[Pa]$	8
T	Temperature $[K]$	8
T_t	Total temperature $[K]$	8
T_w	Wall temperature $[K]$	22
ρ_∞	Free stream density [-]	22
μ_∞	Viscosity [mm]	47
R	Gas constant $[\frac{J}{mol \cdot K}]$	8
c_p	Specific heat $[\frac{J}{kg \cdot K}]$	8
h_{aw}	Enthalpy at a adiabatic wall $[\frac{J}{kg}]$	22
h_w	Enthalphy at the wall $[\frac{J}{kg}]$	22
L_1	Tangent length of the first ramp $[mm]$	14
L_2	Tangent length of the second ramp $[mm]$	14
h_{zz}	Height of the VG [mm]	10
λ_{zz}	Spanwise wavelength of the VG [mm]	61
G	Görtler number [-]	10
σ	Growth rate [-]	66
β	Non dimensional wave number [-]	56
n	Refraction index [-]	15
φ	Rotational angle around the x-axis [°]	74
θ	Rotational angle around the y-axis [°]	74
ω	Rotational angle around the z-axis [°]	74
$\vec{v}$	Velocity vector [-]	27
Vx	Velocity component in the defined x direction $[m/s]$	91
Vy	Velocity component in the defined y direction $[m/s]$	91
Vz	Velocity component in the defined z direction $[m/s]$	91
v'_x	Velocity fluctuation in the defined x direction $[m/s]$	91
v'_y	Velocity fluctuation in the defined y direction $[m/s]$	91
v'_z	Velocity fluctuation in the defined z direction $[m/s]$	91
$\frac{Re}{m}$	Unit reynolds number $[\frac{1}{m}]$	8
ϵ	emissivity [-]	10

I Particle intensity [-] 27
N_{tot} Total number of pixels [-] 28
ppp Particle Per Pixel [-] 28
ppv Particle Per Voxel [-] 78
$\alpha_{i,j}$ Pixel gain [-] 19
$\beta_{i,j}$ Pixel offset [-] 19
U_e Total velocity at the edge of the boundary layer [m/s] 22
St Stanton number [-] 22
c_h Stanton number [-] 22
C_f Friction coefficient [-] 46
q_s Heat transfer $[-k\frac{\partial T}{\partial y}]$ 22
δ Boundary layer thickness [mm] 47
$\vec{d}$ Disparity vector [pix] 31
$\bar{\sigma}$ Disparity vector [pix] 84
N_r Number of runs [-] 84
vox_x Number of voxels in x direction [-] 34
vox_y Number of voxels in y direction [-] 34
vox_z Number of voxels in z direction [-] 34

Abstract

Aerodynamic heating is one of the driving aspects in hypersonic vehicle design. During take-off and re-entry, high heat loads are encountered for which the appropriate measures have to be considered. In particular during the re-entry phase, high maneuverability of the vehicle is preferred such that reusable (manned) spacecraft can land on conventional runways. Control devices are therefore a necessity to improve the maneuverability of the spacecraft. Consequently, the hypersonic flow behaviour around control flaps is thoroughly investigated over the last decades. Boundary layer separation/reattachment and shock wave interaction are general flow phenomena that occur in hypersonic double ramp flow. Furthermore, streamwise periodic counter rotating vortices (Görtler vortices) tend to grow in the boundary layer over the control surface. Görtler vortices are induced by the centrifugal forces associated with the change in direction of motion forced on the fluid by the concave geometry of the surface. Görtler vortices take the form of a striation pattern and considerably modify the heat flux and can cause spanwise heat transfer variations of 100%.

An experimental study is performed in the Hypersonic Test Facility Delft (HTFD) using a scaled double compression ramp wind tunnel model that represents a flap body control surface. A zig-zag Vortex Generator (VG) is pasted near the leading edge of the model to ensure that steady spanwise periodic longitudinal structures are present in the boundary layer. In this way a controlled investigation is performed on the amplification of longitudinal vortices due to the concave geometry of the model.

During this thesis project, Quantitative Infrared Thermography (QIRT) and Tomographic Particle Image Velocimetry (Tomo-PIV) measurements are performed to investigate the development of Görtler vortices in hypersonic double compression ramp flow at Mach 7.5. QIRT is used to obtain results regarding the growth rate of Görtler vortices while Tomo-PIV gives more insight on the local three dimensional flow behaviour. Therefore the concave wind tunnel model also serves as a initial test case to verify whether Tomo-PIV is applicable in the (Hypersonic Test Facility Delft) HTFD.

A $5° - 45°$ double compression ramp model is tested with $L_1 = 150mm$ and $L_2 = 80.9mm$ where L_1 and L_2 are the tangent wedge lengths of the 5° and 45° ramp, respectively.

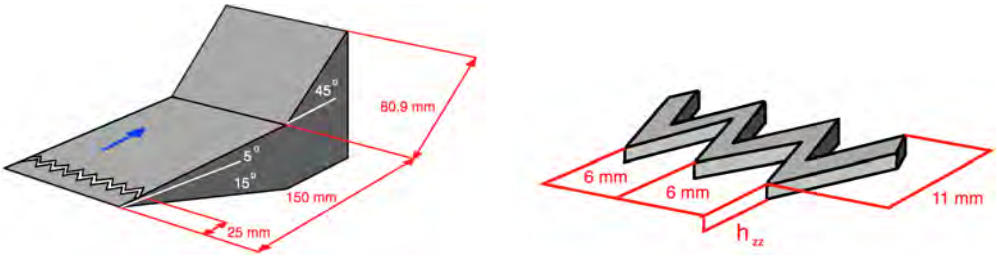

(a) The investigated windtunnel model (b) Sketch of the zig-zag Vortex Generator

Figure 1: Sketch of the investigated windtunnel model and a sketch of the zig-zag Vortex Generator (VG)

The influence of the height of the zig-zag strip (h_{zz}) and the Reynolds number on the amplification of these longitudinal structures is investigated. The wavelength of the VG ($\lambda_{VG} = 6\ mm$) and the streamwise width ($w_{zz} = 11\ mm$) are fixed and the height is varied within the given range of

$h_{zz} = [0, 0.20, 0.40, 0.75, 1.15]$ mm. Measurements are performed at three unit Reynolds numbers, $Re_{unit} = 8.47 \times 10^6[m^{-1}]$, $Re_{unit} = 11.3 \times 10^6[m^{-1}]$ and $Re_{unit} = 14.1 \times 10^6[m^{-1}]$. The VG is located at $2.5mm$ from the leading edge of the model.

Initially, a Schlieren photography measurement campaign is performed to obtain the stability and topology of the shock pattern which is useful for supporting and providing a better understanding of the obtained QIRT and Tomo-PIV results. The flow topology and shock interactions due to the geometry of the model are used to determine the local flow properties by determining the corresponding hodograph. The theoretical analysis based on the quantitative flow overview is used to ascribe local flow behaviour measured during the Tomo-PIV measurement campaign.

QIRT measurements are performed to obtain the heat flux distribution at the surface of the model. Flow characteristics near the wall are obtained such as boundary layer separation and reattachment. Furthermore, the spanwise heat flux distribution is investigated and based on the local spanwise fluctuations induced by the VG, the growth rate of the longitudinal vortices is quantified. The effect of the height of the VG and Reynolds number on the longitudinal vortex propagation is determined.

The QIRT results show a clear sinusoidal spanwise heat flux fluctuation with a wavelength that corresponds to $\lambda_{VG} = 6mm$. The influence of the Reynolds number on the heat transfer distribution is investigated in local streamwise and spanwise direction. The streamwise thermograms indicate that boundary layer separation occurs more downstream when the Reynolds number is increased. In spanwise direction it is found that for the case of $h_{zz} = 1.15mm$, the spanwise heat transfer fluctuations break up into smaller streaks. The intensity of this behaviour is dependent on the Reynolds number. For some test cases, the two dimensional heat transfer map shows a curved separation line which might be caused due to a bad pasting of the VG.

The growth rate is quantified by the ratio of the spanwise heat transfer fluctuation at a local streamwise position on the model and the spanwise heat transfer fluctuation at a fixed position near the leading edge. Since the separation line is curved, it is chosen to locally investigate the growth rate of the Görtler vortices. For all h_{zz} it is found that the growth rate is below 1 on the 5° ramp which indicates that the longitudinal structures dissipate in streamwise direction. The intensity of the spanwise heat transfer fluctuations are again amplified on the 45° ramp. The growth rate reaches a local maximum of 15 for the case $h_{zz} = 0.2$ mm on the 45° while the maximum growth rate for the other cases is significantly lower ($\pm\sigma = 4$). Furthermore a characteristic streamwise $x - \sigma$ profile is found for all cases.

A detail 3D velocity field is obtained using Tomo-PIV. Experiments are performed for $h_{zz} = 1.15$ mm and $Re_{unit} = 14.1 \times 10^6$ $[m^{-1}]$. The 3D velocity field parallel to the 5° ramp and the 45° ramp is locally measured by choosing 2 Field Of Views (FOV) of 60 mm × 40 mm × 6 mm. One FOV parallel to the 5° ramp and one parallel to the 45°.

The application of Tomo-PIV in the HTFD is verified. A flexible set-up is chosen such that both $FOVs$ are optically accessible. The model is placed in the test section such that the surface of the model is aligned with the window of the tunnel. A laser sheet of approximately 6 mm thick is placed parallel to the 5° and 45° ramp such that the velocity field is measured approximately 2 mm above the surface of the model.

Due to the high convective streamwise velocity, difficulties are encountered for the measurement of the out of plane velocity component. In both, the streamwise and spanwise velocity component, clear fluctuations are measured. The fluctuations are rather small with respect to the local convective velocity and in particular on the FOV parallel to the 5° ramp, the wakes induced by the VG are clearly visible. The fluctuations in streamwise and spanwise velocity component are 10 m/s and 1 m/s, respectively. Dividing the fluctuations by the corresponding convective velocity gives a 1 % fluctuation in V_x and a 10 % fluctuation in V_y. The out of plane velocity component shows a fluctuating spanwise behaviour which is difficult to quantify. Furthermore, the in-depth resolution is lower since the velocity in this direction is significantly lower ($\Delta pix_z = 2$ pix) compared to the velocity in streamwise direction ($\Delta pix = 30$ pix).

Similar problems regarding the out of plane velocity component were encountered during the measurement of the 3D velocity field parallel to the 45° ramp. Higher rms values were obtained during the validation process, compared to the velocity field measurement parallel to the 5° ramp. This can be

ascribed to the limited optical accessibility. Furthermore, the complex shock pattern that is located above the 45° caused local particle blurring. This effect influences the quality of the reconstruction, and therefore, the measurement outcome.

Chapter 1

Introduction

1.1 Background

Hypersonic research has been developing since the beginning of the 20th century after Konstantin Tsiolkovsky wrote *The Exploration of cosmic space by means of reaction devices* in 1903, in which he described the general problems regarding rocket flight in space. It was soon found that the compressibility of the flow brings new flow features to investigate such as aerothermaldynamic effects, shock wave interaction and shock wave boundary layer interaction (SWBLI).

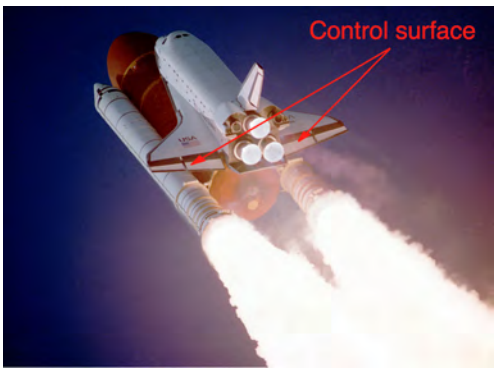

(a) Space shuttle during the launch phase

(b) Artist impression of the X-38 CVR

(c) Artist impression of the X-37 in re-entry phase

Figure 1.1: Maneuverable space vehicles

At first, knowledge about hypersonic aerodynamics was used for military purposes such as the V2 rocket during the second world war. After the second world war, scientists developed an interest in creating space programs which would eventually bring our society to where it is now. In particular during the cold war, hypersonic investigation developed rapidly. Human space flight was realised and engineers came up with concepts of a spacecraft which could return humans back to Earth from outer space. Initially this has been done by using capsule shaped re-entry vehicles but later on, during the late 1970's, the first

concept designs were drawn by U.S engineers for the first reusable spacecraft, the space shuttle. The space shuttle, shown in figure 1.1(a), was operational from 1981 until last year. It launched a variety of satellites, interplanetary probes and during its final years it conducted servicing for the International Space Station (ISS). At the end of its operation, the space shuttle could land on a conventional runway which indicated the potential of (semi)-reuseable space vehicles.

The X-38 program, shown in figure 1.1(b), started in 1995 to provide data for the development of the Crew Return Vehicle (CVR) for the International Space Station (ISS). It was derived from the earlier lifting body concept (X-23/X-24 projects) during the 1960's. It could serve as a manned spacecraft that could be launched on top of a Expandable Launch Vehicle (ELV). During the X-38 program the performance of Thermal Protection System (TPS) was improved. However, this project was cancelled in 2002 because of limited financing and the focus shifted towards Orbital Space Planes (OSP). The X-37, shown in figure 1.1(c), is a OSP and still under development. It is a short winged and unmanned space plane whose design is derived from the Air Force's Space Maneuver Vehicle (SMV) program. In April 2010 a first drop test was performed where the TPS system and the aerodynamic handling was tested. In March 2011 the first orbital flight was performed and the X-37 was launched on top of a Delta 2 or Delta 4 launcher.

During the re-enrty phase, high maneuverability of the vehicle is preferred such that it is possible to decelerate in low density regimes in the atmosphere. This reduces the heat loads significantly. Next to that, the retrieval of payload, for example humans, is made possible and furthermore, the cross range of the vehicle is increased which improves the flexibility of the mission. Control surfaces are used to increase the maneuverable capacity of the space vehicle and these geometrical deflections lead to complex flow structures. In particular boundary layer reattachment leads to a local decrease in boundary layer thickness which causes locally high heat loads for which should be accounted for. Hence, hypersonic flow over flaps and rudders of re-entry vehicles are investigated numerically and experimentally, both on the ground and in space flight operation.

Experimental testbeds

ESA has started the European eXPErimental Reentry Testbed (EXPERT) program whose main objective is to collect aerothermodynamic flight data to validate ground test facilities and verification techniques. The critical aerothermodynamic phenomena such as boundary layer transition, shock layer interactions, plasma chemical composition, SWBLI and real-gas effects are investigated. The data that is gathered during EXPERT missions is used to validate the current computational fluid dynamic codes and the current design modeling tools. Furthermore, the data is used to correlate ground test results. An artist impression of EXPERT in flight is given in figure 1.2(a).

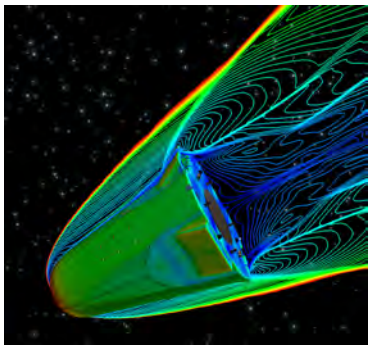

(a) Artist impression of EXPERT in re-entry phase

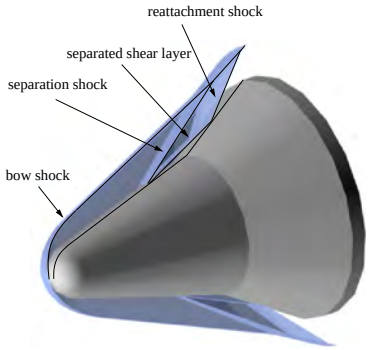

(b) Artist impression of DART with the typical boundary layer separation and reattachment

Figure 1.2: Examples of experimental space flight testbeds

TU Delft proposed the Delft Aerospace Re-entry Test program (DART) project in 1999. The project

consists of a small reusable ballistic re-enty vehicle which is used to collect aerothermodynamic data so that particular flow phenomena, such as, boundary layer separation/reattachment and SWBLI, can be better understood. Computational codes and experimental test results are validated and verified by comparing them with the realtime data. Furthermore, DART gives the opportunity to test micro gravity payloads. An artist impression of the DART design is given in figure 1.2(b).

Experimental research in a ground facility

Flow topology around such control surfaces is investigated on ground facilities as well. A flap-body control surface is represented by a scaled double compression ramp wind tunnel model. In figure 1.3 the deflected control surfaces of the X-38 vehicle is shown together with the double compression ramp wind tunnel model used during this master thesis project.

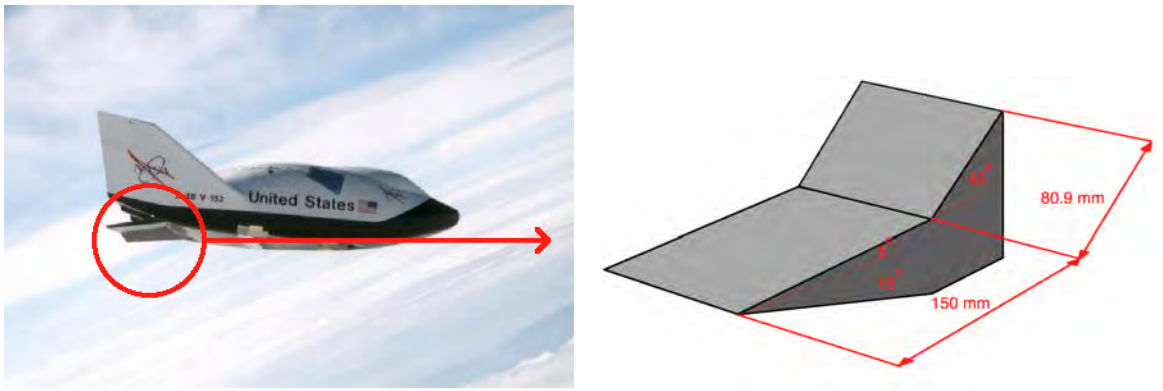

(a) The X-38 model with deflected control surfaces (b) Double compression ramp model

Figure 1.3: Double compression ramp models a flap-body control surface

At ground test facilities such as the Hypersonic Test Facility Delft (HTFD), these double compression ramp wind tunnel models are used to investigate the complex flow behaviour around a flap shaped geometry. Heat transfer measurements for a double compression ramp with various back ramp angles were performed and it was found that a local peak of heat transfer is present at the location where flow reattachment occurs. By means of theoretical analysis, Schlieren photography and 2C-PIV, a better overview of separation and reattachment is obtained, to allowing to infer the influence of this flow behaviour on the isentropic flow.

As a result, new projects are defined to perform flow analysis, particularly to investigate secondary flow phenomena. Streamwise periodic counter rotating vortices (Görtler vortices) are known to grow in the boundary layer over a concave wall. These longitudinal vortices can be induced by leading edge imperfections and amplified by the curvature of the geometry and cause spanwise heat transfer variations of 100 %. Görtler vortices take the form of a striation pattern and considerably modify the heat flux. They are observed in supersonic nozzles, swept wing configuration and flap deflections. Due to large amplitude Görtler vortices, secondary instabilities occur which may lead to boundary layer and transition to turbulence. Also this vortical instability of the flow could promote transition in the shear layer at low Reynolds numbers.

1.2 Project statement

The aim of this thesis project is to obtain a three dimensional impression of hypersonic double compression ramp flow by means of Schlieren photography, 2C-Particle Image Velocimetry (2C-PIV), Quantitative Infrared Thermography (QIRT) and Tomographic Particle Image Velocimetry (Tomo-PIV).

Schlieren photography and 2C-PIV are applied to obtain general flow characteristics such as shock patterns and a first impression of the velocity field around a concave geometry in hypersonic flow. QIRT and Tomo-PIV are applied to obtain quantitative flow characteristics at a overall and detailed scale. These

techniques are used to investigate Görtler vortices in hypersonic double compression ramp flow. The validation and application of Tomographic Particle Image Velocimetry (Tomo-PIV) in the HTFD is a significant part of the results of this thesis.

1.3 Report outline

This report is structured in seven chapters. In chapter 2, the experimental apparatus is discussed. The reader is introduced with a description of the HTFD and the windtunnel model that is investigated during this thesis project. The working principles of the applied flow measurement techniques are discussed in chapter 3.

Chapter 4 consists of a general description of hypersonic double compression ramp flow. The flow analysis is shown for the geometry of the test model. Based on the theoretical analysis and the previously performed literature study, a list of expected results is drawn. This chapter makes clear what the contribution of this research project is with respect to the available literature.

Chapter 5 and 6 form the core part of this thesis report. The measurement campaigns together with the corresponding measurement objectives are given. These chapters reveal the results which were found during the experimental assessment phase of this project. In chapter 7, the conclusions and recommendations are presented.

Chapter 2

Experimental apparatus

In this chapter, the working principle of the Hypersonic Test Facility Delft (HTFD) is described. The operational envelope is given and the reader is introduced to the free stream flow conditions that are valid for the current experiments. Furthermore a detailed description is given of the wind tunnel model. A list of model requirements is determined and further discussed in the last section of this chapter.

2.1 Description of Hypersonic Test Facility Delft (HTFD)

The Hypersonic Test Facility Delft (HTFD) is a Ludwieg tube concept tunnel. This concept relies on the principle of a high pressure difference between the storage tube and the vacuum charge tank with a fast acting valve upstream of the nozzle. When the valve is opened, the fluid flows from the storage tube into the nozzle. The appropriate Mach number is set in the test section by changing the area ratio of the nozzle with respect to the test section. In figure 2.1 a schematic representation of the operating principle of HTFD is given together with a picture of the HTFD.

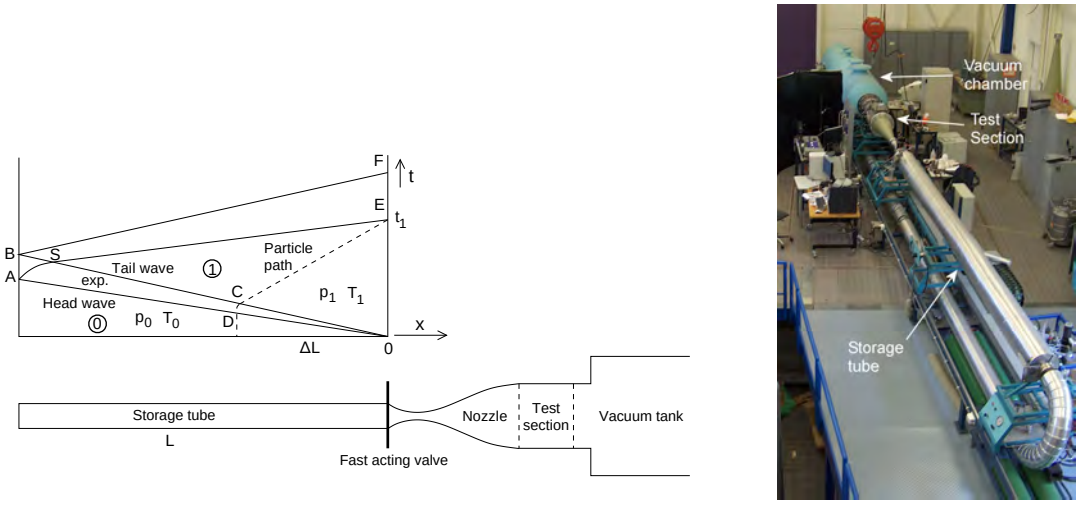

(a) Operating principle of the HTFD

(b) Picture of the HTFD

Figure 2.1: Overview of the HTFD

2.1.1 Storage tube

Air is pressurised, typically 6 to 10 MPa, and stored at high temperature ($500K$) in the storage tube, see figure 2.1(b). When the fast acting valve is opened impulsively, a centered expansion wave travels upstream into the storage tube. Using simple wave theory [Bakker and van Leer, 2005], the flow conditions in the storage tube can be determined. In figure 2.1(a) the (x,t) diagram is given of the flow process. From

this it can be seen that the region under line $0A$ is a simple domain where along the J^+ characteristic connecting domain 0 and 1 the following relation holds:

$$\begin{aligned} J^+ : u_1 + \frac{2a_1}{\gamma-1} = \frac{2a_0}{\gamma-1} \rightarrow \frac{u_1}{a_1} + \frac{2}{\gamma-1} = \frac{2a_0}{a_1(\gamma-1)} \\ \rightarrow a_0 = a_1\frac{(\gamma-1)}{2}M_1 + a_1 \rightarrow \frac{u_1}{a_0} = \frac{M_1}{1+\frac{\gamma-1}{2}M_1} \end{aligned} \tag{2.1}$$

where the subscript 0 indicates the flow condition upfront of the expansion wave and 1 the flow conditions behind the expansion wave. The symbol a indicates the speed of sound and u the local flow velocity. The specific heat ratio is indicated by γ and M represents the local Mach number:

$$M = \frac{u}{a} \tag{2.2}$$

The running time of the HTFD is defined as the time it takes for a particle to move from point 0 to point E in the (x,t) diagram indicated by t_1 in figure 2.1(a).

The measurement time can be determined using the differential equation that holds along J^+ AS with boundary condition $x = -L$ $t_A = \frac{L}{a_0}$ [Schrijer, 2010a]:

$$\frac{dx}{dt} = u + a = \frac{1}{\gamma+1}\left(4a_0 + (3-\gamma)\frac{x}{t}\right) \tag{2.3}$$

From equation 2.3 the time at point (x_S, t_S) can be determined. From the simple domain 0SE it is known that along $J^+ : \frac{dx}{dt} = a_1 + u_1$, hence:

$$t_1 = t_S - \frac{dt}{dx}x_S = t_S - \frac{x_S}{a_1 + u_1} \tag{2.4}$$

Rewritting equation 2.4 gives:

$$t_1 = \frac{L}{a_0}\frac{2}{1+M_1}\left(1 + \frac{\gamma-1}{2}M_1\right)^{\frac{\gamma+1}{2(\gamma-1)}} \tag{2.5}$$

which is defined as the running time of the HTFD. Based on experiments and the theoretical relation given in equation 2.5 $t_1 \approx 120\ ms$. Finally the diameter of the first throat with respect to the tube diameter determines the Mach number. This relation is as follows:

$$\left(\frac{d_{tube}}{d^*}\right)^2 = \frac{1}{M_1}\left[\frac{2}{\gamma+1}\left(1 + \frac{\gamma-1}{2}M_1^2\right)\right]^{\frac{\gamma+1}{2(\gamma-1)}} \tag{2.6}$$

where M_1 is the Mach number behind the expansion wave into the storage tube, $d_{tube} = 48.25mm$ is fixed by the storage tube and the first throat diameter $d^* = 19.35\ mm$ which sets a fixed Mach number $M_1 = 0.09$. Based on this Mach number and the condition upstream of the expansion wave, the measurement time is determined.

Prevention of condensation

Part of the storage tube is heated to prevent condensation in the free stream due to the low static temperature in the test section [Schrijer and Bannink, 2008]. In order to reduce the amount of energy required for heating up the tube and to increase the run time, only the section of the storage tube is heated that contains the air that is used during the run. The most upstream particle that can reach the valve within t_1, determines the length of the storage tube that is heated. This is indicated in figure 2.1(a) by the particle path DCE.

$$\Delta L = M_1\frac{a_1 - u_1}{a_0}2L \tag{2.7}$$

The storage tube consists therefore of a cold and a hot section. Hence the temperature discontinuity at ΔL causes wave reflection [Schrijer, 2010a]. This is prevented by increasing the cross sectional area of the cold storage tube according to equation 2.8

$$\frac{d_{hot}}{d_{cold}} = \left(\frac{T_{cold}}{T_{hot}}\right)^{\frac{1}{4}} \tag{2.8}$$

Equation 2.8 is based on the mass conservation over a contact discontinuity.

2.1.2 Tandem nozzle

From the Area-Mach number relation [Anderson, 2005] it is known that the Mach number at any location downstream of a nozzle is dependent on the ratio of the nozzle diameter and the local diameter squared. The throat diameter is limited by the smallest cross section present in the valve. When the throttle nozzle is connected directly to the test section, the Mach number in the test section exceeds $M = 9$. Hence a tandem nozzle is used to test at lower Mach numbers. The nozzle that guides the flow to the test section has a conical shape with a 15° opening angle. In figure 2.2 the tandem nozzle of the HTFD is shown.

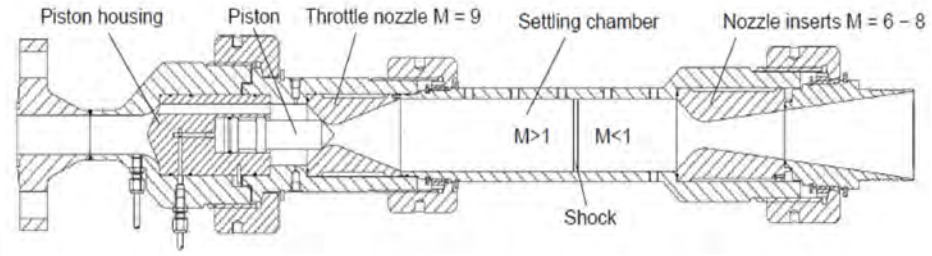

Figure 2.2: Tamdem nozzle of the HTFD. Figure taken from Schrijer [2010a]

The first nozzle has a fixed diameter which sets the Mach number in the settling chamber equal to 9 after which the flow is slowed down by a normal shock. The subsonic flow enters the second nozzle to increase the Mach number again up to a range of $6 \leq M \leq 8$ depending the geometry of the second nozzle. The normal shock causes a total pressure decrease which is dependent on both nozzle diameters d_1^* and d_2^*. From the conservation of mass:

$$\frac{p_{t,1}}{p_{t,2}} = \frac{A_{t,2}}{A_{t,1}} = \left(\frac{d_2^*}{d_1^*}\right)^2 \tag{2.9}$$

Equation 2.9 has been validated by taking pressure measurements in the test section as well. It is observed that for $\frac{d_1}{d_2} = \frac{19.35}{34.3} = 0.32$ and $p_{t,1} = 83\ bar$, $p_{t,2} = 28.8$, so that $\frac{p_{t,2}}{p_{t,1}} = \frac{28.8}{83} = 0.35$. The discrepancy found might be due to a present shock train in the tandem nozzle [Schrijer, 2010a]. The total pressure in the test section, $p_{t,1}$, is used to calculate the unit Reynolds number and therefore $p_{t,1}$ is corrected using the previously obtained values:

$$p_{t,1} = p_{t,2}\left(\frac{d_2^*}{d_1^*}\right)^2 \frac{0.35}{0.32} \tag{2.10}$$

For the Mach 7 nozzle it was found that $M = 7.5 \pm 0.1$ and $p_t = 27.9 \pm 0.1$. When a Mach number higher than 9 is wanted in the test section, the first nozzle is directly connected to the test section. The area ratio of the test section and the second nozzle throat finally determines the Mach number in the test section.

$$\frac{A}{A_{t,2}} = \frac{1}{M}\left(\frac{2}{\gamma+1} + \frac{\gamma-1}{\gamma+1}M^2\right)^{\frac{\gamma+1}{2(\gamma-1)}} \tag{2.11}$$

It has to be taken into account that the displacement thickness of the conical nozzle downstream of the second throat has an influence on the cross sectional area of the test section. For the M7 nozzle, PIV

measurements are performed at the end of the conical nozzle and a displacement thickness of 11 mm was measured [Schrijer, 2010a]. This decreases the cross sectional area and thus the Mach number as well. From 1D inviscid theory a Mach number of 7.7 was calculated which is corrected to $M_{\infty,cor} = 7.5$ based on the boundary layer thickness. This effect is taken into account during the further elaboration of the operation envelope of the HTFD.

2.1.3 Operational envelope

The discontinuity between the conical nozzle and the cylindrical test section causes compression waves which limits the useable free stream flow. These waves make an angle of 7° with respect to the test section when the M7 nozzle is used. This geometry of the connection between the nozzle and the test section is shown in figure 2.3(a). The window is represented by the dashed circle. Particle Image Velocimetry (PIV) result shown in figure 2.3(b), indicates a change in V_y induced by the presence of the shock emanating from the test section junction. It also shows a slight divergent flow behaviour in the test section induced by the cylindrical nozzle. Overall, an undisturbed region of 200 mm by 200 mm around the center line of the test section is observed. Furthermore, a streamwise velocity of $V_x = 1033\ m/s$ was measured.

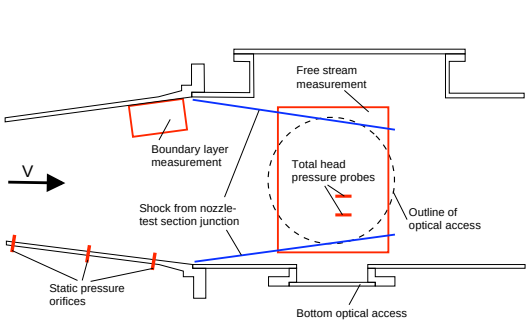

(a) Geometry of the nozzle test section junction and the induced shock wave influence on the uniformity of the test section flow

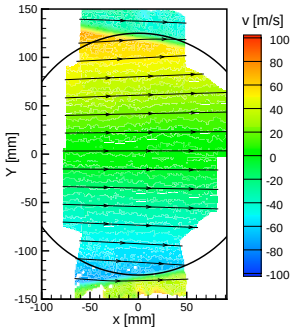

(b) The streamlines plotted obtained from a PIV measurement where the upper and lower shock are clearly visible by plotting the vertical velocity component

Figure 2.3: The undisturbed flow region in the test section [Schrijer, 2010a, Schrijer and Bannink, 2008]

The static and total temperature can be determined since the velocity and the Mach number is known. The static temperature T is dependent on the free stream velocity and the Mach number which follows directly from the definition of the speed of sound ($a = \sqrt{\gamma RT}$).

$$T = \frac{\left(\frac{|V|}{M}\right)^2}{\gamma R} \tag{2.12}$$

where R is the gas constant. The total temperature T_t is given by:

$$T_t = T + \frac{|V|}{2c_p} \tag{2.13}$$

where c_p is the specific heat. The range of unit Reynolds numbers can be determined since the Mach number and total temperature for a given nozzle configuration is known. The free stream velocity is measured with PIV and from equations 2.12 and 2.13 the total temperature is determined. In the same way, the free stream total quantities for the M6, M8, M9 and M10 nozzles are given in table 2.1 .

2.2 Wind tunnel model

The flow topology around a flap-body control surface of a re-entry vehicle is reproduced by means of a double compression ramp wind tunnel model. A double ramp model consist usually of two inclined flat

Table 2.1: Total quantities in the test section depending on the nozzle. The values are taken from Schrijer [2010a]

Nozzle	M	p_t $[bar]$	T_t $[K]$	$Re/m \times 10^6$
M6	6.4 6.5	2.8 14.3	579 579	1.61 7.9
M7	7.4 7.5	5.4 28.0	579 579	2.22 11.05
M8	8.4 8.5	10.0 51.2	579 579	3.07 15.08
M9	9.4 9.5	20 88	585 585	4.65 19.70
M10	10.3 10.5	20 88	585 585	3.76 15.85

plate geometries aligned in streamwise direction. An example of the representation of a double compression ramp model is given in figure 1.3. It shows the X-38 re-entry vehicle with deflected control surfaces together with the double compression ramp model that is tested during the current experiments.

Typical primary flow features that are encountered in hypersonic double compression ramp flow are boundary layer separation, boundary layer reattachment, Shock Wave Interaction (SWI) and Shock Wave Boundary Layer Interaction (SWBLI). In particular, boundary layer separation and reattachment is investigated during the current thesis work.

Measurements are performed regarding the characteristic flow features that occur in hypersonic flow over a double compression ramp. In particular, streamwise longitudinal vortices (Görtler vortices), which are discussed in chapter 4, are investigated by means of Quantitative Infrared Thermography (QIRT) and Tomographic Particle Image Velocimetry (Tomo-PIV).

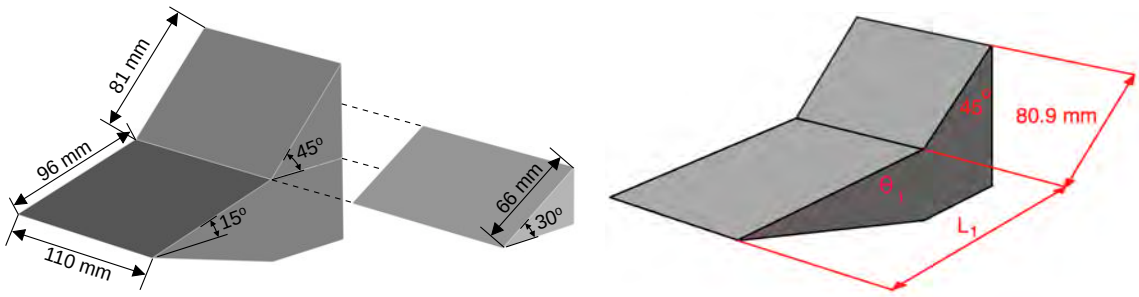

(a) Double compression ramp model used during previous experiments in the HTFD [Schrijer, 2010a].

(b) Double compression ramp model with undetermined dimensions θ_1 and L_1 and the double compression ramp shown inside of the test section

Figure 2.4: Double compression ramp designs

Previous research is performed regarding double compression ramp flow in the HTFD [Schrijer, 2010a]. The tested model is shown in figure 2.4(a). The first ramp had fixed dimensions and two different second wedge angle (30° and 45°) were tested. The boundary layer thickness (δ) on the first ramp is in the order of 1 mm which would limit the visibility of the longitudinal vortices since they scale with δ. Therefore, the driving requirement for the wind tunnel is to improve the visibility of the longitudinal structures by designing for the appropriate new first ramp dimensions. The dimensions of the first ramp (L_1, θ_1), as shown in figure 2.4(b), are determined in this section. The available 45° ramp is used as a fixed second ramp during the current experiments. The list of requirements that the model should fulfill are the following:

1. The model should fit in the limited space of the test section

2. The model should be compatible with the available 45° ramp
3. The model should be optically accessible over its full length
4. The model itself and the boundary layer thickness should be as large as possible
5. The model should have a low thermal product (ρck) where ρ is the density, c the specific thermal capacity and k the thermal conductivity coefficient and high emissivity ϵ.

Requirement 1 and 2 are dependent on the undisturbed flow regime in the test section (200 mm by 200 mm, see figure 2.5) and on the streamwise dimension of the 45° ramp, respectively. It is determined that $L_1 = 150$ mm is the maximum allowed streamwise length of the first ramp since the streamwise dimension of the second ramp is 57 mm. Requirement 3 should be fulfilled to be able to perform PIV measurements over the full streamwise length of the model. This requirement is highly dependent on the first requirement since the windows are sized based on the undisturbed flow regime. Requirement 4 is driven by the measurability of the longitudinal structures and requirement 5 ensures the optimisation of the application of QIRT during the current experiments.

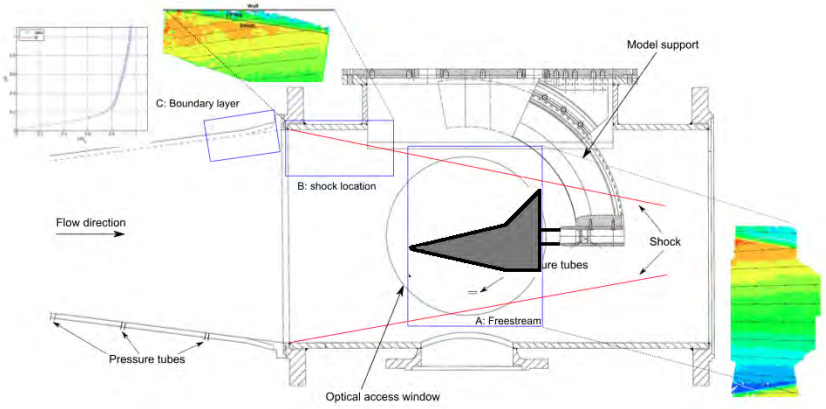

Figure 2.5: Double compression ramp model located in the test section of the HTFD. Image taken from Caljouw [2007]

2.2.1 Measurability

Tomo-PIV is used to investigate the 3D velocity field parallel to the surface of a double compression ramp. In particular the streamwise development of longitudinal vortices (Görtler vortices) in the boundary layer are considered to be the main topic. For visualisation purposes it is therefore desired to increase the boundary layer thickness since the boundary layer instabilities of interest scale with the boundary layer thickness. The boundary layer thickness increases with ramp length:

$$\delta \propto \frac{1}{\sqrt{Re_s}} \tag{2.14}$$

where δ is the boundary layer thickness, s represents the streamwise coordinate tangent to the ramp surface with $s = 0$ at the leading edge. Re_s is the streamwise Reynolds number:

$$Re_s = \frac{\rho U s}{\mu} \tag{2.15}$$

The density is represented by ρ, U is the velocity and μ the viscosity coefficient. According to the oblique shock wave theory, the boundary layer thickness increases with a decreasing wedge angle. In figure 2.6, the boundary layer thickness is plotted against the ramp length and wedge angle.

Based on figure 2.6 and the limited spectral response of the infrared camera, it is chosen to test a double compression ramp model with a upstream ramp of 150 mm and a wedge angle of 5°.

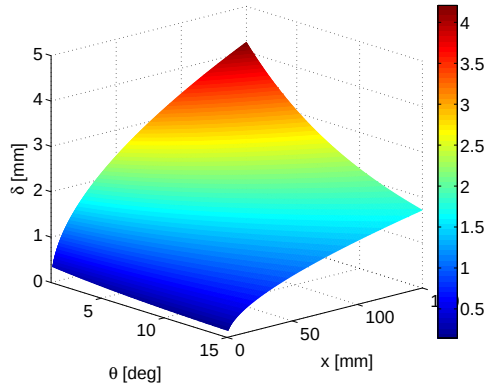

Figure 2.6: Design plot of the boundary layer thickness against the wedge angle (θ) and the wedge length (L) [Ekelschot, 2012]

2.2.2 Undisturbed flow region

Tomo-PIV experiments are performed to measure the 3D velocity field in a thin volume parallel to the first and second ramp. In particular the region in the middle of the model should therefore be free from any unwanted disturbances. The width of the model is determined based on the the undisturbed flow regime above the surface of the model. Mach waves originate from each side of the model due to finite length of the span. The Mach angle can be calculated using equation 2.16:

$$\mu = \arcsin \frac{1}{M_\infty} \tag{2.16}$$

Based on this equation, the undisturbed flow domain can be determined which is shown in figure 2.7:

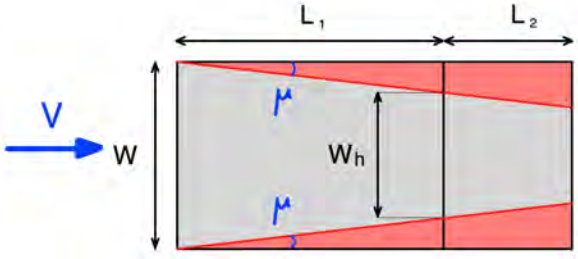

Figure 2.7: Top view of the double compression ramp with Mach waves and the undisturbed region (grey)

The mach angle is calculated since $M_\infty = 7.5$ and thus $\mu = 7.67°$. This results in a undisturbed width at the first-to-second ramp junction of:

$$w_h = w - 2L_1 \tan(\mu) \tag{2.17}$$

Taking the length of the first ramp to be $L_1 = 150\ mm$, the width (w) equal to the width of the second 45° ramp, $w = 115\ mm$, and $\mu = 7.67°$ then the undisturbed width at the first-to-second ramp junction is $w_h = 74.6\ mm$. Based on the current experiments, this is sufficient to perform Tomo-PIV measurements parallel to the surface of the model.

2.2.3 Thermal properties

Requirement 5 ensures the optimisation of the performance of Quantitative Infrared Thermography (QIRT). In order to maximise the surface temperature for a given heat flux, the thermal product should

be as low as possible. Assuming a constant heat transfer $q_s(t) = C$, the equation for the temperature signal can be written as:

$$T_s - T_{s,i} = \frac{2q_s}{\sqrt{\pi}}\sqrt{\frac{t}{\rho ck}} \tag{2.18}$$

Where $T_s - T_{s,i}$ represents the temperature signal. This is maximalised when the thermal product (ρck) is small. This equation follows from the inverse problem defined by the 1D heat equation which is further elaborated in section 3.2.3. For Makrolon, the conductivity is $k = 0.20\ W/Km$, the thermal capacity $c = 1.17 \times 10^3\ J/(kgK)$ and the density is $\rho = 1.2 \times 10^3 kg/m^3$.

The emissivity of the model is of high importance since the camera detects radiation and converts the detected radiation into temperature. Most energy taken from the flow is transferred into heat radiation such that the IR camera is able to obtain the heat flux at the wall. It is necessary to correct for reflected radiation from the ambient surrounding. In general the camera registers two quantities, the emitted radiation by the model and the transmitted radiation from the ambient. Taking Kirchhoff's law into account ($\alpha = \epsilon$) and assuming that the ambient does not reflect energy ($\rho = 0$), the transmissivity can be written as $\tau = 1 - \epsilon$ and thus:

$$I_m = \epsilon I_g + (1 - \epsilon) I_a \tag{2.19}$$

I_m is the measured intensity, I_g is the radiation emitted by the model, which is unknown and I_a is the radiation by the ambient which is determined by the ambient temperature. Rewritting equation 2.19 gives:

$$I_g = \frac{I_m - (1 - \epsilon) I_a}{\epsilon} \tag{2.20}$$

The above equation shows that a high emissive material is wanted since $\lim_{\epsilon \to 1} I_g = I_m$. In section 3.2 the working principle of QIRT is further discussed.

Makrolon is used as the material for the wind tunnel model. It is a polycarbonate with a low thermal conductive coefficient ($k = 0.2\ W/Km$), it withstands temperatures up to 400 K without having its properties changed and it has a specific thermal capacity of $c = 1.17 \times 10^3\ J/Kkg$. To apply QIRT, the model needs to have a low thermal conductivity to minimise the lateral conduction such that most of the radiation is emitted. The required high emissivity ($\epsilon \approx 1$) is further elaborated during the discussion of QIRT in chapter 3.

2.2.4 Forces on the model

The model is kept in place using a support attached to the back of the model (see figure 2.5). During the run, an almost constant pressure distribution is present on the surface of the model. Using the oblique shock relations, the pressure distribution at the surface of the model is calculated. Based on the pressure distribution, the resulting force in vertical direction is determined to investigate the stability of the model during the run. A sketch of the model with the acting forces is given in figure 2.8:

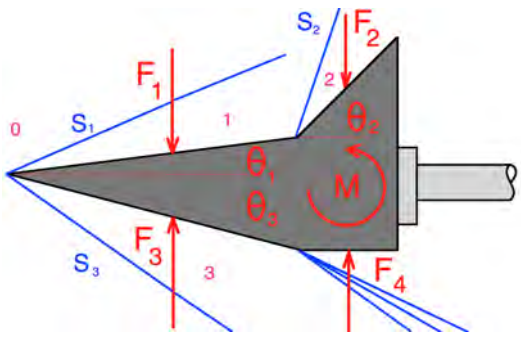

Figure 2.8: Forces and moment on the model

The static pressure in the test section is determined based on the known Mach number, the known total

pressure and the following isentropic relation:

$$\frac{p_{t,0}}{p_0} = \left(1 + \frac{\gamma+1}{2}M^2\right)^{\frac{\gamma}{\gamma-1}} \tag{2.21}$$

with $M = 7.5$ and $p_{t,0} = 28 \times 10^5\ N/m^2$, the static pressure is determined to be $p_0 = 435\ N/m^2$. From the oblique shock relations, the pressure above the first ramp is calculated:

$$\frac{p_1}{p_0} = 1 + \frac{2\gamma}{\gamma+1}\left(M_0^2 \sin^2\beta - 1\right) \tag{2.22}$$

A shock angle of 11.3° for the 5° ramp is determined using:

$$\tan\theta = 2\cot\beta \frac{M_1^2 \sin^2\beta - 1}{M_0^2(\gamma + \cos 2\beta) + 2} \tag{2.23}$$

This results in $p_1 = 1.0 \times 10^3\ N/m^2$ above the first ramp. For simplicity, it is assumed that an attached shock emanates from the first-to-second ramp junction. The second ramp angle is $\theta_2 = 45°$ and the ramp angle on the lower side of the model is $\theta_3 = 15°$. Using equation 2.22 and 2.23 $p_2 = 3.4 \times 10^4\ N/m^2$ and $p_3 = 3.7 \times 10^3\ N/m^2$ is calculated. The forces indicated in figure 2.8 are calculated using:

$$F_i = p_i \cdot S_i \cdot \cos\theta_i \tag{2.24}$$

where $S_1 \approx S_3 = 150 \cdot 115 = 1.73 \times 10^{-2}\ m^2$, $S_2 = 0.15 \cdot 0.08 = 9.2 \times 10^{-3}\ m^2$ and $S_4 = 6.6 \times 10^{-}3\ m^2$:

$$F_1 = -1 \times 10^3 \cdot 1.73 \times 10^{-2} \cdot \cos 5° = -17.2N$$

$$F_2 = -3.4 \times 10^4 \cdot 9.2 \times 10^{-3} \cdot \cos 45° = -221.2N$$

$$F_3 = 3.7 \times 10^3 \cdot 1.73 \times 10^{-2} \cdot \cos 15° = 61.8N$$

$$F_4 = 0.48 \times 10^3 \cdot 6.6 \times 10^{-3} = 3.15N$$

A netto force of approximately $-171.85N$ causes the model to move downwards. Similar values were calculated by [Caljouw, 2007]. However, it is not possible to place a similar second ramp on the lower side since the frontal area of the model is too large and wind tunnel blockage occurs [Caljouw, 2007]. This model instability has to be taken into account during the post processing of the PIV images.

2.2.5 Zig-Zag Vortex Generator

The main objective of this thesis project is to investigate the development of Görtler vortices and to obtain the corresponding three dimensionality of the flow. Previous investigations showed that leading edge imperfections influence the stability of the flow near the wall [Caljouw, 2007, Schrijer, 2010a]. Therefore, a zig-zag Vortex Generator (VG) strip is used to introduce a periodic spanwise boundary layer disturbance. Hence the zig-zag strip with $\lambda = 6\ mm$ ensures that steady longitudinal structures with a corresponding wavelength of 6 mm are present near the wall of the model. The onset of Görtler vortices is then further investigated by looking at the effect of the radius of curvature on the streamwise development of these longitudinal structures. The wavelength and width of the VG are fixed and the height is changed which is further explained in chapter 5. A sketch of the VG with the corresponding dimensions is given in figure 2.9(a). The zig-zag VG is pasted at 25 mm from the leading edge as shown in figure 2.9(b). The reasoning behind this location is further elaborated in chapter 4 where the flow topology around the zig-zag roughness element is further elaborated.

2.2.6 Model coordinate system

Two coordinate systems are used in the discussion of the obtained results. Coordinate system 1 and 2 are shown in figure 2.9(b). Both coordinate systems have a common origin located on the surface of the first-to-second ramp junction. Coordinate system 1 has x_1 defined tangent to the 5° ramp pointing positive in upstream direction, z_1 normal to the 5° ramp pointing upwards and y_1 is the right-handed vector perpendicular to x_1 and z_1. Coordinate system 2 is defined as x_2 parallel to the 45° ramp pointing positive in upstream direction, z_2 normal to the 45° ramp pointing upwards and y_2 the right-handed vector perpendicular to x_2 and z_2.

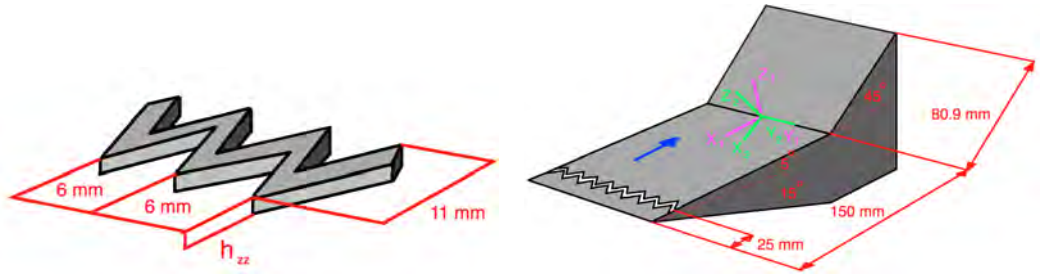

(a) Sketch of the Zig-zag VG (b) Isometric view of the new model

Figure 2.9: Sketch of the zig-zag VG and the model with corresponding coordinate systems

2.2.7 Model characteristics

Görtler instabilities are caused by the combined effect of having a curved flow field (induced by the geometry of the model) and the no-slip condition at the wall. The radius of curvature is therefore an important parameter regarding the onset of Görtler vortices. The radius of curvature of the model is determined based on the same principle applied by Navarro-Martinez and Tutty [2005] and Schrijer [2010b]. Both ramp surfaces are taken to be tangent to the circle which defines the radius of curvature as shown in figure 2.10(a). Based on this method, a radius of curvature $R = 142\ mm$ is determined.

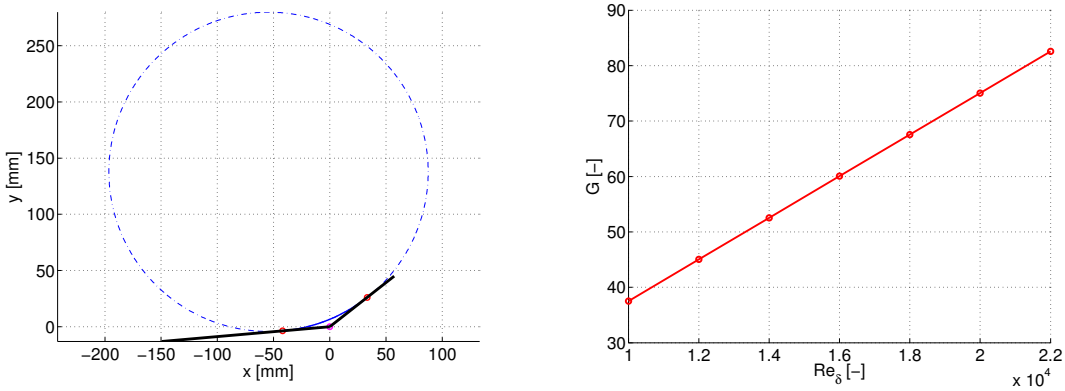

(a) The approximation of the separated region based on Navarro-Martinez and Tutty [2005] for the case $L_1 = 150mm\theta_1 = 5°$ and $\theta_2 = 45°$ $L_2 = 80.9\ mm$

(b) The local Görtler number G_δ plotted against Re_δ for the case $L_1 = 150mm\theta_1 = 5°$ and $\theta_2 = 45°$ $L_2 = 80.9\ mm$

Figure 2.10: Determination of the radius of curvature and Görtler number

The Görtler number is a non-dimensional number used to predict the onset of Görtler vortices. It is defined as the ratio of centrifugal effects to the viscous effects in the boundary layer:

$$G_\delta = Re_\delta \sqrt{\frac{\delta}{R}} \tag{2.25}$$

where Re_δ is the Reynolds number based on the boundary layer thickness (δ):

$$Re_\delta = \frac{\rho U \delta}{\mu} \tag{2.26}$$

In figures 2.10(a) and 2.10(b) the radius of curvature and the range of Görtler numbers is given for the given model specifications. It is assumed that the boundary layer thickness is 3 mm at the first-to-second ramp junction. In chapter 4, 5 and 6 will be referred to this characteristic number.

.

Chapter 3

Flow measurement techniques in the HTFD

This chapter consists of a description of the applied flow measurement techniques during this thesis project. The necessary equipment and the working principles are discussed together with the data handling aspects. Initially, Schlieren photography and planar Particle Image Velocimetry (PIV) are treated. This is followed by the description of Quantitative Infrared Thermography (QIRT) and Tomographic Particle Image Velocimetry (Tomo-PIV).

3.1 Schlieren photography

Schlieren photography is used to visualise shock waves, expansion wave etc. During this thesis project, Schlieren photography is used to obtain a qualitative flow overview of hypersonic double compression ramp flow at $M = 7.5$. The stability of the flow is further investigated using a high speed camera.

3.1.1 Refractive theory

Schlieren photography is a non-intrusive measurement technique which relies on the physical principle that light refracts towards the normal of the refractive interface for a domain having a higher refractive index. The density gradients within the field of interest can be visualised since the refractive index is linearly dependent on the local density. The intensity that is captured by the camera is related to the local density gradient in the object plane. Therefore it is a suitable measurement technique to visualise shocks since shocks represent local density gradients. The Gladstone-Dale equation relates the local density to the local refractive index:

$$n = \frac{c_0}{c} = 1 + k\rho \tag{3.1}$$

where c_0 is the light speed in vacuum, c the local light speed and k is the Gladstone-Dale constant ($k_{air} = 2.26 \times 10^{-4}$). According to Snell's law, the refractive index defines the angle over which the light is refracted:

$$\frac{\sin\theta}{\sin\theta'} = \frac{n}{n'} \tag{3.2}$$

A graphical representation of Snell's law is given in figure 3.1. As shown in the figure, the light ray is refracted towards the normal of the refractive interface, This is due to the fact that the blue domain in figure 3.1 has a higher density than the white domain. In this sense, a shock wave can be considered as a refractive interface since the density downstream of the shock is higher than upstream. The light ray is therefore refracted whenever it encounters a shock wave or a expansion wave.

3.1.2 Measurement set-up

On one side of the test section, a continuous light source is located. The bundle of light is guided through a pinhole (the size of the pinhole defines the sensitivity of the set-up) which is located in the focal point of a parabolic mirror. The parabolic mirror collimates the bundle of light through the test section. On

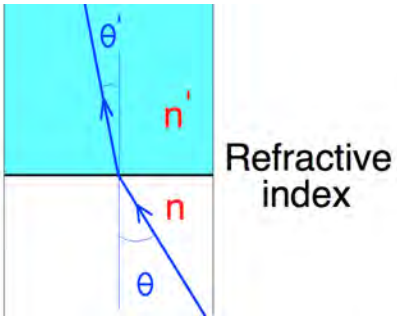

Figure 3.1: Graphical representation of Snell's law

the other side, a similar parabolic mirror is located that directs the light to the camera. A knife edge is located in the focal point of the mirror. This knife edge cuts off a portion of the light and it blocks the bended light beams caused by density changes in the measurement plane. The set-up is shown in figure 3.2.

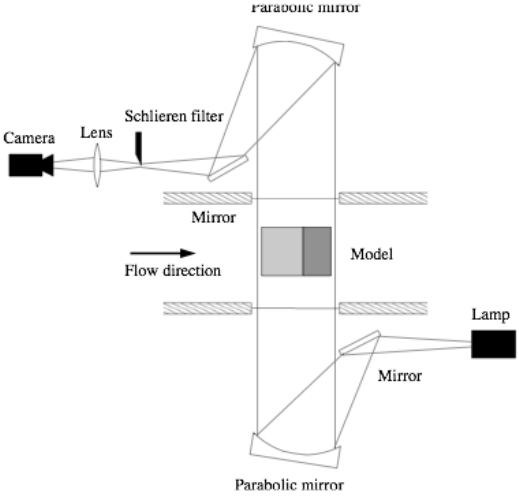

Figure 3.2: Set-up of the Schlieren system in the HTFD. Figure taken from Schrijer [2010a]

The physical principle of Schlieren visualisation is based on the fact that a local density change causes a change in refractive index, as visualised in figure 3.3. The orange light ray that encountered a shock wave, as shown in figure 3.3, is refracted downwards and therefore will appear in the image plane as a dark line.

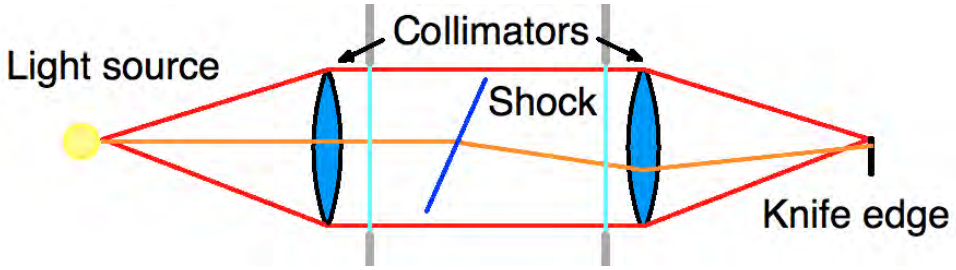

Figure 3.3: General working principle of Schlieren photography

3.1.3 Schlieren example

In figure 3.4, an example is given of a Schlieren image obtained during the current experiments. The knife edge is aligned horizontally with the camera. From the principle explained in section 3.1.1 and 3.1.2, it is determined that the shocks on the upper side of the model refract the light downwards and shocks therefore appears as a black line. For the lower side of the model, the opposite is true. There, the shocks refract the light upwards and they therefore appear as bright white lines. The model is placed in the test section with the 45° ramp pointing downwards since the shock that emanates from the pitot tube in the upper part of the test section impinges on the leading edge shock of the model. This is shown on the lower side of the model in figure 3.4 since the image is flipped horizontally and vertically such that the flow is from left to right.

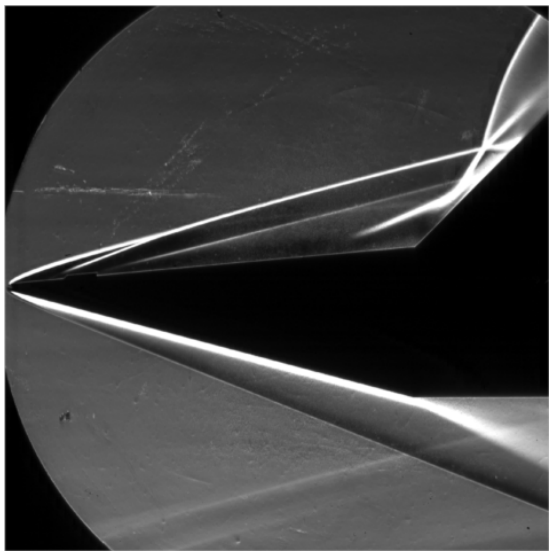

Figure 3.4: Example of one of the obtained Schlieren images for the case of a zigzag VG with $h = 1.15mm$ and a $Re_{unit} = 14.1 \times 10^6 m^{-1}$.

3.2 Quantitative Infrared Theromography (QIRT)

Quantitative Infrared Thermography (QIRT) is often used to investigate the behaviour of the boundary layer (transition, separation etc.) in hypersonic flow. This measurement technique is particularly interesting for this flow regime since there is a clear interaction between the flow and the thermal state of the surface. The surface temperature can be determined to obtain a qualitative description of the boundary layer behaviour. However, the quantitative temperature is required when the surface heat transfer is wanted. First, the basic infrared theory is discussed which is followed by a description of the measurement system and set-up implementation in the HTFD. Finally, the data reduction technique is presented which is used to obtain the surface heat flux.

3.2.1 Infrared theory

The emitted radiation energy of a body is directly related to the temperature of the body. Planck derived an expression which relates the intensity radiated by a black body (perfect radiator) as a function of the wavelength and surface temperature. Planck's law is given by equation 3.3:

$$E_{b,\lambda} = \frac{C_1}{\lambda^5 \left(e^{\frac{C2}{\lambda T_s}} - 1 \right)} \tag{3.3}$$

C_1 and C_2 are constants. A black body is defined as a body that emits and absorbs at any temperature the maximum possible amount of radiation at any given wavelength. The radiated energy by a black body is plotted against the wavelength for a range of temperatures in figure 3.5.

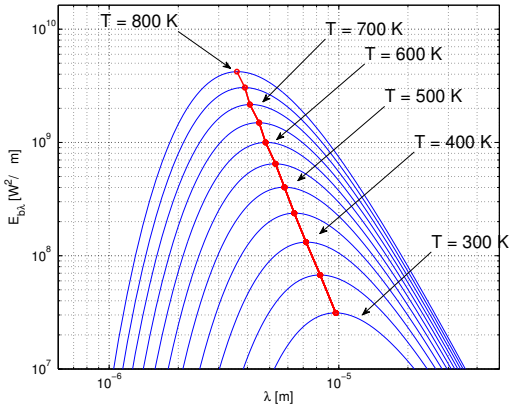

Figure 3.5: Planck's law (blue lines) and Wien's law (red line)

Note that the maxima (λ_{max}) lie on a straight line in the logarithmic plane, which is referred to as Wien's law.

$$\lambda_{max} T_s = 2.898 \times 10^{-3} [m \cdot K] \tag{3.4}$$

The emitted radiation per unit surface area for a black body is then given by the Stefan-Boltzmann equation:

$$E_b = \int_0^\infty E_{b,\lambda} d\lambda = \frac{q_r}{A} = \sigma T_s^4 \tag{3.5}$$

where A is the surface area, q_r the heat transfer, T_s the surface temperature and the Stefan-Boltzmann constant is given by $\sigma = 5.67 \times 10^{-8}\ W/(m^2 K^4)$.

The wind tunnel model does not behave like a black body but is considered to be a so-called gray body since it is not a perfect emitter. In general, a gray body absorbs a fraction (I_α), reflects a fraction (I_ρ) and transmits (I_τ) a fraction of the incident radiation. The allocation of thermal energy after a body is exposed to incident radiation is made clear in figure 3.6:

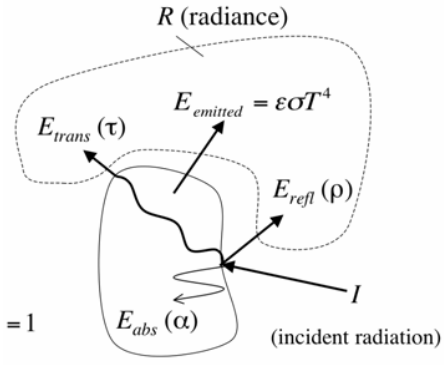

Figure 3.6: radiant thermal budget. Figure taken from Scarano [2007]

Mathematically this can be written as:

$$\alpha_\lambda + \rho_\lambda + \tau_\lambda = 1 \tag{3.6}$$

where α_λ represents the absorbed fraction of the incident radiation, ρ_λ the reflected fraction of the incident radiation and τ_λ the transmitted fraction of the incident radiation [Scarano, 2007]. The subscript λ

indicates that all fractions are wavelength dependent.

For a gray body, the emitted radiation is related to the emitted radiation for a black body in the following way:

$$\epsilon_\lambda = \frac{E_{g,\lambda}}{E_{b,\lambda}} \tag{3.7}$$

where $E_{g\lambda}$ is the radiation of the gray body (i.e. the wind tunnel model) at a given wavelength and ϵ_λ is the emissivity at a given wavelength. The dependence on the wavelength is removed by introducing the gray body hypothesis: the emissivity is a constant for a given wavelength.

$$\epsilon = \int \epsilon_\lambda \frac{E_{b,\lambda}}{E_b} d\lambda \tag{3.8}$$

The emitted radiation of a gray body is then defined as:

$$E_g = \epsilon \sigma T_g^4 \tag{3.9}$$

In thermodynamic equilibrium Kirchhoff's law states that for a body of an arbitrary material, the emissivity is equal to the absorptivity ($\epsilon = \alpha$). As a result, the netto radiant energy transfer per unit surface area of the surroundings to or from the gray body at a certain temperature can be calculated. The radiated power by a gray body is then:

$$E_r = E_g - E_a = \epsilon \sigma (T_g^4 - T_a^4) \tag{3.10}$$

where E_a is the amount of radiant energy received by the measurement system form the surroundings and E_g is the emitted energy by the gray body.

3.2.2 QIRT application in the HTFD

The surface temperature of the model increases rapidly in hypersonic flow due to high shear friction at the wall (high velocity gradient normal to the wall). This enables us to measure the radiated energy of a body directly using an IR camera. Therefore, QIRT is implemented in the passive transient mode in the HTFD. The implementation of QIRT in the HTFD consists of a IR camera, a wind tunnel model made out of a low conductive and high emissive material and the appropriate camera set-up with respect to the wind tunnel model. The required thermal characteristics of the model were discussed in section 2.2.

CEDIP Titanium 530L

At Delft University of Technology (DUT), QIRT measurements are performed using the CEDIP Titanium 530L measurement system (see figure 3.7). This IR camera is equipped with a quantum detector. This type of detector measures the direct excitation of its electrons to conduction states caused by the incoming photons. The detector is an array of Mercury Cadmium Telluride (MCT), which is a photoconductive material. It has 320×256 pixels and a spectral response of $7.7 - 9.3\ \mu m$, which is the bandwidth of IR radiation at which passive thermography techniques can be applied (example of expected temperature $350K$, Wien's law: $\lambda_{max} = 8.28 \times 10^{-6}\ m$). The camera has a maximum frame rate of 218 Hz at full resolution. The camera is connected to a PC and the software package *Altair* is used to record and save the images. A cooling system is present in the camera which cools the detector array to a temperature of approximately 60 K to reduce thermal noise.

The pixels in the array sensor have a gain $\alpha_{i,j}$ and an offset $\beta_{i,j}$ which defines their response on a certain energy input. A Non-Uniformity Correction (NUC) procedure is applied to ensure that every pixel on the IR detector has the same gain and offset and therefore the same response. Next to that, a Bad Pixel Reduction (BPR) procedure is performed to eliminate and replace the signal of all noisy pixels in the image plane.

The sensitivity of the camera is adjusted depending on the expected temperature range during the measurement. The array sensor measures the radiated energy and the pixels in the detector have a

Figure 3.7: The CEDIP camera

saturation level. The sensitivity of the detector is therefore determined by the exposure time. For a temperature range of $323K \leq T \leq 473K$, an exposure/integration time of $\tau = 72\mu s$ is used while for a lower temperature range, $253K \leq T \leq 323K$, the integration time is increased to $\tau = 340\mu s$. For both integration times, a calibration function is available so that the energy levels measured by the camera are transformed into temperature levels. Both integration times are used since the model tested in the current experiments, consists of two ramps and each ramp is exposed to a different range of temperature. For this reason, two FOVs are determined which are given in figure 3.8. For both FOVs the domain of interest is highlighted by the red lines.

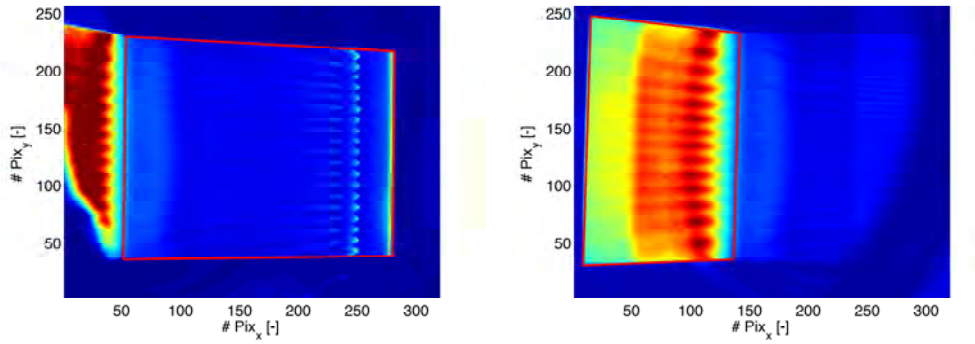

(a) The FOV when the surface temperature is measured of the 5° ramp ($\theta_1 = 5°$) with $\tau = 340\mu s$

(b) The FOV when the surface temperature is measured of the 45° ramp ($\theta_2 = 45°$) with $\tau = 72\mu s$

Figure 3.8: The two FOVs for the test case $h_{zz} = 1.15\ mm$ and $Re_{unit} = 14.1 \times 10^6[m^{-1}]$

The expected temperature range on the 5° ramp lies below 320 K. The integration time is therefore set to 340 μs to increase the sensitivity of the camera. For the 45° ramp holds that the expected temperature range lies beyond 320 K, hence, the integration time of the sensor is set to 72 μs. Note the occurrence of pixel saturation in the FOV with the 5° ramp in focus (see figure 3.8(a)). On the left hand side a small part of the 45° ramp can be seen. The uniform dark red colour indicates that the maximum energy level of the pixel is reached due to the long integration time. In figure 3.8(b), the integration time is set to $\tau = 72\ \mu s$ since for this (lower) integration time, no pixel saturation occurs at the second ramp.

Measurement set-up

An optical window does not have a sufficient transmissivity for the IR camera to register the temperature at a surface within the test section. Therefore, a Germanium window is fitted in the test section of the HTFD since Germanium has a transmissivity of approximately 0.8 [Schrijer, 2010b]. This is indicated in figure 3.9(a).

As mentioned before, the sensor of the camera is cooled to reduce thermal noise. Hence, self reflection occurs whenever the camera is placed normal with respect to the test section window. Therefore, the camera is set under an angle with respect to the normal of the test section window (see figure 3.9(a)). The emissivity changes with the optical angle θ which is the angle between the surface normal and the

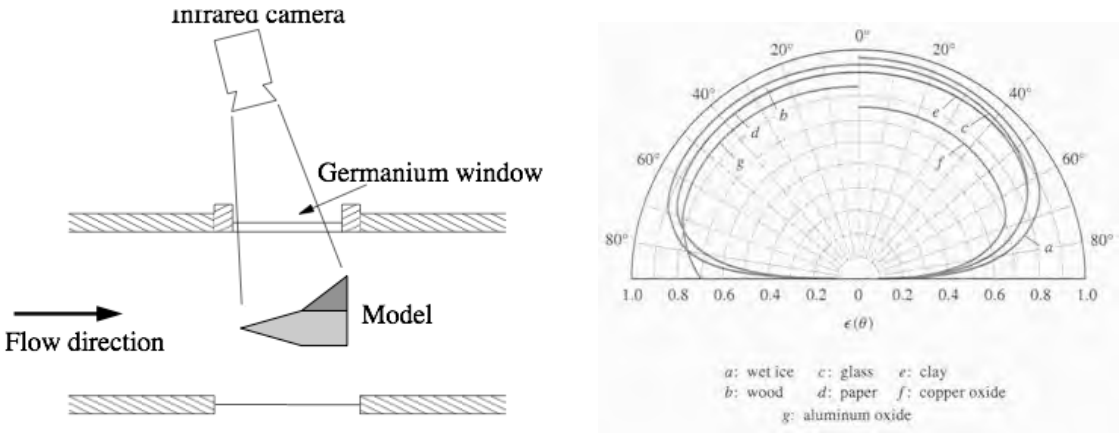

(a) The camera set-up with respect to the test section and the model during a QIRT experiment. Image taken from Schrijer [2010a]

(b) The variation in directional emissivity for several electrical nonconductors

Figure 3.9: The camera set-up with respect to the test section and the model during a QIRT experiment and the variation in directional emissivity for several electrical nonconductors [Scarano, 2007]

direction of the radiant beam emitted from the surface of the model. Based on the polar plot given in figure 3.9(b), the directional emissivity is taken to be constant for optical angles smaller than 50°. Therefore, the viewing angle of the camera with respect to the radiating surface, cannot exceed 50°.

3.2.3 Data reduction technique

While recording, the tunnel is fired and a short movie of 3 seconds is recorded using *Altair*. A typical data set consists of approximately 20 frames since the acquisition frequency of the camera is set to 218 Hz and the measurement time is approximately 120 ms. The data acquired with the CEDIP IR camera is saved in *.ptw* format which is read into *Matlab*. The pixel energy level at a fixed point in the image plane is plotted against the measurement time and a typical profile is shown in figure 3.10.

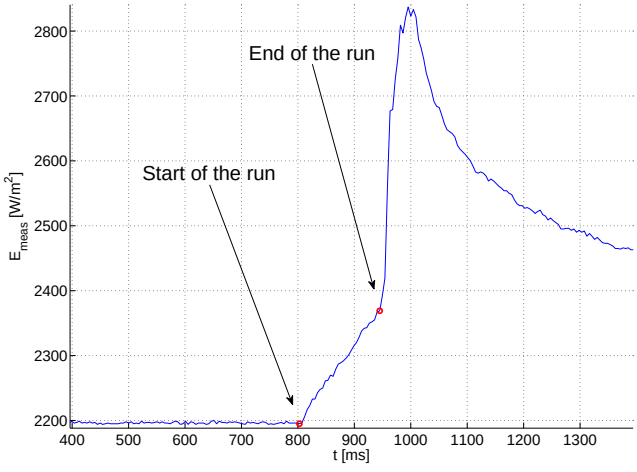

Figure 3.10: The measured data at a local point in the measurement plane $(x_{pix}, y_{pix}) = (150, 150)$

Note the small jump at $t = 800$ ms which indicates the start of the run. The starting point is located by setting a threshold on the gradient of the signal. Based on the starting point, a range of images is

taken such that the start and the end of the measurement are subtracted from the large data set. The average heat transfer distribution is calculated using 15 images during the run. The energy jump at the end of the run is caused when the valve of the wind tunnel is closed and the model is still present in the low speed hot gas flow. After that, the gradual cooling of the gas takes place, indicated by a decrease in energy level from $t = 1000\ ms$. A run time of approximately 120 ms is determined when observing the energy profile at a single point in the image plane (see figure 3.10).

The quantitative temperature is acquired using a conversion function that is obtained during the calibration procedure for the IR camera. The 1D semi infinite heat equation is solved to determine the heat flux at the wall. This is a inverse problem since the surface temperature is measured and one of the boundary conditions $-k\frac{\partial T(0,t)}{\partial y} = q_s(t)$ is unknown. Schultz and Jones [1973] obtained the following solution:

$$q_s(t) = \sqrt{\frac{\rho ck}{\pi}} \int_0^t \frac{\frac{dT_s(\tau)}{d\tau}}{\sqrt{t-\tau}} d\tau \tag{3.11}$$

This is a rather inconvenient expression to work with since it requires the temperature gradient. Therefore a cumulative heat input, $Q(t)$, is taken instead of the instantaneous convective heat flux, q_s.

$$Q(t) = \int_0^t q_s(\tau)d\tau = \sqrt{\frac{\rho ck}{\pi}} \int_0^t \frac{T_s(\tau)}{\sqrt{t-\tau}} d\tau \tag{3.12}$$

Equation 3.12 is numerically integrated by taking $\phi(\tau) = T(t) - T(0)$. Cook and Felderman approximated $\phi(\tau)$ by a linear function:

$$\tilde{\phi}(\tau) = \phi(t_{i-1}) + \frac{\phi(t_i) - \phi(t_{i-1})}{\Delta t}(\tau - t_{i-1}) \tag{3.13}$$

where $t_{i-1} \leq \tau \leq t_i$ and $i = 1, 2, 3, ..., n$ and determined this directly into equation 3.12:

$$Q(t_n) = \sqrt{\frac{\rho ck}{\pi}} \sum_{i=1}^{n} \frac{\phi(t_{i-1}) + \phi(t_i)}{\sqrt{t_n - t_{i-1}} + \sqrt{t_n - t_i}} dt \tag{3.14}$$

using a finite difference scheme, equation 3.14 is numerically implemented in the following way:

$$q_s(t_n) = \frac{Q(t_n)}{dt_n} = \frac{-2Q(t_{n-8}) - Q(t_{n-4}) + Q(t_{n+4}) + Q(t_{n+8})}{40(t_n - t_{n-1})} \tag{3.15}$$

The quantity of interest during the QIRT measurement campaign is the surface heat flux, which is given in W/m^2. This is non dimensionalised by dividing the surface heat flux by the enthalpy potential at the wall, the density and the velocity. The Stanton number is defined in equation 3.16.

$$St = \frac{q_s}{\rho_e U_e (h_{aw} - h_w)} \tag{3.16}$$

where ρ_e and U_e are the density and the streamwise velocity at the edge of the boundary layer, respectively. The enthalpy for the adiabatic wall is indicated by h_{aw} and the wall enthalphy is indicated by h_w. The Stanton number relates the convective surface heat transfer to the convected enthalpy in the free stream and this is often determined when dealing with a short duration measurement. Because the density and the streamwise velocity at the edge of the boundary layer are not available and the adiabatic wall temperature in a short duration measurement facility cannot be determined accurately, a slightly modified version of the Stanton number is used:

$$c_h = \frac{q_s}{c_p \rho_\infty u_\infty (T_t - T_w)} \tag{3.17}$$

where T_t is the total temperature and T_w the wall temperature. The free stream density and free stream velocity are easily determined and it is assumed that the gas is calorically perfect so that $h = c_p T$.

3.3 Particle Image Velocimetry (PIV)

Particle Image Velocimetry (PIV) is a non-intrusive flow measurement technique, which is based on the direct measurement of particle displacement in a planar field by means of image cross correlation. A plane is illuminated by laser light and tracer particles are introduced in the flow. The camera records the particle distribution in the Field Of View (FOV) at two time instants. By means of image cross correlation, the velocity field is obtained. A typical PIV measurement consists of following steps.

Step 1: Determine the Field Of View (FOV)

Step 2: Align the laser sheet with the FOV

Step 3: Align the calibration plate with the laser sheet

Step 4: Introduce tracer particles in the flow

Step 5: Double pulsed laser illuminates the tracer particles with laser light

Step 6: Record the particle distribution at $t_1 = t_0$ and $t_2 = t_0 + \Delta t$

Step 7: Image processing using 2D-cross correlation to determine the velocity field

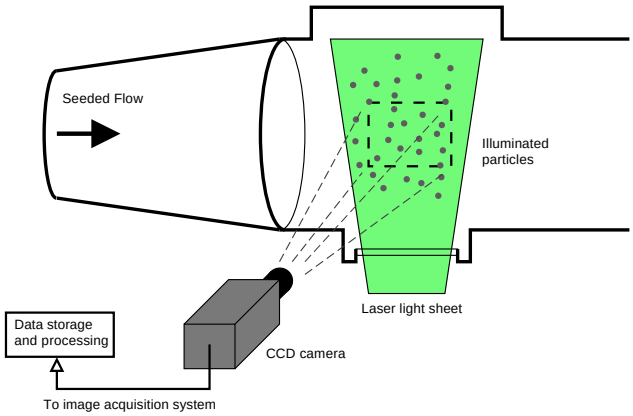

Figure 3.11: Schematic representation of the working principle of a 2C-PIV experiment. Figure taken from Schrijer [2010a]

The tracer particles, particle illumination and imaging and the image processing are discussed in the coming sub-sections.

3.3.1 The tracer particles

The tracer particles are directly introduced in the hot storage tube by means of a cyclone seeder. This is a cylindrical vessel with a tube inside through which air is blown against the side of the vessel. In this way a cyclone is created which is driven by the pressure difference between the hot storage tube and the reservoir tanks. The lightest particles are then located in the upper part of the vessel. The particles are driven into the hot storage tube by opening the valve between the cyclone seeder and the storage tube. The cyclone seeder implemented in the HTFD together with a visualisation of the working principle is shown in figure 3.12.

Because of the high temperature conditions present in the storage tube, the thermal properties have to be taken into account while choosing for the appropriate material of the tracer particle. Titanium dioxide (TiO_2) tracer particles are used during PIV measurements in the HTFD since these particles can easily withstand heating up to 800 K in the HTFD storage tube, follow the flow smoothly and they have good light scattering properties.

The tracer particles encounter high velocity gradients (shocks) when PIV is applied in compressible

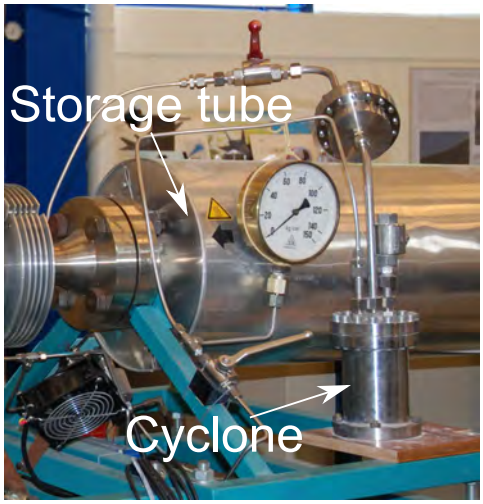

(a) Cyclone seeder at the HTFD. Image taken from Caljouw [2007]

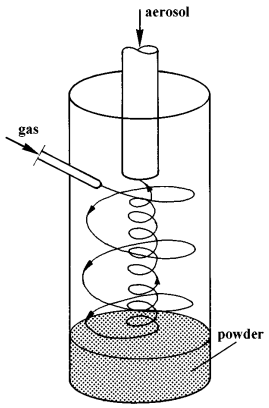

(b) Working principle of the cyclone seeder. Image taken from Melling [1997]

Figure 3.12: Cyclone seeder.

flow. A tracer particle needs a specific amount of time to adjust to the local surrounding velocity whenever it passes through a shock which is defined as the particle response time. The response time is highly dependent on the particle diameter and it plays therefore a significant role when selecting the tracer particle for PIV in compressible flow. Considering the simplified equation of motion of a spherical particle in air [Melling, 1997].

$$\frac{\pi d_p^3}{6}\rho_p\frac{d\vec{u_p}}{dt} = -3\pi\mu d_p\left(\vec{u}-\vec{u_p}\right) \rightarrow \frac{\partial\vec{u_p}}{\partial t} = \frac{\vec{u}-\vec{u}_p}{\tau_p} \tag{3.18}$$

$\vec{u}_p$ and $\vec{u}$ represent the particle velocity and the local flow velocity respectively. Furthermore, ρ_p represents the particle density, μ the viscosity coefficient, d_p the particle diameter. The particle response time is indicated by τ_p where τ_p is defined as:

$$\tau_p = \frac{d_p^2\rho_p}{18\mu} \tag{3.19}$$

The response time is generally modeled as a exponential function of time when a shock is present. To determine the response time of the particle crossing a shock wave, the following relation is used:

$$e^{-\frac{t}{\tau_p}} = \frac{u_{n,p}-u_{n,1}}{u_{n,2}-u_{n,1}} \tag{3.20}$$

where u is the velocity of the particle, $u_{n,1}$ the normal velocity of the flow in front of the shock and $u_{n,2}$ the normal velocity behind the shock. The particle velocity and fluid velocity are plotted against $\frac{t}{\tau}$ in figure 3.13.

It can be seen from figure 3.13 a small particle diameter or low density, results in a short response time which is wanted during PIV measurements in short duration test facilities.

A spatial displacement is measured with PIV and therefore it is interesting what consequences are attached to the response time in terms of spatial behaviour of the particle. Therefore, equation 3.20 is rewritten in terms of u_p:

$$u_p = e^{\frac{t_p}{\tau}}\left(u_1-u_0\right)+u_1 \tag{3.21}$$

Equation 3.21 can be integrated to determine x_p which represents the particle displacement with respect to the velocity discontinuity (shock):

$$\int_0^{t_p} u_p dt = x_p = \int_0^{t_p} e^{\frac{t_p}{\tau}}\left(u_1-u_0\right)+u_1 dt = -\tau e^{\frac{t_p}{\tau}}\left(u_1-u_0\right)+u_1\tau+\tilde{C} \tag{3.22}$$

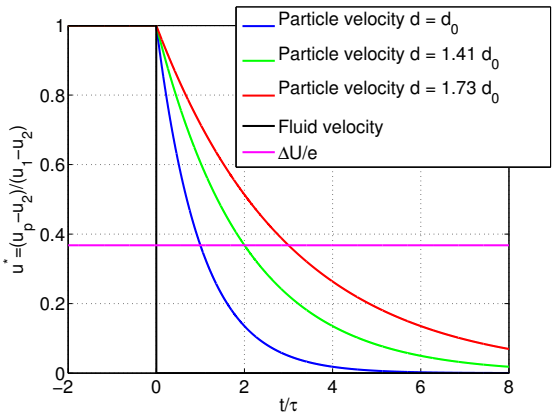

Figure 3.13: Particle velocity plotted together with the velocity of the fluid passing through a shock

Taking the initial condition $(x_0, t_0) = (0, 0)$ and substituting $t_p = \tau \ln \frac{u_p - u_1}{u_1 - u_0}$ into equation 3.22 results in:

$$x_p = u_1 \tau \ln \frac{u_0 - u_1}{u_p - u_1} + \tau \left(u_0 - u_p\right) \tag{3.23}$$

It is assumed that the term $(u_u - u_p)$ is small compared to the first right hand side term and therefore, the particle response time can be written in terms of the particle displacement:

$$u^* = e^{\frac{-x_p}{\xi}} \tag{3.24}$$

where x_i is the relaxation length which is related to the response time using equation 3.23:

$$\xi = \tau \left(u_0 - (u_0 - u_1)e^{-1}\right) \tag{3.25}$$

It is then concluded that for larger particle sizes, the response time and thus the relaxation length increases. The choice for 50 nm TiO_2 tracer particle is therefore based on a trade-off between short response time and proper scattering characteristics. The eventual particle size is $400 - 500$ nm due to particle agglomeration. A scanning electron microscopy image of the 50 nm TiO_2 particles is given for both single particles and a agglomeration of particles in figure 3.14.

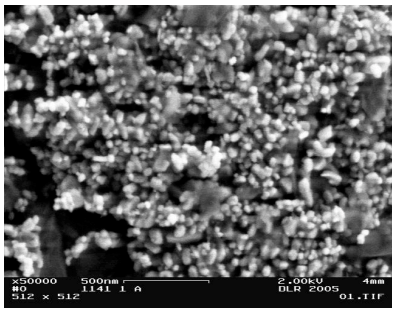

(a) Electron scan of TiO_2 particles which shows an indication of the diameter of a single TiO_2 particle (50 nm)

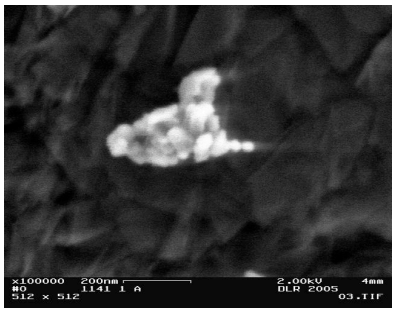

(b) Agglomeration of TiO_2 particles with an approximate mean diameter of 376 nm

Figure 3.14: Scanning Electron Microscope (SEM) images of the TiO_2 50 nm particle tracers. Figures taken from Schrijer et al. [2005]

3.3.2 Particle imaging and illumination

A Quanta-Ray double-cavity Nd:YAG laser from Spectra-Physics is used to illuminate the particles. This device generates light pulses at a wavelength of 532 nm with a maximum energy of 400 mJ per pulse and a duration of 6 ns. The Quanta-Ray double-cavity Nd:YAG laser is located below the test section.

In figure 3.15, a sketch of the laser set-up underneath the test section is shown.

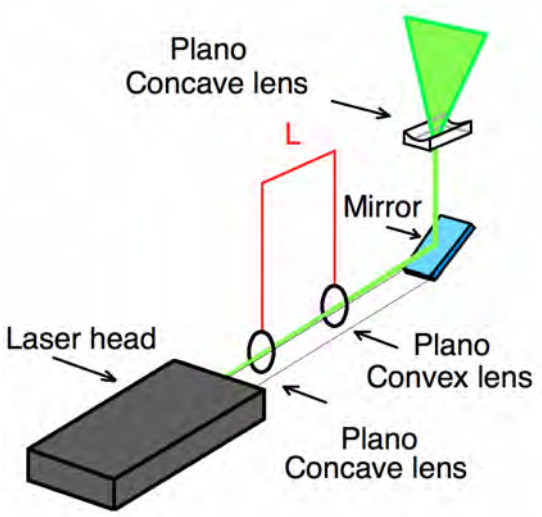

Figure 3.15: The laser set-up

The laser head creates a green bundle of laser light which has a wavelength of $\lambda = 532nm$. The first plano concave lens that the laser beam encounters, widens the beam in one direction. The plano convex lens is rotated with respect to the plano concave lens to widen the beam in the other direction. Hence, the thickness of the beam is increased by a combination of a plano-concave and convex lenses. A mirror points the optically widened laser beam upwards where the beam meets again a plano-concave lens which creates the wide sheet. The thickness of the laser sheet is controlled by changing the distance between the first plano-concave lens and plano-convex lens (L) below the test section.

The images are recorded using a 1376 $\times$ 1040 pixel SensiCam Quantum Efficiency (QE) camera. This type of camera records with a minimum separation time of 0.5 μs and has a high sensitivity. The size of the pixel is 6.45 $\times$ 6.45 μm^2. This type of camera has a maximum frame rate of 10 Hz and therefore one image is recorded during the measurement time of 120 ms. The camera and the laser are synchronised with the wind tunnel so that at 30 ms from the start of the run, a measurement is taken. The images are recorded using *Lavision Davis 7.4*.

The magnification is determined by placing a *Lavision Type 10* calibration plate with equally spaced dots in the Field Of View (FOV). The distance between the dots is 10 mm. A magnification factor is found using the *imtool* in *Matlab*:

$$M = \frac{d_{dot}}{d_{pix}} = \frac{0.01m}{273.39pix} = 3.66 \times 10^{-5} m/pix \tag{3.26}$$

where d_{dot} is the spacing between the dots on the calibration plate and d_{pix} is the measured length in pixels on the image plane obtained using *Matlab*. Based on the magnification factor and the expected velocity magnitude, u, the separation time between the two captured frames (Δt) is determined:

$$\Delta pix = \frac{u}{M} \cdot \Delta t \rightarrow \Delta t = \frac{M \Delta pix}{u} = \frac{3.66 \times 10^{-5} \cdot 20}{1000} = 730ns \tag{3.27}$$

whereΔ pix_x is the wanted pixel displacement which is based on the one-quarter rule for the in-plane particle image displacement. Due to an inaccurate synchronisation of the camera and the laser, the separation time is set toΔ $t = 1\mu s$ for 2C-PIV measurements performed during this thesis project. The recording system captures the scattered light from the particles in the flow. The image particle diameter is dependent on the magnification, the particle diameter and the diffraction spot diameter:

$$d_\tau = \sqrt{(M d_p)^2 + d_d^2} \tag{3.28}$$

where the diffration spot diameter is determined by:

$$d_d = 2.44 f_{\#}(M+1)\lambda \tag{3.29}$$

where $f_{\#}$ is the ratio between the focal length and the aperture of the camera. The aperture of the camera is adjusted such that no particle streaking is present and a particle image of approximately 2 pixels is obtained.

3.3.3 Image processing

The recorded images are processed using *Lavision Davis 7.4* using a 2D-cross correlation procedure. Initially the background is extracted using a non-linear sliding minimum filtering which is a build in function in *Lavision Davis 7.4*. The particles in the second image are displaced with respect to the first image and therefore, 2D cross correlation is suitable to obtain the particle displacement. The image at $t_1 = t$ is referred to as image A and the image at $t_2 = t + \Delta t$ is referred to as image B. Both image A and B are split up into interrogation windows which represent the local particle intensity map. The interrogation window in image A is cross correlated with the corresponding interrogation window in image B. As a result, a local peak is found in the correlation map. The displacement in x and y of the peak with respect to the center of the correlation map represents the mean local particle displacement within the interrogation window. This is shown in figure 3.16.

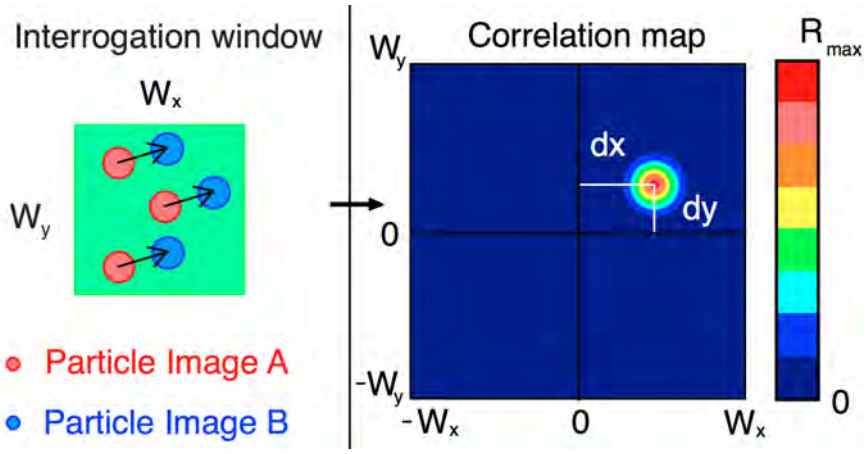

Figure 3.16: 2D cross correlation procedure

The particle intensity images are represented by $E_a(x,y)$ and $I_B(x,y)$ for each interrogation window. The cross correlation consists of the convolution of the $E_a(x,y) - \bar{I}_A$ with $I_B(x+\Delta x, y+\Delta y) - \bar{I}_B$ which is then divided by the corresponding standard deviation:

$$R(\Delta x, \Delta y) = \frac{\sum_{x=1,y=1}^{x<w_x, y<w_y} (E_a(x,y) - \bar{I}_A) I_B(x+\Delta x, y+\Delta y) - \bar{I}_B)}{\sqrt{\sum_{x=1,y=1}^{x<w_x, y<w_y} (E_a(x,y) - \bar{I}_A)^2 \sum_{x=1,y=1}^{x<w_x, y<w_y} (I_B(x+\Delta x, y+\Delta y) - \bar{I}_B)^2}} \tag{3.30}$$

where w_x and w_y are the size of the interrogation window in x and y given in pixels. From $R(\Delta x, \Delta y)$ the peak is determined and the velocity vector is calculated based on the peak displacement with respect to $(0,0)$ in the correlation map.

$$\vec{u} = M \frac{\Delta \vec{x}}{\Delta t} \tag{3.31}$$

where M is the magnification,$\Delta\ \vec{u} = [\ \Delta u, \Delta v]^T$ and$\Delta\ \vec{x} = [\ \Delta x \Delta y]^T$. This procedure is applied for every interrogation window such that the local velocity vector is determined in the complete measurement

domain.

The spatial resolution is increased by decreasing the interrogation window size using a multi-iterative correlation procedure. Initially, a large interrogation window is chosen to ensure the one-quarter rule for the in-plane particle image displacement. A typical final window size is 32×32 pixels with 75% overlap. Based on the obtained magnification factor, the spatial resolution is given in table 3.1.

Table 3.1: Number of vectors in x and y direction during the performed 2C-PIV measurements in the HTFD

	x	y
vec/mm	3.78	3.71

Typically it is wanted to have at least 9 particle pairs within the interrogation window since the height of the correlation peak (S/N) is directly dependent on the amount of particle pairs. This argument follows directly from the definition of cross correlation. For a uniform particle distribution, the amount of pixels in the interrogation window is determined using equation 3.32.

$$N_{tot} = \frac{ppp}{9} \tag{3.32}$$

where ppp is Particle Per Pixel. For a square interrogation window, the window size is determined by $N = \sqrt{N_{tot}}$. However, there are particle density gradients present in the images since the flow is compressible and particle slip occurs [Schrijer, 2010a, Elsinga, 2008] (see section 3.3.1). The shape of the interrogation window is adjusted such that the spatial resolution is increased in a particular region and/or direction as long as the total amount of pixels per interrogation window fulfills equation 3.32.

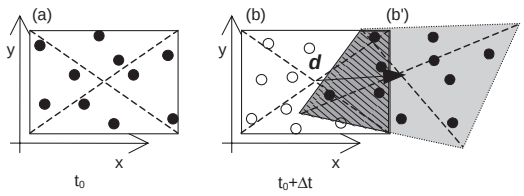

Figure 3.17: graphical representation of window deformation

By means of window deformation, a higher spatial resolution is achieved while maintaining a sufficient S/N. The velocity vector which is obtained after the first iteration is used as a initial predictor. Using a iterative correlation procedure, the interrogation window A and B are deformed based on the previously determined velocity field in the following way [Scarano, 2002].

$$I_{A,new} = E_a(x + \frac{u_p \Delta t}{2}, y + \frac{v_p \Delta t}{2})$$

$$I_{B,new} = I_B(x + \Delta x - \frac{u_p \Delta t}{2}, y + \Delta y - \frac{v_p \Delta t}{2})$$

where u_p and v_p are the local velocity at a pixel. The velocity vector at every pixel location is determined using bilinear interpolation and the window is deformed as shown in figure 3.17. The iterative window deformation procedure is presented by the block diagram given in figure 3.18:

The velocity vector is then updated accordingly:

$$\vec{v}_{new} = \vec{v} + C_{new} \tag{3.33}$$

where C_{new} is the corrector and defined as $C_{new} = I_{A,new} \otimes I_{B,new}$.

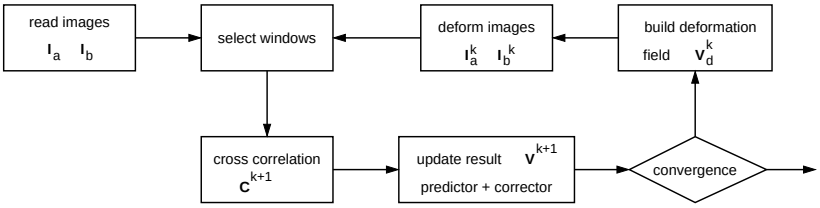

Figure 3.18: Block diagram of the iterative image deformation interrogation method

3.4 Tomographic Particle Image Velocimetry (Tomo-PIV)

Tomographic Particle Image Velocimetry (Tomo-PIV) is a measurement technique derived from conventional PIV previously discussed and used to obtain a three dimensional velocity field. It consists of the same four fundamental components as planar PIV, the image recording system, the illumination system, the tracer particles and a post processing computer. A laser illumination system is used to illuminate a thin ($5-10\ mm$) measurement volume and the scattered light is captured from multiple viewing angles (Typically 3 or 4 cameras). To obtain a larger depth of field, a larger $f_\#$ is set compared to planar PIV since:

$$\delta z = 4.88\lambda f_\#^2 \left(\frac{M+1}{M}\right)^2 \tag{3.34}$$

Based on the particles distributions in the image plane from the different cameras, a most likely 3D particle distribution at $t = t_0$ (Image A) and $t = t_0 + \Delta t$ (Image B) is then determined using the Multiplicative Algebraic Reconstruction Technique (MART). The particle distribution based on Image A and the particle distribution based on image B are then cross correlated using a 3D cross correlation algorithm. In this section, the calibration and reconstruction are discussed in more detail since those are the aspects that are different compared to a planar PIV experiment. In figure 3.19 a schematic representation of the working principle of a general Tomo-PIV experiment is given.

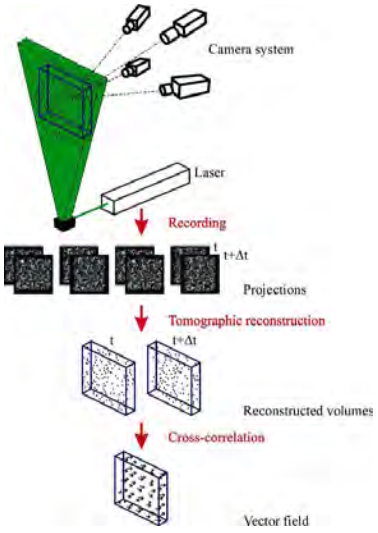

Figure 3.19: Schematic representation of the working principle of a Tomo-PIV experiment [Elsinga, 2008]

Below, a step program is given which is applied to perform a Tomo-PIV experiments in the HTFD:

Step 1: Determine the Field Of View (FOV)

Step 2: Align the laser sheet with the FOV

Step 3: Align the calibration plate with the laser sheet

Step 4: Perform plate calibration at vacuum conditions

Step 5: Perform a run/Take a measurement

Step 6: Perform the self-calibration on the residue images

Step 7: Reconstruct the particle distribution

Step 8: Validate the measurement set-up

Step 9: Volume reconstruction

Step 10: Vector field determination/Post processing

3.4.1 Calibration

The measurement system is calibrated such that an accurate relation is found for the physical coordinates in the measurement volume to the image plane coordinates. First, a plate calibration is performed which is improved by applying a volume self-calibration. Both procedures are described in this section.

Plate calibration

A *Lavision Type 10* calibration plate is used (see figure 3.20(a)) which has a series of markers with a 10 mm spacing on two different planes ($z = 0$ and at $z = -1mm$). The plate is mounted on a sting which allows the user to align the calibration plate with the laser sheet. The plate calibration is performed in vacuum conditions to compensate for refraction effects (see section 6.3).

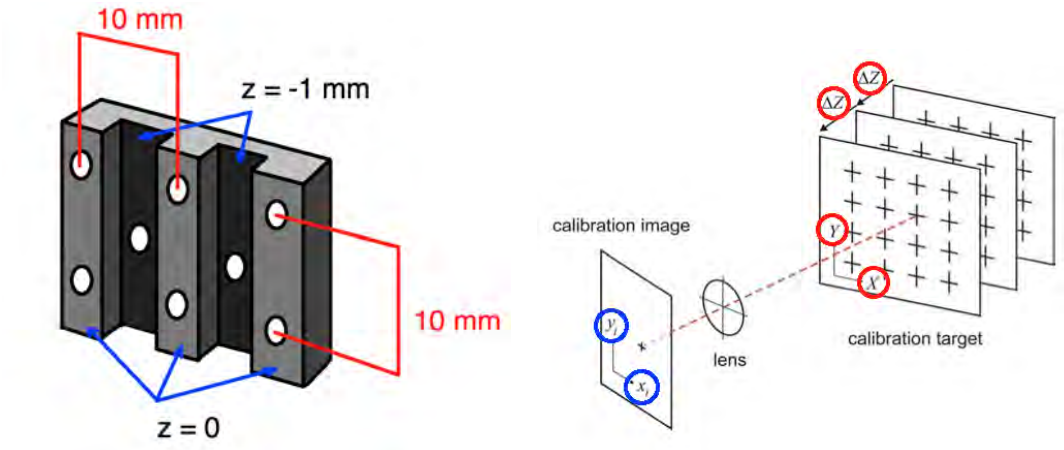

(a) Sample of a *Lavision Type 10* calibration plate (b) A third order polynomial is fitted through a fixed set op point for every z position

Figure 3.20: Plate calibration procedure

A third order polynomial is used as a mapping function between the markers in the measurement volume and their corresponding locations in the image plane of each camera. The (X, Y) position in the measurement domain for a fixed Z position, indicated by the red circles, are connected to the (x_i, y_i) position in the image plane (blue circles) using a third order polynomial. (X, Y, Z) represent the coordinates in the object plane and (x_i, y_i) the coordinates in the image plane, as shown in figure 3.20(b). The polynomials for a given z position in the measurement volume are given by the equation 3.35 and 3.36 [Soloff et al., 1997].

$$x_i' = a_0 + a_1X + a_2X^2 + a_3X^3 + a_4Y + a_5Y^2 + a_6Y^3 + a_7XY + a_8X^2Y + a_9XY^2 \tag{3.35}$$

$$y_i' = b_0 + b_1X + b_2X^2 + b_3X^3 + b_4Y + b_5Y^2 + b_6Y^3 + b_7XY + b_8X^2Y + b_9XY^2 \tag{3.36}$$

The coefficients, a_i and b_i, are only dependent on the physical Z position in the measurement volume.

Volume self-calibration

Tomo-PIV requires calibration accuracies of a fraction of pixel throughout the complete measurement volume. A volumetric self-calibration technique had been developed based on particle triangulation [Wieneke, 2008]. In figure 3.21, the triangulation error of a three camera set-up is shown.

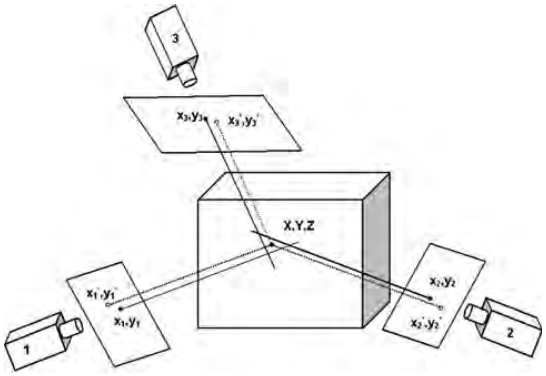

Figure 3.21: Schematic representation of the triangulation error. Figure taken from Wieneke [2008].

The first step is a 2D particle detection in the images captured by all the cameras. This is followed by a particle triangulation procedure. The sum of distances between the projected particle coordinates (x'_i, y'_i) in the image and the actual particle position (x_i, y_i) in the measurement domain is minimised:

$$min\left\{\sum_{i=1}^{N}|(x'_i, y'_i) - (x_i, y_i)|\right\} = min\left\{\sum_{i=1}^{N}\left|\vec{d}\right|\right\} \tag{3.37}$$

where $\vec{d}$ is the disparity vector.The measurement domain is subdivided into n_x by n_y by n_z sub-volumes. Per sub-volume, a particle triangulation procedure is performed [Wieneke, 2008]. As a result, the local disparity map, $\vec{d}$, is determined which defines the misalignment of the lines of sight of the cameras. During this triangulation procedure, d_i should lie within the search radius of $\pm\epsilon_{max}$ which is set by the user. Typically this value is set initially to $\pm\epsilon_{max} = 4\ pix$. The disparity vector that follows from the local particle triangulation is represented by a peak that is found in a given sub-volume. In figure 3.22, a typical 2D Gaussian blob is shown which represents the local disparity. To obtain a better statistics, the disparity vector is calculated for typically 20 images. The improvement of the local disparity map is indicated in figure 3.22. In this way the disparity is obtained locally and a disparity map is created such that the orientation of the laser sheet with respect to the calibration plate is observed.

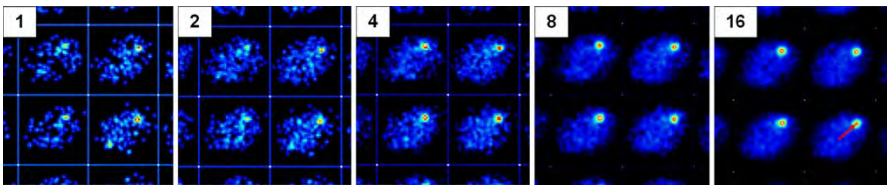

Figure 3.22: Summed disparity map over 1 - 16 images [Wieneke, 2008]

A measurement volume of 60 mm × 40 mm × 6 mm is taken as a reference case to illustrate the relevance of the important parameters that are considered during the volume self-calibration procedure. Typically large sub-volumes are used initially. A typical subdivision of the number of sub-volumes in each direction is given by $(n_x, n_y, n_z) = (5, 4, 4) = (12\ mm,\ 10\ mm,\ 1.5\ mm)$. Initially it is checked if particle triangulation occurs. With this number of sub-volumes the amount of fitting points for the third

order polynomial is nearly the same. After vector validation and a $3 \times 3 \times 3$ vector smoothening the disparity map is used to optimise the calibration set and a new mapping function is calculated:

$$M_i'(X,Y,Z) = M_i(X,Y,Z) - d_i(X,Y,Z) \tag{3.38}$$

After an update of the calibration set, the same steps are performed, which are described above but now with a smaller $\pm\epsilon_{max}$ and a lower threshold such that the number of ghost particles reduces. This also provides a rejection criteria for overlapping particles. The amount of sub-volumes is increased to typically $(n_x, n_y, n_z) = (9, 7, 7) = (6.7\ mm, 5.7\ mm, 0.86\ mm)$ such that the amount of fitting points is increased. This iterative procedure is carried out until the disparity is approximately zero which means that the three lines of sight of all the cameras intersect in a single point in the measurement domain. Therefore, the final outcome of the self-calibration is an improved definition of the mapping of the measurement domain coordinate system on the image plane coordinate system.

3.4.2 Multiplicative Algebraic Reconstruction Technique (MART)

Based on the images captured by the different viewing points, a most likely 3D particle distribution is determined using Multiplicative Algebraic Reconstruction Technique (MART). The raw images are pre-processed before the reconstruction of the particle distribution is calculated. The background is subtracted in two steps. First, the average of the images before the run image are subtracted. After that, a non linear Subtract Sliding Minimum 5×5 filter is used. Based on the pre-processed images, the particle distribution during the run is reconstructed. The measurement volume is therefore subdivided in voxels which have the dimensions of a pixel. The projection of this intensity on an image pixel, returns a pixel intensity which is expressed by the following relation:

$$I(x_i, y_i) = \sum_{j \in N_i} w_{i,j} E(X_j, Y_j, Z_j) \tag{3.39}$$

In this expression N_i indicates the number of voxels on the line of sight corresponding to the i^{th} pixel (x_i, y_i). The weighting matrix w_{ij} represents the contribution of each voxel to each pixel and is therefore only a dependent on the camera orientation and measurement volume configuration. The weighting matrix w_{ij} is build up with row wise having the pixels for the defined camera and column wise the voxels which are seen by the corresponding pixels [Elsinga, 2008].

Multiplicative Algebraic Reconstruction Technique (MART) involves iteratively correcting the intensity value in each voxel until the difference between the projected pixel intensity $\sum_j W_{ij} I_j^k$ and the k^{th} iteration and the recorded pixel intensity P_i is minimised [Atkinson and Soria, 2009]. The algorithm of MART is the following:

for each pixel in each camera i
  for each voxel j

$$E(X_j, Y_j, Z_j)^{k+1} = E(X_j, Y_j, Z_j)^k \left(\frac{I(x_i, y_i)}{\sum_{j \in N_i} w_{i,j} E(X_j, Y_j, Z_j)^k} \right)^{\mu w_{i,j}} \tag{3.40}$$

  end loop voxel
end loop pixel

This reconstruction technique updates the element $E(X,Y,Z)$ by looking at the ratio of the measured pixel intensity $I(x_i, y_i)$ with the projection of the current element $\sum_{j \in N_i} w_{i,j} E(X_j, Y_j, Z_j)$. The exponent ensures that only the elements in $E(X,Y,Z)$ that affects the i^{th} pixel are updated [Elsinga, 2008].

Ghost particles

Ghost particles are a consequence of the non-uniqueness of the solution found of the inverse problem given in equation 3.39. In figure 3.23, the existence of ghost particles is further elaborated. Red indicates

a real particle at time instance $t_1 = t$ and a blue indicates a real particle at $t_2 = t + \Delta t$. Whenever a line of sight of camera 1 crosses with a line of sight of camera 2 and both register an image of a particle, it can lead to a false particle registration as shown on the left side in figure 3.23. For instance, the line of sight of camera 1 captures particle B in its second state and crosses the line of sight of camera 2 which captures particle A in its second state. Hence, the recording system registers that there will be a particle behind B_2 and behind A_2 which is indicated by G_2. These false particles are referred to as ghost particles and are therefore indicated by G in figure 3.23.

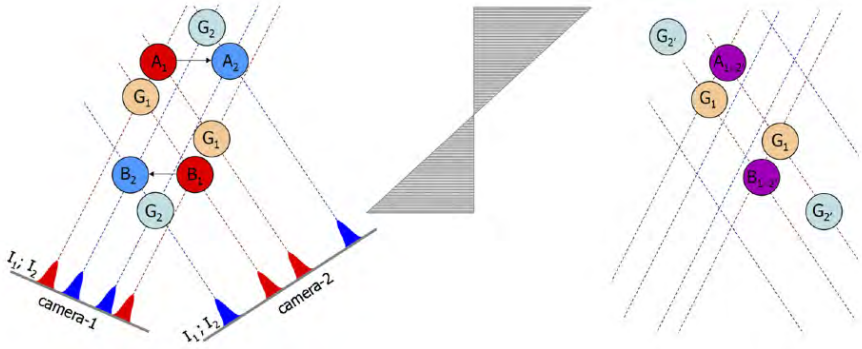

Figure 3.23: Ghost particles seen by the recording system [Novara et al., 2010]

The amount of ghost particles is dependent on the amount of simultaneous views, the seeding density and the thickness of the measurement volume. Typically a seeding density of 0.05 particle per pixel (ppp) is taken which corresponds to 50000 particles per megapixel. The ratio of actual particles over ghost particles is given in equation 3.41 [Novara et al., 2010].

$$\frac{N_p}{N_g} = \frac{1}{ppp^{N_C-1} \cdot A_p^{N_C} \cdot \delta_z} \tag{3.41}$$

The number of cameras is represented by N_C, A_p represents the area of the particle image ($A_p = \frac{\pi d_{image}{}^2}{4}$) and δ_z is the measurement volume thickness given in voxels.

Novara et al. [2010] discusses an enhanced MART reconstruction technique for which the motion of the particles is tracked (MTE). This technique relies on the following five steps:

1. reconstruction of $E(X_j, Y_j, Z_j)_n$ and $E(X_j, Y_j, Z_j)_{n+1}$ using the MART algorithm given in equation 3.40
2. Calculate the particle velocity $U(X_j, Y_j, Z_j)_n$, $V(X_j, Y_j, Z_j)_n$ and $W(X_j, Y_j, Z_j)_n$ by performing a cross correlation analysis $E(X_j, Y_j, Z_j)_n \otimes E(X_j, Y_j, Z_j)_{n+1}$
3. Deform one tracer particle field depending on the estimated displacement field $E_{n+1'} = E(X + U\Delta t, Y + V\Delta t, Z + W\Delta t)$ and $E_{n'} = E(X - U\Delta t, Y - V\Delta t, Z - W\Delta t)$
4. Take the linear combination of $E_{G,n} \frac{1}{2}(E_n + E_{n+1'})$ and $E_{G,n+1} = \frac{1}{2}(E_{n+1} + E_{n'})$
5. Take $E_{G,n}$ as a first guess for the MART reconstruction

If an estimation of the displacement field is available, it is possible to deform the intensity pattern found at $t_2 = t + \Delta t$ into the intensity pattern at $t_1 = t$. The ghost particles G_2 are eliminated since they do not coincide two crossing line of sights. This is shown on the right side of figure 3.23. It is noted that the total intensity is build up into a coherent part (E_C) and a incoherent part (E_I) [Novara et al., 2010].

$$E_{MART} = E_C + E_I \tag{3.42}$$

When the deformation of the intensity pattern of t_2 is performed, a intensity field is determined:

$$E_G = E_C + \frac{1}{2}\left(E_{I,1} + E_{I,2'}\right) \tag{3.43}$$

where $E_{I,1}$ is the intensity field at $t_1 = t$ and $E_{I,2'}$ is the deformed intensity field at $t_2 = t + \Delta t$. E_G is substituted back into the MART algorithm given in equation 3.40.

Reconstruction quality

The output of the reconstruction procedure is a volumetric particle distribution where the volume is divided into 3D pixels often referred to as voxels. As a result, the measurement volume is given in vox_x by vox_y by vox_z voxels. vox_x and vox_y are in the same order as during a planar PIV experiment. During the current experiments, a thin sheet measurement volume is the field of interest and therefore the number of voxels in z-direction is typically one order lower.The quality of the reconstruction is quantified by Q which is defined as Elsinga [2008]:

$$Q = \frac{\sum_{X,Z} E_1(X,Z) \cdot E_0(X,Z)}{\sqrt{\sum_{X,Z} E_1^2(X,Z) \cdot \sum_{X,Z} E_0^2(X,Z)}} \tag{3.44}$$

where $E_1(X,Z)$ represents the in-depth reconstructed object and $E_0(X,Z)$ the in-depth reconstructed object when with the particles are represented by a Gaussian intensity distribution of 3 voxel diameter. Elsinga [2008] investigated the dependence of Q on the different experimental parameters such as the number of cameras the viewing angles and the Particle Per Pixels (*ppp*). Adding cameras is always beneficial since more information of the measurement domain is obtained. Elsinga [2008] investigated the effect of change of the viewing angle, the number of cameras etc. for a symmetrical camera set-up. The viewing angle is defined as the angle that the optical axis of the camera makes with the out of plane coordinates of the measurement domain.Elsinga [2008] concluded that for a viewing angle of 30° Q reached an optimal value of 0.85 shown in figure 3.24(b).

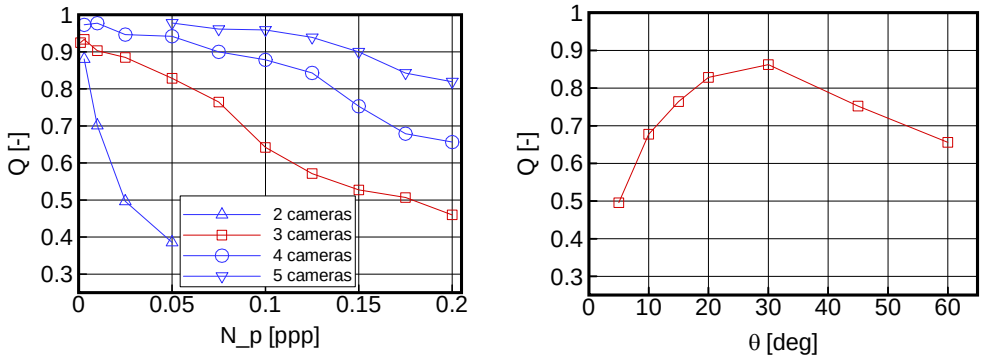

(a) The quality factor plotted against the *ppp*

(b) The quality factor plotted against the viewing angle θ

Figure 3.24: Quality factor plotted against *ppp* and viewing angle θ figures are all taken from Elsinga [2008]

The viewing angle should not be too small since the depth resolution decreases which results in elongation of the reconstructed particle in depth. For larger angles the length of the line of sight in the volume increases. This increases the probability of false particle triangulation (ghost particles). The *ppp* should be below 0.05 such that ghost particles are not disturbing the reconstruction process Elsinga [2008] (see figure 3.24(a)). Finally, the particle displacement within a chosen interrogation volume is obtained by the 3D cross-correlation of the reconstructed particle distribution at the two exposures. This correlation

procedure is, similar to planar PIV, based on the iterative multi-grid window deformation technique discussed in section 3.4.2.

Chapter 4

Hypersonic double compression ramp flow

In this chapter, the characteristic features of hypersonic double compression ramp flow are discussed. Topics of interest within the framework of hypersonic double compression ramp flow are shock wave interaction, boundary layer separation and reattachment, and the formation of Görtler vortices. Both theoretical tools and flow measurement techniques (Schlieren and PIV) are used to obtain more insight of these topics. A typical flow topology of a single compression ramp is given in figure 4.1.

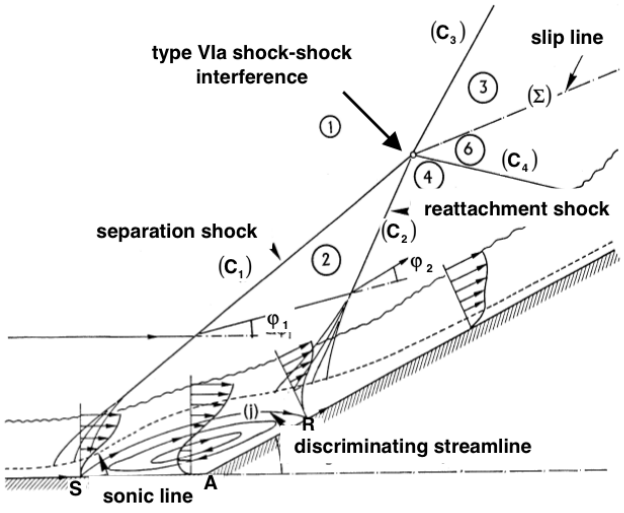

Figure 4.1: Flow topology for a single compression ramp. Figure taken from Arnal and Delery [2004]

In supersonic flows, disturbances in the flow domain cannot travel upstream. The oblique shock relations tell us that the pressure increases whenever the flow passes a shock. As a result, the pressure on the second ramp is higher than at the first ramp. The streamwise pressure rise is also present in the boundary layer. From hypersonic boundary layer theory it is derived that the pressure gradient in normal direction is zero [Anderson, 2006]:

$$\frac{\partial p}{\partial y} = 0 \tag{4.1}$$

Hence, equation 4.1 dictates that the local pressure in the boundary layer is equal to the local pressure in the isentropic flow domain normal to the surface of the model. As a result it can be stated that the pressure in the boundary layer at the second ramp is higher than at the first ramp since the pressure is increased due to the large second ramp angle. Due to the subsonic incompressible regime in the boundary layer (no-slip condition at the wall), disturbances *can* travel upstream in the boundary layer. The velocity

parallel to the wall decreases due to the adverse pressure gradient, and consequently, the boundary layer separates. From the momentum equation at the wall where $u = 0$ and $v = 0$ the following is obtained:

$$\left.\frac{\partial^2 u}{\partial y^2}\right|_{y=0} = \frac{1}{\mu}\frac{dp}{dx} \tag{4.2}$$

Equation 4.2 tells us that the curvature of the velocity at the wall has the sign of the pressure gradient whereas further away from the surface, the velocity profile must have negative curvature when it merges with the free stream. For a positive (adverse) pressure gradient, the curvature changes sign and the velocity profile is S-shaped. The increasing downstream pressure slows down the velocity and the boundary layer separates and forces the flow to go in opposite direction. The velocity profile at point A in figure 4.1 is a typical profile for separated flow (S-shaped). At point S, the curvature is zero and the flow is about to separate. In figure 4.2, the boundary layer velocity profile for a laminar boundary layer (Blasius profile) together with a typical boundary layer profile at separation is shown.

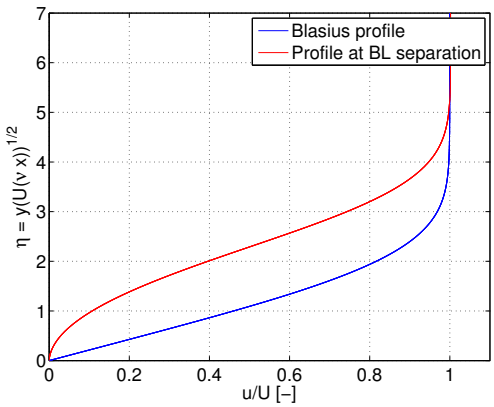

Figure 4.2: Typical laminar boundary layer profile compared to a typical separated boundary layer profile

The separated boundary layer velocity profile is characterised by a decreased du/dy at the wall. The velocity in the subsonic region of the boundary layer is reduced due to the adverse pressure gradient. Back flow occurs when the adverse pressure gradient is too large and the velocity near the wall becomes negative.

Going back to point S in figure 4.1, the boundary layer separates here and a shear layer starts. A recirculation bubble is formed over point A and an example of back flow is given underneath the shear layer. The boundary layer reattaches again at point R and it propagates downstream parallel to the ramp. A shock originates from point S (shock C_1) due to the local flow deflection induced by the separation/recirculation bubble. From reattachment point R, a shock emerges (shock C_2) based on the same argument. The reattachment shock interacts with the separation shock and a shock interaction is present above the second ramp. Depending of the angle of the ramp, the interaction is strong or weak.

In the coming section, the quality of the flow around the previously introduced $5° - 45°$ double ramp model is observed using Schlieren visualisation. A theoretical isentropic flow domain analysis is performed by determining the particular hodograph for the $5° - 45°$ model. This is followed by a quantitative velocity field description obtained by PIV. During the current experiments, a Vortex Generator (VG) (see section 2.2) is used to ensure the presence of steady longitudinal vortices so that their streamwise propagation can be further studied. Therefore, the boundary layer thickness is theoretically determined so that the height of the VG can be scaled with the boundary layer thickness. Furthermore, the flow topology around the zig-zag VG strip is discussed and this chapter ends with a discussion of a stability analysis regarding Görtler vortices and the literature regarding the onset of Görtler vortices.

4.1 General flow topology of the 5°-45° model

Schlieren visualisation and Particle Image Velocimetry (PIV) is used to determined a qualitative and quantitative flow overview of the 5°-45° model. Furthermore, a theoretical flow analysis is performed to predict and compare the final results given in chapter 5 and 6.

4.1.1 Schlieren Photography

Schlieren experiments are performed to get a better understanding of the overall flow field, the curvature of the boundary layer and the unsteadiness of the shock interaction on the 45° ramp. Furthermore the Schlieren results support the theoretical analysis given in this section. In figure 4.3 an instantaneous Schlieren image is shown for the $5° - 45°$ double compression ramp introduced in section 2.2. The shocks seem rather thick which is ascribed to shock movement during the run and to the fact that a continuous light source is used. Small shock interactions at the second ramp can therefore not be observed. Hence the purpose of this measurement is to obtain a qualitative flow overview (shock interaction pattern, flow stability). The flow topology around the introduced $5° - 45°$ double compression ramp model is discussed during the remainder of this report.

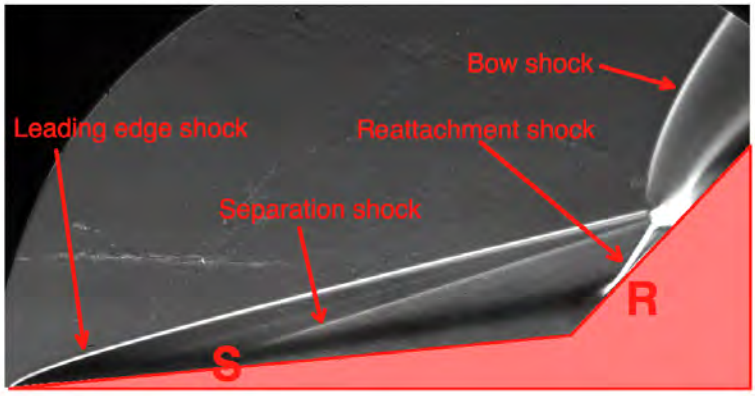

Figure 4.3: Instantaneous schlieren image for the case $h_{zz} = 0mm$ and $Re = 8.47 \times 10^6 m^{-1}$

4.1.2 General shock lay-out

A leading edge shock originates form the first ramp. It is determined using the oblique shock relations, that this shock makes an angle (β_l) of approximately 11°. From figure 4.3 it is determined that $\beta_l \approx 12°$.

A shock that originates downstream of the leading edge shock can be ascribed to boundary layer separation as shown in figure 4.1 at point S. Near the wall of the second ramp, the reattachment shock originates and interacts with the leading edge shock and the separation shock. Due to the large second ramp angle, a bow shock originates which can be considered as a strong shock. The flow behind the bow shock will therefore be slowed down to subsonic level and the density and pressure increase significantly.

4.1.3 Influence of the VG on the shock lay-out

The influence of the height of the VG, h_{zz}, on the onset of Görtler vortices is one of the topics investigated in the coming two chapters. The influence of the VG on the shock pattern is therefore further studied and compared with the case that no VG is pasted. The shock pattern on the 45° ramp for the highest VG strip ($h_{zz} = 1.15mm$) pasted at 25 mm from the leading edge, is different compared to the case that no VG is pasted.

Again a shock originates form the leading edge which compresses the flow. Two shocks emanate from the VG of which the first shock interacts with the leading edge shock while the second more weak compression

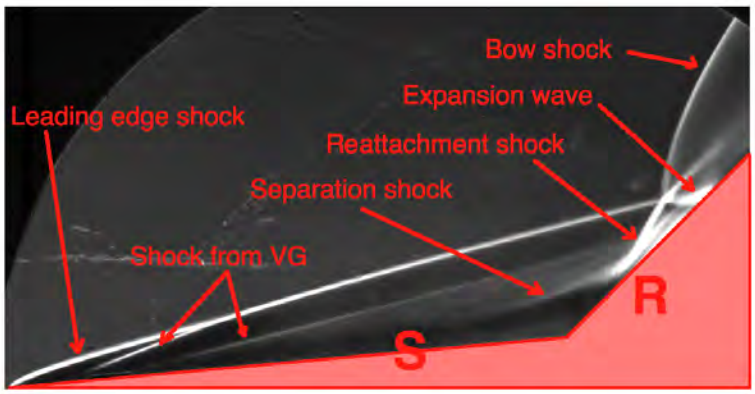

Figure 4.4: Instantaneous schlieren image for the case $h_{zz} = 1.15mm$ and $Re = 8.47 \times 10^6 m^{-1}$

wave interacts on the merged separation and reattachment shock. This is shown in figure 4.4. The VG creates a local stagnation point which deflects the flow upwards inducing a weak shock upfront of the VG. In a similar fashion, a weak shock is created just downstream of the VG where the flow is deflected downwards. The leading edge shock merges with the first VG shock and the merged shock has a shock angle of approximately $\beta_l = 14°$ based on the Schlieren images.

Note the difference in position of the separation point S in figure 4.3 and 4.4. The separation shock originates more downstream which indicates that the separated region is significantly smaller and more close to the first-to-second ramp junction. This can be ascribed to the turbulent nature of the boundary layer due to the presence of the VG. The local normal velocity gradient is higher and therefore a higher adverse pressure gradient is needed to induce separation. Consequently, for the case of $h_{zz} = 1.15mm$, it is shown in figure 4.4 that the separation shock merges together with the reattachment shock and interacts with the leading edge shock above the 45° ramp. This effect on the shock interaction above the second ramp is noted to be the main difference between the shock patterns given in figure 4.3 and 4.4. Similar to the case that no VG is applied, a bow shock originates above the second ramp.

4.1.4 Theoretical pressure distribution on the $5° - 45°$ ramp

The inviscid compressible flow domain over the $5° - 45°$ double compression ramp model can be theoretically analysed using shock polars [Delery, 1994]. The local pressure normalised by the free stream pressure is determined. From the oblique shock relations, the Mach number, pressure, density etc. can be obtained given the Mach number upstream of the shock and the wedge angle of the geometry. Given that $M_\infty = 7.5$ and the first ramp angle is 5°, the flow conditions downstream of the leading edge shock can be calculated. The flow deflection induced by the separation bubble (see the blue area in figure 4.5(a)) is estimated from the Schlieren image given in figure 4.4. The separated region is modeled as an extra ramp with $\theta_s = 12°$ based on the Schlieren image given in figure 4.4. In figure 4.5(a), the different flow regions are indicated and three streamlines are given. The blue, green and pink streamline are used to discuss the hodograph corresponding to the $5° - 45°$ model given in figure 4.5(b) and 4.5(c).

Blue stream line

The dark blue shock polar given in figure 4.5(b) corresponds to the free stream flow conditions ($M_0 = M_\infty = 7.5$). The blue streamline passes through the leading edge shock and the pressure is increased to $(p/p_0)_1 = 1.35$. The minor pressure rise is induced by the weak leading edge shock. Based on the oblique shock relations, the Mach number downstream of the leading edge shock is determined to be $M_1 = 6.48$. The separated region is modeled as an extra ramp with $\theta_s = 12°$ based on the Schlieren image given in figure 4.4. The pressure increases due to the weak shock originating from the separation point. Hence, the Mach number reduces to $M_2 = 5.09$. Further downstream, the blue streamline encounters the reattachment shock which is considered to be strong due to the large deflection angle of the second ramp. The pressure rises up to $p/p_0 = 120$ and the total pressure reduces locally to $(p_t/p_{t,0})_3 = 1.276 \times 10^{-1}$. A local Mach number of $M_3 = 1.91$ is calculated.

From figure 4.5(a) can be seen that domain 1 and 4 are connected. As a result, point 4 lies on the intersection of the light blue shock polar (C_1) and the red shock polar (C_3) which indicates a small pressure drop and thus an expansion wave (see figure 4.5(c)). The intersection lies on the strong shock solution of the light blue shock polar. This indicates that a strong shock is present between domain 1 and 4. A similar analysis holds for the connection between domain 1 and domain $(5,6)$. Domain 6 is incompatible with domain 4 and therefore there is an intermediate state present (domain 5). Point $(5,6)$ is found by the intersection point of the green and dark blue shock polar shown in figure 4.5(c). For this case the pressure drop is larger (see the green line in figure 4.5(c)) and therefore a second stronger expansion wave originates from the shock interaction above the second ramp.

The flow passes a Prandtl-Meyer expansion going from domain 3 to domain 4. From figure 4.5(c), a change in flow direction of 2° can be observed and therefore according to the Prandlt-Meyer function, $M_4 = 1.97$. Prandtl-Meyer expansion waves are isentropic and therefore $(p_t/p_{t,0})_3 = (p_t/p_{t,0})_{4,5} = (p_t/p_{t,0})_{6,7,8}$. A similar analogy is applied to determine the Mach number in domain 6. Based on the change in flow direction ($\Delta\varphi_{4-6} = 8°$) which is obtained from figure 4.5(c), and the Prandlt-Meyer function the Mach number in domain 6 is determined to be $M_6 = 2.19$.

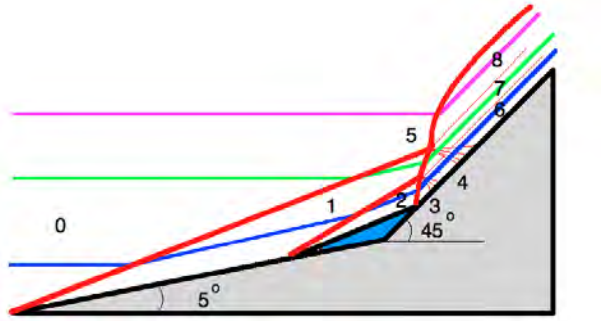

(a) Sketch of the $5° - 45°$ model with its shock pattern

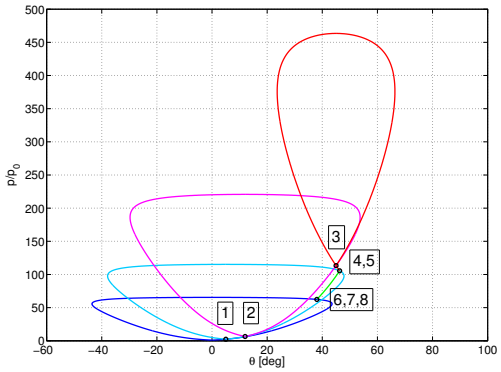

(b) Hodograph for the $5° - 45°$ model with a $h_{zz} = 1.15mm$ at $2.5cm$ from the leading edge

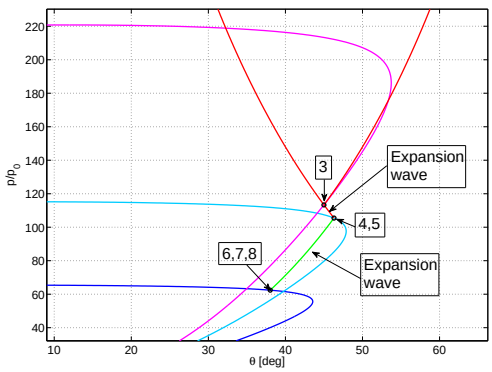

(c) Detail of the hodograph for the $5° - 45°$

Figure 4.5: Sketch of the $5° - 45°$ model

Table 4.1: Local Mach number for all domains

Domain	0	1	2	3	4	5	6	7	8
M	7.5	6.49	5.40	1.96	2.03	1.31	2.42	1.57	0.39

Green stream line

The green stream line encounters the leading edge shock. Further downstream it passes through the combined separation/reattachment shock from domain 1 to domain 4 which is considered to be a strong shock based on the argument given in the previous paragraphs. The pressure increases from $(p/p_0)_1 = 10$ to $(p/p_0)_5 = 110$. This is represented by the light blue shock polar connecting point 1 with point $(4, 5)$. A deflection angle of$\Delta\ \varphi_{1-5} = 40°$ is obtained. The oblique shock relations are then used to obtain $M_5 = 1.2$. This does not correspond with the value found in the previous paragraph forM_4. The blue stream line experienced multiple weak oblique shocks while the green stream line experienced one weak and one very strong shock. As a result, the entropy in domain 5 differs from domain 4 causing a locally different Mach number, velocity, temperature and density. Therefore it is expected that a slip line originates from the point where the separation and reattachment shock interact. Furthermore, the green line passes through the expansion wave that originates from the shock interaction above the second ramp. Due to the slip line between domain 4 and 5, a different velocity is found in domain 7 compared to domain 6.

Pink stream line

Finally, the pink stream line experiences just one strong shock. In the hodograph, this is represented by the path at the dark blue shock polar moving from point 1 directly to point $(6, 7, 8)$. This point lies on the strong solution of the dark blue shock polar. The pressure increases therefore from $(p/p_0)_0 = 1$ to $(p/p_0)_{5,6} = 65$. The velocity directly behind the bow shock is expected to be lower than near the wall of the second ramp. The flow passes through a strong (nearly normal) shock which experiences a significant entropy drop while for the flow passing through multiple oblique shocks (see the blue and green stream line), the entropy loss is significantly lower. Therefore the Mach number is higher near the wall (domain 6 and 7) compared to the conditions directly behind the bow shock (domain 8). As a result, another slip line is present between domain 7 and 8. Assuming the bow shock is nearly normal, the Mach number directly behind the bow shock is expected to be $M_8 = 0.39$. It is therefore concluded that the flow downstream of the bow shock is divided into three different velocity fields where the domain nearest to the wall has the highest velocity. All local Mach numbers are also presented in table 4.1.

4.1.5 Particle Image Velocimetry (PIV) measurement campaign

Particle Image Velocimetry is used to obtain a two dimensional velocity field over the $5° - 45°$ ramp. Measurements are performed for three different FOVs to increase the spatial resolution of the overall velocity field. A sketch of the three separate FOVs is given in figure 4.6.

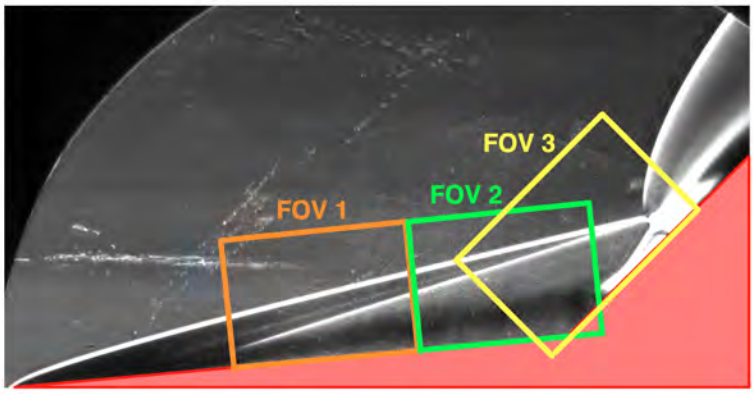

Figure 4.6: Overview of the domain of interest during the PIV measurement campaign

Examples of the raw and processed images for the separate FOVs are given in Appendix A. Using vector field rotation and bilinear interpolation, the three FOVs are merged together such that an overall two dimensional velocity field is obtained. Due to the limited time and the high work intensity of PIV in

the HTFD, it is chosen to determine a mean velocity field for the case that no VG is applied, at a unit Reynolds number of $11.3 \times 10^6 [m^{-1}]$.

Typically $30 - 40$ runs are performed per FOV to obtain a converging mean of the velocity data. An example of the converging mean for a local measurement point in the free stream in FOV 1 is given in figure 4.7. The mean total velocity at a fixed point is plotted against the number of runs:

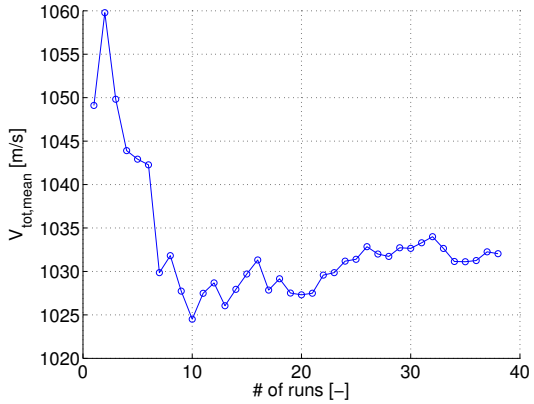

Figure 4.7: Converging mean of V_x at a local data point in the free stream

It can be seen that the velocity converges to the free stream velocity $V_\infty = 1033\ m/s$. In figure 4.8, the overall total velocity (V_{tot}) contour plot is given with the corresponding stream lines. The bow shock is visible above the second ramp. Upstream of the bow shock, V_{tot} is equal to the free stream velocity ($V_\infty = 1033 m/s$) which is also shown in more detail in figure 4.13. Furthermore, the separated flow domain near the wall of the 5° is clearly visible and a clear recirculation bubble is present at the first-to-second ramp junction. Next to that, the compression due to the reattachment shock is visualised by the converging stream lines parallel to the second ramp.

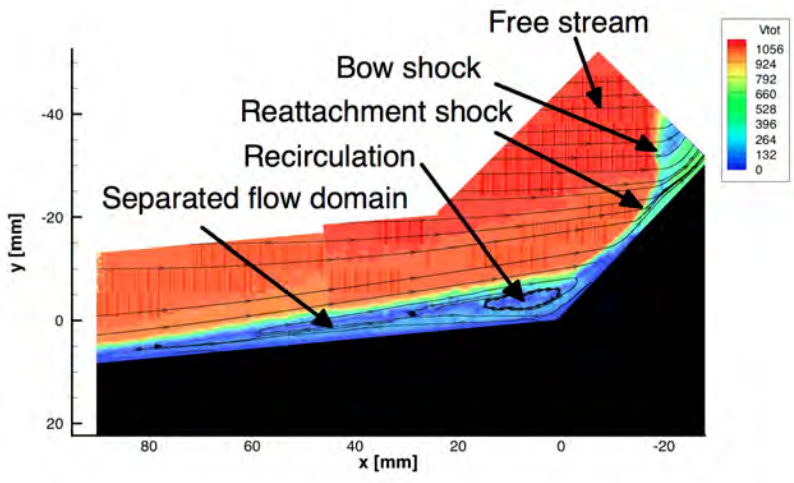

Figure 4.8: Macroscopic flow overview by means of a contour map for V_{tot}. V_{tot} is given in m/s

Downstream of the leading edge shock, the flow travels parallel to the 5° ramp and a compression wave induced by boundary layer separation deflects the flow to approximately $\theta = 9°$. Hence, an increase in V_y is expected downstream of the shock. In figure 4.9, the leading edge shock and the separation shock are visualised by plotting a small range of V_y. From figure 4.9 can be obtained that the vertical velocity component increases from approximately $V_{y,1} = 75\ m/s$ to $V_{y,2} = 125\ m/s$.

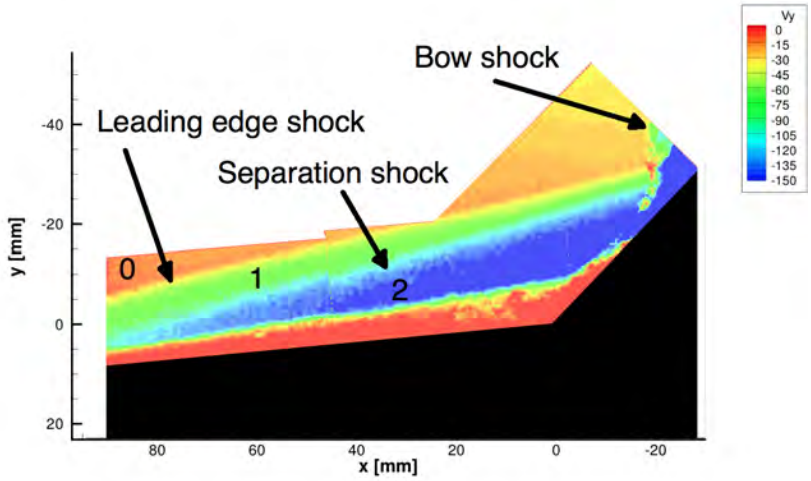

Figure 4.9: Leading edge shock and separation shock indicated by the colormap of the V_y. V_y is given in m/s

The local flow angle is calculated using V_x and V_y:

$$\theta = \arctan \frac{V_y}{V_x} \tag{4.3}$$

In figure 4.10, the flow angle, downstream of the bow shock is plotted. It is shown that the flow is deflected parallel to the wall and thus $\theta \approx 45°$ downstream of the reattachment shock where the streamlines converge. Downstream of the bow shock, the flow is deflected slightly towards the model ($\theta \approx 30°$) which corresponds to what is found in section 4.1.4. In the hodograph given in figure 4.5(b), it was shown that the flow angle decreases directly behind the bow shock to $\varphi_{6,7,8} = 39°$. From figure 4.10 the flow angle measured directly behind the bow shock (green domain), corresponds to $\varphi_{6,7,8}$. However, more downstream of the second ramp, the flow is deflected away from the model since $\theta \approx 54°$ which differs with what is determined in section 4.1.4. Furthermore, note that the leading edge shock and separation shock do not interact before the bow shock. Their relative position corresponds with the Schlieren image given in figure 4.3

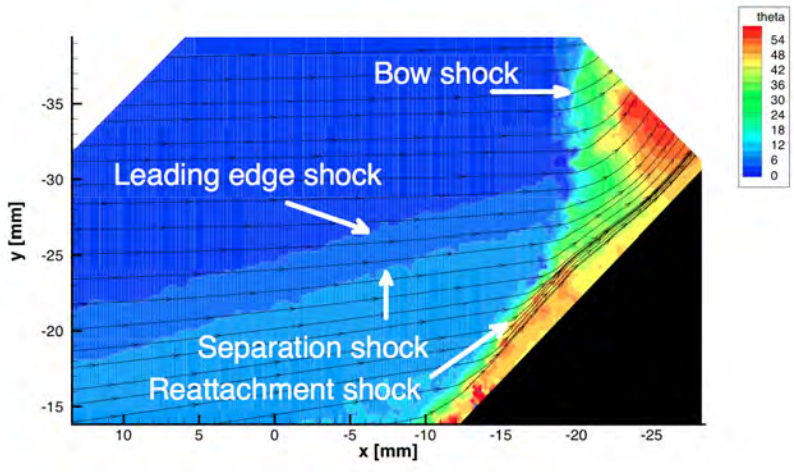

Figure 4.10: Detailed colormap of the flow angle on the 45° ramp. Flow angle is given in degrees

In figure 4.11, a detail is given of the velocity field near the leading edge of the model. The flow domain behind the separation shock is indicated by orange. A gradual increase of thickness is noticed of the blue low velocity domain. Note, the typical S-shaped boundary layer velocity profile which is discussed in the introduction of this chapter. It is therefore determined that the boundary layer is separated in figure 4.11. Hence, the upstream location where separation occurs lies outside the FOV. The length from the start of separation with respect to the first-to-second ramp junction is estimated to be 95 mm.

Note the back flow over the complete captured length of the separated flow field at the 5° ramp. A shear layer is present in the separated flow domain. Below the shear layer, a secondary boundary layer appears and on top of the shear layer, the separated boundary layer profile is present. Again this is in agreement with the boundary layer profile plotted in figure 4.2 and the characteristics sketched in figure 4.1.

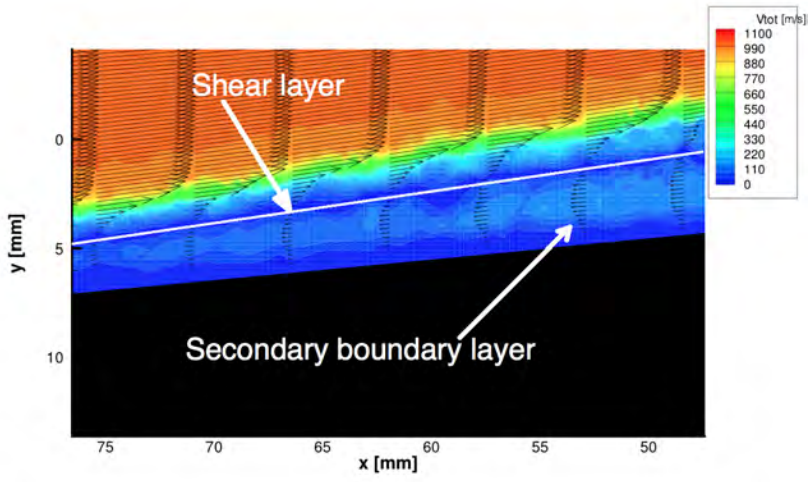

Figure 4.11: Detail of the separation bubble upstream of the hinge line of the model. V_{tot} is given in m/s

In figure 4.12 a detailed, velocity field near the first-to-second ramp junction is given. The development of a secondary boundary layer is again visible. It starts downstream on the 45° ramp and develops along the geometry of the double compression ramp in positive x direction.

The white line in figure 4.12 indicates the shear layer. The radius of curvature ($R = 20\ mm$) of is determined based on the curvature of the shear layer as shown in figure 4.12. This number is significantly lower than the radius of curvature found using the similar analogy as shown in [Navarro-Martinez and Tutty, 2005]. A radius of curvature of $R = 142\ mm$ was obtained (see section 2.2). Furthermore, it is noted that the flow is not smoothly curved over the surface, but it is slowed down abruptly by the reattachment shock as shown by the compressed streamlines in figure 4.10.

In figure 4.13, the velocity field above the 45° ramp is given. For the measurement of the velocity field above the 45° ramp, the x-axis of the image plane is aligned with the 45° ramp indicated in figure 4.6 and A.3. As a result, elongated interrogation windows are chosen in wall tangent direction so that the spatial resolution in wall normal direction can be improved. Hence, the velocity profile behind the bow shock and the velocity profile near the wall can be determined more accurately.

Three velocity domains are present behind the bow shock which are indicated in figure 4.13 by 1, 2, and 3. The shock interaction results in two slip lines which divide the flow regime behind the bow shock into three velocity regimes. This corresponds with what is determined theoretically in section 4.1.4. Based on the velocity profile near the wall, flow expansion is measured since the flow is accelerated from 350 m/s up to 700 m/s. Directly behind the bow shock a subsonic flow domain is present where the velocity is locally $150 - 200\ m/s$. The bow shock is therefore considered to be a strong shock solution which also corresponds to the obtained solution in the hodograph given in figure 4.5(b) for the case that $h_{zz} = 1.15\ mm$. Furthermore there is a low velocity domain indicated in figure 4.13 by 4. From Schlieren visualisation and the shock polar analysis, the strong local velocity gradient is ascribed to the strong

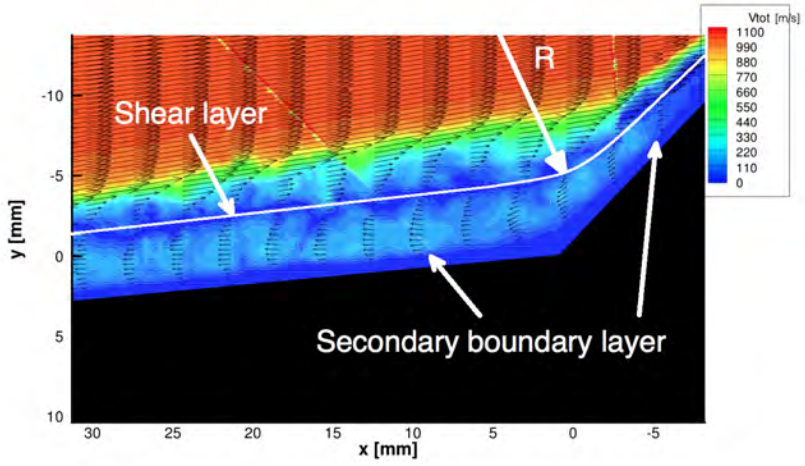

Figure 4.12: Recirculation bubble near the hinge line of the model. V_{tot} is given in m/s

reattachment shock.

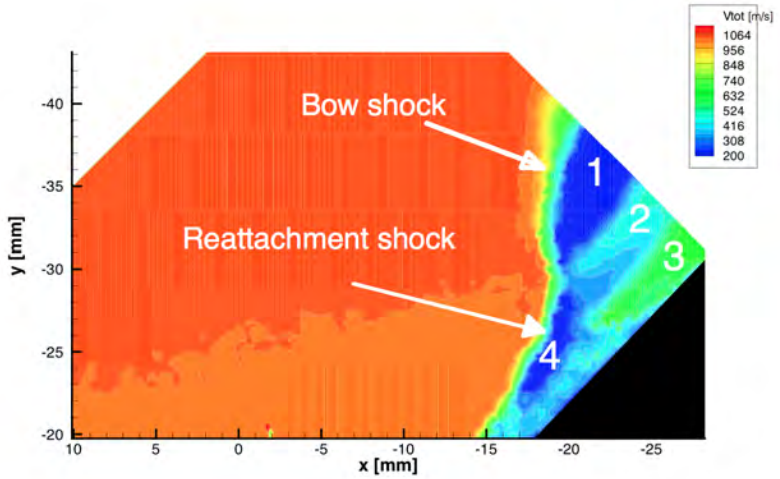

Figure 4.13: Detailed velocity field behind the bow shock on the 45° ramp. V_{tot} is given in m/s

Based on the energy equation, the local Mach number is calculated using equation 4.4:

$$M = \frac{V_{tot}}{\sqrt{\left(\frac{V_\infty}{M_\infty}\right)^2 + \frac{\gamma R}{2c_p}(V_\infty^2 - V_{tot})}} \tag{4.4}$$

The free stream Mach number is $M = 7.5$ while the Mach number behind the separation is approximately 6.0. This corresponds with what is found using the oblique shock relations (for $\theta_1 = 5°$, $M_1 = 6.48$ and $\theta_{sep} = 8.5°$, $M_2 = 5.93$). Behind the bow shock a clear subsonic domain is measured while near the wall the Mach number again increases up to approximately $M = 1.42$. In table 4.2 the Mach numbers of the four indicated domains are given:

Using shock polars, it was determined that the Mach number near the wall should be higher than the Mach number just downstream of the bow shock. Next to that, three velocity regimes downstream of the strong bow shock were determined in section 4.1.4. The values do not correspond which can be ascribed to the fact that the hodograph was created for the case that $Re = 14.1 \times 10^6 [m^{-1}]$ and a VG strip of

Table 4.2: Local Mach number for all domains

Domain	1	2	3	4
M	0.31	0.90	1.42	0.28

1.15 mm while the PIV experiments were performed for $Re = 11.3 \times 10^6[m^{-1}]$ and no VG. The shock interaction, as explained in section 4.1.1 is therefore slightly different.

4.2 Reference Temperature Method (RTM)

The Reference Temperature Method (RTM) can be used to determine boundary layer characteristics like the boundary layer thickness (δ), the friction coefficient (C_f) and the Stanton number (c_h) for compressible boundary layer flow using the simplified equations for incompressible boundary layers [Anderson, 2006]. A so-called reference temperature, T^*, is determined based on the free stream Mach number and the local temperature and used to obtain the reference flow quantities (p^*, ρ^*, μ^*, etc.). From this, the characteristic quantities can be determined by implementing the reference quantities in the known boundary layer equations for incompressible boundary layer flow. The application of the RTM is shown for the determination of the boundary layer thickness and the Stanton number at the 5° ramp of the double compression ramp model.

As stated in section 2.2, a zig-zag Vortex Generator (VG) is used to introduce a spanwise periodic boundary layer disturbance to induce steady longitudinal vortices. The influence of the height of the VG on the progression of the longitudinal vortices is further investigated during this thesis project. The boundary layer thickness is therefore determined so that the height of the VG can be scaled based on the local boundary layer thickness. Furthermore, the Stanton number is wanted to compare a typical measured streamwise heat flux map with the theoretically obtained streamwise heat flux map.

4.2.1 Boundary layer thickness

The boundary layer thickness is generally defined as $u = 0.99u_e$. Examining the Blasius boundary layer profile given in figure 4.2 more closely, it shows that at $\eta \approx 5$ $u = u_e$ and therefore:

$$\eta = y\sqrt{\frac{U}{\nu x}} = \delta\sqrt{Re_x} = 5 \tag{4.5}$$

or:

$$\delta = \frac{5x}{Re_x} \tag{4.6}$$

RTM relies on the available equations for incompressible flow over a flat plate. Therefore, equation 4.6 can be used to determine the boundary layer thickness for a compressible boundary layer. It is required to determine the reference Reynolds number indicated by Re_x^*.

$$\delta = \frac{5x}{\sqrt{Re_x^*}} \tag{4.7}$$

where:

$$Re_x^* = \frac{\rho^* U_e x}{\mu^*} \tag{4.8}$$

The flow over the first compression angle is deflected in the direction parallel to the 5° ramp. The free stream Mach number is 7.5 in this example case. Using the oblique shock relations, the following flow properties parallel at the 5° ramp are determined:
The reference temperature method states [Anderson, 2006]:

$$\frac{T^*}{T_t} = 1 + 0.032M_1^2 + 0.58\left(\frac{T_w}{T_e} - 1\right) \tag{4.9}$$

Table 4.3: Flow conditions behind the leading edge shock

M_1	$p_{t,1}$ $[Pa]$	$T_{t,1}$ $[K]$	T_1 $[K]$	p_1 $[Pa]$	ρ_1 $[kg/m^3]$
6.48	26.3×10^5	579	61	1.02×10^3	5.81×10^{-3}

The ratio between the wall temperature and the temperature at the edge of the boundary layer is determined using the following equation:

$$\frac{T_w}{T_e} = 1 + r\frac{\gamma - 1}{2}M_1^2 \tag{4.10}$$

where r is the recovery factor and taken to be equal to $r = \sqrt{Pr} = \sqrt{0.71} = 0.83$. The flow conditions at the edge of the boundary layer are taken equal to the conditions downstream of the oblique shock. The reference density is now determined assuming $dp/dy = 0$ ($p^* = p_\infty$) and using the equation of state:

$$\rho^* = \frac{p_\infty}{RT^*} \tag{4.11}$$

where $p_\infty = p_1$. The reference viscosity coefficient, μ^*, is calculated using Sutherlands law [Anderson, 2006]:

$$\frac{\mu^*}{\mu_r} = \left(\frac{T^*}{T_r}\right)^{\frac{3}{2}} \left(\frac{T_r + S}{T^* + S}\right) \tag{4.12}$$

In equation 4.12, $\mu_r = 1.789 \times 10^{-5}\,\frac{kg}{ms}$, $T_r = 288K$ and $S = 110$. The velocity behind the shock is given by:

$$U_e = M_1 a_1 = M_1\sqrt{\gamma R T_1} \tag{4.13}$$

At this point, the reference Reynolds number and thus the local boundary layer thickness can be evaluated based on equation 4.8.. In this analysis, x starts from the leading edge and runs parallel with respect to the 5° ramp. The VG is introduced at 25 mm from the leading edge at which the boundary thickness is approximately 1.45 mm. The maximum VG height is $h_{zz} = 1.15$ mm and therefore $(h_{zz}/\delta)_{max} = 0.92$. In figure 4.14 a detail of the boundary layer thickness is plotted against the streamwise coordinate x (blue line). In figure 4.14, the available VG heights are indicated with different colours in the same figure. This is done to show the size of the roughness element compared to the local boundary layer thickness.

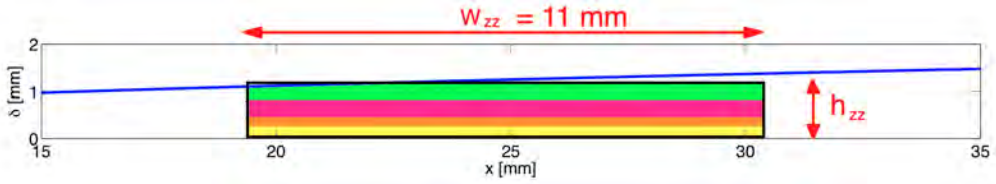

Figure 4.14: The boundary layer thickness plotted against the streamwise coordinate s

4.2.2 Streamwise heat transfer distribution

In chapter 3 the quantity q_s is introduced which represents the surface heat flux. This quantity is numerically determined based on the measured temperature distribution as shown in section 3.2. During the discussion of the results obtained using QIRT, typical heat transfer maps are presented. For now, the theoretically obtained surface heat flux is compared with the measured heat flux. The heat transfer distribution is given in figure 4.15 for the case that no VG is applied and a Reynolds number of $Re = 14 \times 10^6$ $[m^{-1}]$. The RTM is used to evaluate the Stanton number for a laminar boundary layer. According

to Reynolds analogy, the Stanton number is related to the friction coefficient and the Prandtl number for a laminar incompressible boundary layer [Anderson, 2006]:

$$\frac{c_h}{C_f} = \frac{1}{2} Pr^{-2/3} \tag{4.14}$$

The incompressible expression for c_f is:

$$c_f = \frac{0.664}{\sqrt{Re_x}} \tag{4.15}$$

The following expression is then used to calculate c_h^* [Anderson, 2006]:

$$c_h^* = \frac{0.332}{\sqrt{Re_x^*}} (Pr^*)^{-\frac{2}{3}}. \tag{4.16}$$

where $Pr^* = \frac{\mu^* cp^*}{k^*}$ and Re_x^* are evaluated at the reference temperature. The reference thermal conductivity is calculated using Sutherland's law and $c_p^* = 1004$. In figure 4.15 the theoretically obtained c_h distribution for a 5° ramp angle (red line) is compared with the measured c_h streamwise distribution for a 5° ramp angle (blue line).

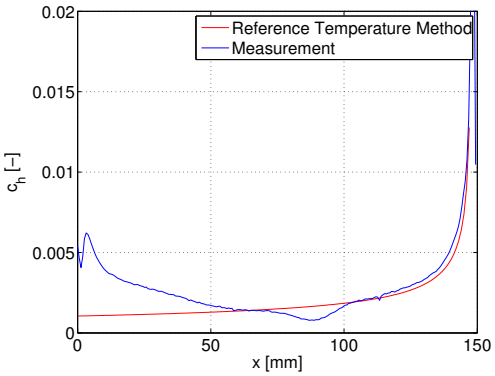

Figure 4.15: Comparison between the measured c_h on the 5° ramp and c_h determined by the Reference Temperature Method

From Reynolds analogy it is known that:

$$c_h \propto \frac{1}{\sqrt{Re_s}} \tag{4.17}$$

where s is the streamwise coordinate from the leading edge of the model ($s = 0$ at $x = 150$, see model coordinate system defined in section 2.2). From this point, the measured streamwise heat flux map correspond nicely with Reynolds analogy. The boundary layer is thin at the leading edge and grows proportionally with $\sqrt{s}$:

$$\delta \propto \sqrt{s} \tag{4.18}$$

The temperature gradient in normal direction becomes smaller when the boundary layer thickness increases. As a result, the surface heat flux decreases with increasing boundary layer thickness and therefore, the measured c_h profile shows that it is inversely proportional to Re_s which corresponds to the theoretically obtained c_h distribution shown in figure 4.15.

Boundary layer separation can be observed using the streamwise heat flux distribution. From figure 4.2 it is known that the du/dy decreases for a laminar boundary layer when an adverse pressure gradient is present and the boundary layer tends to separate. The friction force decreases since:

$$C_f = \frac{\tau_w}{\frac{1}{2}\rho u_e^2} \tag{4.19}$$

where u_e is the velocity at the edge of the boundary layer and τ_w is defined as:

$$\tau_w = \left[\mu \frac{du}{dy}\right]_w \tag{4.20}$$

At boundary layer separation, it is therefore expected to see a local decrease in Stanton number since the c_h is directly proportional to the C_f (see equation 4.14). At $x = 95\ mm$ ($s = 55\ mm$) a local decrease of c_h is present which can be ascribed to boundary layer separation. The location of boundary layer separation corresponds to what has been observed in the PIV images. The origin of the separation shock was estimated to be at $x = 95\ mm$.

To emphasise the typical local streamwise heat flux distribution, the Stanton number is multiplied by $\sqrt{s}$ such the heat flux distribution for a laminar boundary layer appears as a horizontal straight line. Therefore $c_h \times \sqrt{s}$ is plotted against the streamwise coordinate tangent to the surface of the model in figure 4.16 with the y-axis in log scale.

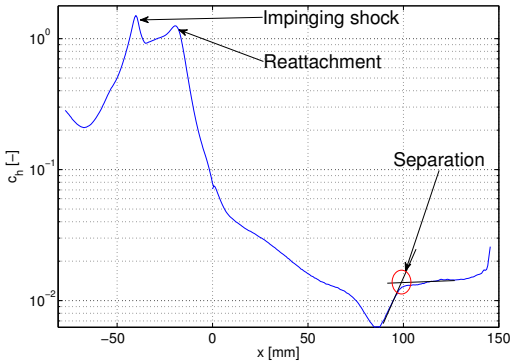

Figure 4.16: Example of a streamwise Stanton number distribution for the case of $h_{zz} = 0$, $Re = 14.1 \times 10^6$ $[m^{-1}]$

The streamwise location $x = 150\ mm$ corresponds with the leading edge while $x = -80.9\ mm$ corresponds with the trailing edge of the model The decrease in c_h related to boundary layer separation is more clear in figure 4.16. The first peak near $x = -24\ mm$ is caused due to the local boundary layer necking caused by the boundary layer reattachment. The boundary layer thickness decreases locally and the temperature gradient in normal direction increases. The second peak in figure 4.16 near $x = -45\ mm$ is ascribed to a shock that impinges at this location on the 45° ramp. The heat flux in surface normal direction increases due to local flow compression.

From the PIV results presented in section 4.1.5, it was concluded that a secondary boundary layer develops below the shear layer near the wall. The effect of this behaviour can be traced back in the heat transfer map given in figure 4.16 by looking at the gradual increase in c_h for $0\ mm \leq x \leq 50\ mm$. In general it can be stated that the Stanton number decreases with increasing boundary layer thickness. However, a thin boundary layer develops just downstream of the first-to-second ramp junction. This is seen by the locally increased c_h near $x = 0\ mm$.

In figure 4.17 the heat transfer distribution mapped on the model surface is given for the case that no VG is applied and $Re = 14.1 \times 10^6$ $[m^{-1}]$.

In figure 4.17, the $\ln(c_h)$ is plotted. The spanwise separation line is indicated by the dark blue line near the leading edge figure 4.17. This line represents the same local decrease in heat transfer coefficient shown in figure 4.16 at $x \approx 95\ mm$. Based on figure 4.16 and 4.17 and the undisturbed flow domain, the boundary layer separated at $x = 95\ mm$ and reattachment takes place at $x = -24\ mm$. Similar heat transfer maps are presented in chapter 5.

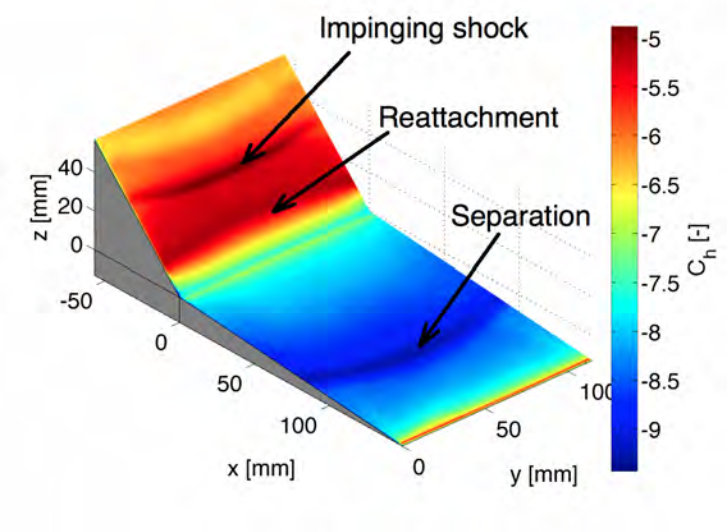

Figure 4.17: The logarithm of the Stanton number (c_h) mapped on the surface coordinate system for the case $h_{zz} = 0mm$, $Re = 14.1 \times 10^6\ m^{-1}$

4.3 Flow topology around a zig-zag Vortex Generator (VG)

A zig-zag Vortex Generator (VG) strip is used to introduce a periodic spanwise boundary layer disturbance. The zig-zag VG is used to control the flow during the measurement since it is noticed that small bumps on the leading edge significantly influence the stability of the flow [Schrijer, 2010a]. Hence the zig-zag strip with $\lambda = 6\ mm$ is used to make sure that the longitudinal structures are steady. The flow topology around the VG is clarified in figure 4.18.

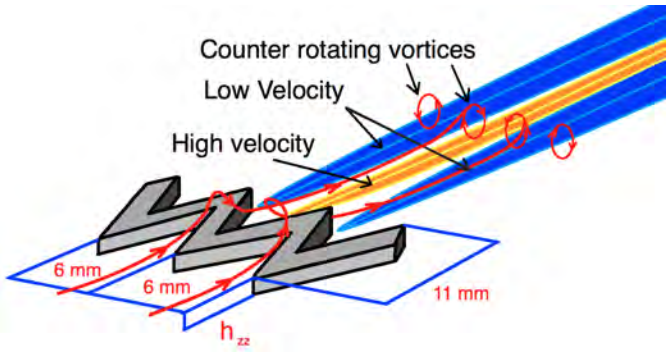

Figure 4.18: Expected flow topology behind a zig-zag VG

The red lines indicate the streamlines over the zig-zag VG. A vortex builds up along each tooth of the strip. The zig-zag geometry induces a spanwise velocity gradient. The flow then separates at the end of each tooth causing a downwards velocity component which forces the flow to curl around the backwards point zig-zig tooth. Two counter rotating vortices emanate from the backward pointing zig-zag teeth and the velocity points away from the surface of the model indicated by the pink stream lines in figure 4.18.

The longitudinal vortices cause a movement of low momentum fluid regions away from and high momentum fluid regions towards the wall in the upwash and downwash sections respectively as shown in figure 4.19 [Saric, 1994, Swearingen and Blackwelder, 1987]. This results in low and high speed regions in the boundary layer in longitudinal direction which can be seen in the periodicity of the V_x velocity component in spanwise direction. The spanwise V_x profile shows a spanwise sinusoidal behaviour.

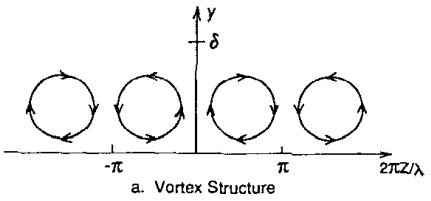

(a) Orientation of the vortex motion

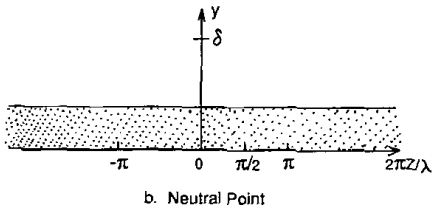

(b) Low momentum fluid indicated by the shaded area and the higher momentum fluid is indicated by the blank area

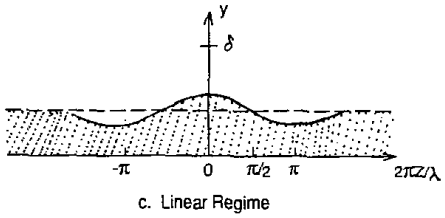

(c) The VG/initial disturbance causes fluctuations in the momentum distribution

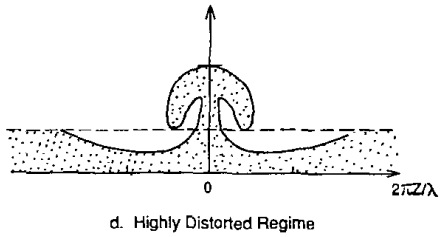

(d) Mushroom shaped distribution is formed

Figure 4.19: Evolution of the secondary instability [Saric, 1994]

A typical spanwise velocity profile is given in figure 4.20 where V_y represents the spanwise velocity component and V_z the wall normal velocity component. As a result, a high velocity regime is present where the velocity vector points towards the surface of the model. This results in longitudinal streaks of locally low and high momentum regimes. Local heat loss occurs when the kinetic energy increases based on the conservation of energy. The heat transfer coefficient and thus the Stanton number increases locally. Hence near wall high kinetic longitudinal streaks induce higher heat flux levels. The longitudinal high velocity domain can therefore be identified using QIRT. Based on figure 4.18, a periodic spanwise heat transfer distribution is expected as shown by a sketch of the spanwise q distribution in figure 4.20.

Not much is known about the persistence of the introduced disturbances and what kind of flow structures are present behind this particular VG. Therefore Elsinga and Westerweel [2012] performed research on the flow around a similar zig-zag strip by means of Tomographic Particle Image Velocimetry (Tomo-PIV) in subsonic flow ($V = 0.21\ m/s$). Streak-like structures are obtained directly behind the strip. Furthermore, back flow is noticed in the near-wall part of the boundary layer directly behind the strip. This is shown in figure 4.21(a). In figure 4.21(b) the velocity field is plotted in the (y, z) plane at $x = \frac{x}{\delta_0}$ where δ_0 is the undisturbed boundary layer thickness. Note the cross flow which is caused due to the yaw angle of approximately 5° that the VG makes with respect to the oncoming flow.

Elsinga and Westerweel [2012] concluded that behind each downstream pointing tip a low velocity domain and behind each upstream pointing tip of the VG a high velocity domain is present. This corresponds with the sketch given in figure 4.18 and the results found by Schülein and Trofimov [2011].

Near the point of average reattachment, the spanwise vortices break up into arches and subsequently form hairpin-like structures. Furthermore it was noted that the average velocity field differs significantly from the instantaneous snap shots. Instead of spanwise vortices, the meain co-rotating streamwise vortices were measured directly behind the VG. The lack of symmetry is explained by the previously discussed yaw-angle of the trip strip.

Schülein and Trofimov [2011] performed research regarding hypersonic flow over a flat plate with downstream, a ramp with varying wedge angles (20°, 25° or 30°). The length of the flat plate is 500 mm. The distance between the ramp and the leading edge of the flat plate is indicated by x_s. The distance x_s could be varied between 225 mm and 475 mm. The second compression ramp has a length of 300 mm and the complete model has a width of 400 mm. Experiments were performed at two free stream

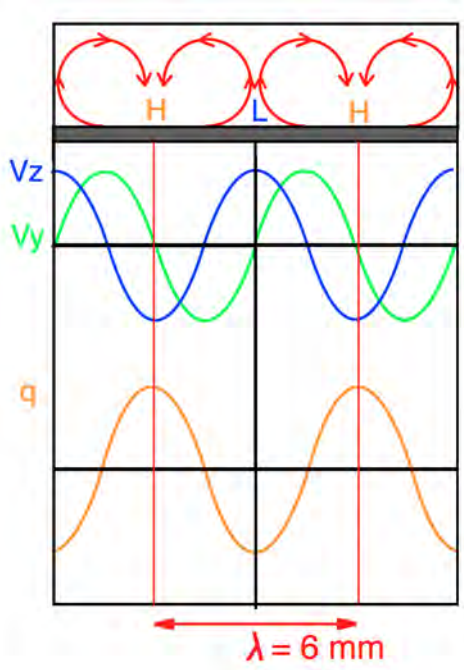

Figure 4.20: The expected V_y and V_z distribution together with the expected surface heat flux

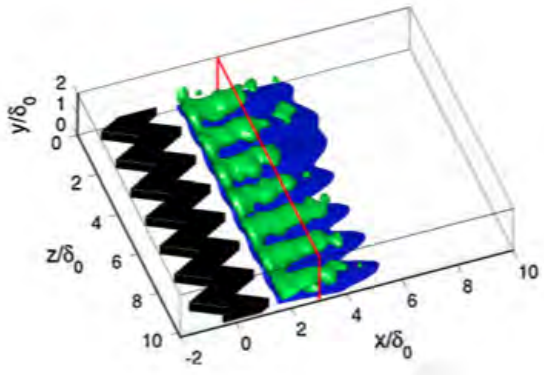

(a) Three-dimentional rendering of the mean velocity field showing back flow (blue) and vortical motion.

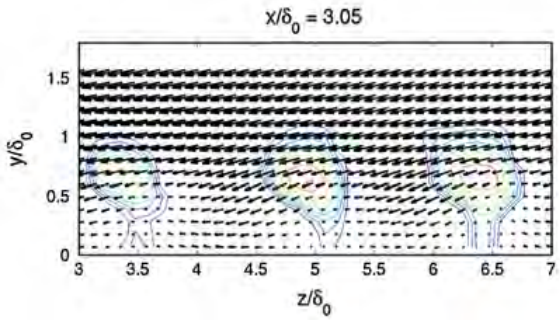

(b) Velocity vectors in the cross plane $\frac{x}{\delta_0} = 3.05$.

Figure 4.21: Results regarding the flow topology around zig-zag in subsonic flow by Elsinga and Westerweel [2012]

Mach numbers namely at $M_\infty = 3$ with $T_0 = 260K$, $P_0 = 0.32\ MPa$ and a unit Reynolds number of $Re = 30 \times 10^6\ m^{-1}$ and at $M_\infty = 5$, $T_0 = 400K$, $P_0 = 2.55\ MPa$ and $Re = 45 \times 10^6\ m^{-1}$.

The difference between two different VGs, a zigzag strip and a single triangular prism, were investigated. The height and the wavelength of the VG were varied in combination with the position of the VG with respect to the leading edge. Schülein and Trofimov [2011] applied a mineral oil with TiO_2 pigment powder on the surface to visualize the streamlines near the wall.

Oil flow visualisation relies on the no-slip condition at the wall, the velocity and shear stress at air-oil interface are continuous and a balance is present between the viscous forces and the pressure gradient. Hence, the flow direction in oil depends on the wall shear stress and the pressure gradient [Scarano, 2007]. In figure 4.22 a typical skin friction pattern is given for the separated flow domain.

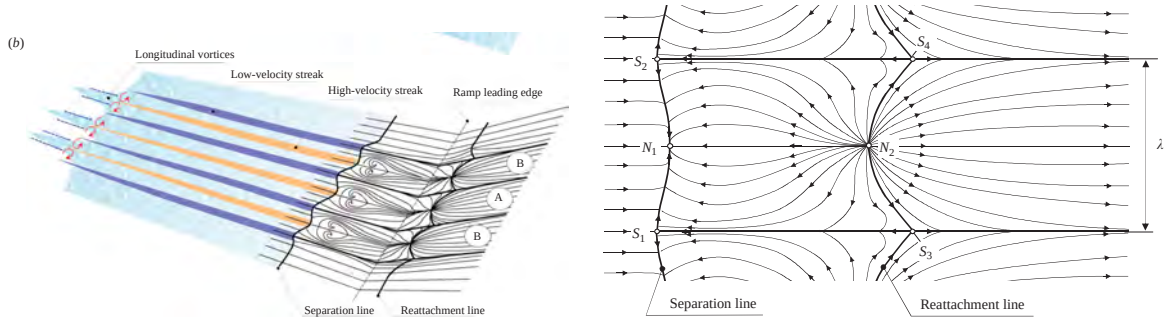

(a) 3D overview of separation and reattachment found by Schülein and Trofimov [2011]

(b) Oil visualization indicating the skin friction pattern between the separation and reattachment line. The above impression is for the case of small $\frac{\lambda}{\delta}$ and a long 5° ramp found by Schülein and Trofimov [2011]

Figure 4.22: Results regarding the flow topology around zig-zag in subsonic flow by Schülein and Trofimov [2011]

The horizontal lines connecting S_2 with S_4 and S_1 with S_3 represent local reattachment lines. The separation line and reattachment lines are indicated in the figure. In between those lines, the separated flow domain is shown where overall back flow is present. The shape of the separation line is influenced by the upstream VG indicated by the wavy spanwise separation line. Furthermore, downstream of the reattachment line, a diverging streamline pattern is noticed.

It is found that the dimensions of the VG have an influence on the intensity of separation. Schülein and Trofimov [2011] show that for large $\frac{h}{\delta}$, where δ is the boundary layer thickness and h the height of the VG, and a short x_s, the intensity of the vortical disturbance is high. The flow is then characterised by the formation of a secondary separation bubble with a pair of focus points inside the separation bubble indicated in figure 4.22(a).

Schülein and Trofimov [2011] measured coherent longitudinal so-called superstructures in undisturbed turbulent boundary layers as unsteady longitudinal clusters. However, when the boundary layer is tripped by a VG, these superstructures become steady. It is stated that downstream of the VG, a vortical disturbance is present after which a transition takes place into self-sustained superstructures. These longitudinal superstructures are amplified and the formation and reappearance of longitudinal vortices occurs on the 45° ramp.

Schülein and Trofimov [2011] also investigated the influence of the angle of the compression ramp on the wavelength of the longitudinal vortices in combination with the boundary layer thickness. It is found that the vortex wavelength increases when the second ramp angle is increased from $\theta_2 = 20°$ to $\theta_2 = 25°$. The superstructures are amplified at reattachment and due to the increase of compression angle, the size of the separation bubble increases together with the streamwise pressure gradient and pressure jump. These parameters amplify the induced disturbance, hence, an increase of vortex intensity in the streamwise scale of the structure is measured.

4.4 Görtler instability

Görtler vortices are induced by the centrifugal forces associated with the change in direction of motion forced on the fluid by the geometry of the surface. The viscous boundary layer flow fulfills the no-slip condition when a flow propagates over a wall. The curvature of the wall leads to an unstable situation depending on the local velocity profile and the local radius of curvature. Figure 4.23 presents an example of the contradictory flow situation which induces the Görtler instability:

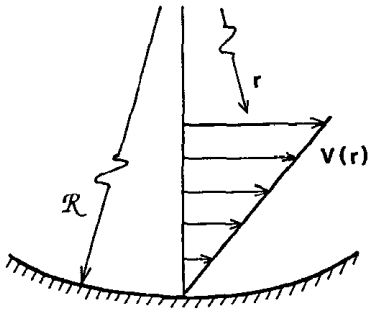

Figure 4.23: Instable flow situation causing the Görtler instability. Figure taken from Saric [1994]

From mechanics it is known that the angular velocity increases with increasing radius of curvature which is in conflict with the no-slip condition at the wall. This instability causes a longitudinal vortex structure in the boundary layer which is often referred to as Görtler vortices. Mathematically, this instability is prescribed by the Rayleigh criterion which is defined in equation 4.21 [Saric, 1994]. If$\Gamma(\ r) = rV(r)$:

$$\frac{d\Gamma^2}{dr} < 0 \tag{4.21}$$

The influence of the wall radius of curvature on the behaviour of the boundary layer flow is discussed. The general assumptions that are taken into account in this section are:

- The boundary layer thickness is much smaller than the radius of curvature ($\delta/R \ll 1$)
- The basic flow is nearly parallel to the wall which means that centrifugal effects are neglected in the description of the basic flow, although, they are partially retained in the disturbance equations.
- A local stability analysis is considered for which the basic flow is assumed to be independent of the streamwise and wall normal coordinate

Consider the double compression ramp model as an obstacle which forces the flow to curve. Yet, the no-slip condition holds at the surface of the model. Therefore, a similar instability as in figure 4.23 occurs in double compression ramp flow. The curvature of the flow is therefore simplified by taking the red curved plane as shown in figure 4.24(b). The red curved plane indicates the space where the boundary layer is separated. Point S indicates the separation line and A the reattachment line. R indicates the radius of curvature over which the flow is turned. The coordinate system shown in figure 4.24(b) is used to investigate the characteristic flow properties for Görtler instabilities. For now the radius of curvature is taken to be constant but for a double compression ramp this will not be the case [Navarro-Martinez and Tutty, 2005].

In figure 4.24(b), $x = R\theta$, $y = R - r$ and z is the spanwise coordinate. Using the following non-dimensional coordinates:

$$\bar{x} = \tfrac{x}{L},\ \bar{y} = \tfrac{y}{\delta},\ \bar{z} = \tfrac{z}{\delta}$$

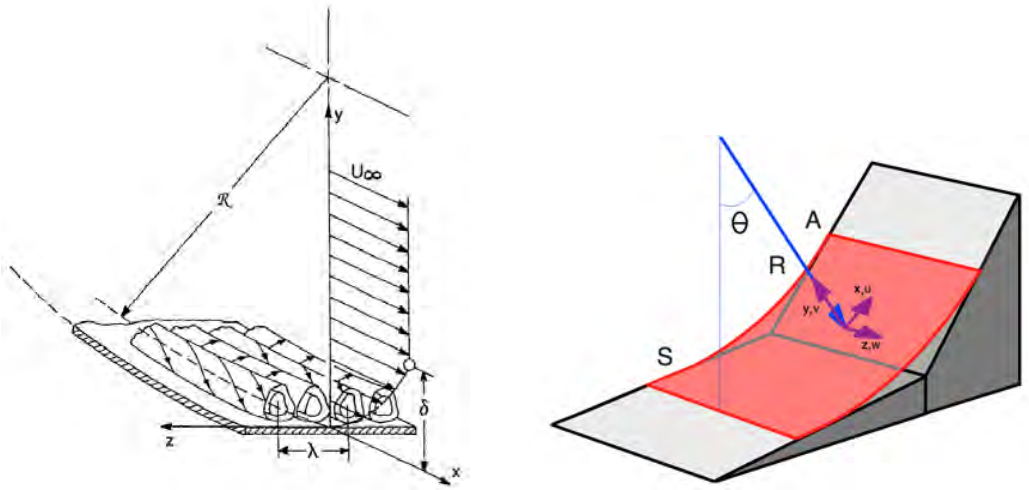

(a) Sketch of Görtler vortices together with a typical boundary layer profile and a curved geometry Saric [1994]

(b) The defined coordinate system that is used during the local linear stability analysis

Figure 4.24: Sketch of Görtler vortices in a boundary layer and a sketch of the model with cylindrical coordinate system

and assuming that $L \gg \delta$, the Navier Stokes equations are given in cylindrical coordinates. The cylindrical N-S equations are linearised in the following way and as a result, the following equations are obtained:

$$\frac{u'}{u_\infty} = u(\bar{x},\bar{y}) + \xi u(\bar{x},\bar{y},z) + \mathcal{O}(\xi^2)$$

$$\frac{v'Re}{u_\infty} = v(\bar{x},\bar{y}) + \xi v(\bar{x},\bar{y},z) + \mathcal{O}(\xi^2)$$

$$\frac{w'Re}{u_\infty} = \xi w(\bar{x},\bar{y}) + \mathcal{O}(\xi^2)$$

$$\frac{p'}{\rho u_\infty^2} Re^2 = p(\bar{x})Re^2 + p_0(\bar{x},\bar{y}) + \xi p'(\bar{x},\bar{y},\bar{z}) + \mathcal{O}(\xi^2)$$

and applying an order estimation, the following is obtained for the free stream: [Goulpie et al., 1996, Batchelor and Miles, 1981]:
$\mathcal{O}(1)$:

$$\frac{\partial u}{\partial \bar{x}} + \frac{\partial v}{\partial \bar{y}} = 0 \tag{4.22}$$

$$u\frac{\partial u}{\partial \bar{x}} + v\frac{\partial u}{\partial \bar{y}} = -\frac{\partial p}{\partial \bar{x}} + \frac{\partial^2 u}{\partial \bar{y}^2} \tag{4.23}$$

$$u\frac{\partial v}{\partial \bar{x}} + v\frac{\partial v}{\partial \bar{y}} = -\frac{\partial p_0}{\partial \bar{y}} + \frac{\partial^2 v}{\partial \bar{y}^2} - (Gu)^2 \tag{4.24}$$

For the perturbation terms of order $\mathcal{O}(\xi)$ where $\mathcal{O}(\xi) \ll \mathcal{O}(1)$ holds:
$\mathcal{O}(\xi)$:

$$\frac{\partial u'}{\partial \bar{x}} + \frac{\partial v'}{\partial \bar{y}} + \frac{\partial w'}{\partial \bar{z}} = 0 \tag{4.25}$$

$$u\frac{\partial u'}{\partial \bar{x}} + u'\frac{\partial u}{\partial \bar{x}} + v\frac{\partial u'}{\partial \bar{y}} + v'\frac{\partial u}{\partial \bar{y}} = \frac{\partial^2 u'}{\partial \bar{y}^2} + \frac{\partial^2 u'}{\partial \bar{z}^2} \tag{4.26}$$

$$u\frac{\partial v'}{\partial \bar{x}} + u'\frac{\partial v}{\partial \bar{x}} + v\frac{\partial v'}{\partial \bar{y}} + v'\frac{\partial v}{\partial \bar{y}} = -\frac{\partial p}{\partial \bar{y}} + \frac{\partial^2 v'}{\partial \bar{y}^2} + \frac{\partial^2 v'}{\partial \bar{z}^2} - 2G^2 uu' \tag{4.27}$$

$$u\frac{\partial w}{\partial \bar{x}} + v\frac{\partial w'}{\partial \bar{y}} = -\frac{\partial p'}{\partial \bar{z}} + \frac{\partial^2 w}{\partial \bar{y}^2} + \frac{\partial^2 w'}{\partial \bar{z}^2} \tag{4.28}$$

Equation 4.24 shows that a pressure gradient in normal direction balances the centrifugal term $(Gu)^2$. The influence of the local radius of curvature is incorporated in the Görtler number which is defined as:

$$G = Re\sqrt{\frac{R}{L}} \tag{4.29}$$

Saric [1994], Goulpie et al. [1996], Bottaro and Luchini [1999] performed a linear stability analysis in which the perturbation quantities are given by $(\bar{u}, \bar{v}, \bar{w}, \bar{p}) = (\hat{u}(y), \hat{v}(y), \hat{w}(y), \hat{p}(y))e^{\sigma x + i\beta z}$ where σ is the growth rate of the vortices and β is the spanwise wavenumber . Equations 4.25-4.28 are rewritten such that:

$$\mathbf{L}(\sigma, G, \beta)\hat{f} = \lambda \hat{f} = 0 \tag{4.30}$$

where $\hat{f} = (\hat{v}(y), \hat{u}(y))$ is the eigenvector and $\mathbf{L}$ is a linear operator which depends on (U, V, P, β, σ). (U, V, P) are determined by using the Falkner-Skan equation which is solved numerically using the Euler shooting method. The derivation of the entries of the linear operator $\mathbf{L}$ are given in Appendix B

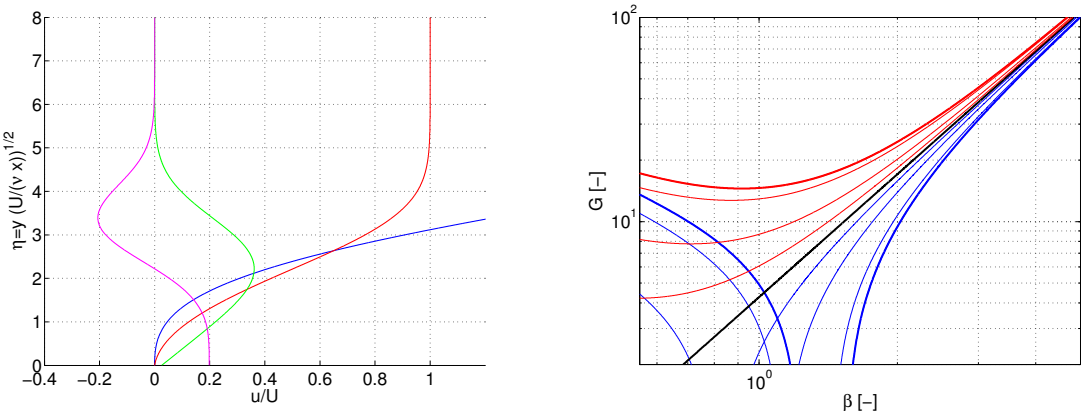

(a) Solution to the Falkner-Skan equation from which U, U_y and U_{yy} are locally determined

(b) Stability plot in the $\beta - G$ plane for the case of $\gamma = 0$ and $\eta = 1$

Figure 4.25: Stability plot [Ekelschot, 2012]

Assuming that the Görtler vortices propagate in the top part of the boundary layer, the stability plot is shown for a typical boundary layer profile at separation given in figure 4.25(a) at $\eta = 1$. The wavelength of the VG is fixed since $\lambda_{zz} = 6\ mm$. Assuming a Görtler number of 100 and β is given in equation 4.31:

$$\beta = \frac{2\pi\xi L}{\lambda} = \frac{2\pi\frac{1}{100}115}{6} = 1.20 \tag{4.31}$$

where $\xi \approx \frac{1}{R}$, L is a reference length which in this case is equal to the width of the model. In figure 4.25(b), the stability plot is given in the (β, G) plane. The red lines represent positive growth rates. The most positive red line represents the highest σ and the black line represents $\sigma = 0$ (neutral curve). Hence the absolute value of the growth rate approaches zero for the red or blue lines that are closer to the neutral curve. The blue lines represent the negative growth rates. From figure 4.25(b) it can be seen that the point $(1.20, 100)$ in the (β, G) plane, lies above the neutral curve, hence, a positive growth rate is expected based on the linear stability analysis. The reproduction of the local linear stability analysis is performed as an exercise during the literature study phase of this thesis project. A comparison is made between a Blasius boundary layer profile and a typical boundary layer profile at separation for different η. The results are presented in Ekelschot [2012].

4.5 Görtler vortices

In this section the previously performed research is discussed. The valuable characteristic numbers are presented which are used to compare experimental and computational results. As a result, this section emphasises the contribution of this thesis to field of Görtler instabilities in hypersonic flow.

Schrijer [2010a] performed Quantitative Infrared Thermography (QIRT), Schlieren photography, and Particle Image Velocimetry (PIV) experiments on double compression ramp flow in the HTFD at $M = 7.5$. The free stream flow conditions are therefore similar to the conditions present during the measurement described in this thesis. Two double compression ramp configurations are compared. The two configurations are given in the test matrix given below:

Table 4.4: Dimensions of the two tested configurations test by Schrijer [2010b,a]

	L_1 $[mm]$	$\hat{\theta}_1$ $[^\circ]$	L_2 $[mm]$	$\hat{\theta}_2$ $[^\circ]$
Configuration 1	96	15	66	30
Configuration 2	96	15	81	45

The model has a width of 115 mm. The unit Reynolds number is changed from $5 \times 10^6 [m^{-1}]$ to 11×10^6 $[m^{-1}]$. The total temperature is constant and equal to $T_t = 579K$ similar to the cases that are presented during this thesis.

With Schlieren photography and PIV, the flow topology is determined. It is found that for the first configuration, an Edny type VI interaction is present while for the second configuration a Edney type V interaction as shown in figure 4.26(a) and 4.26(b), respectively.

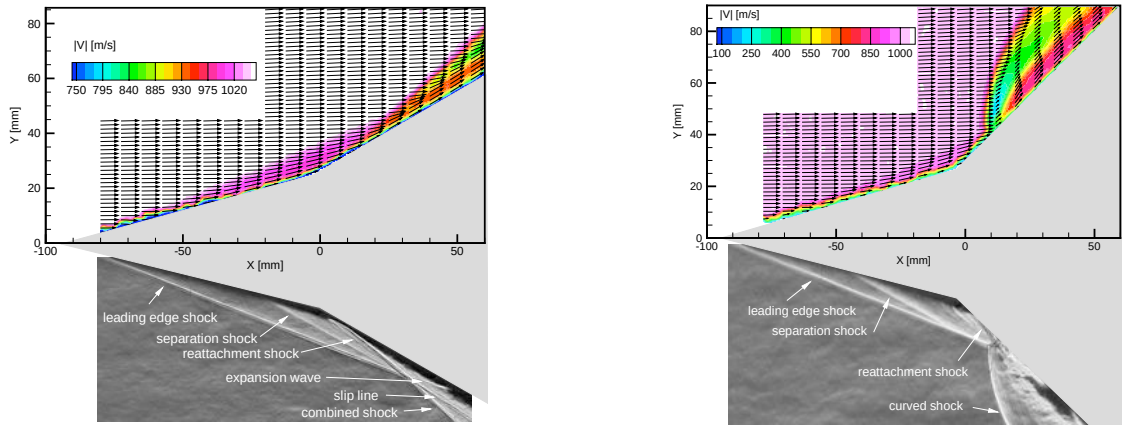

(a) Schlieren and PIV results for the second configuration $\hat{\theta}_1 = 15^\circ$ $\hat{\theta}_2 = 30^\circ$

(b) Schlieren and PIV results for the second configuration $\hat{\theta}_1 = 15^\circ$ $\hat{\theta}_2 = 45^\circ$

Figure 4.26: PIV results obtained by Schrijer [2010a]

PIV measurements are performed to obtain a general flow description for the $15^\circ - 30^\circ$ and a $15^\circ - 45^\circ$ model given in table 4.4. Leading edge irregularities caused an irregular spanwise boundary layer separation which caused an inaccurate measurement of the separation bubble.

The heat flux distribution over the surface is determined by means of QIRT. As a result it is found that the maximum heat flux at reattachment is comparable with the result found by Navarro-Martinez and Tutty [2005] namely$\Delta\ q_{max} = 18.73\%$. A slightly adjusted definition of the growth rate is determined where not the maximum but the mean amplitude is taken at separation and at reattachment. The ratio of the spanwise heat transfer fluctuations at reattachment and at separation is defined as the growth rate.

$$\sigma = \frac{\Delta q_r}{\Delta q_s} \tag{4.32}$$

where$\Delta\ q_{s,max}$ represents the spanwise heat transfer fluctuations at separation and$\Delta\ q_{r,max}$ the spanwise heat transfer fluctuations at reattachment. The Görtler number is defined based on the boundary layer thickness δ defined in equation 4.33:

$$G_\delta = Re_\delta \sqrt{\frac{\delta}{R}} \tag{4.33}$$

The spanwise wavelength of the VG is varied and the influence on the growth rate and Görtler number are discussed. Therefore the non dimensional wavelength parameter is defined in equation 4.34 [Schrijer, 2010b]:

$$\Lambda = Re_\lambda \sqrt{\frac{\lambda}{R}} \tag{4.34}$$

The wavelength of the VG is varied and the growth rate, σ is plotted against G_δ for both configurations in figure 4.27. It is found that the growth rate decreases with increasing Görtler number. This can be explained by the fact that an increase in Görtler number means also an increase in Reynolds number which means that the longitudinal vortices break up more easily leading to lower measured fluctuations. Schrijer [2010b] related the non dimensional wavenumber, the growth rate and the Görtler number and

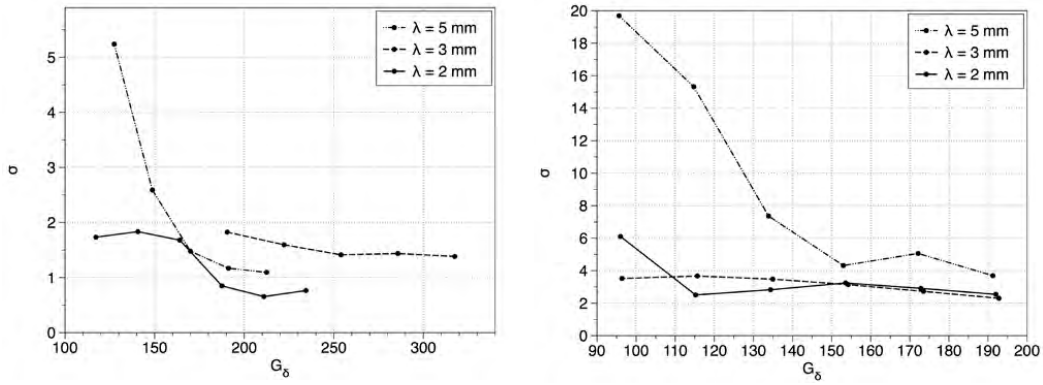

(a) Growth rate plotted against the Görtler number for three different wavelengths for the $15° - 30°$ configuration

(b) Growth rate plotted against the Görtler number for three different wavelengths for the $15° - 45°$ configuration

Figure 4.27: Growth rate plotted against the Görtler number for three different wavelengths for the two configurations presently discussed [Schrijer, 2010b]

plotted them for both configurations. These plots are shown in figure 4.28. It is found that the lines for constant spanwise wavelength, λ, in the $G_\delta - \Lambda$ plane are straight with a slope of 3/2. A subtle trend is seen of an increase in growth rate with the wavelength parameter.

Luca de et al. [1993] investigated Görtler instabilities in a hypersonic boundary layer (M=7) by means of QIRT experiments. This is done by looking at a flat plate at zero angle of attack which is followed by a concave wall with a constant radius of curvature (see figure 4.29(a)). Three different cases are tested:

Table 4.5: Dimensions of the two tested configurations test by Luca de et al. [1993]

	L_1 $[mm]$	L_2 $[mm]$	R $[mm]$
Model A	50	150	2000
Model B	50	120	1000
Model C	100	100	1000

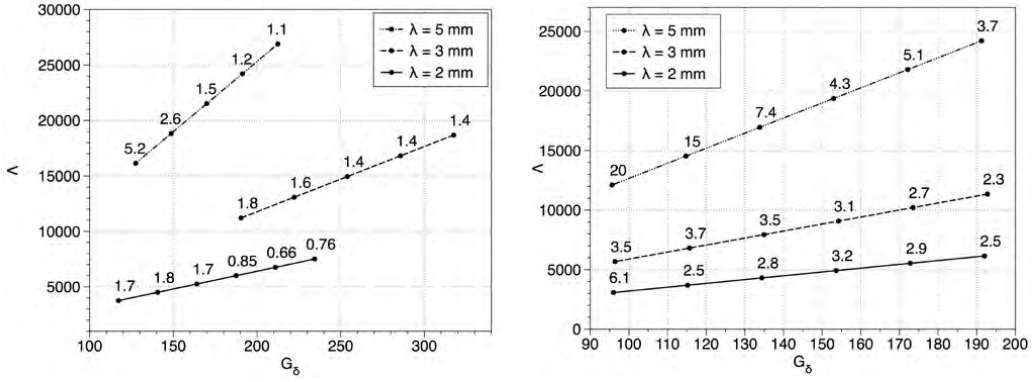

(a) Görtler number plotted against the wavelength parameter for the $15° - 30°$ configuration where the labels indicate the growth rate

(b) Görtler number plotted against the wavelength parameter for the $15° - 45°$ configuration where the labels indicate the growth rate

Figure 4.28: Görtler number plotted against the wavelength parameter for the two configurations presently discused [Schrijer, 2010b]

The unit Reynolds numbers ranges from $0.89 \times 10^7 m^{-1}$ to $1.91 \times 10^7 m^{-1}$ and the $T_t = 800K$. The amplitude in heat flux with respect to the spanwise mean distribution increased in downstream direction. No initial disturbance is introduced and the heat flux distribution on the surface of the model is determined. Sinusoidal fluctuations are obtained in spanwise direction which is an indication for the longitudinal vortex structures. The spanwise fluctuations have an average wavelength of 8 mm. In the stability plot, given in figure 4.29(b), the models are plotted and it can be seen that they are not located on the side where all the vortices will be amplified. The spanwise wavenumber $\beta = \frac{2\pi\lambda}{\delta}$ where δ is boundary layer

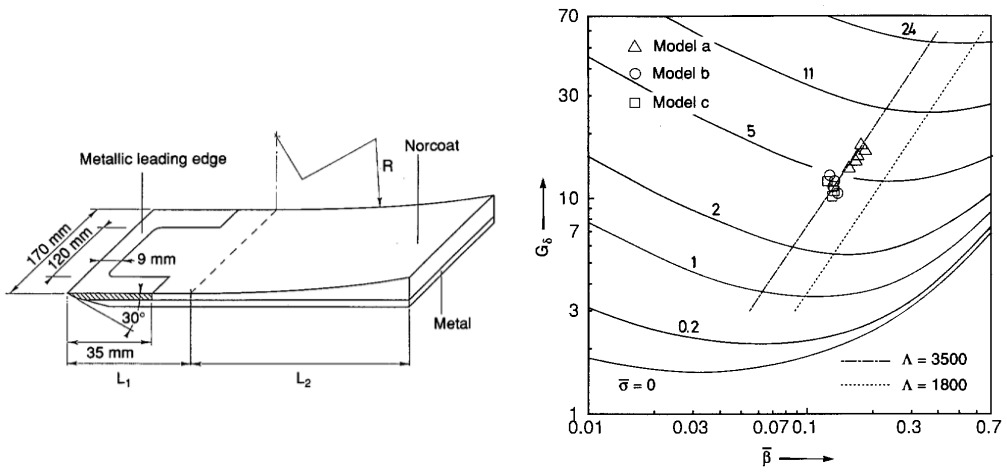

(a) The model with characteristic dimensions used by Luca de et al. [1993]

(b) Correlation of present experimental data as compared to the stability plot

Figure 4.29: Test case presented in Luca de et al. [1993]

thickness and λ is the spanwise wavelength of the longitudinal vortices.

Navarro-Martinez and Tutty [2005] performed numerical work regarding hypersonic double compression ramp flow. Numerical simulations are performed for the case of $M = 6.85$ and $Re = 2.45 \times 10^6\ m^{-1}$. The free stream temperature is set to $T_\infty = 57.8\ K$ and the free stream velocity $U_\infty = 1061\ ms^{-1}$ which are comparable values to the case which will be further discussed during this thesis. Next to that, the length of the 5° ramp is 155 mm and the 45° ramp $55mm$. Again a spanwise disturbance is imposed on the flat plate ahead of the separation.

Navarro-Martinez and Tutty [2005] solved the 3D compressible Navier-Stokes equations written in conser-

vative form by using the implicit Godunov scheme approach. A significant part of their paper is dedicated to the comparison between their numerical solver and previously performed experiments of a similar case which is outside the scope of this thesis. Navarro-Martinez and Tutty [2005] stated in their conclusive section, that there are other types of instabilities which can play an important role in double compression ramp flow. Take for example the non-linear secondary instabilities described by Saric [1994], Li and Malik [1995], Floryan [1991], Swearingen and Blackwelder [1987]. Navarro-Martinez and Tutty [2005] did not see mushroom shaped non-linear secondary instabilities of Görtler vortices which are presented in Saric [1994]. It is also concluded that due to the high Reynolds number, and thus the high Görtler number, there are multiple unstable solutions to the normal mode eigenvalue problem.

Like Schülein and Trofimov [2011], Navarro-Martinez and Tutty [2005] placed the initial disturbance at different locations in the computational domain and found corresponding results. The amplitude of the disturbance is fixed to $A_p = 0.01V_\infty$. Navarro-Martinez and Tutty [2005] found that at $x_{VG} = 3.1mm$, the maximum heat flux at reattachment$\Delta\ q_{max} = 20\%$ while for $x_{VG} = 31mm\ \Delta q_{max} = 12.5\%$. It is concluded that$\Delta\ q_{max}$ at reattachment increases when $\frac{h}{\delta}$ increases. Furthermore, Navarro-Martinez and Tutty [2005] quantified the growth rate of the longitudinal vortices based on the spanwise amplitude (relative to the mean) heat flux at separation and reattachment defined in the following way:

$$\sigma = \frac{\Delta q_{s,max}}{\Delta q_{r,max}} \tag{4.35}$$

where$\Delta\ q_{s,max}$ represents the spanwise heat transfer fluctuations at separation and$\Delta\ q_{r,max}$ the spanwise heat transfer fluctuations at reattachement. For the case of $\lambda = 6.4mm$ a growth rate of $\sigma = 6.6$ is found. For $\lambda = 12.8mm$, $\sigma = 8.3$. Navarro-Martinez and Tutty [2005] stated that the experimental data are significantly underpredicted and that it is unlikely that the Görlter vortices alone are responsible for the discrepancy found between the experimental and computational data. The most probable explanation would be that the flow becomes turbulent in the experiments.

Chapter 5

Quantitative Infrared Thermography measurement campaign

In this chapter, the results obtained using Quantitative Infrared Thermography (QIRT) are discussed. The goal of the measurement campaign is to gather more information on the growing behaviour of Görtler vortices. A zig-zag VG, introduced in chapter 2 and 4, is pasted at 25 mm from the leading edge as shown in figure 2.9(b). The zig-zag strip introduces a periodic spanwise disturbance in the boundary layer. Two counter rotating vortices originate from the downstream pointing zig-zag tooth as discussed in section 4.3. The streamwise development of these longitudinal vortices (Görtler vortices) are further discussed in this chapter. The influence of the height of the VG (h_{zz}) and the Reynolds number on the surface heat flux is discussed in more detail. The spanwise wavelength is fixed ($\lambda_{zz} = 6\ mm$) . For a recapitulation of the general flow topology around the $5° - 45°$ model (shock pattern, velocity field, boundary layer separation/reattachment and streamwise heat flux distribution) and the flow topology around the applied VG, the reader is referred to chapter 4. In Table 5.1 the test matrix is given.

		$Re\ [m^{-1}]$		
		8.47×10^6	11.3×10^6	14.1×10^6
$h_{zz}\ [mm]$	0	0	0	0
	0.20	$h_{zz}/\delta = 0.16$	$h_{zz}/\delta = 0.16$	$h_{zz}/\delta = 0.16$
	0.40	$h_{zz}/\delta = 0.32$	$h_{zz}/\delta = 0.32$	$h_{zz}/\delta = 0.32$
	0.75	$h_{zz}/\delta = 0.60$	$h_{zz}/\delta = 0.60$	$h_{zz}/\delta = 0.60$
	1.15	$h_{zz}/\delta = 0.92$	$h_{zz}/\delta = 0.92$	$h_{zz}/\delta = 0.92$

Table 5.1: Test matrix

During the theoretical local stability analysis of Görtler vortices it is concluded that there are three parameters which characterise the onset of Görtler vortices. The Görtler number (G), the spanwise wavelength (β) and the growth rate (σ). The last section the investigation of the growth rate parameter is discussed in detail.

5.1 Influence of the VG on the heat transfer distribution

The local heat transfer values determined in the image plane are mapped on the physical coordinate system using a mapping function which is written in *Matlab*. It allows the user to select the four corner points in the image plane such that the domain of interest is determined. The image plane coordinates corresponding to the domain of interest are mapped on the physical model coordinates using bilinear interpolation. The mapped heat transfer distribution is then shown in figure 5.1 for $h_{zz} = 0\ mm$ and $h_{zz} = 1.15\ mm$ both at a unit Reynolds number of $14.1 \times 10^6 [m^{-1}]$.

The logarithm of c_h is plotted so that the separation line and spanwise heat flux fluctuations are clearly visible as discussed in section 4.2.2. In Appendix C, the other test cases are presented in a similar

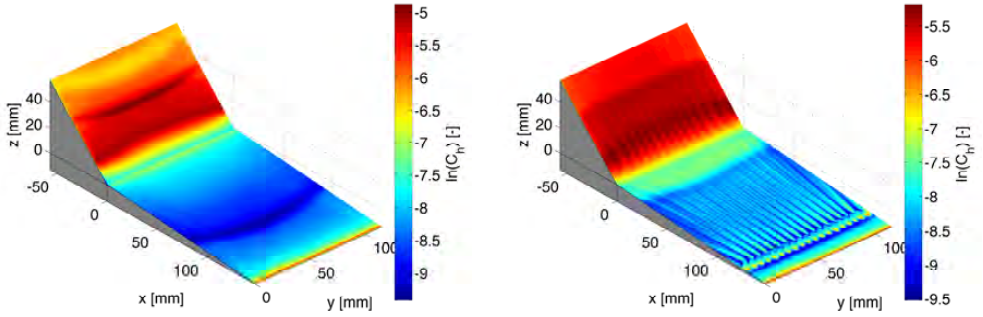

(a) The logarithm of the Stanton number (c_h) mapped on the surface coordinate system for the case $h_{zz} = 0\ mm$, $Re_{unit} = 14.1 \times 10^6\ m^{-1}$

(b) The logarithm of the heat transfer mapped on the surface coordinate system for the case $h_{zz} = 1.15mm$, $Re_{unit} = 8.47 \times 10^6\ m^{-1}$

Figure 5.1: The mapped heat transfer distributions for all the tested Reynolds numbers and $h_{zz} = 1.15mm$

fashion for all unit Reynolds numbers. In the remainder of this chapter the case $h_{zz} = 1.15\ mm$, $Re_{unit} = 14.1 \times 10^6\ [m^{-1}]$ is used as a show case.

Three main differences can be noted when comparing the heat transfer distributions presented in figure 5.1. Firstly, the spanwise wavy pattern induced by the VG is noted in figure 5.1(b). The longitudinal higher and lower momentum streaks are clearly visible and correspond with the discussion given in section 4.3.

The VG causes a sinusoidal spanwise heat flux distribution due to the local higher and lower velocity regions which indicate a vortical behaviour near the wall (which is also shown in chapter 4). The spanwise heat flux fluctuations are obtained by filtering the spanwise heat flux distribution. A higher order polynomial is fitted through the data points to estimate the mean spanwise heat transfer profile. The residual of the spanwise heat flux distribution is then found by subtracting the mean distribution from the measured data points [Schrijer, 2010b]. In figure 5.2, a sample together with the residual is graphically shown.

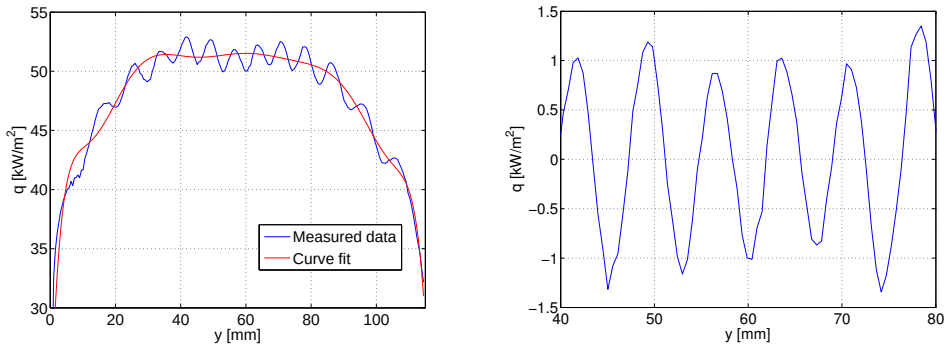

(a) Curve fit through the spanwise heat flux distribution at reattachment for $h_{zz} = 1.15$ mm and $Re_{unit} = 14.1 \times 10^6\ m^{-1}$

(b) Residual of the heat flux distribution at reattachment

Figure 5.2: Filtering procedure illustrated for $h_{zz} = 1.15\ mm$ and $Re_{unit} = 14.1 \times 10^6\ [m^{-1}]$

Again h_{zz} and $Re_{unit} = 14.1 \times 10^6\ m^{-1}$ is chosen as a reference case since the wavy pattern in the spanwise heat transfer distribution is clearly visible. In figure 5.2(a) the distribution at reattachment is indicated by the blue line and the red line indicates the mean profile. The heat transfer fluctuations are $\Delta q = 2\%$ for $h_{zz} = 1.15\ mm$ and $Re_{unit} = 14.1 \times 10^6\ [m^{-1}]$.

Secondly, the flow separates more downstream ($x \approx 20\ mm$) for $h_{zz} = 1.15\ mm$. In figure 5.3(a),

the separation and reattachment points are found by looking at the streamwise heat flux distribution where separation is indicated by a local drop in c_h. The reattachment point on the other hand is determined by a local peak of c_h due to the local decrease of the boundary layer thickness which is discussed in section 4.2.2. In figure 5.3 the streamwise heat transfer map is given for every h_{zz}. Note the decreasing trend of the second peak ($x = -45\ mm$) with increasing h_{zz}. This indicates that the VG has an influence on the shock pattern above the 45° ramp. The boundary layer separates more downstream for h_{zz} which results in a change in shock interaction since the separation shock originates more downstream.

As a third difference, note that the heat flux distribution on the 45° ramp shows a different pattern for $h_{zz} = 1.15\ mm$, $Re_{unit} = 14.1 \times 10^6\ [m^{-1}]$ than for $h_{zz} = 0\ mm$, $Re_{unit} = 14.1 \times 10^6\ [m^{-1}]$ (see figure 5.1). The local high heat flux induced by the impinging shock on the 45° shown in figure 5.1(a) (see section 4.2.2) does not appear in figure 5.1(b) which indicates that the local flow compression is reduced. Hence, the presence of the local second peak on the 45° ramp is also dependent on the Reynolds number.

5.2 Influence of the Reynolds number on the heat transfer distribution

For the four different VGs, the streamwise heat flux distribution is plotted against the streamwise coordinate x. Two measurements are performed for each test case to validate the measurement outcome. Reynolds analogy states that the Stanton number is related to the friction coefficient which is inversely proportional to the square root of the local Reynolds number. For the discussion at hand, let us consider again equation 4.14:

$$c_h = \frac{C_f}{2} Pr^{-2/3} \rightarrow c_h = \frac{0.332}{2\sqrt{Re_s}} Pr^{-2/3}$$

where s indicates the distance in streamwise direction from the leading edge. For $s = 0$ the Stanton number is expected to be large since it is inversely proportional to $\sqrt{Re_s}$. Therefore, the Stanton number is multiplied by $\sqrt{Re_s}$ such that a flat heat flux distribution is found for a laminar boundary layer, as discussed in section 4.2.2. Plotting $c_h \times \sqrt{x}$ on a logarithmic scale, emphasises the local heat flux drop at separation (see figure 5.3).

A laminar boundary layer develops at the leading edge (see the straight line) for $h_{zz} = 0\ mm$ at $100\ mm \leq x \leq 150\ mm$. Apart from the case that $h_{zz} = 0\ mm$ it is observed that for all the cases a local heat flux jump is present at $x = 125\ mm$. This is due to the VG which is pasted 25 mm from the leading edge. For $h_{zz} = 0\ mm$, the flow separates at $x = 95\ mm$ which corresponds with the estimated separation location based on PIV. The heat flux decreases locally due to boundary layer separation. A new boundary layer starts to grow due to the large back flow region which was also noticed in the 2C-PIV results. At the 45° ramp, two peaks are detected. The first peak is ascribed to the local boundary layer necking due to flow reattachment. The second peak ($x = -45\ mm$) indicates flow compression due to a strong shock caused by the shock interaction which impinges on the surface of the model. In general it can be said the the streamwise heat transfer distribution increases with increasing Reynolds number. Furthermore, a shift in boundary layer separation can be noted while the position of boundary layer reattachment together with the impinging shock is rather fixed.

The effect of the Reynolds number on the spanwise heat flux distribution is investigated by comparing the residuals at six fixed streamwise locations for the case $h_{zz} = 1.15\ mm$. The fixed x positions are indicated in figure 5.4(a). The spanwise heat flux distributions are given in figure 5.4.

Initially, at $x = 100\ mm$, a clear wavy pattern is present with one fixed wavelength of approximately 6 mm, corresponding to the spanwise wavelength of the VG. Note that at $x = 80\ mm$ for $Re_{unit} = 11.3 \times 10^6\ [m^{-1}]$ and $Re_{unit} = 14.1 \times 10^6\ [m^{-1}]$, the amplitude decreases (see figure 5.4(c)). Additionally, a secondary, smaller wavelength is present in the spanwise heat flux distribution. This indicates that the high velocity streaks break up into two separate smaller high velocity streaks. This is also shown in the mapped heat transfer plots given in figure 5.1(b). Multiple possible explanations are considered for this local break up of the longitudinal streaks. It might be, that the longitudinal vortices are bended upwards, and secondary counter rotating vortices of lower intensity appear near the wall. Another explanation would be, that the vortical structure dissipates in disturbed coherent structures and the breaking up of the high velocity streaks is a coarse representation of energy cascading. Furthermore it can be stated that the

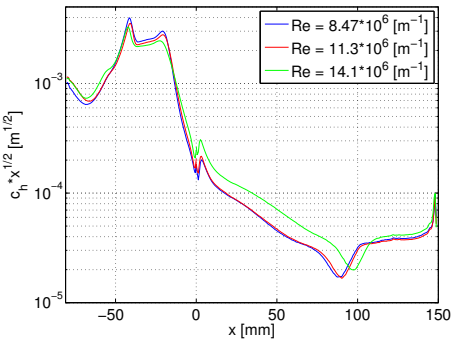

(a) The mean streamwise heat flux profiles (based on the two measurement per Reynolds number) for the three Reynolds numbers for the case $h_{zz} = 0$ mm

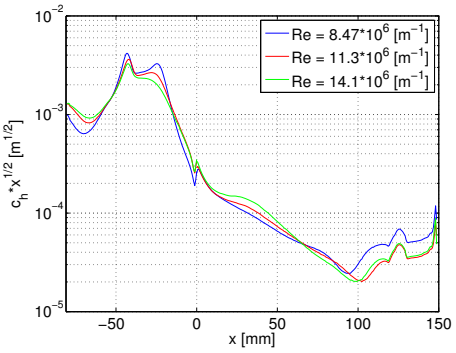

(b) The mean streamwise heat flux profiles (based on the two measurement per Reynolds number) for the three Reynolds numbers for the case $h_{zz} = 0.20$ mm

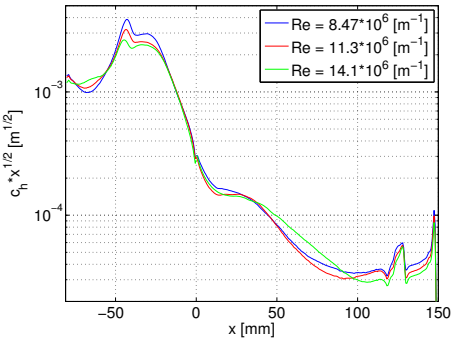

(c) The mean streamwise heat flux profiles (based on the two measurement per Reynolds number) for the three Reynolds numbers for the case $h_{zz} = 0.40$ mm

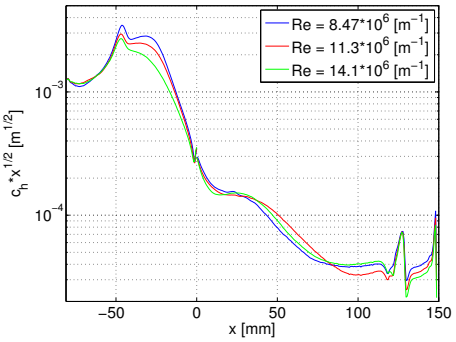

(d) The mean streamwise heat flux profiles (based on the two measurement per Reynolds number) for the three Reynolds numbers for the case $h_{zz} = 0.75mm$

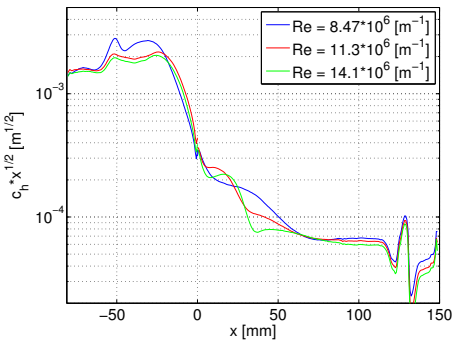

(e) The mean streamwise heat flux profiles (based on the two measurement per Reynolds number) for the three Reynolds numbers for the case $h_{zz} = 1.15mm$

Figure 5.3: The effect of the Reynolds number on the stream wise heat transfer distribution for all h_{zz}.

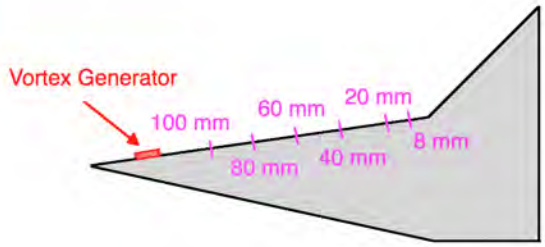

(a) Fixed x positions where the spanwise heat flux distribution is locally investigated

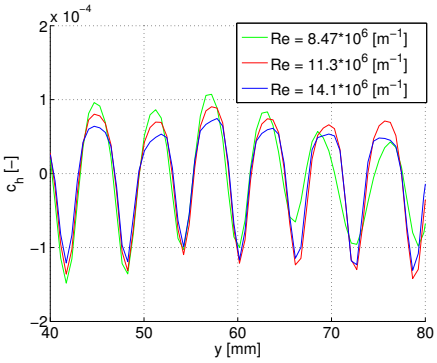

(b) Spanwise heat flux distribution for the three Reynolds numbers at $x = 100mm$

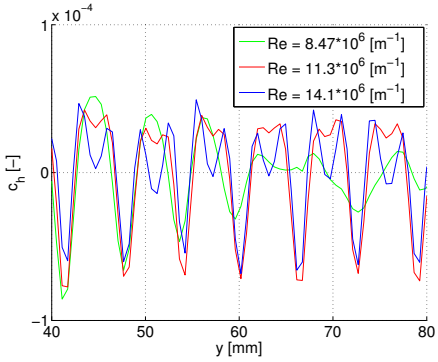

(c) Spanwise heat flux distribution for the three Reynolds numbers at $x = 80mm$

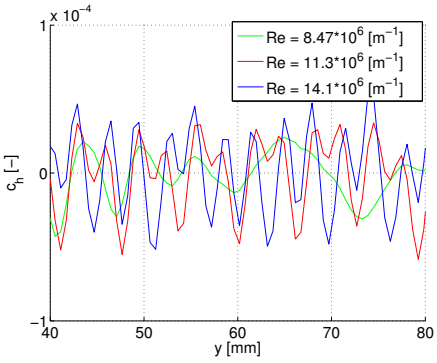

(d) Spanwise heat flux distribution for the three Reynolds numbers at $x = 60mm$

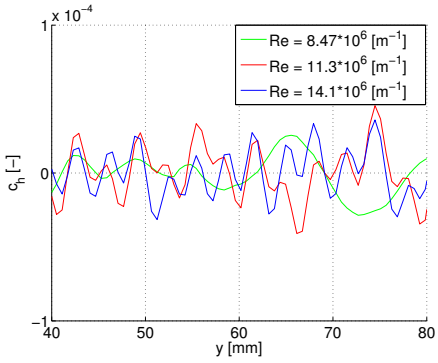

(e) Spanwise heat flux distribution for the three Reynolds numbers at $x = 40mm$

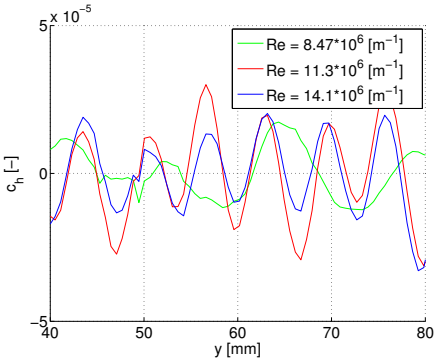

(f) Spanwise heat flux distribution for the three Reynolds numbers at $x = 20mm$

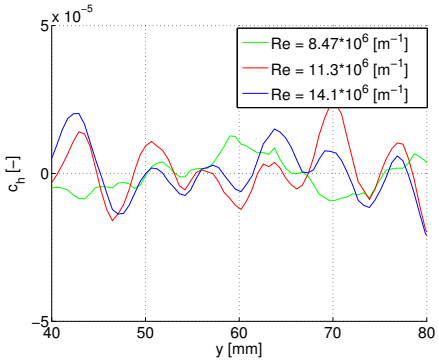

(g) Spanwise heat flux distribution for the three Reynolds numbers at $x = 8mm$

Figure 5.4: The effect of the Reynolds number on the spanwise heat transfer distribution at fixed x for all h_{zz}

spanwise heat transfer distribution gradually decreases when moving further downstream. Going back to figure 4.19(d), it can be seen that mushroom shaped momentum distribution occurs which indicates that the flow is highly disturbed. The low momentum flow in the top of the the mushroom can therefore be possibly directed back towards the sides causing a local heat flux drop on both sides of the the center line. At $x = 20mm$ again a smooth sinusoidal pattern is measured with an approximate restored wavelength of 6 mm. This indicates that the VG influences the flow in the separated region near the first-to-second ramp junction of the model. This indicates that somehow the break up of the high velocity structures restores and weaker spanwise fluctuations are present with a similar wavelength as initial introduced by the VG.

5.3 Growth rate

The onset of Görtler vortices can be predicted using the Görtler number (G), the growth rate (σ) and spatial wavelength (β). For a fixed geometry holds that G varies only with Reynolds number according to the definition of G (see equation 4.29). However, for double compression ramp flow holds that the curvature of the flow (and thus the radius of curvature) is dependent on the location of flow separation and reattachment. During the previously discussed analysis, it is observed that h_{zz} influences the location of boundary layer separation. Consequently, the radius of curvature and the Görtler number varies. However during the current investigation, the Görtler number is assumed to be solely dependent on the Reynolds number and the growth rate is determined for the previously introduced test cases.

During previous research (see chapter 4), the growth rate is defined as the ratio of mean spanwise heat flux amplitude at reattachment and separation [Schrijer, 2010b, Navarro-Martinez and Tutty, 2005].

$$\sigma = \frac{\overline{\Delta q_r}}{\overline{\Delta q_s}} \tag{5.1}$$

where $\overline{\Delta q_r}$ is the mean spanwise fluctuation at reattachment and $\overline{\Delta q_s}$ the mean spanwise fluctuation at separation. However, in this report, the growth rate is defined differently. The mean spanwise heat transfer fluctuations are normalised by the spanwise heat transfer fluctuations just downstream of the VG:

$$\sigma(x) = \frac{\overline{\Delta q_x}}{\overline{\Delta q_{100}}} \tag{5.2}$$

where $\overline{\Delta q_x}$ is the mean spanwise amplitude at a chosen x position and $\overline{\Delta q_{100}}$ the mean spanwise amplitude at the fixed position $x = 100$ mm. In general, the mean is calculated over 10 mm in streamwise direction to obtain a mean spanwise heat flux distribution.This definition of the growth rate enables us to monitor the streamwise progression of the growth rate in x direction and typical streamwise growth rate profiles are presented in the coming sections.

During the current measurements, the boundary layer is disturbed using a zig-zag VG. Furthermore, the undisturbed is further investigated. Due to the concave geometry, it is possible that longitudinal vortices are formed. The spanwise fluctuations are therefore self-induced by the concave geometry of the wind tunnel model. However, for the undisturbed case (no VG applied), the spanwise heat transfer fluctuations might be dominated by camera noise. Therefore, a spanwise heat flux profile, measured before the run started, is compared with a spanwise heat flux profile during the run. This is shown in figure 5.5.

In figure 5.5(a), the x position at which the spanwise heat flux during the run is compared with the spanwise heat flux before the run, is indicated by the pink line. In figure 5.5(b), the spanwise distribution measured during the run is given by the blue line, the red line represents the measured spanwise heat flux distribution just before the run and the green line represents the filtered heat flux distribution during the run. It can be seen that the filtered data looks very similar to the red line and therefore it can be concluded that the measured spanwise distribution during the run is very noisy. For both the filtered data as the data obtained before the run, a standard deviation of 170 W/m^2 which can be considered as the spanwise noise estimate during the current experiments. Based on this estimate, it is concluded that the spanwise heat flux distribution is too noisy to determine a correct and significant indication for the growth of longitudinal vortices for the undisturbed flow case. From figure 4.12, it is determined that

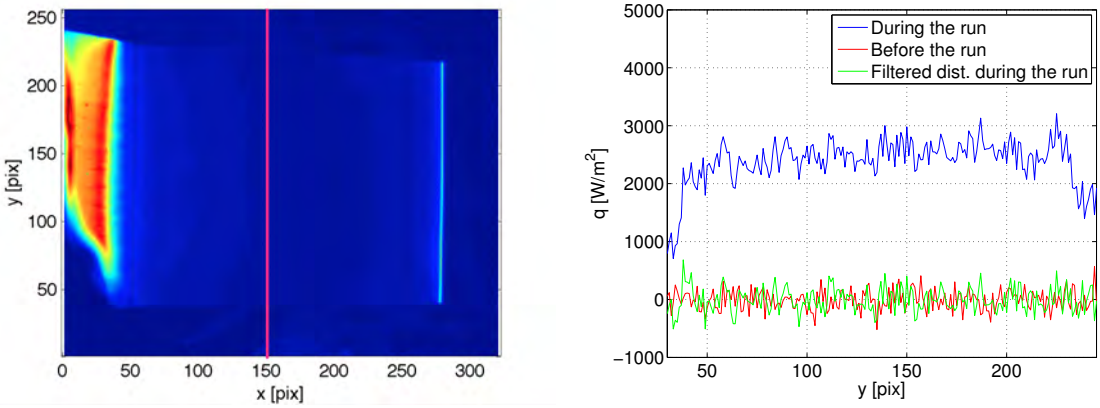

(a) Sample image with the noise test location indicated by the pink line

(b) Comparison of the local noise level at $x = 150$ *pix*

Figure 5.5: Noise level comparison

the flow is curved upwards just before flow reattachment occurs, right above the first-to-second ramp junction. The radius of curvature is estimated to be 20 mm . Based on the radius of curvature, the order of magnitude of the Görtler number can be determined:

$$G = Re\sqrt{\frac{R}{L}} \rightarrow \mathcal{O}(G) = \mathcal{O}(10^5)\frac{\mathcal{O}(10^{-2})}{\mathcal{O}(10^{-1})} = \mathcal{O}(10^4) \tag{5.3}$$

From the stability plot given in figure 4.25(b), it can be concluded that the growth rate is positive knowing that $\beta = 1.20$ (see equation 4.31). The streamwise progression of the counter rotating vortices induced by the VG is further investigated. For now, the growth rate profiles for the two ramps are discussed separately since the four different strip heights are compared in more detail. At first, the streamwise growth rate distribution parallel to the 5° ramp is discussed for the different h_{zz}. This is followed by a discussion of the streamwise growth rate distribution parallel to the 45° ramp.

5.3.1 Growth rate evaluation parallel to the 5° ramp

From figure 5.4, it was determined that the amplitude of the spanwise heat flux fluctuations decreases when moving further downstream. It is therefore expected that the growth rate on the 5° ramp will be below 1 based on equation 5.2. In figure 5.6, the growth rate is plotted against the streamwise coordinate x parallel to the 5° ramp for the four tested VG heights and for the three different unit Reynolds numbers.

It can be seen that the growth rate is indeed smaller than 1 for all cases on the 5° ramp. The intensity of the longitudinal vortices appears to be decreasing in downstream direction since the absolute spanwise heat flux amplitude decreases. For $h_{zz} = 0.20$ mm, a clear peak is present for all three Reynolds numbers which indicates that after the decreased intensity of the initial VG disturbance, an amplifying effect takes place and locally the growth rate becomes larger than 1 (see $x = 30$ mm for $Re_{unit} = 11.3 \times 10^6$ $[m^{-1}]$ in figure 5.6(b)). This occurs within the separated flow domain since the separation line for $h_{zz} = 0.20$ mm is approximately at $x = 95$ mm (see figure 5.3(b)).

The origin of the peak at $x = 30$ mm for $h_{zz} = 0.2$ mm is further investigated in more detail by observing the local spanwise surface heat flux profile. In figure 5.7, the spanwise heat flux at $x = 100$ mm and at $x = 30$ mm is plotted for $h_{zz} = 0.20$ mm and $Re_{unit} = 11.3 \times 10^6$ m^{-1}. For a fixed streamwise location, the mean is taken over 12 mm in streamwise direction to obtain a mean spanwise heat flux distribution.

An amplified spanwise heat flux distribution is observed at $x = 30$ mm. In particular at a spanwise location of $y = 55$ mm. At $x = 100$ mm a disturbance of the spanwise distribution is observed. The heat transfer peaks determined at $x = 30$ mm might therefore be induced by an disturbance that originates

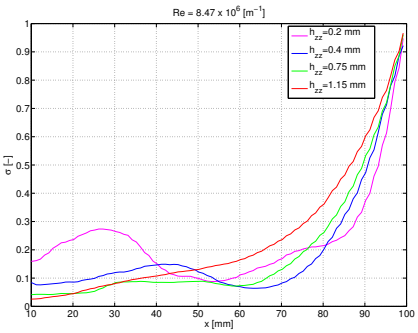

(a) Growth rate plotted on the 5° against the stream wise coordinate x for the various VG heights and $Re_{unit} = 8.47 \times 10^6$

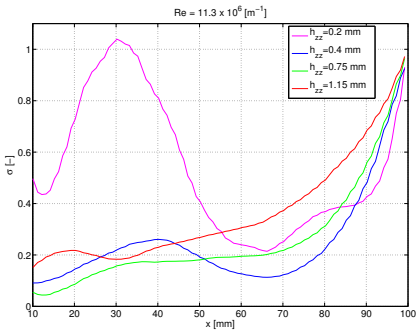

(b) Growth rate plotted on the 5° against the stream wise coordinate x for the various VG heights and $Re_{unit} = 11.3 \times 10^6$

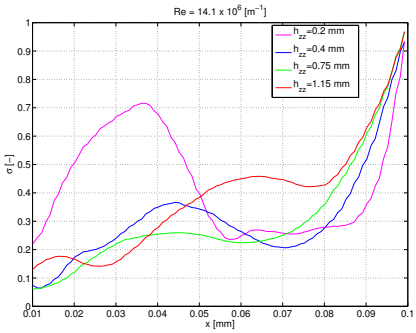

(c) Growth rate plotted on the 5° against the stream wise coordinate x for the various VG heights and $Re_{unit} = 14.1 \times 10^6$

Figure 5.6: Growth rate plotted in x direction for all h_{zz}

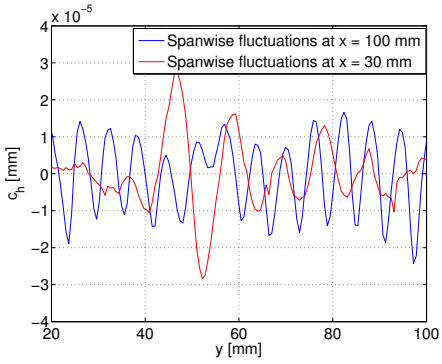

Figure 5.7: Example of initial disturbance

from the VG strip. This local disturbance induces a local amplification as shown in figure 5.7. A bad pasted VG strip might therefore be the cause of the local peak at $x = 30\ mm$ in the growth rate plots given in figure 5.6.

In figure 5.8, the mapped heat transfer distribution is given for $h_{zz} = 0.40\ mm$, $h_{zz} = 0.75\ mm$ at $Re_{unit} = 11.3 \times 10^6\ [m^{-1}]$ and $h_{zz} = 1.15\ mm$ at $Re_{unit} = 8.47 \times 10^6\ [m^{-1}]$. It can be concluded that the

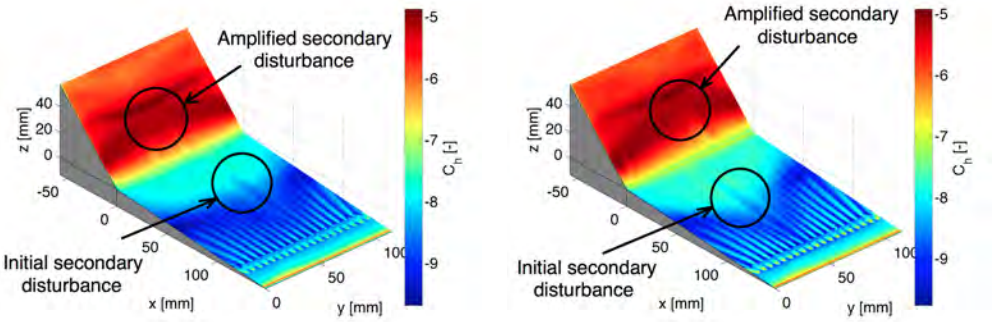

(a) The heat transfer mapped on the surface coordinate system for $h_{zz} = 0.4mm$, $Re_{unit} = 11.3 \times 10^6\ m^{-1}$

(b) The heat transfer mapped on the surface coordinate system for $h_{zz} = 0.75mm$, $Re_{unit} = 11.3 \times 10^6\ m^{-1}$

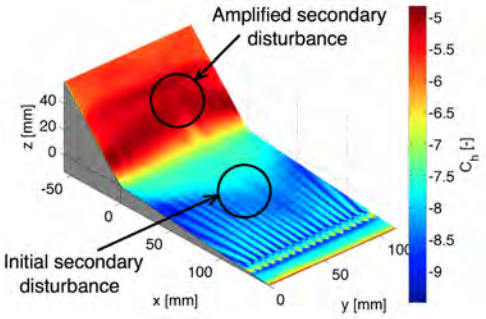

(c) The heat transfer mapped on the surface coordinate system for $h_{zz} = 1.15mm$, $Re_{unit} = 8.47 \times 10^6\ m^{-1}$

Figure 5.8: Examples of secondary disturbance amplification

stability of the longitudinal streaks is highly influenced on the pasting of the VG. Small disturbances that originate from the VG, amplify and disturb the flow downstream significantly. Even for the $h_{zz} = 1.15\ mm$ at the lowest unit Reynolds number ($Re_{unit} = 8.47 \times 10^6\ [m^{-1}]$), an amplification of an initial VG disturbance at $y \approx 75\ mm$ is observed and a non-symmetric separation line is present as shown in figure 5.8(a)-5.8(c). As a consequence, large spanwise heat flux fluctuation are present locally at the reattachment line.

In general it is noted that the influence of the VG disturbances appears to be decreasing with increasing Reynolds number. This is shown in particular for $h_{zz} = 75\ mm$ and $h_{zz} = 1.15\ mm$ (see figure C.4 and C.5). Diverging longitudinal streaks are found for $Re_{unit} = 11.3 \times 10^6\ [m^{-1}]$ while for $Re_{unit} = 14.1 \times 10^6\ [m^{-1}]$, the longitudinal streaks appear to be spatially stable.

Similar flow behaviour is observed for $h_{zz} = 1.15\ mm$ and it is determined that the longitudinal streaks are steady for $Re_{unit} = 14.1 \times 10^6\ [m^{-1}]$ (see figure C.4 and figure C.5). A constant spanwise heat flux distribution is obtained further downstream of the VG. Furthermore, the amplitude of the spanwise heat flux fluctuations, and therefore the visibility (depending on the dynamic range, see chapter 6), increases with increasing h_{zz}. These two requirements need to be fulfilled to be able to measure the 3D velocity field by means of Tomographic Particle Image Velocimetry in the HTFD.

The argument of the spatial steadiness of the longitudinal streaks is supported by plotting the normalised autocorrelation factor of the local spanwise heat transfer distribution. This is done for a fixed x position just downstream of the VG at $x = 110\ mm$. The autocorrelation factor is plotted against the spanwise coordinate in figure 5.9:

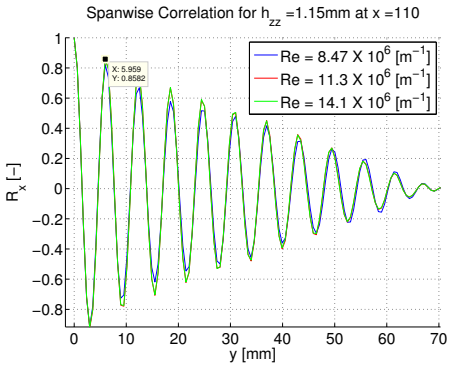

Figure 5.9: Example of obtaining the spanwise wavelength by means of autocorrelation

The spanwise wavelength of the heat flux distribution is approximately 6 mm ($\lambda_{VG} = 6\ mm$) indicated by the second peak from the left in figure 5.9. For all three unit Reynolds numbers, the wavelength for $h_{zz} = 1.15\ mm$ is the same. This procedure can be performed over the complete streamwise coordinate x. In this way, the development of the spanwise wavelength is monitored in streamwise direction. In figure 5.10, the spanwise heat transfer distribution for $h_{zz} = 1.15\ mm$ and varying unit Reynolds number, is autocorrelated and plotted for every x position such that a spectrum plot of the normalised autocorrelation factor is given for every x position.

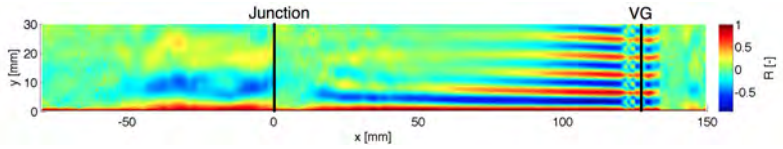

(a) Spanwise autocorrelation for $h_{zz} = 1.15mm$ for varying x for $Re_{unit} = 8.47 \times 10^6\ m^{-1}$

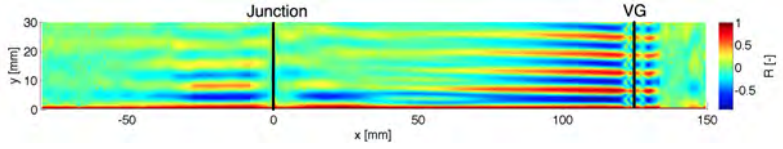

(b) Spanwise autocorrelation for $h_{zz} = 1.15mm$ for varying x for $Re_{unit} = 11.3 \times 10^6\ m^{-1}$

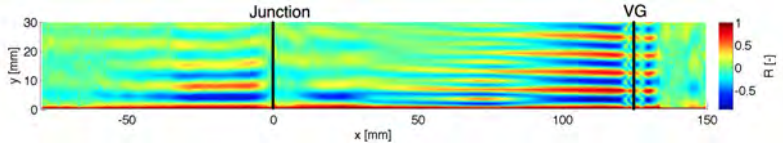

(c) Spanwise autocorrelation for $h_{zz} = 1.15mm$ for varying x for $Re_{unit} = 14.1 \times 10^6\ m^{-1}$

Figure 5.10: Correlation analysis of the spanwise heat transfer fluctuations

For the lowest unit Reynolds number can be seen that the wavelength increases locally to $\lambda_x = 11\ mm$ (with a lowered quality correlation signal) while for the highest two unit Reynolds number, a wavelength of $\lambda = 6\ mm$ is observed at reattachment which corresponds to λ_{VG}. Furthermore, the breakdown of the longitudinal streaks (see $x = 75\ mm$ in figure 5.10(c)) is obtained and $\lambda_{x=75mm} = 3\ mm$. Just upstream of the first-to-second ramp junction in figure 5.10(c), again a weak signal is present which indicates that

the spanwise wavelength restores to $\lambda \approx 6\ mm$.

5.3.2 Growth rate evaluation parallel to the 45° ramp

The growth rate profile for the flow parallel to the 45° ramp is investigated in a similar fashion as in the previous section. In figure 5.11 the growth rate is plotted in x direction where the x-axis is defined parallel to the 45° ramp.

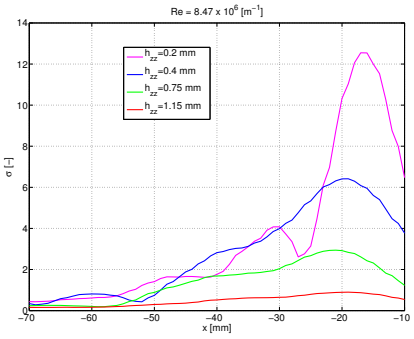

(a) Growth rate on the 45° ramp plotted against the stream wise coordinate x for the various VG heights and $Re_{unit} = 8.47 \times 10^6$

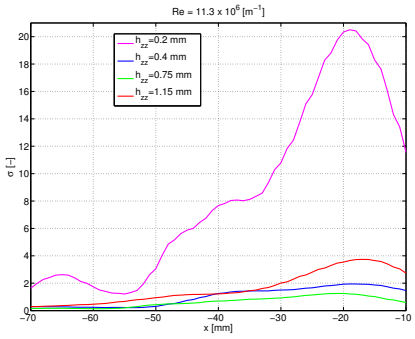

(b) Growth rate on the 45° ramp plotted against the stream wise coordinate x for the various VG heights and $Re_{unit} = 11.3 \times 10^6$

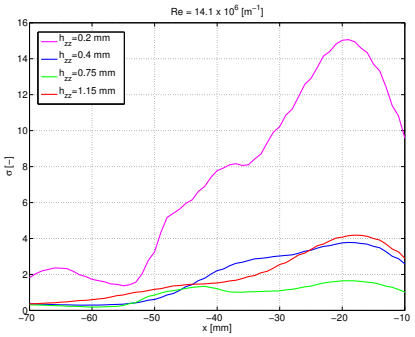

(c) Growth rate on the 45° ramp plotted against the stream wise coordinate x for the various VG heights and $Re_{unit} = 14.1 \times 10^6$

Figure 5.11: Growth rate plotted in x direction for all h_{zz}

For all tested h_{zz}, a peak appears at $x \approx -20\ mm$ while the flow reattaches at $x_r = -24\ mm$. This coincides with the PIV results, discussed in chapter 4. It was obtained, that flow curvature occurs near the reattachment point (see figure 4.12). The peak at $x \approx -20\ mm$ therefore corresponds with the theory, described in section 4.4, which describes that the longitudinal vortices grow due to the local curvature of the flow. In general can be stated that the amplification of Görtler vortices is a local phenomena in hypersonic double compression ramp flow which takes place just downstream of flow reattachement. No conclusive statement can be made regarding the influence of the Reynolds number on the growth rate. For $h_{zz} = 0.40\ mm$ and $Re_{unit} = 8.47 \times 10^6\ [m^{-1}]$, the growth rate peak is 6 while for higher Reynolds numbers, this peak decreases to below 2. However for the $h_{zz} = 1.15\ mm$ a gradual increase of the growth rate peak at $x = -0.20\ mm$ with increasing Reynolds number is observed.

The difference between the profile corresponding to $h_{zz} = 0.20\ mm$ and the other profiles can be ascribed to the very weak initial disturbance which develops in downstream direction. Furthermore, the secondary disturbance described in the previous section, is amplified effecting the growth rate profile. The effect of the secondary disturbance is generally larger for smaller h_{zz} since the initial disturbance is very weak.

The spanwise heat flux distribution is locally investigated and compared for $h_{zz} = 0.20\ mm$ and $h_{zz} = 1.15$

mm. The spanwise profiles are plotted for $x = 100\ mm$, $x = -26\ mm$ and $x = -60\ mm$ in one figure for the three different Reynolds numbers. On the left hand side of figure 5.12, the plots are given for $h_{zz} = 0.20\ mm$ and on the right hand side for $h_{zz} = 1.15\ mm$.

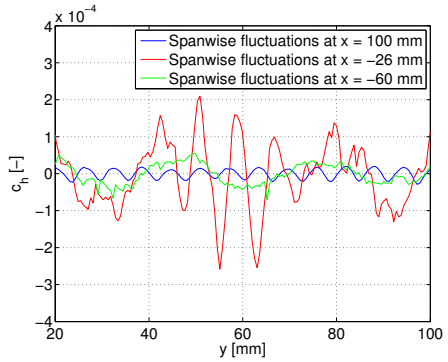

(a) $h_{zz} = 0.20\ mm$ and $Re_{unit} = 8.47 \times 10^6\ m^{-1}$

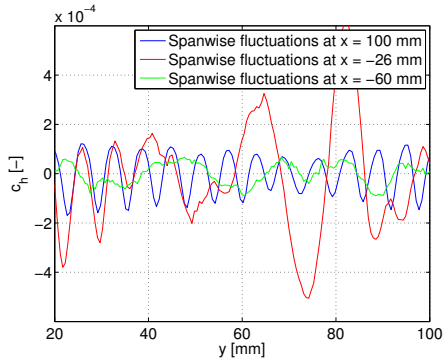

(b) $h_{zz} = 1.15\ mm$ and $Re_{unit} = 8.47 \times 10^6\ m^{-1}$

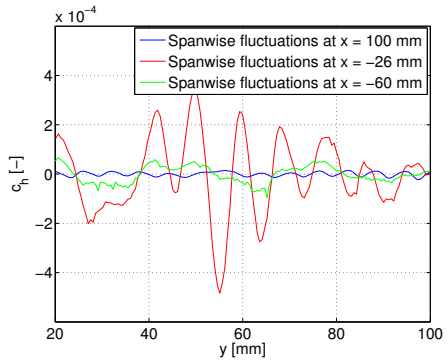

(c) $h_{zz} = 0.20\ mm$ and $Re_{unit} = 11.3 \times 10^6\ m^{-1}$

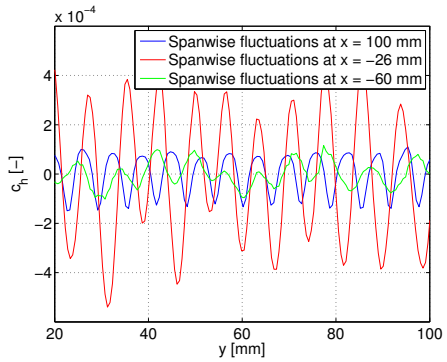

(d) $h_{zz} = 1.15\ mm$ and $Re_{unit} = 11.3 \times 10^6\ m^{-1}$

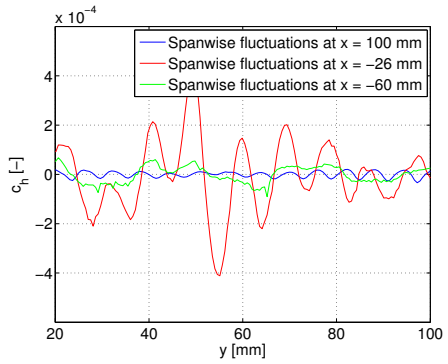

(e) $h_{zz} = 0.20\ mm$ and $Re_{unit} = 14.1 \times 10^6\ m^{-1}$

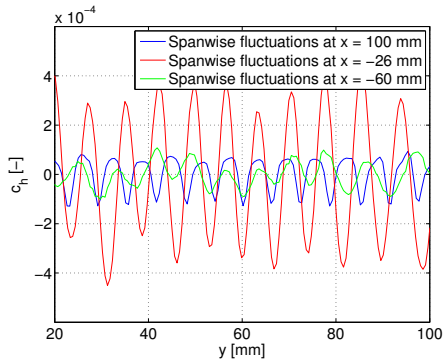

(f) $h_{zz} = 1.15\ mm$ and $Re_{unit} = 14.1 \times 10^6\ m^{-1}$

Figure 5.12: Comparison of the spanwise surface heat flux at three different locations for $h_{zz} = 0.20\ mm$ and $h_{zz} = 1.15\ mm$

The spanwise heat flux distribution for $h_{zz} = 0.20\ mm$ corresponds to the expected heat flux distribution for a VG with $\lambda_{VG} = 6\ mm$ indicated by the blue curves. Parallel to the second ramp, it is noted that the spanwise distribution seems noisy and local fluctuations are clearly visible.

On the right hand side, the plots are given for $h_{zz} = 1.15\ mm$. For the lowest Reynolds number, it is observed that the spanwise heat flux distribution shows a similar . This might indicate that the streaks are not spatially stable hence the longitudinal streaks move during the run. This causes a noisy distribution since the mean of 10 run images is taken. This might be an explanation. Furthermore, it is possible that the longitudinal streaks are weak and the reattachment of the flow occurs instantaneously

(as indicated in the PIV images in chapter 4) that boundary layer transition occurs. The spanwise heat flux distribution at reattachment for the higher Reynolds number shows a clear resemblance with the distribution observed directly after the VG. It is therefore concluded that an increase in Reynolds number has a stabilising effect on the spanwise disturbance.

Chapter 6

Tomographic Particle Image Velocimetry applied in the HTFD

The velocity field near the wall of the double compression ramp is measured using Tomographic Particle Image Velocimetry Tomo-PIV. A detailed flow description is given for the case of $h_{zz} = 1.15\ mm$ and a unit Reynolds number of $14.1 \times 10^6\ [m^{-1}]$. A quantitative flow field around the double compression ramp is obtained by defining a measurement volume parallel to the 5° ramp and a measurement volume parallel to the 45° ramp. Both FOVs with respect to the model are shown in figure 6.1.

First the different measurement set-ups are discussed. This section is followed by a discussion of the laser set-up for both FOVs. The verification procedures are discussed and the performance of Tomo-PIV in the HTFD is further elaborated. Finally, the results are presented, a general flow topology is given and a detailed flow description is given for each FOV.

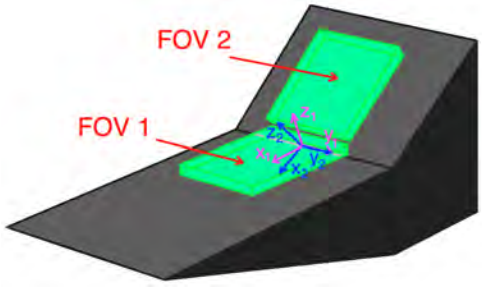

Figure 6.1: Sketch of the double compression ramp with the FOVs

6.1 Camera set-up

Each FOV needs a specific camera set-up. Both set-ups are discussed in this section. In figure 6.2 an overview is given of the camera set-up for measuring the velocity field parallel to the 5° ramp. The model is placed in the test section as shown in figure 6.2(b). The FOV is highlighted by the rectangular white domain on the model shown in figure 6.2(b).

Elsinga [2008] found that the maximum quality factor Q (introduced in chapter 3) is approximately 0.8 for a symmetric 3 camera set-up (see section 3.4.2). To obtain a sufficient quality of reconstruction it is wanted to have a viewing angle between $15° - 45°$ with respect to the out of plane z-axis of the measurement domain. For a larger angle, the amount of ghost particles increases since the line of sight is longer. Furthermore, the probability of false triangulation increases. For smaller angles, the in depth resolution decreases. The test section window of the HTFD is small and therefore optical accessibility limits the camera set-up.

For the measurement domain parallel to the 5° ramp, camera 1 and 3 are horizontally aligned and camera

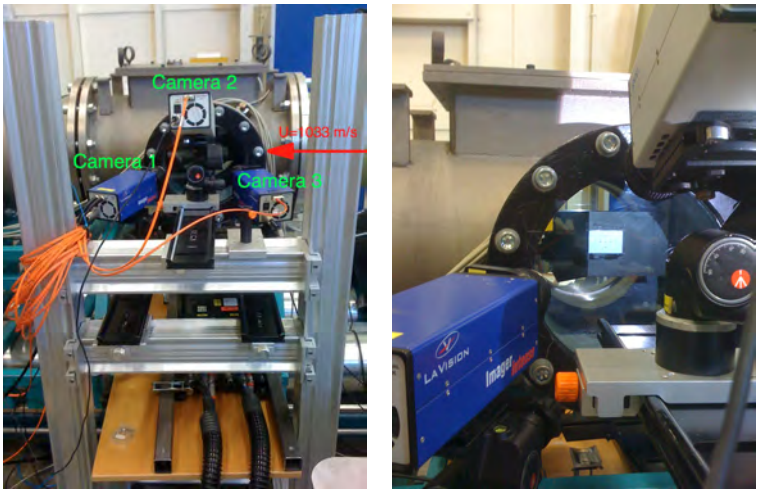

(a) Tomo-PIV set-up next to the test section of the HTFD

(b) The cameras are focussed on the FOV indicated by the white rectangular domain.

Figure 6.2: Overview of the Tomo-PIV set-up in the HTFD for the first FOV

2 is placed approximately 15 cm higher in between camera 1 and 3. The distance between the measurement domain and the camera is based on the magnification factor. The magnification factor is estimated based on the width of the FOV ($w \approx 60\ mm$), the pixel shift ($\Delta_{pix} = 6.45 \times 10^{-6}$) and the number of pixels in the width of the image plane ($\#_{pix,w} = 1376$).

$$M = \frac{w}{\#_{pix}\Delta_{pix}} = \frac{0.06}{1376 \cdot 6.45 \times 10^{-6}} \approx 0.15 \tag{6.1}$$

The lenses that are used have a focal length of $f = 60\ mm$:

$$\frac{1}{f} = \frac{1}{d_i} + \frac{1}{d_0} \tag{6.2}$$

Based on the definition of M

$$M = \frac{d_i}{d_0} \tag{6.3}$$

where d_i is the distance between the lens and the image plane and d_0 the distance between the lens and the object. Rewriting equation 6.2 such that an expression for d_0 is obtained:

$$d_0 = \frac{f}{M}(M + 1) \tag{6.4}$$

Filling in $M = 0.14$ and $f = 60\ mm$ results in $d_0 \approx 460\ mm$. The characteristic parameters of each individual camera are given in table 6.1

Table 6.1: Geometrical characteristics of the measurement set-up parallel to the 5° ramp

	$\varphi[°]$	$\theta[°]$	$\omega[°]$	distance in $z[mm]$
Camera 1	3	−30	−1	394
Camera 2	−17	−7	0	451
Camera 3	3	15	1	519

In table 6.1 φ is the rotation angle around the x-axis, θ the rotation angle around the y-axis and ω the rotation angle around the z-axis. The angles are determined using the pin-hole calibration model from *Davis* hence all the angles are determined with respect to the coordinate system defined for the measurement domain. A right handed coordinate system is applied during the discussion of the Tomo-PIV

results. The right handed coordinate system of the measurement domain is shown in figure 6.3 together with the camera orientation vector.

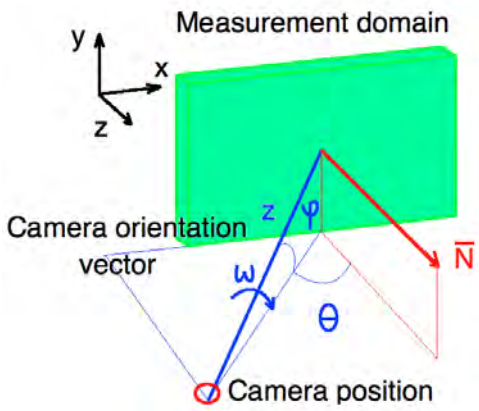

Figure 6.3: Camera orientation with respect to the measurement domain

The set-up for the measurement domain parallel to the 45° is more complicated since the angle between the object and the window is large. The model is kept in place in the test section using a sting. This sting is moved more upstream such that the 45° ramp is located in front of the test section window. In this way, the optical accessibility of the measurement domain parallel to the 45° ramp is increased. The cameras are placed more to the right with respect to the window such that the view angle with respect to the z-axis is not too large. Camera 1 and 2 are aligned vertically and camera 3 is placed to the right side and in the middle of camera 1 and 2. This is shown in figure 6.4.

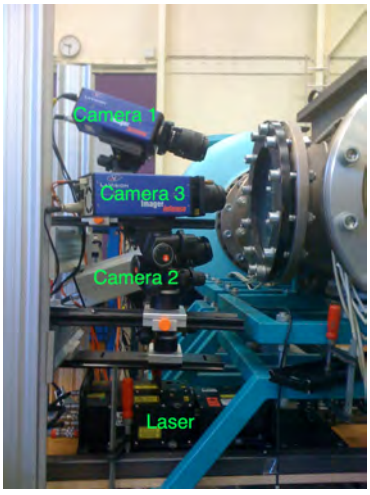

(a) Tomo-PIV set-up next to the test section of the HTFD

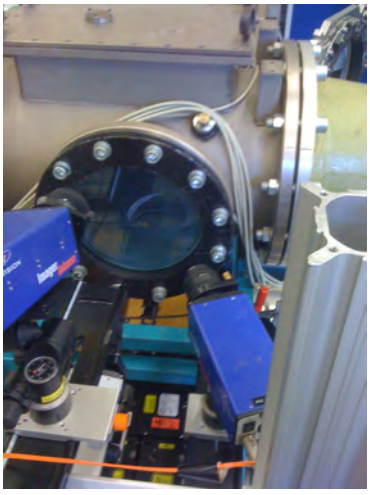

(b) The cameras are focussed on the FOV indicated by the white rectangular domain.

Figure 6.4: Overview of the Tomo-PIV set-up in the HTFD for the first FOV

6.2 Laser set-up

The same laser set-up is used as described in section 3.3.2. The thickness of the laser sheet is controlled by shifting the first plano concave lens with respect to the plano convex lens below the test section.

Table 6.2: Geometrical characteristics of the measurement set-up parallel to the 45° ramp

	$\varphi[°]$	$\theta[°]$	$\omega[°]$	distance in $z[mm]$
Camera 1	-40	-31	30	426
Camera 2	-1	-44	26	408
Camera 3	-9	-19	23	430

During the current experiments, a laser sheet thickness of approximately 6 mm is wanted. Furthermore, a relative small velocity in wall-normal direction is expected compared to the high convective streamwise velocity. Therefore, the time interval (Δt) between the two laser pulses and camera snap shots is increased to$\Delta\ t = 2\mu s$. The particle displacement in z direction is increased which is often referred to as an increase in dynamic range. In figure 6.5(a) and 6.5(b) the laser sheet alignment with respect the model for both both FOVs is given. In figure 6.5(c) and 6.5(d), the illuminated domain is indicated in the corresponding Schlieren image for $Re = 14.1 \times 10^6 m^{-1}$ and $h_{zz} = 1.15mm$.

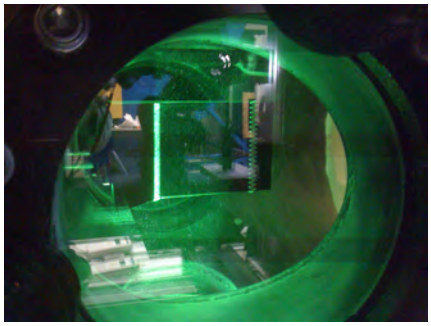

(a) The laser set-up parallel to the 5° ramp

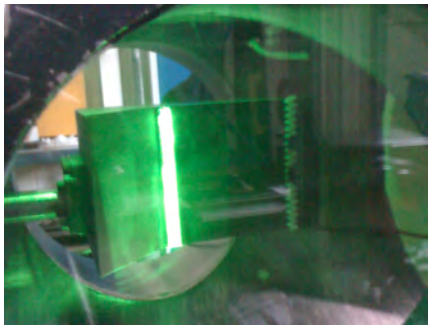

(b) The laser set-up parallel to the 45° ramp

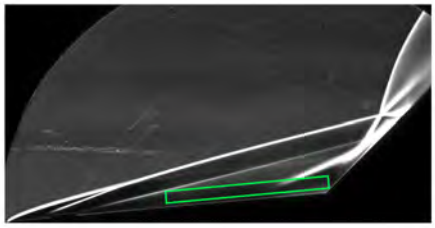

(c) The illuminated domain indicated in the Schlieren image for the case that $Re = 14.1 \times 10^6 m^{-1}$ and $h_{zz} = 1.15mm$

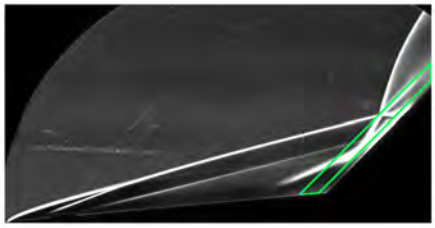

(d) The illuminated domain indicated in the Schlieren image for the case that $Re = 14.1 \times 10^6 m^{-1}$ and $h_{zz} = 1.15mm$

Figure 6.5: Laser sheet orientation for both measurements parallel to first and parallel to the 45° ramp

Based on the Schlieren image given in figure 6.5(c), it is expected to see the influence of the separation shock parallel to the 5°. At the 45° ramp there are expansion waves and shocks impinging on the surface of the wall and wave reflection takes place. Based on figure 6.5(d), it expected to see the influence of the reattachment shock and an expansion wave that originates from the shock interaction above the 45° ramp.

For both measurement volumes, the spacing between the laser sheet and the surface of the model is set at $2mm$. The laser sheet thickness is checked by looking at the mean particle intensity per plane in the reconstructed data. During the self-calibration, the laser sheet thickness is roughly determined based on the appearance of peaks in the z-plane. The self-calibration is applied and the particle distribution is reconstructed for the measurement domain and a large domain outside of the illuminated volume. This procedure gives the following information:

- Distance between the laser sheet and the model surface
- Laser sheet thickness

- Estimate of the ghost particle intensity

In figure 6.6 the mean intensity is plotted in z-direction. the coordinate system is right handed and therefore the z-axis is positive pointing away from the model. The position of $z = 0$ varies per new calibration procedure.

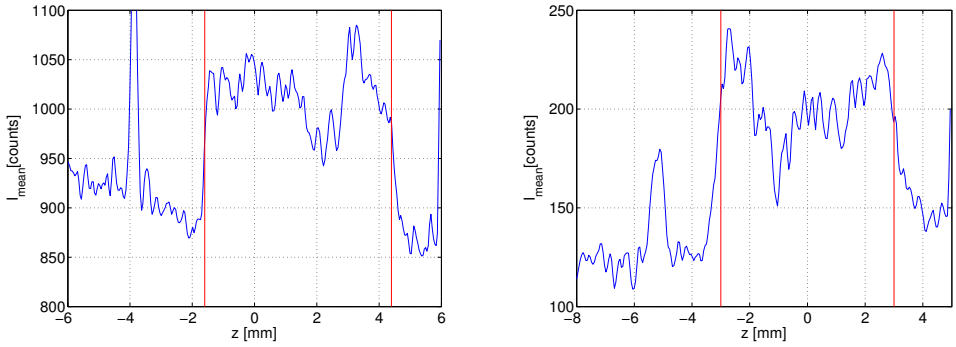

(a) The mean intensity plotted in z direction for the measurement domain parallel to the 5° ramp

(b) The mean intensity plotted in z direction for the measurement domain parallel to the 45° ramp

Figure 6.6: The mean Intensity plotted in z direction to check the sheet thickness

The red lines shown in figure 6.6(a) and 6.6(b) indicate the estimated location of the laser sheet edges based on the self-calibration procedure. The blue line indicates a significant increase in intensity level due to the laser light. It is concluded that for both FOVs, the estimated sheet thickness based on the self-calibration corresponds with the reconstructed thickness.

The reconstruction treats the reflections of the model as illuminated particles which are fixed in space. The peaks in negative z direction with respect to the laser sheet, shown in figure 6.6(a) and 6.6(b), represent the position of the model. For both measurement volumes, the distance with respect to model is approximately $2.2mm$.

6.3 Refractive effect

Light refraction has to be taken into account when an optical flow measurement technique is used in a pressurised test facility such as the HTFD. Vacuum conditions are present in the test section and consequently, a difference in density between the ambient and the test section is present. As a result, the refractive index changes which influences in particular optical measurement techniques that require highly accurate calibration procedure such as Tomo-PIV.

During the initial test phase it was noticed that the particle triangulation during the self-calibration procedure is significantly influenced when particle images are taken in ambient conditions. This can be ascribed to the light refraction that occurs during the measurement. As a result, it is chosen to collect typically 30 images more after the run such that a summed disparity map over these 30 images can be obtained. The influence of the number of calibration images on the quality of the disparity map is elaborated in section 3.4.1. Directly after the run, the pressure is then still significantly low and therefore a self-calibration is performed on the residual images of the run to compensate for refractive effects. This section serves as a validation and indication of the relevance of the refractive effect during a Tomo-PIV experiment in the HTFD.

From refractive theory it is known that the refractive index is linearly dependent on the density of the medium. Mathematically, this is described using the Gadstone-Dale relation.

$$n = 1 + k\rho \tag{6.5}$$

where n is the refractive index, $k = 2 \times 10^{-4}$ and ρ is the density. The analogy presented in this section relies on the pointing of a single pixel and therefore the pixel shift is considered to be the error in the

pointing of the cameras.

Snell's law is used to determined the pixel offset induced by light refraction.

$$\theta' = \arcsin\left(\frac{\sin(\theta)n_1}{n_2}\right) \tag{6.6}$$

In figure 6.7(a) a sketch is given of one camera with its corresponding pointing error *dpix* due to the pressure difference between the test section and the ambient surroundings.

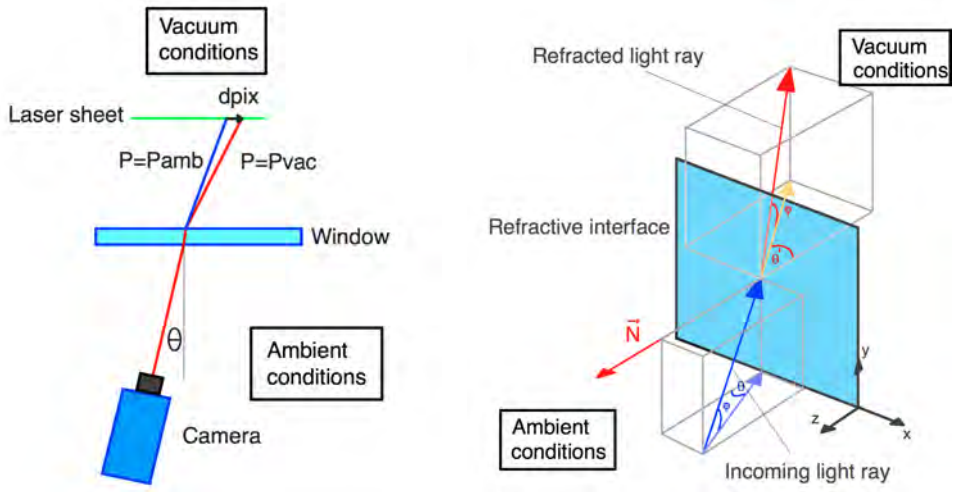

(a) Sketch of the refractive effect and the corresponding pixel shift

(b) Sketch of the incoming light ray (blue), the refractive interface (window) and the refracted light ray (red) with the corresponding angles

Figure 6.7: Graphical representation of the refractive effect

The refractive effect for a three-camera set-up is worked out for the camera set-up parallel to the 5° ramp. It is assumed that the distance between the image and the object plane are the same ($z = 400mm$) for all cameras. Furthermore it is assumed that the window is in the middle between the image and the object plane. In figure 6.7(b) a sketch is given of a incoming light ray (blue arrow) together with the refractive interface (window) and the refracted light ray (red arrow). The light ray is refracted in two directions indicated by the angles θ and φ. Snell's law (see equation 6.6) is used to obtain the two relevant refraction angles for the lines of sight for all three cameras.

The error is determined and a graphical representation is given in figure 6.8.

The coloured dots represent the three different cameras (camera 1 red, camera 2 mangenta and camera 3 green). The blue lines represent the lines of sight for every camera for the case that there is no pressure difference between the test section and the ambient. The green lines that start from the refractive interface (window is represented by the black dots), represent the light refracted when it passes the refractive interface.

Snell's law states that light refracts further away from the normal since the density is lower behind the interface. As a result of the refracted light beam, it can be seen that the three cameras are not pointing in the same direction but they span a triangular two dimensional plane which represents the pointing error for this particular three-camera set-up. Note that the case presented in figure 6.8 is not physical since the pixel shift for each camera is in the order of 1 pixel rather than 10 mm as given in figure 6.8.

The norm is taken for the individual cameras and given in table 6.3. Based on table 6.3, the relative pixel shift is in the order of 1 pixel.

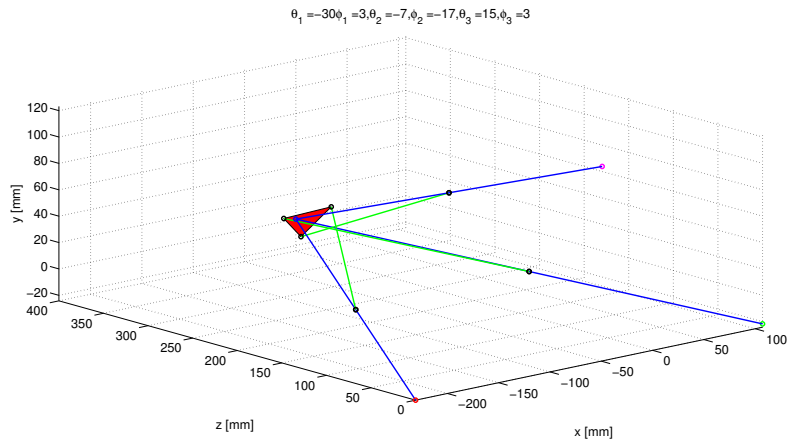

Figure 6.8: Three dimensional theoretical error estimation due to the refractive effect

Table 6.3: Pixel shift

	$Camera1$	$Camera2$	$Camera3$
Δpix	$\pm 0.75 pix$	$\pm 0.3 pix$	$\pm 0.4 pix$

The pixel shift is determined experimentally by taking an image of a *Lavision type 10* calibration plate at 6 different a test section conditions. An image is taken at ambient pressure. The vacuum tank is switched on and images are taken at $p = 476\ mbar$, $p = 171\ mbar$, $p = 80\ mbar$, $p = 27\ mbar$ and $p = 1\ mbar$. The images taken at lower pressure are then cross-correlated with the image taken at ambient pressure. In this way, the pixel shift for all three cameras are determined. In figure 6.9, the disparity map is given for the three camera set-up used to measure the velocity field parallel to the 5° ramp.

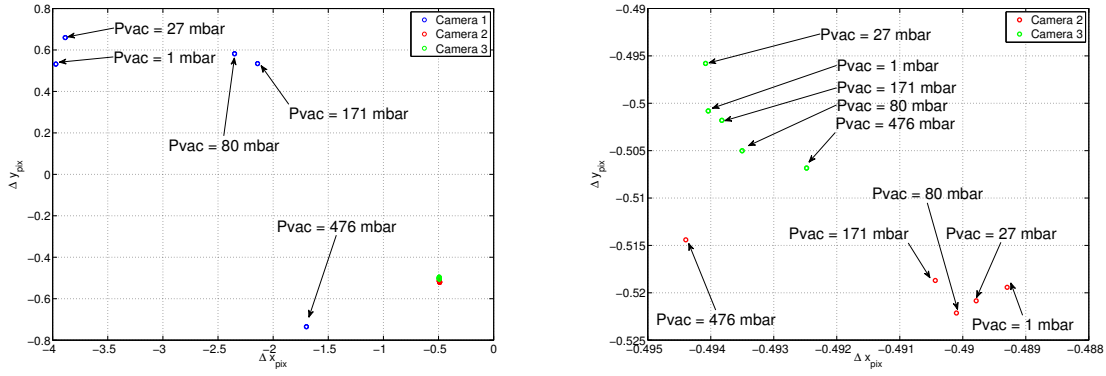

(a) The experimentally determined pixel shift for the three camera set-up used for FOV 1

(b) Detail of the experimentally determined pixel shift for camera 2 and 3

Figure 6.9: Experimentally determined pixel shift for the three camera set-up used for FOV 1

Note, that the pixel shift of camera 1 is in the order of 2 to 3 pixels while for camera 2 and 3 the pixel shift is significantly lower (0.5 pixel). Furthermore, it is observed that for camera 1 the pixel shift becomes larger when the pressure drops which is also expected from theory. However, this is not the case for camera 2 and 3 shown in figure 6.9(b).

Note, that the pixel shift is in negative direction for all three cameras. From theory, it was expected,

that refraction takes place in opposite direction for the opposite cameras (see camera 1 (red) and camera 3 (green) in figure 6.8). The large overall pixel shift might be due to the fact that the window tilts with respect to the image plane due to the pressure difference between the ambient conditions outside and the vacuum conditions inside the test section. A tilted refractive interface results in an overall pixel shift in one direction (depending on the tilt angle) for opposite viewing angles. The pixel shift obtained experimentally, is in negative direction for all three cameras. Therefore, a tilted refractive index might be the cause of this and therefore this is further investigated. A graphical representation is given in figure 6.10.

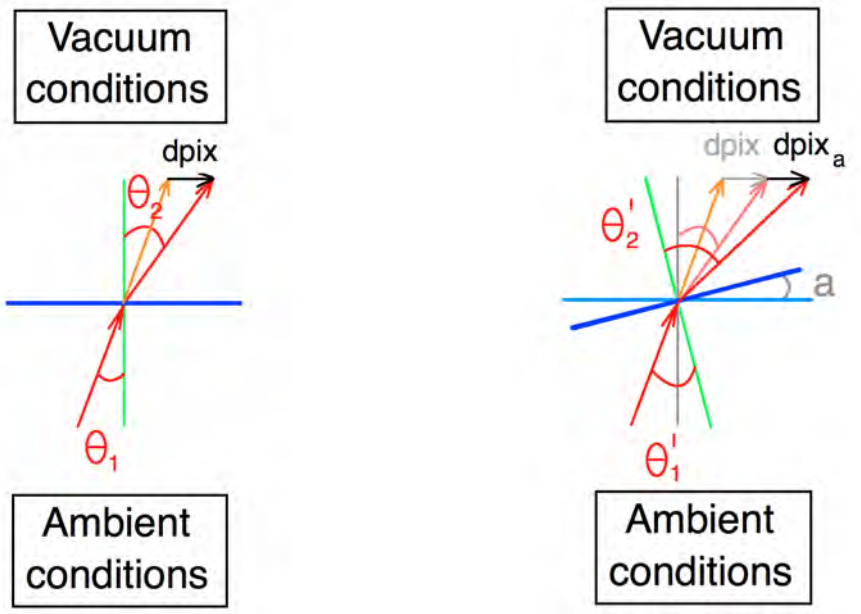

(a) Refractive effect without a titled window

(b) Refractive effect with a titled window

Figure 6.10: Graphical representation of the pixel shift caused by a tilted refractive interface

The orange arrow indicates the propagation direction of the light ray when the test section would be at ambient pressure. The red arrow indicates the refracted light ray. On the right hand side, a similar sketch is given but now the refractive interface is tilted. The angle θ_1' can be defined in terms of a:

$$\theta_1' = \theta_1 + a \tag{6.7}$$

Using Snell's law, the refracted angle θ_2' becomes:

$$\theta_2' = \arcsin\left(\frac{\sin(\theta + a)n_2}{n_1}\right) \tag{6.8}$$

The refracted angle, θ_2', can then be written in terms of the original coordinate system:

$$\theta_{2,new} = \theta_2' - a = \arcsin\left(\frac{\sin(\theta + a)n_2}{n_1}\right) - a \tag{6.9}$$

The pixel shift due to the tilted window can be written as:

$$dpix_a = \| \sin(\theta_2) \cdot l - \sin(\theta_{2,new}) \cdot l \| \tag{6.10}$$

where l is the distance between the refractive interface and the object. The theoretical pixel shift $dpix_a$ is plotted against the viewing angle (θ_1) and different tilt angles (a) of the refractive interface in figure 6.11(a). To see the direct influence of the tilt in refractive index, the refractive effect present for a aligned

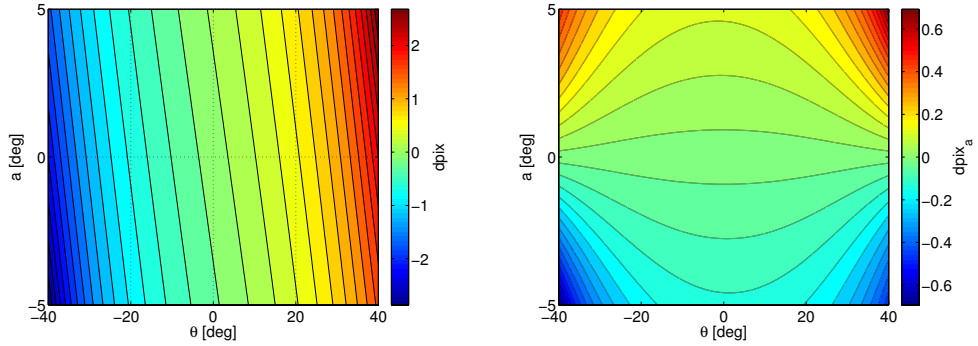

(a) The total pixel displacement plotted against de viewing angle (θ) and the tilt angle of the window (a)

(b) The pixel shift solely induced by the tilt angle (a), plotted against the viewing angle (θ) and the tilt angle of the window

Figure 6.11: Pixel shift induced by the tilting of the window

refractive index has to be subtracted ($dpix_a - dpix$). This is plotted in figure 6.11(b).

Figure 6.11(b) confirms that a positively tilted window, refracts the light more positively for both a camera with a positive and a camera with a negative viewing angle. Hence, this could explain why the pixel shift found during the experimental analysis are all in the same direction. A tilted refracted interface can therefore be considered as the cause of the discrepancy found between the theoretical analysis shown in figure 6.8, and the experimental analysis shown in figure 6.9.

Furthermore, it can be concluded, that the absolute pixel shift solely induced by the tilting angle of the window, does not correspond with the large pixel displacement obtained during the experimental analysis (at least 0.5 pixel). However, during the theoretical analysis as shown above, only one direction is taken into account. Nevertheless, this effect occurs in two directions as shown in figure 6.7(b).

6.4 Self-calibration

As shown in the previous section, the line of sight of each camera is influenced by the pressure difference between the test section and the ambient surrounding. Based on the 2D images from the different viewing angles, a particle triangulation procedure is performed and the disparity with respect to the plate calibration is determined (see section 3.4.1). The calibration function is updated based on the disparity map. One needs to make sure that the disparity map is calculated under similar conditions as present during the measurement. Therefore, it is not possible to perform a self-calibration procedure at ambient conditions since the lines of sight will differ when the pressure in the test section decreases (see previous section). Consequently, the self-calibration is performed based on the extra images that are taken after the run. The particle density in these images is sufficient and the pressure in the test section while taking these images is nearly similar to the pressure during the run.

The self-calibration procedure improves the plate calibration. The plate calibration is rather rough since it is based on one plate position and thus two z-positions. As a result, the third order polynomial is rather inaccurate due to the limited amount of fitting points. A typical fit rms is found in the order of 0.2 pix. The *Lavision Type 10* calibration plate has a 10 mm spacing between the dots. Local positions in between the dots in the measurement domain are determined using bilinear interpolation. The measurement domain has the following dimensions:

$$(x_{vol}, y_{vol}, z_{vol}) = (60mm, 40mm, 6mm)$$

The voxel distribution within the measurement domain for both FOVs is given in table 6.4 The volume is split up in sub-volumes to refine the set of calibration data points. The definition and typical values for a sub-volume size, threshold value and search radius were introduced in section 3.4.1. The measurement volume is split up in ($n_x \times n_y \times n_z = 6 \times 6 \times 5 = 10\ mm \times 6.7\ mm \times 1.2\ mm$) sub-volumes where the

Table 6.4: Geometrical characteristics of the measurement set-up parallel to the 5° ramp

	$vox_x[-]$	$vox_y[-]$	$vox_z[-]$
FOV parallel to 5° ramp	1300	940	140
FOV parallel to 45° ramp	1420	980	120

local disparity vector is determined based on particle triangulation. The threshold value ($T = 150 - 200$ *counts* depending on the average particle intensity) is set such that the particle triangulation lies below 10000 (rule of thumb) for all the three cameras. The search radius is initially set to $\epsilon = 4$. After refinement ($n_x \times n_y \times n_z = 9 \times 9 \times 8 = 6.7\ mm \times\ 4.44\ mm\ \times\ 0.75\ mm$) ,$\epsilon = 0.5$ and $T = 100 - 150$), the self-calibration is performed again and the peak displacement is reduced in the order of $\vec{d} = \mathcal{O}(10^{-3})$. The calibration function is refined by taking a larger number of sub-volumes since the third order polynomial is fit through more points.

In Appendix D, the disparity maps are given for two iteration steps for both FOVs. It is forced by geometrical limitations of the test section to place the calibration in a rotated position for the measurement domain parallel to the 45° ramp. This can be seen in the self-calibration images, since no signal is present in upper right and lower left corner (see figure D.1(c)). In figure D.1(c) can be seen that a high amount of particle triangulations is found in the lower right corner due to local reflection of the laser light on the model. It is made sure that no spurious vectors are present. After a vector smoothening procedure, the calibration file is updated. Finally the fit *rms* of the third order polynomial is reduced to $\mathcal{O}(10^{-3})$.

6.5 Interrogation volume size

In section 3.3, the importance of the *ppp* during a 2C-PIV experiment is emphasised. An estimate of the Particles Per Voxel (*ppv*) is presented based on the 2D raw images. A function is written in *Matlab* which determines the local maxima in the image. The user gives in a threshold value and a search radius. The threshold is based on a priori investigation of the raw image, hence the user finds an estimate of the particle pixel intensity. The search radius is dependent on the size of the particles. In figure 6.12 a sample of an image is given with a zoomed-in view of the particle intensity map highlighted by the red lines in figure 6.12(a). The red dots in figure 6.12(b) represent points which are counted as particles by the *Matlab* script.

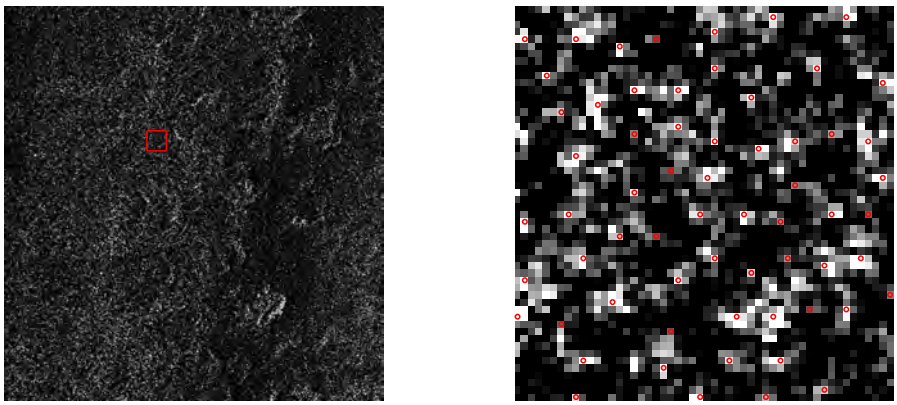

(a) Sample image from which the *ppp* is determined (b) Zoomed in on the sample image to indicate the particle detection

Figure 6.12: Determination of the *ppp*

The *ppp* is estimated to be 0.018. Based on this number the correlation volume size is determined. Again

it is assumed to have 9 particle pairs per volume to obtain a qualitative correlation peak. Assuming a cubic correlation volume this results in a interrogation volume of the following size:

$$\frac{9}{w^3} = \frac{ppp}{z_{vox}} \rightarrow w = \sqrt[3]{\frac{9}{\frac{ppp}{z_{vox}}}} = \sqrt[3]{\frac{9}{\frac{0.018}{120}}} \approx 45pix \tag{6.11}$$

The longitudinal vortical structures are identified by the rotational flow behaviour in the (y, z) plane and hence it is wanted to have a high spatial resolution in y and z. Therefore, the correlation volumes are elongated in x direction such that the spanwise and normal width of the correlation volume can be decreased. During the 3D cross-correlation procedure, a correlation volume of $65 \times 56 \times 32$ voxels is used which corresponds to 3.2 mm × 2.8 mm × 1.6 mm. Typically 120 voxels in z-direction are taken such that with an overlap of 75% approximately 15-20 vectors are found in normal direction. An estimate of the amount of vectors per mm is given in the table below:

Table 6.5: Number of vectors

	x	y	z
vec/mm	3.33	2.5	3.33

6.6 Spurious vector determination

For both FOVs typically 20-30 runs are taken to obtain a statistical average. Spurious vectors occur due to low local particle density, bad flow conditions, bad windtunnel/acquisition timing or flaws during the data analysis procedure. These vectors have to be accounted for to obtain a plausible average velocity field. A local statistical procedure is performed based on the number of runs. Initially, the standard deviation at every local point in the measurement domain is determined in the following way:

$$\bar{\sigma_i} = \frac{1}{N_r} \sum_{i=1}^{N_r} (\vec{u_i} - \bar{u_i})^2 \tag{6.12}$$

where N_r is the number of runs, $\vec{u_i} = [V_x, V_y, V_z]$ and $\bar{u_i} = [\bar{V_x}, \bar{V_y}, \bar{V_z}]$ is the mean velocity. Consider the local measurement data to be normally distributed. Hence, a local velocity measurements should fulfill the following relation to be considered as valid.

$$\bar{u_i} - 3\sigma \leq \vec{u_i} \leq \bar{u_i} + 3\sigma \tag{6.13}$$

When the vector is considered to be spurious, it is replaced by the new mean value based on the other corresponding local data points. From this point on, a new standard deviation value is determined based on the replaced vectors. This procedure is iterated until no more spurious vectors are replaced.

6.7 Accuracy estimation

Little is known regarding the error estimation of a Tomo-PIV experiments due to the complexity of the technique. The accuracy of the measurement is therefore estimated by applying the appropriate statistical analysis for a case of known flow conditions. Hence, the relative fluctuations for a steady, undisturbed, uniform flow situation are determined.

As a case study for the measurement domain parallel to the 5° ramp, a validation run is taken during which the model is removed from the test section. The particle density is uniform since no shocks are present. It is expected to have a high streamwise velocity ($V_x \approx cos(5) \times 1033 = 1021 m/s$) and a slightly diverging V_y. Since the light sheet is already positioned parallel to 5° ramp, it is expected to have a negative V_z component since the flow is aligned with the longitudinal wind tunnel axis instead of the 5° inclined model surface such that $V_z = \sin(5) \times 1033 \approx 90 m/s$.

The standard deviation in the (y, z) plane is of interest since the flow rotation in this plane is further studied. Therefore, the standard deviation in each (y_1, z_1) plane is determined for the case that no

model is present and the unit Reynolds number is equal to $Re = 14.1 \times 10^6$ $[m^{-1}]$. In figure 6.13(a), the in-plane mean velocity component is plotted in x_1 direction and in 6.13(b) the in-plane standard deviation of V_x, V_y and V_z is plotted in x_1 direction.

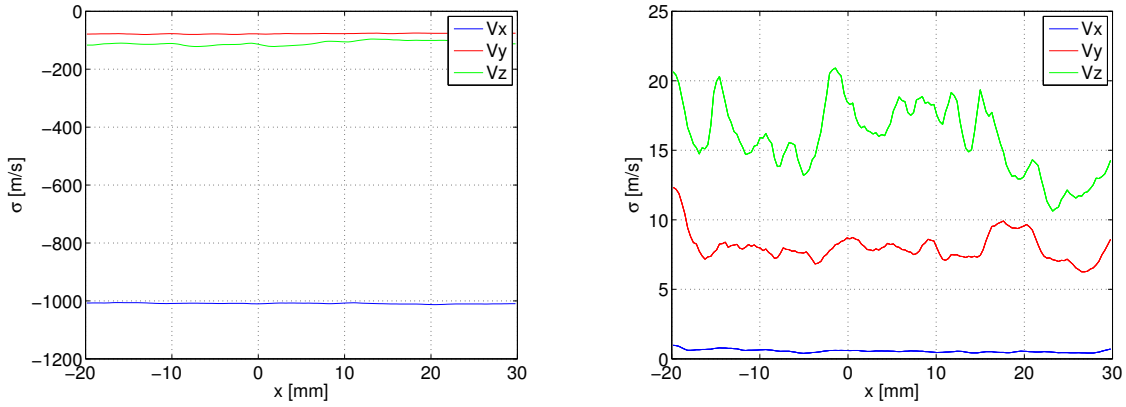

(a) Mean V_x V_y and V_z in the (y, z) plane plotted in x direction for the velocity field parallel to the 5° ramp

(b) The (y, z) plane rms values for all the velocity components plotted in x direction for the velocity field parallel to the 5° ramp

Figure 6.13: Measurement accuracy assessment for FOV 1

Table 6.6: Standard deviation and mean for every velocity component in the (y_1, z_1) plane for the presented test case

	$std[m/s]$	$mean[m/s]$	$std[\%]$
V_x	0.56	1008	0.056
V_y	6.2	77.5	8.0
V_z	17.4	109.7	15.9

It is found that the standard deviation for V_z is significantly higher (approximately a factor 3) than for V_x and V_y. Fluctuations that exceed this percentage are impossible to measure in a single instantaneous (y_1, z_1) plane based on the presented case study.

During the measurement campaign for the measurement domain parallel to the 45° ramp, a validation run is taken during which the model is still present in the test section. For this case, the model is present in the test section but it is moved away from the window (in spanwise direction of the windtunnel) such that the distance between the model and the laser sheet becomes approximately 25 mm. In this way, the local free stream velocity is obtained. It is noted that the bow shock is present such that only a small portion of the free stream flow domain is captured. A similar procedure is then performed as described for the FOV parallel to the 5° ramp. The free stream flow parallel to the model is measured and it is made sure that no fluctuations are present in the flow. The mean of all velocity components in the (y_2, z_2) plane is plotted in x_2 direction in figure 6.14(a) and the corresponding standard deviation is given in 6.14(b).

Due to the shock, two velocity field are present governed by their convective velocity V_x. This effects the standard deviation in the (y, z) plane and therefore both cases are presented in table 6.7 separately. Again a high standard deviation for V_z is found especially upstream of the shock which indicates that the flow is not uniform since the standard deviation for V_z downstream of the shock is significantly lower and of the same order as the standard deviation in V_y. With respect to the mean corresponding velocity component, the standard deviation of V_z is very large. This gives an indication of the range of velocities that can be measured in x, y and z direction.

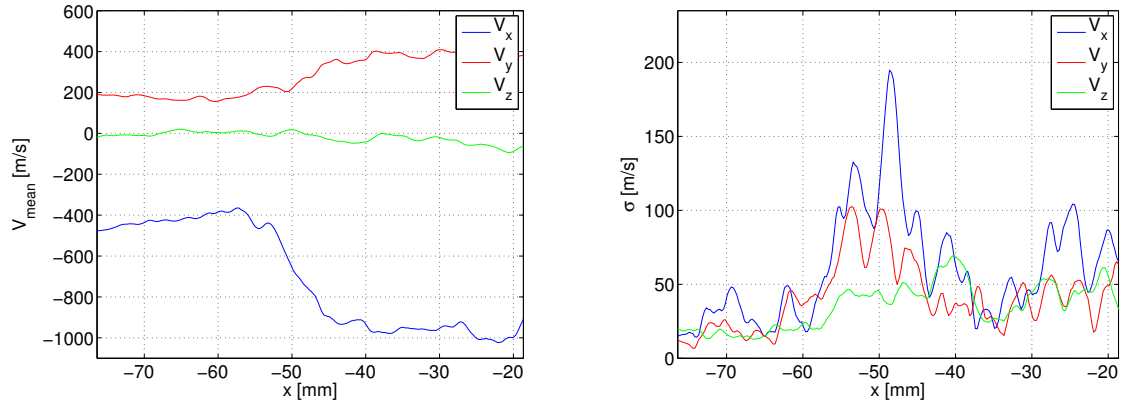

(a) Mean V_x V_y and V_z in the (y, z) plane plotted in x direction for the velocity field parallel to the 45° ramp

(b) The (y, z) plane rms values for all the velocity components plotted in x direction for the velocity field parallel to the 45° ramp

Figure 6.14: Measurement accuracy assessment for FOV 2

Table 6.7: Standard deviation and mean for every velocity component in the (y, z) plane for the presented test case

	Upstream of the shock			**Downstream of the shock**		
	$mean[m/s]$	$std[m/s]$	$std[\%]$	$mean[m/s]$	$std[m/s]$	$std[\%]$
V_x	-441	26.5	6	963	59	6
V_y	177	16.3	9.2	385	38	10
V_z	-2.9	16.3	565	-41	45	110

In general it can be stated that the pixel displacement in x and y direction are considered to be large enough to measure the local velocity. Unfortunately, the convective velocity in z direction is low and the dt is small ($dt = 2\mu s$, see section 6.2). The short$\Delta\ t$ therefore limits the dynamic range in z direction. This effect becomes even worse if the particles are stretched in z direction as well. For now, this is considered to be the reason for the high noise level in the V_z determination. Consider that $V_z = 20\ m/s$ and estimating the magnification to be $M = 1376/0.06 = 2.3 \times 10^4$ then:

$$\Delta_{pix,z} = V_z \cdot M \cdot \Delta t = 20 \cdot 2.3 \times 10^4 \cdot 2 \times 10^{-6} = 0.92 pixel \tag{6.14}$$

The displacement in z direction is in the order of the radius of the particle.

6.8 Reconstruction quality estimation

An indication of the particle shaped is obtained by analysing the reconstructed particle distribution. The particle distribution is saved as a *-ascii* from *Davis 7.4* and read into *Matlab*. The data set consists of vox_z planes with each having a size of $vox_x \times vox_y$. Using a 2D correlation procedure, an estimate of the pixel shape is determined. The correlation factor in z direction is determined using:

$$R(z) = \frac{\sum_x \sum_y I(x,y,z) \otimes I(x,y,z+\Delta z)}{\sum_x \sum_y I(x,y,z)^2} \tag{6.15}$$

For a fixed z position, typically 10 planes in normal direction are correlated to investigate the shape of the reconstructed particles in this particular direction. This procedure is also performed for x and y direction. Based on priori investigation of the reconstructed data, it is determined that the particle images in the (x, y) look Gaussian shaped. Furthermore, this procedure is performed at several locations in the measurement and the mean of each individual correlation signal is obtained. The results for both the measurement domain parallel to the 5° and the 45° ramp are shown in figure 6.15(a) and 6.15(b) respectively.

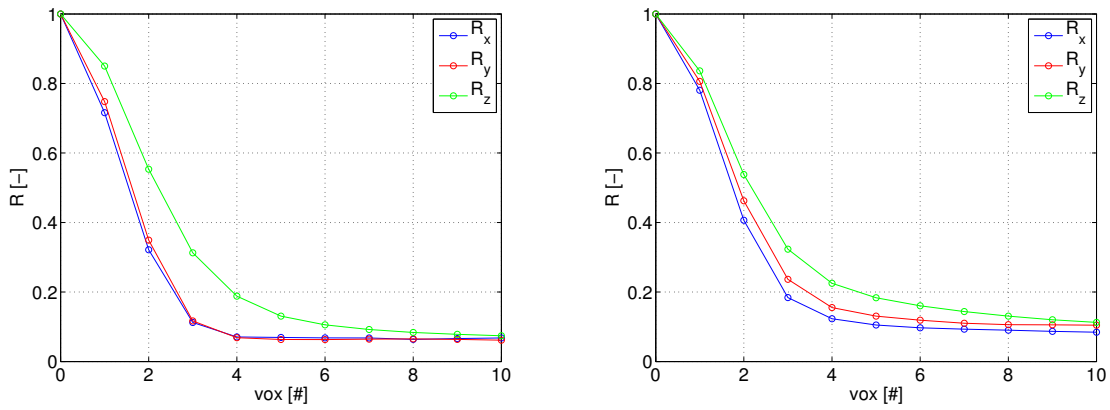

(a) Correlation factor in x, y and z for the measurement domain parallel to the 5° ramp

(b) Correlation factor in x, y and z for the measurement domain parallel to the 45° ramp

Figure 6.15: Correlation factor in x, y, z based on the reconstructed particle distribution

From figure 6.15(a) can be seen that the correlation factor in x and in y direction are nearly similar. During the observation of the reconstruction image, it was determined that the pixels looked round and not stretched. The result shown in figure 6.15(a) therefore corresponds to this observation. However, for the correlation factor in z direction, it can be seen that it takes a larger amount of voxels in z direction to have uncorrelated image planes. This indicates that the size of the particles is stretched in z direction.

Similar results are shown for the FOV parallel to the 45° in figure 6.15(b). However, it is observed, that there is a discrepancy present between R_x and R_y. which indicates that the particles are not completely round but slightly stretched in y direction. Again an offset for R_z with respect to R_x and R_y

is observed which indicates that the particles are stretched in z direction as well. This will widen the correlation peak significantly and cause an uncertainty that might be in the order of the value that is given in equation 6.14.

6.9 General flow topology

In figure 6.16 an overview of the flow is given. For interpretation purposes, it is decided to show first the general flow overview. In section 6.10 and 6.11 the individual velocity fields are discussed in more detail. The outline of the surface of the model is indicated by the thick black lines. The velocity field behind the leading edge shock is indicated by orange ($V_{tot} \approx 1000\ m/s$) corresponds with the values found during the planar PIV campaign and theory, shown in chapter 4. The flow is then rapidly decelerated by the separation shock at $x \approx 15mm$. The flow is curved upwards which is indicated by the streamlines in the following section. The flow reattaches at the 45° ramp and the velocity is increased by a Prandtl-Meyer expansion fan that emanates from the shock interaction above the surface of the model. This is indicated by the green domain parallel to the 45° ramp where the flow is accelerated from $450m/s$ up to locally $750m/s$. The flow is then compressed and slowed down to approximately $550m/s$ after which again a graduate acceleration takes place up to approximately $675m/s$.

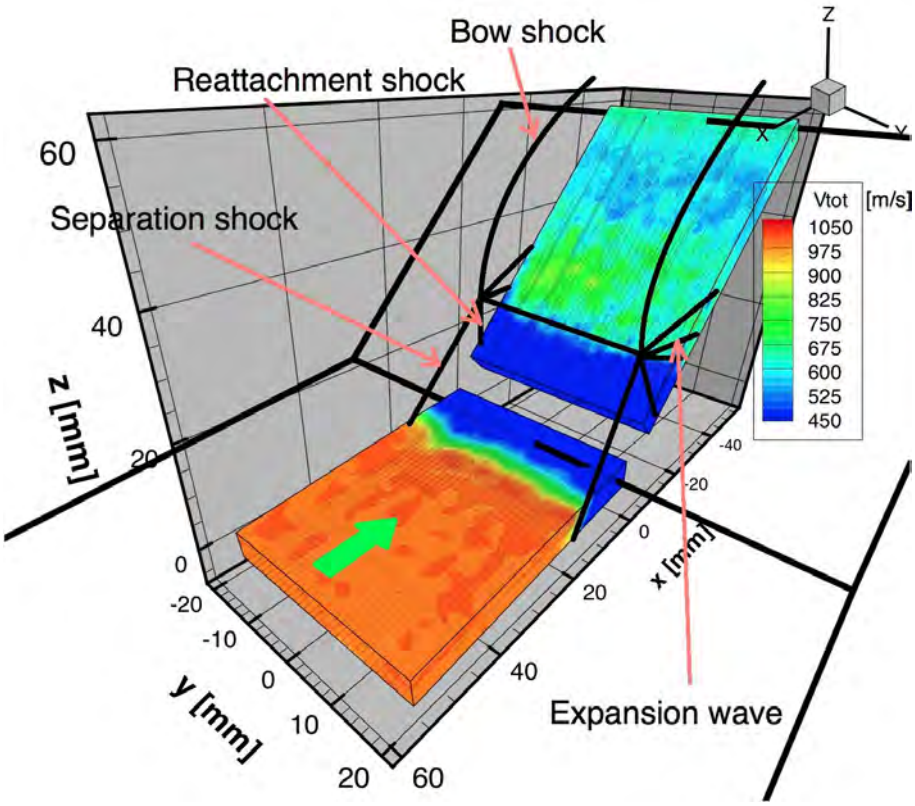

Figure 6.16: General 3D flow overview

In figure 6.17 an iso-surface plot is given of the total velocity. Note longitudinal iso-surfaces for $V_{tot} = 990$ m/s parallel to the 5° ramp. The velocity decreases due to the separation shock at $x \approx 15\ mm$. Note the isoplanes in normal direction with respect to the surface of the model at $x \approx 20\ mm$ and at $x \approx -10\ mm$. The separation and reattachment shock are present at these streamwise locations respectively. Furthermore, note the locally high velocity regime ($V_{tot} \approx 750\ m/s$) parallel to the second ramp corresponding to the local high c_h domains determined using QIRT (see chapter 5). The characteristic local velocity fields are discussed in detail in the following sections.

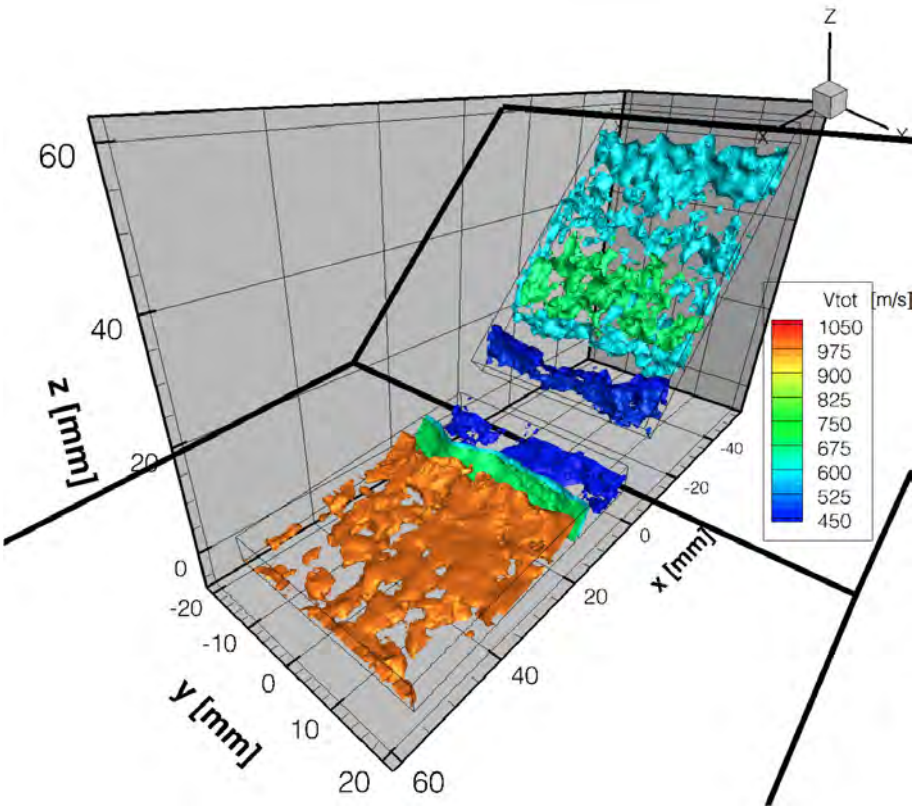

Figure 6.17: General 3D flow overview

6.10 Flow topology parallel to the 5° ramp

Parallel to the 5° ramp, it is expected to have a upstream velocity equal to the velocity determined behind the leading edge shock using 2C-PIV. Furthermore, the separation shock and the separated flow domain just upstream of the first-to-second ramp junction of the model is expected. The QIRT measurements indicated that the size of the separation bubble decreases for higher VGs and separation takes place at approximately $x = 20$ mm based on the QIRT results presented in chapter 5. A flow overview is given in figure 6.18 where the contours of the total velocity is plotted together with a rake of streamlines. The influence of the separation shock on the velocity is clearly visualised in the (x, z) planes. In this section the coordinate system (x_1, y_1, z_1) is used, as indicated in figure 6, and referred to as (x, y, z) such that x is tangent to the 5° ramp, y the spanwise coordinate and z the normal coordinate, positive pointing away from the model.

The velocity field shown in figure 6.18 corresponds with the Schlieren image given in figure 6.5(c). At approximately 20 mm, the flow separates and a free stream velocity field is measured upstream of the separation line. Furthermore, the flow will slow down near the deflection point and no back flow is present which is shown in figure 6.19.

In figure 6.19 the mean streamwise velocity profile is given. it can be seen that velocity measured upstream of the shock is slightly below the value which is found using the oblique shock relations ($V_{tot} = 1015$ m/s). This is caused by the extra shock wave that emanates from the VG. The planar PIV results show a local velocity of 1020 m/s. The gradient near the deflection point induced by the separation shock is high since the velocity in streamwise direction decreases from 900 m/s to 200 m/s over 15 mm. In contrast to the planar PIV experiments carried out for the case $h_{zz} = 0$, there is no circulation bubble and thus no back flow present. In figure 6.20 the normal velocity component (V_z) is plotted in the (x, z) plane. This velocity component is approximately 1% of V_x and the gradient in z-direction is relatively small. This indicates that the flow is not smoothly curved upwards but a radical velocity change is present. V_z increases away from the model surface which lies within the expectations.

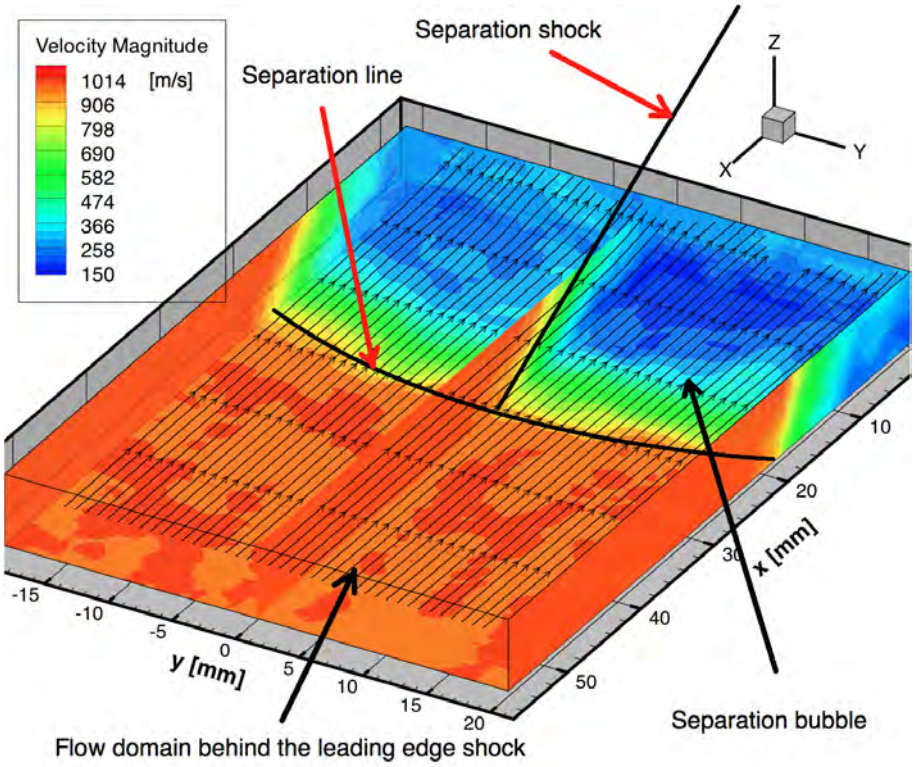

Figure 6.18: Flow overview parallel to the 5° ramp. Velocity magnitude is given in m/s

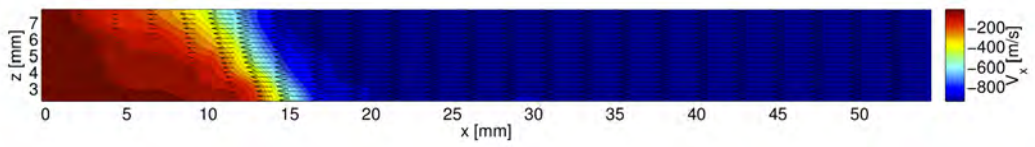

Figure 6.19: Contour map V_x parallel to the 5° ramp

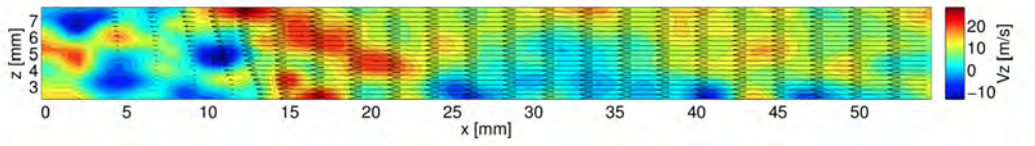

Figure 6.20: Contour map V_z parallel to the 5° ramp

The VG introduces a spanwise perturbation in the near-wall flow regime. Therefore, the spanwise velocity field is further investigated. To identify perturbations in the flow, the data is filtered using a Savitzky-Golay smoothing filter which is often used in the field of noisy signal processing Savitzky and Golay [1964]. The perturbations induced by the VG are very small compared to the convective velocities in particular V_x and V_y. The main goal is to relate the longitudinal heat flux streaks to the velocity profile measured using Tomo-PIV. Longitudinal vortices are expected and therefore the v'_y and v'_z profile is expected in the spanwise direction given in figure 4.18. On the left hand side of figure 6.21, the spanwise V_y and V_z distribution is given for four fixed x positions. On the right hand side, the corresponding filtered spanwise v'_x, v'_y and v'_z distribution is given.

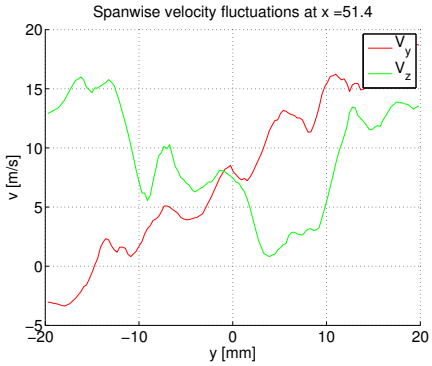

(a) V_y and V_z distribution in the middle of (y,z) plane at $x = 51.4mm$

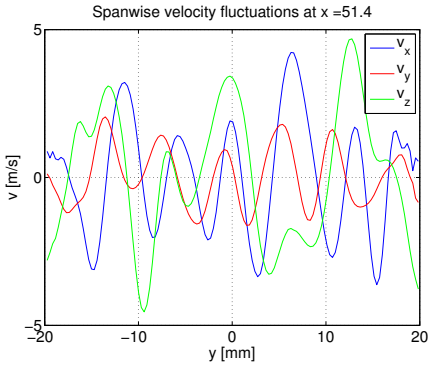

(b) Perturbations v'_y and v'_z distribution in the middle of (y,z) plane at $x = 51.4mm$

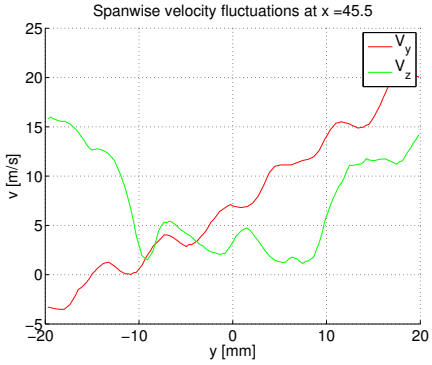

(c) V_y and V_z distribution in the middle of (y,z) plane at $x = 45.5mm$

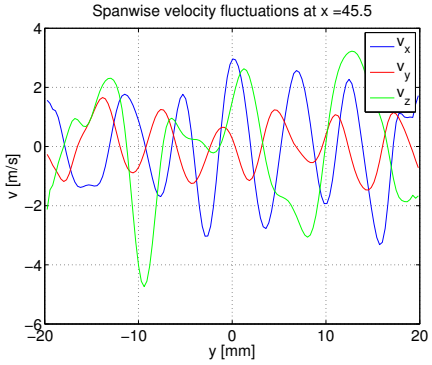

(d) Perturbations v'_y and v'_z distribution in the middle of (y,z) plane at $x = 45.5mm$

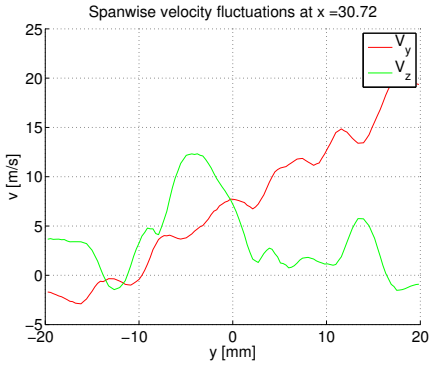

(e) V_y and V_z distribution in the middle of (y,z) plane at $x = 30.72mm$

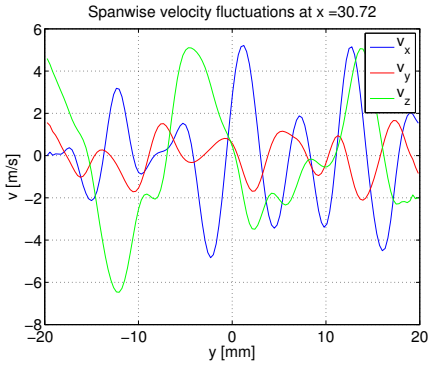

(f) Perturbations v'_y and v'_z distribution in the middle of (y,z) plane at $x = 30.72mm$

Figure 6.21: The spanwise v'_y and v'_z distribution for four fixed x positions

During the data analysis, it has been noticed that the influence of the VG on the velocity field is relative

small compared to the convective speed V_x. By specifying the range of interest to $980 \leq V_x \leq 1005\ m/s$, clear fluctuations are visualised which are induced by the VG. The spanwise V_x and v_y' distributions at four fixed x positions are plotted in figure 6.22.

For every fixed x position, the 10 upstream and 10 downstream spanwise velocity profiles are taken and the mean is calculated. This corresponds with taking the average over a range of approximately 6 mm in streamwise direction.

It can be seen that clear velocity fluctuations are present which correspond with the wavelength of the VG ($\lambda_{VG} = 6mm$). The gradient is relatively low which can be seen by the contour values indicated in figure 6.22. The difference between the higher and lower velocity regions is approximately 10 m/s while the total velocity is in the order of 1000 m/s.

The standard deviation of V_x is determined based on the individual snap shots. The spanwise V_x distribution is given together with the corresponding contour plot of the standard deviation in Appendix E. Based on this figure, it can be seen that the position of the longitudinal streaks is rather fixed and within each streak, no velocity fluctuations are present. This indicates that the streaks are not turbulent.

The v_y' and v_z' vectors do not show clear vortical behaviour. Within the measurement domain parallel to the 5° ramp, the influence of the VG is clearly noticed on the streamwise and spanwise velocity component. However, not a clear fluctuating behaviour of V_z is noticed which would be expected when having longitudinal vortices. This is due to the fact that v_z' are expected to be of the same order as v_y' ($\mathcal{O}(1m/s)$). The high rms value in V_z does not allow an accurate measurement of such small spanwise fluctuations as shown in the previous section.

The correlation of V_x and v_y' show a similar pattern that is found by Schülein and Trofimov [2011]. A higher V_x domain is measured at spanwise position where the perturbation vectors point towards each other and a lower local V_x domain is measured where the perturbation vectors are pointing away from each other. This corresponds to what is presented in figure 4.22(a) Schülein and Trofimov [2011]. This follows as well from the perturbation plots given in figure 6.22. The velocity fluctuations,v_x' and v_y' are slightly out of phase which is expected based on the image given in figure 4.22(a).

6.11 Flow topology parallel to the 45° ramp

A similar flow description is given for the velocity field parallel to the 45°. During this discussion, the coordinates (x_2, y_2, z_2) given in figure 6 are referred to as (x, y, z) such that x is tangent to the 45° ramp, y the spanwise coordinate and z the normal coordinate, positive pointing away from the model.

During the calibration phase it is noted that the calibration could not be properly aligned with the surface of the 45° ramp. Therefore the calibration plate is rotated around the z-axis. The rotation angle, $\omega = 22°$ is determined during the self-calibration phase and checked with the extra runs taken for measurement validation. The velocity components and the (x, y) domain are therefore rotated to obtain the correct velocity components parallel to the 45° ramp.

The measurement domain is defined 2.2 mm away from the surface of the 45° ramp. In figure 6.23 the contour plot of the total velocity together with the corresponding streamlines are given within the 3D measurement domain.

The streamlines at reattachment indicate a typical pattern of cropped streamlines that diverge and progress into straight longitudinal streaks. This is also found by Schülein and Trofimov [2011] using oil flow visualisation (see figure 4.22(b)). Furthermore, a local low velocity domain near reattachment is observed upstream at $x = -15\ mm$. The primary features of the flow parallel to the 45° ramp are discussed by looking at the streamwise development of the velocity field. The spanwise mean of V_x is plotted in x direction as shown in figure 6.24.

The V_x streamwise distribution indicates velocity drop near the first the second ramp junction due to the reattachment shock at $x > -15mm$. Locally, the velocity parallel to the 45° ramp increases at $x \approx -30mm$. This can be ascribed to the expansion wave which originate from the shock interaction

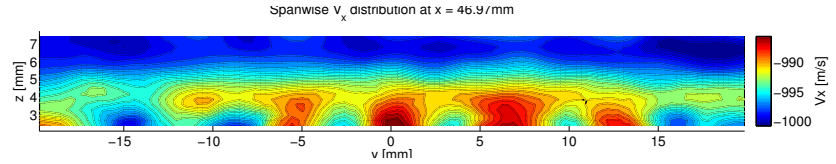

(a) V_x distribution in the (y,z) plane at $x = 47mm$

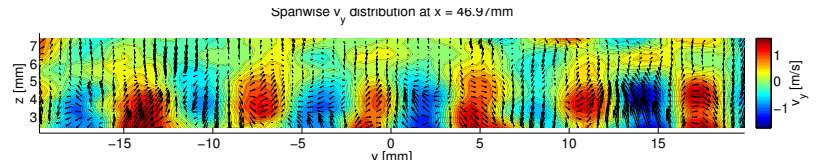

(b) Contour map of v'_y plotted with the v'_y and v'_z (y,z) perturbation vector field at $x = 47mm$

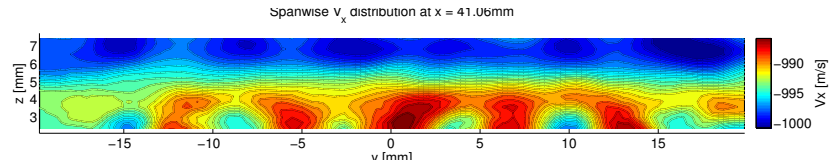

(c) V_x distribution in the (y,z) plane at $x = 41mm$

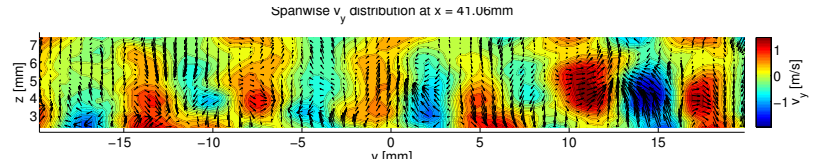

(d) Contour map of v'_y plotted with the v'_y and v'_z (y,z) perturbation vector field at $x = 41mm$

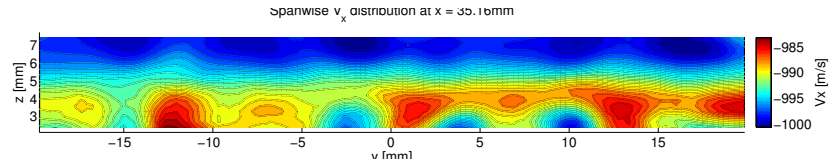

(e) V_x distribution in the (y,z) plane at $x = 35mm$

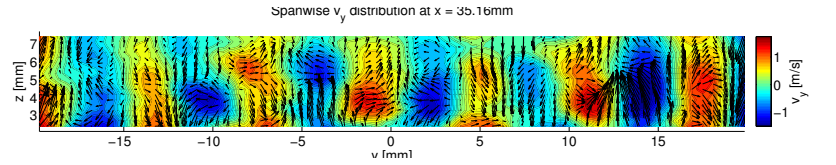

(f) Contour map of v'_y plotted with the v'_y and v'_z (y,z) perturbation vector field at $x = 35mm$

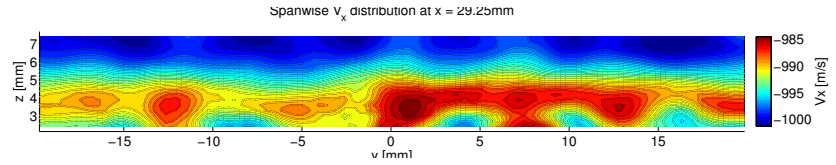

(g) V_x distribution in the (y,z) plane at $x = 29mm$

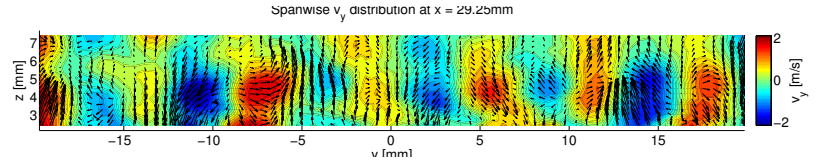

(h) Contour map of v'_y plotted with the v'_y and v'_z (y,z) perturbation vector field at $x = 29mm$

Figure 6.22: Contour map of V_x with its corresponding contour map v'_y for four different fixed streamwise positions on the 5° ramp

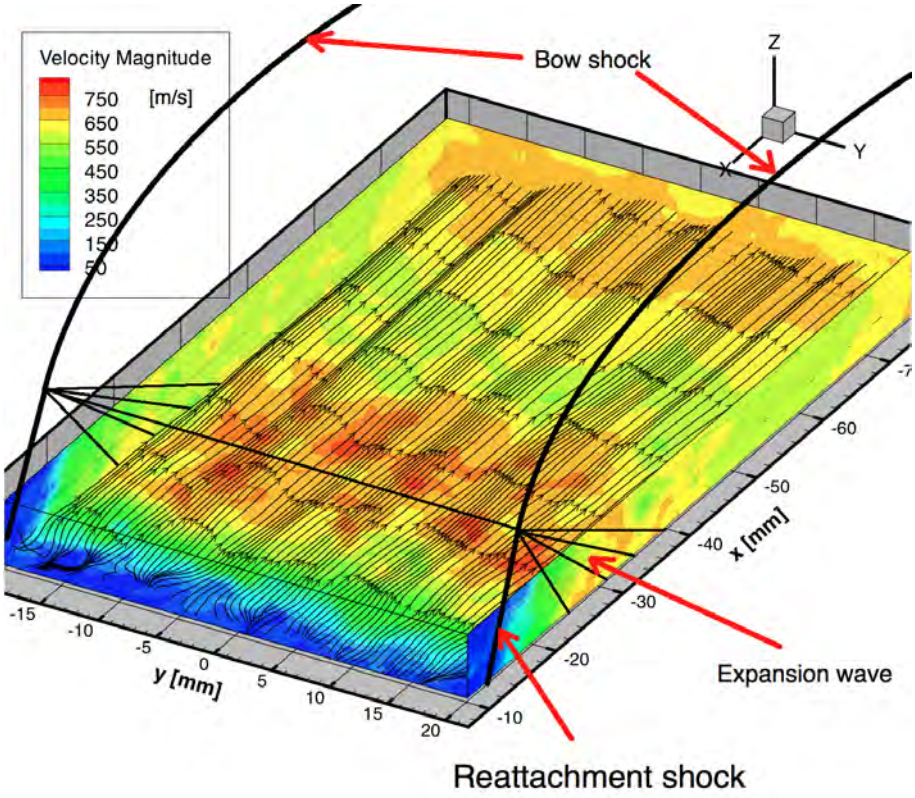

Figure 6.23: Flow overview parallel to the 45° ramp. Velocity magnitude is given in m/s

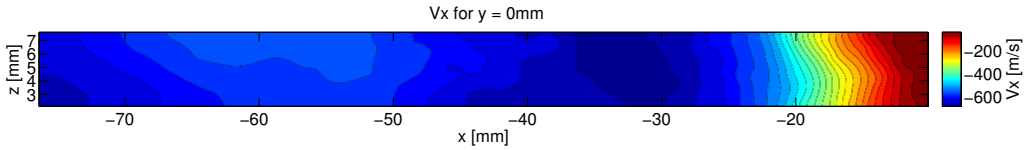

Figure 6.24: The mean streamwise V_x velocity distribution parallel to the 45° ramp

above the 45° ramp. This is further elaborated based on the streamwise wall-normal velocity distribution.

A similar plot is given for V_z in figure 6.25. Note, the two red domains in the streamwise V_z plot given in figure 6.25. It appears, that the flow is locally parallel to the surface ($-30 \leq x \leq -10$). Further downstream it is curved upwards ($-45 \leq x < -30$) after which it is curved back parallel to the wall ($-60 < x \leq -50$). Downstream, at $x > 60mm$, the flow is again curved away from the model. Similar flow behaviour is noticed in figure 4.10. The streamlines parallel to the 45°, shown in figure 4.10, indicate a small bump where the flow is curved away from the model twice. Parallel to the 45° ramp and further downstream behind the bow shock, the flow is curved away from the model which can be seen at the downstream part of the plot where V_z. Here, a gradual increase in V_z is noticed from $V_z \approx 20\ m/s$ at $z = 2.2mm$ to $V_z \approx 35\ m/s$ at $z = 7\ mm$. In figure 4.10, it was noticed that the flow angle increases approximately $3° - 5°$ with respect to the 45° ramp further downstream behind the bow shock. This can be ascribed to the curvature of the shear layer, shown in figure 4.10. The local increase in V_z at $x < 60$ mm is related to this phenomena.

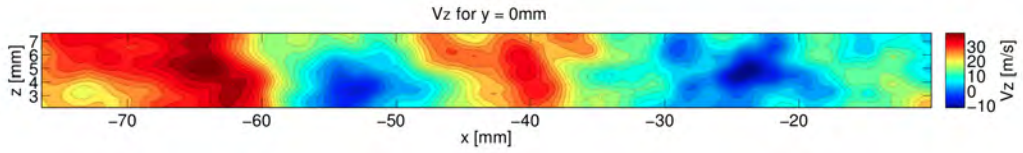

Figure 6.25: The mean streamwise V_z velocity distribution parallel to the 45° ramp

The velocity parallel to the wall (V_x) increases at $-45 \leq x \leq -30mm$ (see figure 6.24) and the velocity component normal to wall (V_z) increases as well (see figure 6.24). The indicates that the flow is curved away from the model with an increase in total velocity. Based on this argument, it is assumed that the velocity field at $-45 \leq x \leq -30mm$ is dominated by the expansion wave that originates from the shock interaction above the 45° ramp.

In figure 6.26, the colour map of V_x is plotted in the (x, y) plane for four fixed z values. In general it can be seen that there is a gentle decrease of V_x when z increases. For V_z the opposite is observed. V_z increases with z in particular at the downstream part of the 45° ramp. Also note the blobs where V_x is locally higher.

Note, the local, relatively high velocity domain at $-40\ mm \leq x \leq -20\ mm$ after which the flow is slowed down and accelerated again. The flow domain $-40\ mm \leq x \leq -20\ mm$ corresponds with the high heat flux domain on the 45° ramp measured using QIRT and shown in figure C.5. An explanation for the local high surface heat flux can therefore be the combination of a local thin boundary layer, and high convective velocity causing a high local high shear stress and thus a high local Stanton number according to Reynold's analogy [Anderson, 2006].

The streamwise velocity component decreases when z increases in particular for $-70\ mm \leq x \leq -45\ mm$ where the velocity decreases from approximately 700 m/s to 550 m/s over a normal distance of 3.4 mm. The V_x velocity profile at $x \approx 30\ mm$ indicates local high velocity blobs but the spanwise fluctuations are in the order of the standard deviation obtained in section 6.7.

The local high V_z at $x \approx 40\ mm$ in figure 6.25 can be found over the the whole width of the model which is shown on the right hand side of figure 6.26. Note two spanwise high V_z domains at $x \approx -40$ mm and $x \approx -65\ mm$. The latter flow domain is dominated by the curved shear layer behind the bow shock.

Again, the fluctuations in the velocity map can not be observed properly due to the high convective velocity scales compared to the perturbation velocity scales (limited dynamic range in V_z). The local spanwise V_y and V_z profile is plotted since these velocity components indicate longitudinal vorticity in the flow. These velocity profiles are filtered using the Stavinsky-Goulay filtering procedure to obtain the spanwise fluctuation distribution v'_x, v'_y and v'_z. The perturbations are plotted next to the absolute

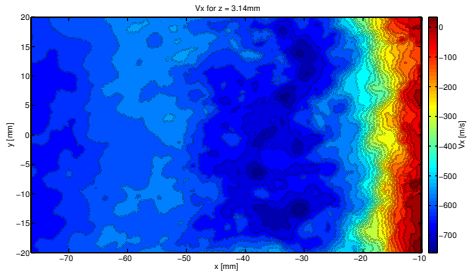

(a) colourmap of the total velocity together with the (x, y) plane velocity component for $z = 3.14mm$

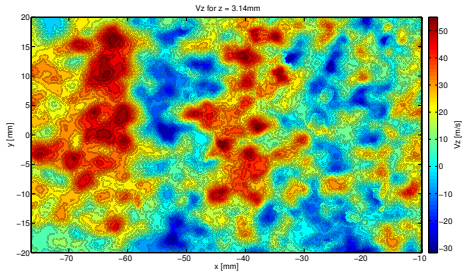

(b) colourmap of the total velocity together with the (x, y) plane velocity component for $z = 3.14mm$

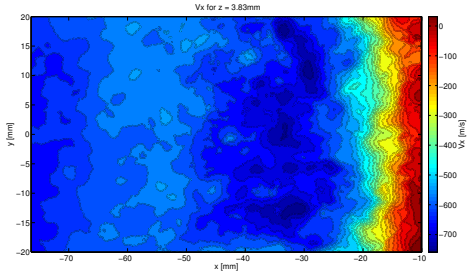

(c) colourmap of the total velocity together with the (x, y) plane velocity component for $z = 3.83mm$

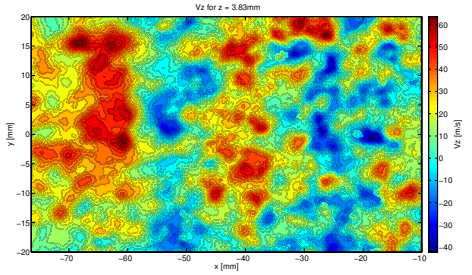

(d) colourmap of the total velocity together with the (x, y) plane velocity component for $z = 3.86mm$

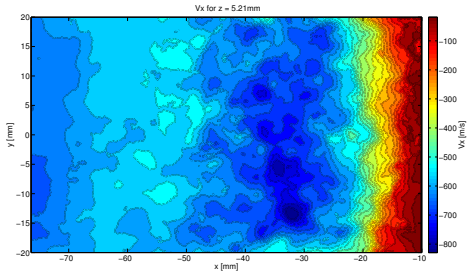

(e) colourmap of the total velocity together with the (x, y) plane velocity component for $z = 5.21mm$

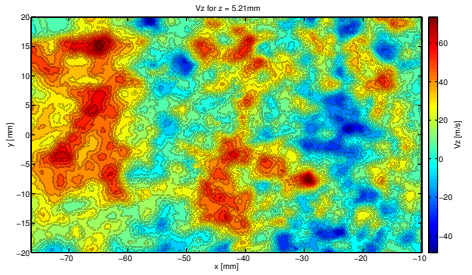

(f) colourmap of the total velocity together with the (x, y) plane velocity component for $z = 5.21mm$

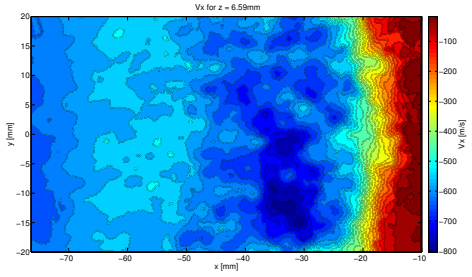

(g) colourmap of the total velocity together with the (x, y) plane velocity component for $z = 6.59mm$

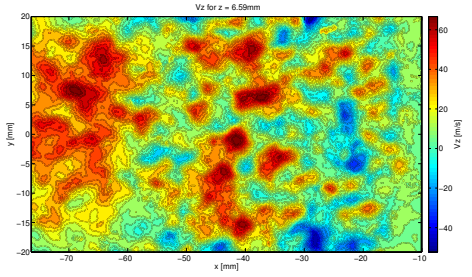

(h) colourmap of the total velocity together with the (x, y) plane velocity component for $z = 6.59mm$

Figure 6.26: Contour map for V_x and V_z for four fixed z positions parallel to the 45° ramp

velocity profiles for various fixed x positions in figure 6.27.

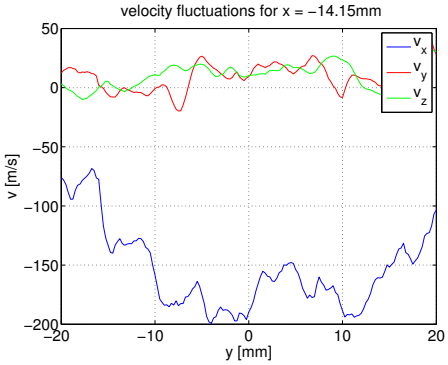

(a) Spanwise V_y and V_z distribution in the middle of (y, z) plane at $x = -14.15mm$

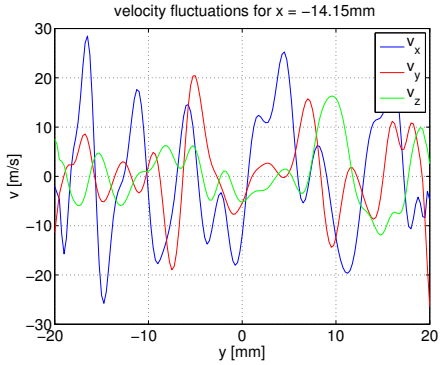

(b) Perturbations v'_y and v'_z distribution in the middle of (y, z) plane at $x = -14.15mm$

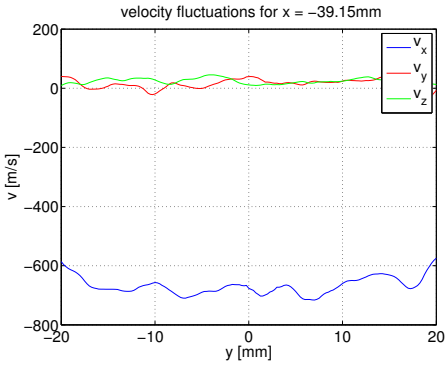

(c) Spanwise V_y and V_z distribution in the middle of (y, z) plane at $x = -39.15mm$

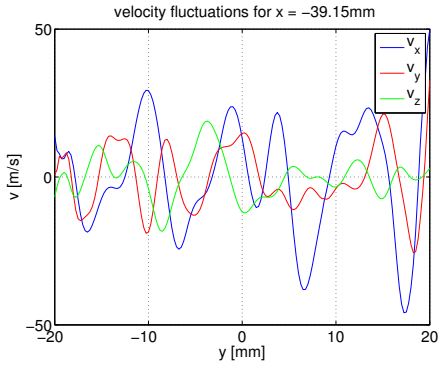

(d) Perturbations v'_y and v'_z distribution in the middle of (y, z) plane at $x = -39.15mm$

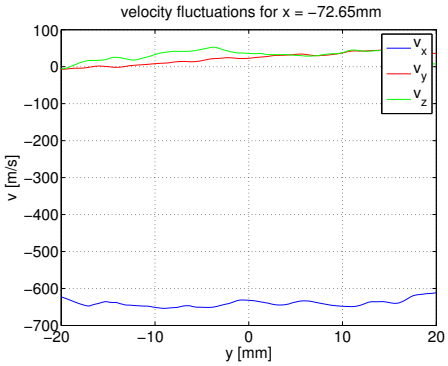

(e) Spanwise V_y and V_z distribution in the middle of (y, z) plane at $x = -72.65mm$

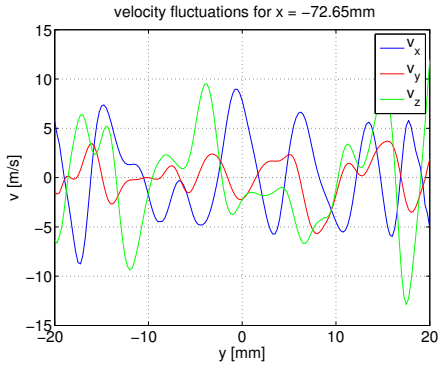

(f) Perturbations v'_y and v'_z distribution in the middle of (y, z) plane at $x = -72.65mm$

Figure 6.27: Spanwise velocity perturbations v'_y and v'_z for four fixed x positions

The complete data set is filtered and smoothened in spanwise direction by taking the local spanwise mean of 10 planes upstream and 10 planes downstream and apply the the Stavinsky-Goulay filter. As a result, v'_x, v'_y and v'_z are obtained. On the left hand side, the spanwise v'_y fluctuations are plotted and on the right hand side the spanwise v'_z fluctuations. Note that clear fluctuations in v'_y are present for $-40\ mm \leq x \leq -10\ mm$ while v'_y decreases for $x \leq 40\ mm$. For v'_z this is not the case. The intensity of the fluctuations at $-40\ mm \leq x \leq 0\ mm$ is also significantly higher but near the wall, the fluctuations in v'_z become larger for the domain $-70\ mm \leq x \leq -40\ mm$.

The colormap of v'_y and v'_z are plotted for four different z position on the left hand side and right

hand side of figure 6.28 respectively.

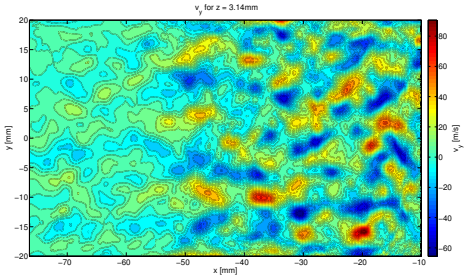

(a) colourmap of the perturbation velocity (v'_y) in the (y, z) plane for $z = 3.14mm$

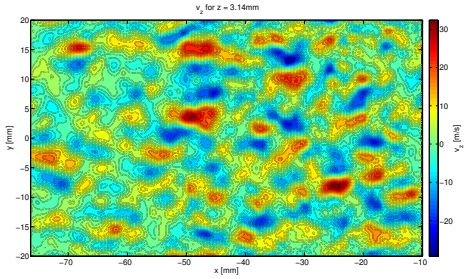

(b) colourmap of the perturbation velocity (v'_z) in the (y, z) plane for $z = 3.14mm$

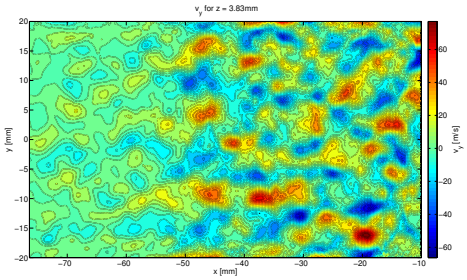

(c) colourmap of the perturbation velocity (v'_y) in the (y, z) plane for $z = 3.83mm$

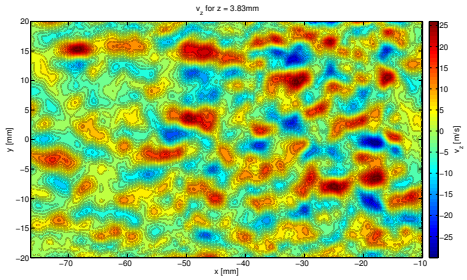

(d) colourmap of the perturbation velocity (v'_z) in the (y, z) plane for $z = 3.83mm$

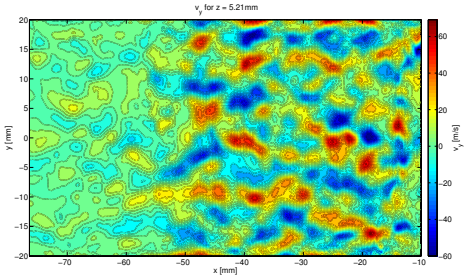

(e) colourmap of the perturbation velocity (v'_y) in the (y, z) plane for $z = 5.21mm$

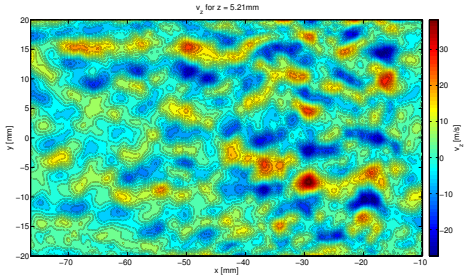

(f) colourmap of the perturbation velocity (v'_z) in the (y, z) plane for $z = 5.21mm$

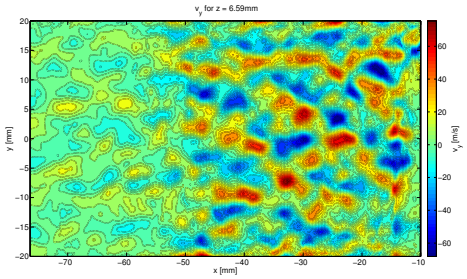

(g) colourmap of the perturbation velocity (v'_y) in the (y, z) plane for $z = 6.59mm$

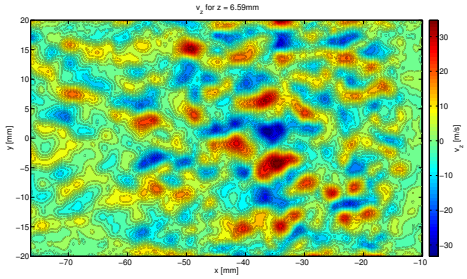

(h) colourmap of the perturbation velocity (v'_z) in the (y, z) plane for $z = 6.59mm$

Figure 6.28: Contour map of the velocity perturbations v'_y and v'_z for four fixed z positions

Both v'_y and v'_z are of the same order. However, it is clear that the map appears to be rather noisy. At $x = -50\ mm$ a clear drop in absolute value for v'_y is noticed for all four z planes. This position corresponds with the last characteristic of the expansion wave that originates from the shock interaction above the 45° ramp. For v'_z, the absolute value for $x < 50\ mm$ and $x > 50\ mm$ seem to be equal and are

in the order of $\mathcal{O}(v_z') \approx \pm 20 m/s$. Based on the error estimation discussed in section 6.7, the v_z' data is not very reliable.

Chapter 7

Conclusions and recommendations

Based on the results presented in chapter 4, 5 and 6, conclusions are drawn regarding the macroscopic and detailed flow topology. Next to that, Tomo-PIV is verified as an applicable measurement technique in the HTFD and recommendations are given for the application of Tomo-PIV for this particular case study presented in this thesis report.

7.1 Conclusions based on the results obtained by QIRT

The QIRT measurements show that there are sinusoidal spanwise heat transfer fluctuations present for the case that a Vortex Generator (VG) is applied. A zigzag VG strip is pasted 25 mm from the leading edge to induce longitudinal vortices and investigate the growth of Görtler vortices. Next to that, the influence of the Reynolds number on the streamwise heat transfer distribution is investigated. It is found that the height of the VG and the Reynolds number both have an influence on the location of boundary layer separation.

A clear heat transfer drop for $h_{zz} = 0$ mm and $h_{zz} = 0.2$ mm is determined which indicates boundary layer separation shown in figure 5.3(a) and 5.3(b). A similar heat transfer drop is noticed for $h_{zz} = 1.15$ mm at $Re_{unit} = 14.1 \times 10^6$ $[m^{-1}]$. Hence, the boundary layer separation takes place at approximately $x = 95$ mm for the undisturbed case while separation occurs at $x = 20$ mm for $h_{zz} = 1.15$ mm at $Re_{unit} = 14.1 \times 10^6$ $[m^{-1}]$. The downstream heat transfer distribution seems monotone for $h_{zz} = 0.4$ mm and $h_{zz} = 0.75$ mm which makes it difficult to obtain a exact location of the boundary layer separation.

The location of reattachment is considered to occur at $x \approx 24$ mm for all test cases. Note the second peak that appears at $x \approx -45$ mm at the second ramp which can be ascribed to local flow compression due to an impinging shock on the model. This second peak reduces for the case that $h_{zz} = 1.15$ mm which can be attributed to the change in shock interaction above the model.

For $h_{zz} = 1.15$ mm and $Re_{unit} = 14.1 \times 10^6$ $[m^{-1}]$ it is interesting to see the formation of secondary wavelength fluctuations further downstream on the first ramp (see figure 5.1(b)). This indicates that the initial vortices break up into smaller longitudinal (vortical) streaks. This phenomena can possible be ascribed to secondary flow instability as described in figure 4.19 and section 4.3. Furthermore, it is observed in figure 5.4, that the absolute amplitude decreases. It seems that within the separated region $x = 20$ mm the heat transfer fluctuations are still present and that the initial wavelength is restored (see figure 5.4(f)).

A spanwise disturbance wavelength of $\lambda = 6$ mm is determined directly downstream of the VG. This corresponds with the wavelength of the VG since $\lambda_{VG} = 6$ mm. For $h_{zz} = 1.15$ mm and $Re_{unit} = 14.1 \times 10^6$ $[m^{-1}]$ $Re_{unit} = 11.3 \times 10^6$ $[m^{-1}]$, the wavelength on the second ramp corresponds with the wavelength determined at the first ramp. This does not hold for the case that $h_{zz} = 0.20$ mm, $h_{zz} = 0.40$ mm and $h_{zz} = 0.75$ mm. The wavelength increases to approximately $10 - 12$ mm. For the lowest Reynolds number and $h_{zz} = 1.15$ mm again a larger wavelength is found while for higher Reynolds numbers a similar wavelength ($\lambda_{zz} = 6$ mm) is observed. This behaviour can be ascribed to a badly pasted VG strip or a combination of low Reynolds number and low VG strip. It has been noticed that secondary disturbances influence the measurement outcome since a significant amplification takes place as shown in

figure 5.7 and 5.8.

The growth rate is defined and determined at fixed streamwise positions for the different VG heights. In figure 5.6, the streamwise growth rate profile for the disturbed test cases are given. The streamwise growth rate profile for the undisturbed flow case is not determined since it is noticed that the spanwise noise dominates the spanwise surface heat flux fluctuations. For the other cases, longitudinal vortices are already induced by the VG at $x = 125\ mm$. Note that the growth rate decreases when h_{zz} increases which can be attributed to the small initial disturbance for a low h_{zz}. The peak for $h_{zz} = 0.20\ mm$ given in figure 5.6 can be ascribed to a secondary disturbance that originates from the VG as described in the previous paragraph.

In figure 5.11, the growth rate is plotted parallel to the 45° ramp. For all test cases, a clear peak is noticed at $x = -20\ mm$. As mentioned before, the flow reattaches at $x = -24\ mm$. Based on the PIV result shown in figure 4.12 can be concluded that the local radius of curvature amplifies the spanwise heat flux distribution significantly, indicating that the longitudinal vortices grow locally. Hence, the measurement outcome corresponds to the predictions made in chapter 4. For all test cases, it seems that the Reynolds number does not effect the position of the peak.

The show case presented in the report ($h_{zz} = 1.15\ mm$ and $Re_{unit}14.1 \times 10^6\ [m^{-1}]$), shows a sinusoidal spanwise heat transfer fluctuation. Furthermore, the longitudinal vortices are spatially stable and no movement occurs in spanwise direction. Therefore, this case is investigated in detail using Tomographic Particle Image Velocimetry (Tomo-PIV).

7.2 Conclusion regarding the application of Tomo-PIV in the HTFD

Tomo-PIV is applied in the HTFD for first time. Hence several validation steps were carried out to determine the specific measurement capacities. As stated in Elsinga [2008], the quality of the reconstruction is dependent on the geometry of the measurement set-up (viewing angles, Particle Per Voxel (ppv) and light refraction etc). Refraction has been taken into account since it was found during the self calibration procedure that this has a significant influence on the measurement outcome. Due to the pressure difference (ambient outside and vacuum inside the test section), light refraction takes place and a pixel displacement of approximately 1.2 pixel was found theoretically. Experimentally, a pixel shift of approximately 3 pixels was found for the first camera while the pixel shift for the other two cameras was significantly lower. This corresponds with theoretically found pixel deviations. The self calibration has to be performed on the residual images of the run.

The laser sheet is aligned with the surface of the model. Due to reflections on the surface, the height of the laser sheet with respect to the model can be measured more accurately. During the reconstruction procedure a peak is found in the mean light intensity distribution at the z location of the surface of the model such that the distance between the laser sheet edge and the surface of the model can be measured in the order of $10^{-1}\ mm$.

The particle density distribution varies due to the particle slip induced by the present shocks. However, in general, a *ppv* of 0.018 is found which lies within the acceptable range found by Elsinga [2008].

Streamwise longitudinal vorticity is expected and therefore the fluctuation s in the (y, z) plane are of main interest. Hence the (y, z) measurement fluctuations are of critical importance for the measurement accuracy. For this reason, one test run is carried out during which the model is removed from the test section. A uniform undisturbed flow field is expected dependent on the laser sheet geometry as described in chapter 6. the measurement fluctuations are then determined by looking at the in plane standard deviation for the three velocity components. It was found that the standard deviation for V_z is significantly higher than for V_x and V_y. The values are given in table 7.1:

The relatively high mean V_z velocity is due to the fact that the laser sheet is 5° rotated towards the camera set-up. It can be concluded that the standard deviation in V_z is approximately 3 times higher than for V_x and V_y. This is ascribed to an elongated particle shape in z-direction as shown in figure 6.15. This

Table 7.1: Standard deviation and mean for every velocity component in the (y, z) plane for the presented test case

	$std[m/s]$	$mean[m/s]$	$std[\%]$
V_x	5.6	1008	0.6
V_y	6.2	77.5	8.0
V_z	17.4	109.7	15.9

widens the correlation peak causing an inaccurate sub-pixel velocity determination. Furthermore, the dynamic range in z direction is limited due to the high convective velocity in x direction ($0 \leq V_x \leq 1000$ m/s while $30\ m/s \leq V_z \leq 30\ m/s$). Due to the high V_x a relatively short time separation of$\Delta\ t = 2 \times 10^{-6}$ s is used. As a consequence, the relative particle displacement in pixels in z direction is in the order of one pixel (see equation 6.14).

A similar procedure is performed for the measurement domain parallel to the second ramp only this time, the model is present in the test section. By moving the model further back, the distance between the laser sheet and the surface of the model is increased such that a far field velocity field is measured. Unfortunately, the measurement was disturbed by the presence of the bow shock. The rms value is determined upstream and downstream of the shock, as shown in figure 6.14(b). Note that the rms downstream of the shock is significantly smaller than upstream of the shock (see figure 6.14(b)). At $x = -50\ mm$ a clear peak in the rms of V_x and V_y can be seen which is caused by the rather inaccurate measurement of the velocity due to the presence of the shock. Downstream of the shock, the rms value of V_y and V_z are approximately 16 m/s and for V_x the rms is slightly higher ($\sigma_{V_x} = 26\ m/s$). Downstream of the shock the mean velocity is approximately 1000 m/s and the rms values are:

Table 7.2: Standard deviation and mean for every velocity component in the (y, z) plane for the presented test case

	Upstream of the shock			**Downstream of the shock**		
	$mean[m/s]$	$std[m/s]$	$std[\%]$	$mean[m/s]$	$std[m/s]$	$std[\%]$
V_x	-441	26.5	6	963	59	6
V_y	177	16.3	9.2	385	38	10
V_z	-2.9	16.3	565	-41	45	110

Due to the limited optical accessibility, the quality of the outcome for the velocity field parallel to the second ramp is relatively poor compared to the measurement domain parallel to the first ramp. This can be attributed to the large viewing angles with respect the z-axis of the measurement domain. Especially the cameras which are vertically aligned with each other make a large viewing angle and therefore a poor triangulation is performed during the reconstruction procedure. A large optical axis means a large amount of ghost particles and thus a bad particle triangulation. On the other hand, the camera on the side makes a rather small viewing angle which on its turn causes a poor depth resolution which again can be seen in the poor quality of the measurement of V_z.

Furthermore, the pixel displacement en x and y direction is in the order $\mathcal{O}(25)$ and $\mathcal{O}(12)$ respectively while the pixel displacement in z direction is in the order of one pixel. This is due to the small time separation$\Delta\ t = 2\mu s$ and the low velocity in z direction. The measurement noise is therefore dominating in this particular direction.

7.3 Conclusion regarding the detailed flow topology of the 5°-45° ramp

The velocity field measured parallel to the first ramp shows clear spanwise longitudinal fluctuations in V_x and V_y. Coherent spanwise V_x domains are determined with a spanwise gradient of approximately 10 m/s

(see figure 6.22. This is approximately 1 % of the convective streamwise velocity component. By filtering the spanwise velocity (V_y) component in spanwise direction, the fluctuations (v'_y) are determined. The amplitude with respect to the mean spanwise V_y distribution is measured to be 1 m/s. This indicates that the rotation in the (y, z) has a very low intensity and the initial disturbance can be considered as weak. The fluctuations in V_z are expected to be of the same order. Based on the validation run, it can be concluded that the standard deviation of V_z is too large to measure such small fluctuations. The ability of this set-up to measure the three dimensionality of the flow is limited by the large standard deviation in V_z.

The percentages given in table 6.6 correspond with the found fluctuations parallel to the first ramp. Typical fluctuations of 10 m/s in V_x and 1 m/s in V_y which are 1% and 10% with respect to their corresponding convective velocity components. The fluctuations that were measured are therefore valid.

Based on figure 6.22 clear spanwise wakes can be seen which correspond to the expected v'_y distribution. Conclusions can be drawn based on the three dimensional V_x and V_y velocity field. The correlation between V_x and v'_y looks similar to what is discussed by Schülein and Trofimov [2011] and in section 4.3 regarding counter rotating vortices emanating from the VG tips. A higher V_x domain is measured at spanwise position where the perturbation vectors converge. The high momentum flow domain is pushed towards the surface causing a high velocity streak. A lower local V_x domain is measured where the perturbation vectors diverge and point away from the model. This corresponds to what is presented in figure 4.22(a) Schülein and Trofimov [2011].

Some of the main flow features parallel to the second ramp could be captured such as the high velocity domain for both V_x and V_z. This indicates the presence of an expansion wave which was also predicted during the theoretical analysis presented in chapter 4.

Again local fluctuations where measured in V_x and V_y but the outcome for V_z seems rather noisy and not reliable. The spanwise fluctuations in V_y are present locally ($x = -39.15$ mm and even further downstream $x = -72.65$ mm, see figures 6.27(b)-6.27(e)). Based on the absolute values of the v'_y it can be concluded that the local fluctuations are reliable and in the order of 20 m/s and locally even nearly 50 m/s. This indicates that there is a significant increase of longitudinal vorticity if it is assumed that v'_z and v'_y are of the same order. The spanwise fluctuations parallel to the first ramp where in the order of 1 m/s while the spanwise fluctuations parallel to the second ramp are in the order of 20 m/s (based on the v'_y distribution).

The higher c_h domains on the second ramp can be ascribed to the locally high V_x velocity component and thus a locally high kinetic energy . Corresponding high velocity blobs were found in the V_x colourmap given in figure 6.23 and 6.26. These local high V_x regions induce a local high friction coefficient which is directly proportional to the Stanton number. Due to the lack of a larger amount of measurement samples, this is not as clear as expected.

7.4 Recommendations

At first it is recommended to perform more runs to obtain more statistical data. Since the measurement time is short, the tuning of the tunnel and the camera set-up is rather rough. It can happen that an image is taken which is near the end of the run which is indicated by the poor particle distribution. This makes the measurement campaign time consuming.

Regarding the accuracy of Tomo-PIV is the HTFD, the blurring effect and particle stretching needs to be further investigated. The effect of particle stretching in the out of plane direction on the volume reconstruction requires further attention. Hence, based on the currently used Tomo-PIV measurement configuration, it is recommended to investigate the influence of aero-optical disturbances present during the current experiment. The change in particle shape induced by the refractive index changes due to the presence of shocks has been investigated by Elsinga [2005]. However, this investigation considered an oblique shock wave measured by 2C-PIV. So far, no error estimations are obtained regarding the current Tomo-PIV experiments.

Furthermore, it is recommended to perform Schlieren experiments with a pulsed light source to identify the small scale shock structures near the 45° ramp. In this way a better correlation can be made

between the shock pattern and the velocity field measured by means of Tomo-PIV.

Görtler vortices are induced by the centrifugal forces associated with the change in direction of motion forced on the fluid by the geometry of the surface. To obtain the three dimensional flow behaviour it is proposed to use a model with a fixed radius of curvature like Luca de et al. [1993]. It is noticed that the flow direction angle is abruptly changed for hypersonic double compression ramp flow such that the flow is not gradually curved. No fixed radius of curvature is present which effects the persistence of Görtler vortices in hypersonic double compression ramp flow. It has been noticed, that the development of Görtler vortices is a local phenomena in hypersonic double ramp flow. For fundamental research regarding Görtler vortices in hypersonic flow, it is therefore recommended to used a model with a fixed radius of curvature.

During the current experiments it is attempted to measure spatially steady longitudinal vortices over a double ramp. For Tomo-PIV, it is therefore suggested, to perform measurements with the high-speed measurement set-up (high speed laser, high speed cameras). In this way, the time development of the longitudinal streaks can be determined and more statistical data can be acquired to obtain a nice converging mean 3D velocity field.

Appendix A

The three separate FOV for 2C-PIV

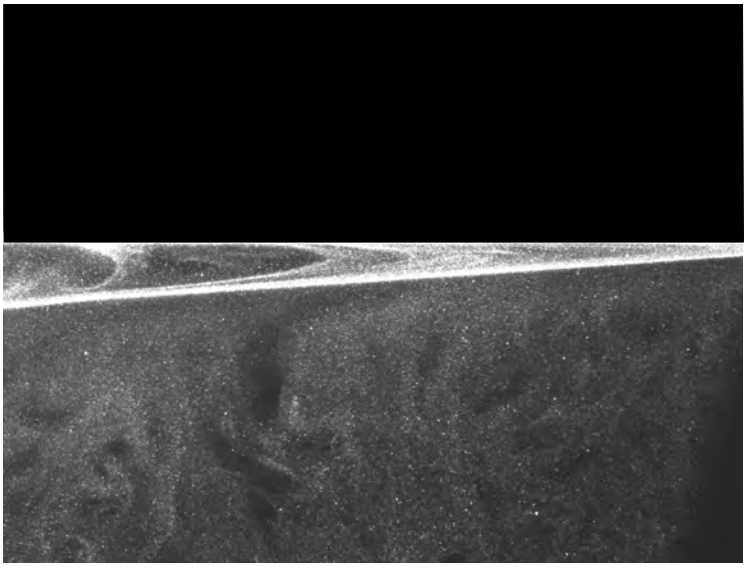

(a) Particle intensity image at the first ramp which is aligned with the x axis

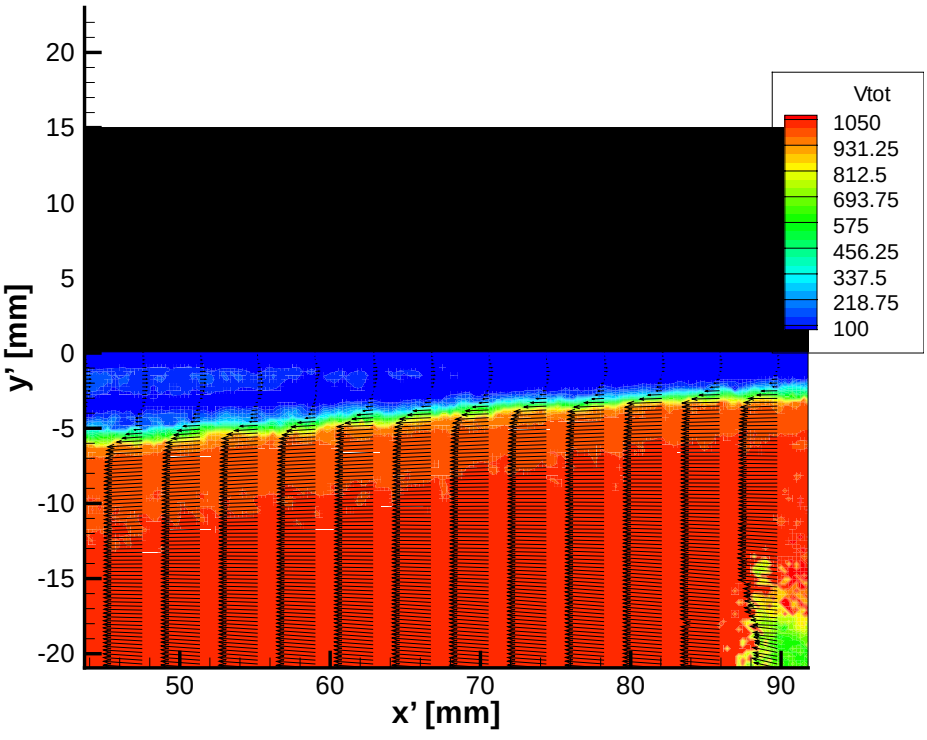

(b) Mean velocity field at the first ramp which is aligned with the x axis

Figure A.1: Sample of a raw PIV images and the corresponding mean velocity field for the first FOV

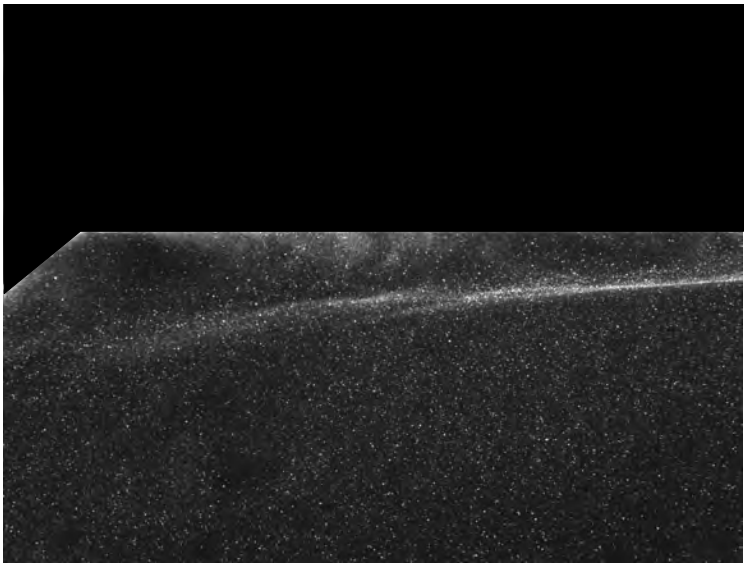

(a) Particle intensity image at the first ramp which is aligned with the x axis

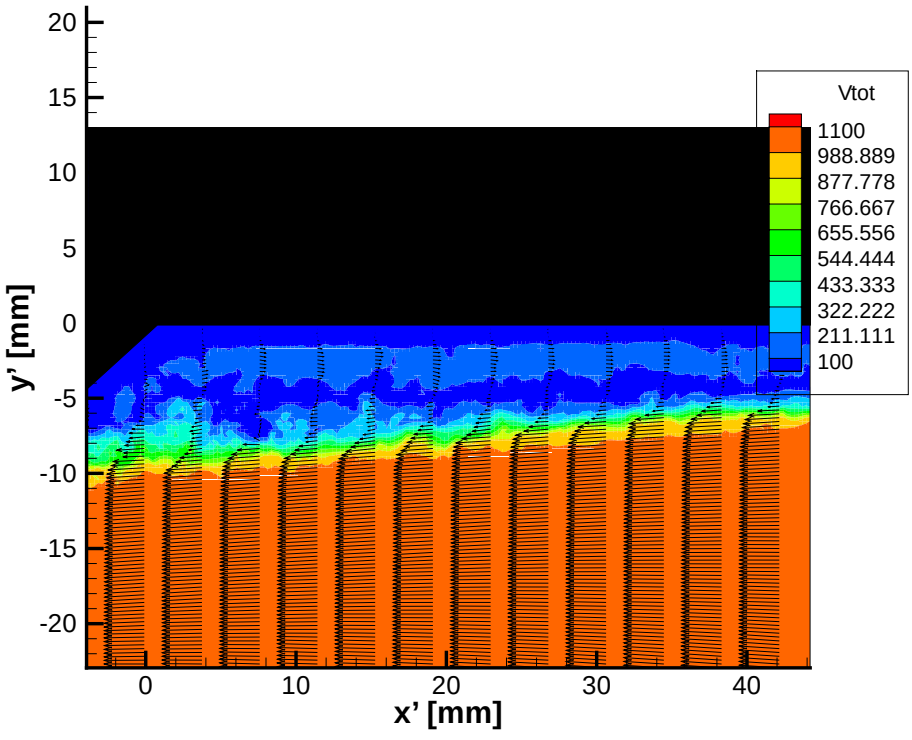

(b) Mean velocity field at the first ramp which is aligned with the x axis

Figure A.2: Sample of a raw PIV images and the corresponding mean velocity field for the second FOV

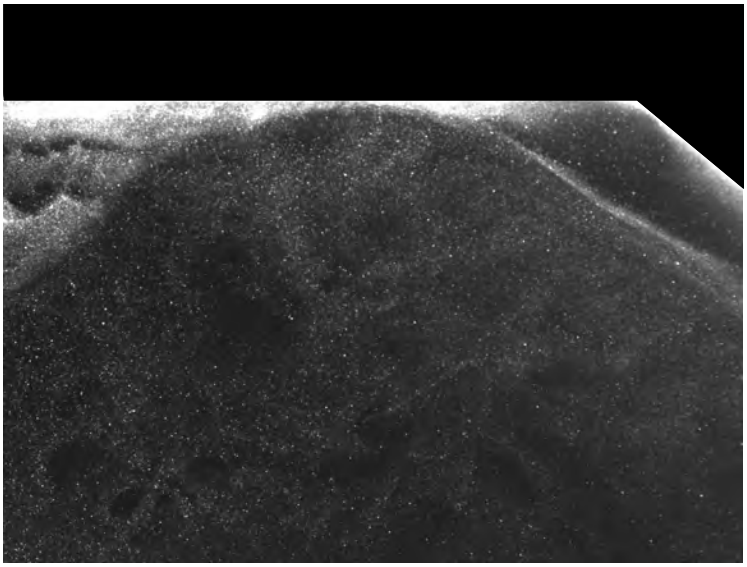

(a) Particle intensity image at the second ramp which is aligned with the x axis

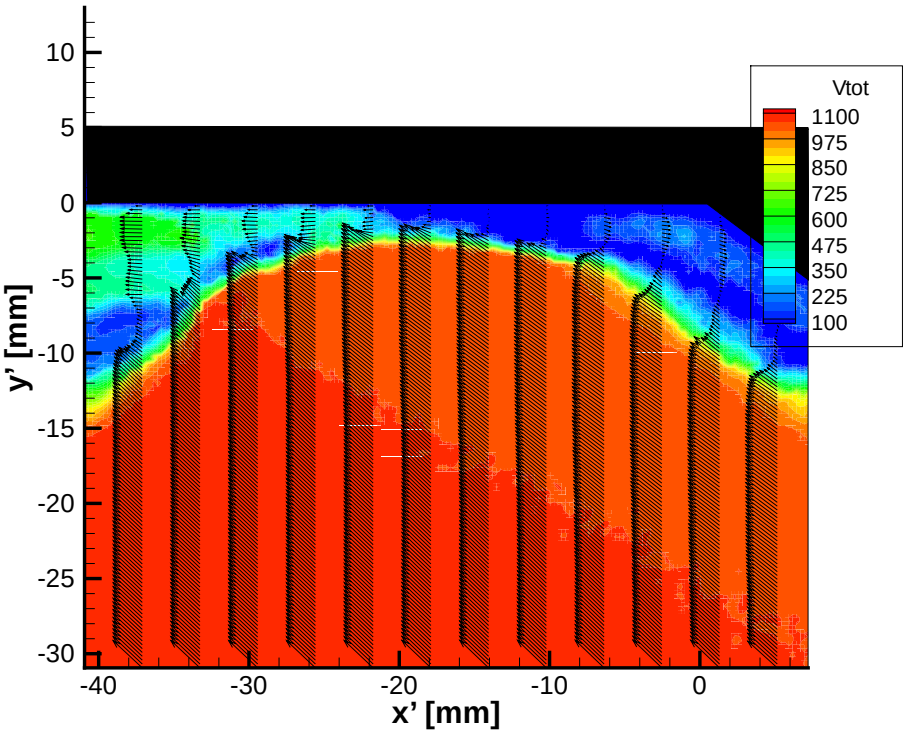

(b) Mean velocity field at the second ramp which is aligned with the x axis

Figure A.3: Sample of a raw PIV images and the corresponding mean velocity field for the third FOV

Appendix B

Derivation of the entries $(L_{11}, L_{12}, L_{21}, L_{22})$ of the local stability eigenvalue problem

Starting off from the perturbation equations 4.25-4.28 obtained from the order analysis shown in section **??** and substituting $(u, v, w, p) = (\bar{u}(y), \bar{v}(y), \bar{w}(y), \bar{p}(y))e^{\sigma x + i\beta z}$ for the purtubated quantities gives:

$$\sigma\bar{u} + D\bar{v} + i\beta\bar{w} = 0 \tag{B.1}$$

$$\sigma U\bar{u} + U_x\bar{u} + VD\bar{v} + U_y\bar{v} = D^2\bar{u} - \beta^2\bar{u} \tag{B.2}$$

$$\sigma U\bar{v} + V_x\bar{u} + VD\bar{v} + V_y\bar{v} = -D\bar{p} + D^2\bar{v} - \beta^2\bar{v} - 2G^2U\bar{u} \tag{B.3}$$

$$\sigma U\bar{w} + VD\bar{w} = -i\beta\bar{p} + D^2\bar{w} - \beta^2\bar{w} \tag{B.4}$$

The D stands for derivative with respect to the normal coordinate y. From this point, $\bar{w}$ and $\bar{p}$ can be eliminated using cross differentiation of equation B.3 and B.4 and substituting the obtained expression for $\bar{w}$ in terms of $\bar{u}$ and $\bar{v}$ into equation B.1. First equation B.4 is differntiated with respect to Y which will give:

$$\sigma U_y\bar{w} + \sigma UD\bar{w} + V_yD\bar{w} + VD^2\bar{w} - D^3\bar{w} + \beta^2D\bar{w} = -Di\beta\bar{p} \tag{B.5}$$

and differentiating equation B.3 with respect to Z and eliminate the the terms where U and V are differentiated w.r.t Z:

$$\sigma Ui\beta\bar{v} + V_xi\beta\bar{u} + VDi\beta\bar{v} + V_yi\beta\bar{v} - D^2i\beta\bar{v} + \beta^2i\beta\bar{v} + 2G^2U_z\bar{u} + 2G^2Ui\beta\bar{u} = -Di\beta\bar{p} \tag{B.6}$$

With equation B.5 and B.6, $\bar{w}$ can be expressed in terms of $\bar{v}$ and $\bar{u}$ and substituted in equation B.1:

$$\begin{aligned} \bar{u}\left\{-V_x\beta^2 - 2G^2U\beta^2 + \sigma^2U_y + \sigma^2UD + \sigma V_yD + VD^2\sigma - D^3\sigma + D\beta^2\sigma\right\} \\ +\bar{v}\left\{-(D^2-\beta^2)^2 + \sigma U(D^2-\beta^2) + VD(D^2-\beta^2) + V_y(D^2-\beta^2) + D\sigma U_y\right\} = 0 \end{aligned} \tag{B.7}$$

This expression can be simplified by differentiating equation B.2 with respect to Y and multiply by σ

and taking continuity equation ($U_x = -V_y$) into account, it can be seen that several terms can be written in terms of the mean stream velocities:

$$\begin{aligned} \sigma\left(V_{yy} + DV_y\right)\bar{u} &= \bar{u}\left(\sigma^2U_y + \sigma UD + \sigma V_yD + \sigma VD^2 - D^3\sigma + \beta^2D\sigma\right) + \bar{v}\left(U_{yy} + \sigma U_yD\right) \\ \rightarrow \bar{u}\sigma\left(V_{yy} + V_yD\right) - \bar{v}\sigma U_{yy} &= \bar{u}\left(\sigma^2U_y + \sigma UD + \sigma VD^2 - D^3\sigma + \beta^2D\sigma\right) + \sigma DU_y\bar{v} \end{aligned} \tag{B.8}$$

The right hand side of equation B.8also shows up on the right hand side of equation B.7 and thus the

final equation will look like:

$$\begin{aligned} \bar{u}\left\{-V_x\beta^2 - 2G^2U\beta^2 + \sigma\left(V_{yy} + V_yD\right)\right\} \\ +\bar{v}\left\{-(D^2-\beta^2)^2 + \sigma U(D^2-\beta^2) + VD(D^2-\beta^2) + V_y(D^2-\beta^2) - \sigma U_{yy}\right\} = 0 \end{aligned} \tag{B.9}$$

which are the entries L_{11} and L_{12} of the linear operator discussed in chapter 4. The entries L_{21} and L_{22} follow directly from equation B.2.

Appendix C

Heat transfer distribution mapped on the physical coordinates

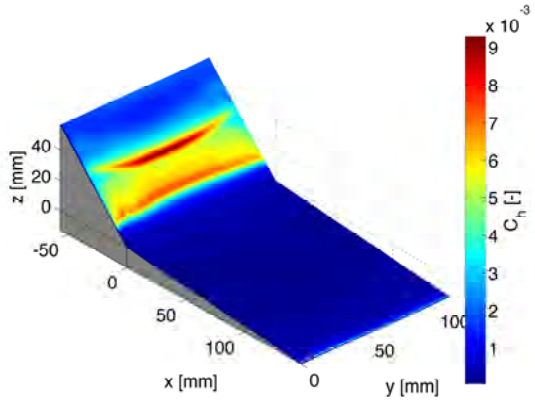

(a) The heat transfer mapped on the surface coordinate system for the case $h_{zz} = 0mm$, $Re = 8.47 \times 10^6\ m^{-1}$

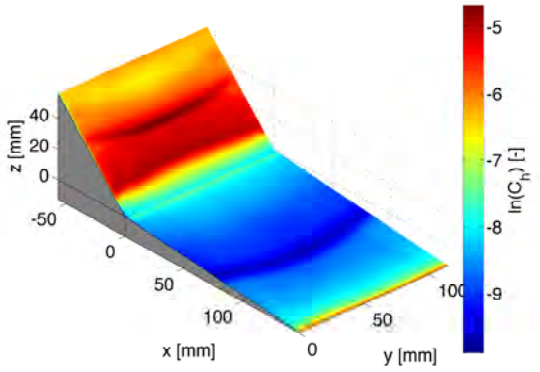

(b) The logarithm of the Stanton number (c_h) mapped on the surface coordinate system for the case $h_{zz} = 0mm$, $Re = 8.47 \times 10^6\ m^{-1}$

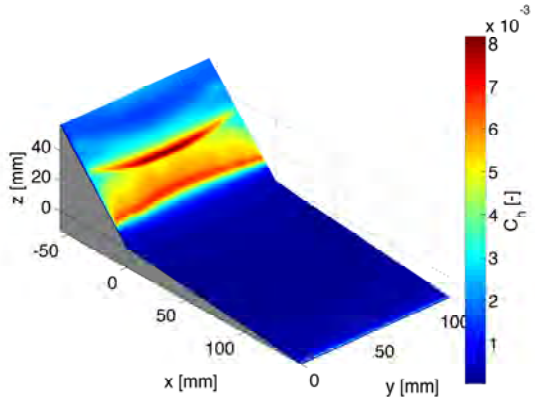

(c) The heat transfer mapped on the surface coordinate system for the case $h_{zz} = 0mm$, $Re = 11.3 \times 10^6\ m^{-1}$

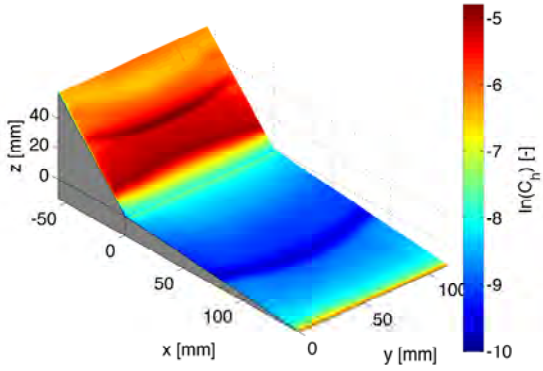

(d) The logarithm of the Stanton number (c_h) mapped on the surface coordinate system for the case $h_{zz} = 0mm$, $Re = 11.3 \times 10^6\ m^{-1}$

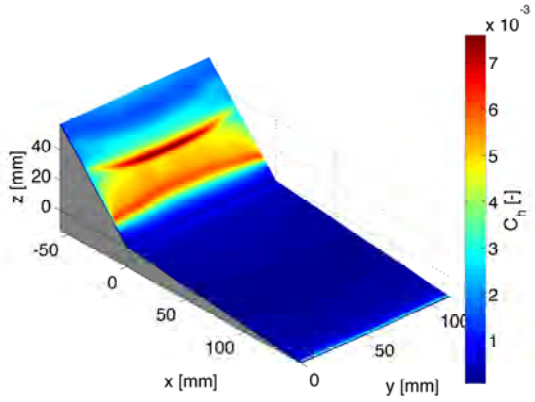

(e) The heat transfer mapped on the surface coordinate system for the case $h_{zz} = 0mm$, $Re = 14.1 \times 10^6\ m^{-1}$

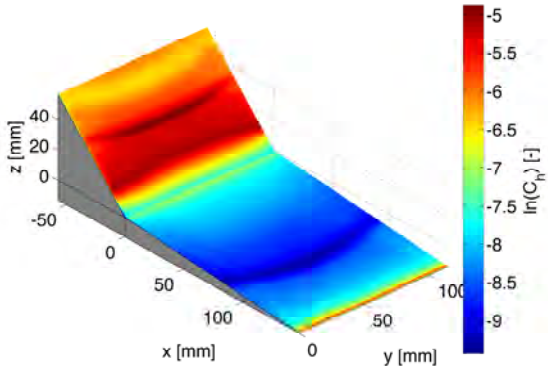

(f) The logarithm of the Stanton number (c_h) mapped on the surface coordinate system for the case $h_{zz} = 0mm$, $Re = 14.1 \times 10^6\ m^{-1}$

Figure C.1: The Stanton number (c_h) plotted on the physical model coordinates for the three Reynolds numbers and $h_{zz} = 0\ mm$

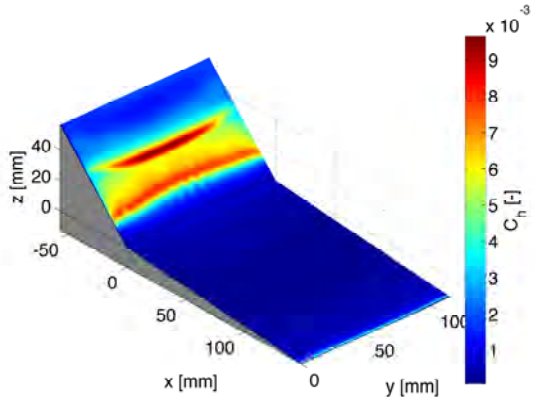

(a) The heat transfer mapped on the surface coordinate system for the case $h = 0.2mm$, $Re = 8.47 \times 10^6\ m^{-1}$

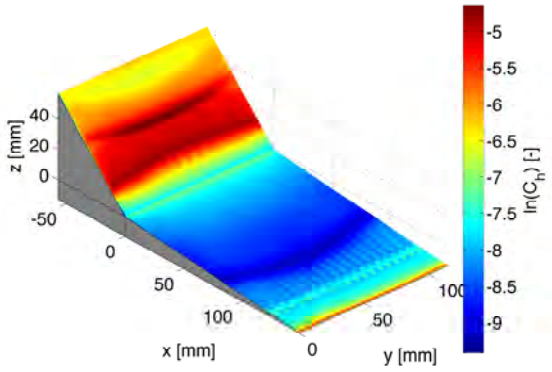

(b) The logarithm of the Stanton number (c_h) mapped on the surface coordinate system for the case $h_{zz} = 0.2mm$, $Re = 8.47 \times 10^6\ m^{-1}$

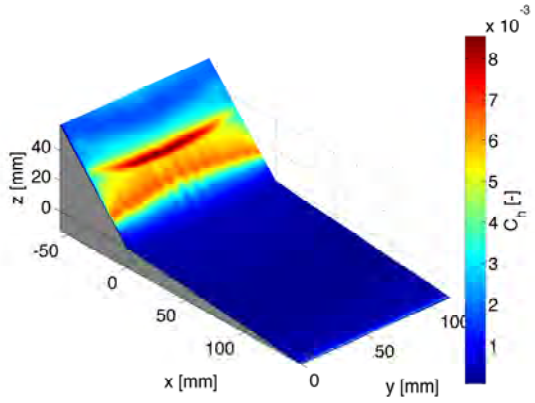

(c) The heat transfer mapped on the surface coordinate system for the case $h = 0.2mm$, $Re = 11.3 \times 10^6\ m^{-1}$

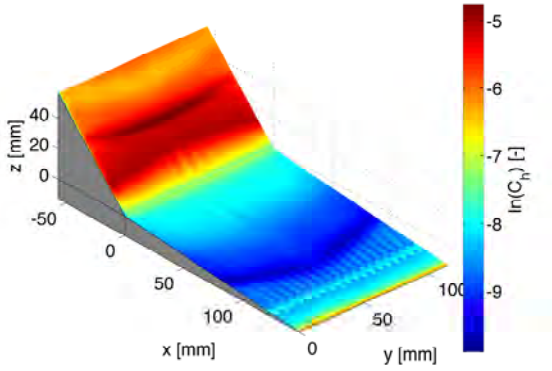

(d) The logarithm of the Stanton number (c_h) mapped on the surface coordinate system for the case $h_{zz} = 0.2mm$, $Re = 11.3 \times 10^6\ m^{-1}$

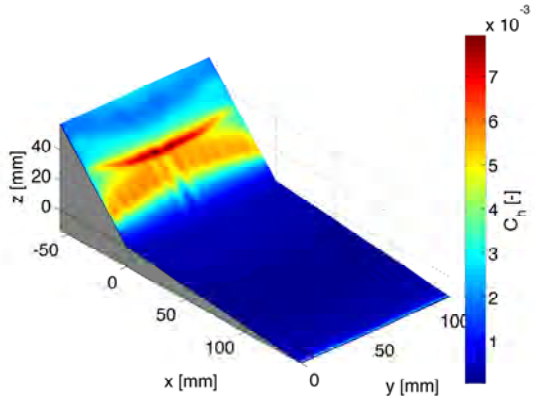

(e) The heat transfer mapped on the surface coordinate system for the case $h = 0.2mm$, $Re = 14.1 \times 10^6\ m^{-1}$

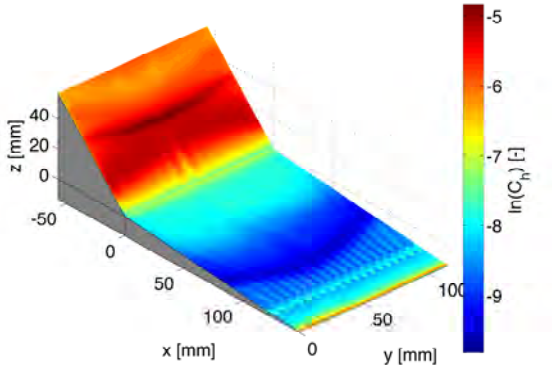

(f) The logarithm of the Stanton number (c_h) mapped on the surface coordinate system for the case $h_{zz} = 0.2mm$, $Re = 14.1 \times 10^6\ m^{-1}$

Figure C.2: The Stanton number (c_h) plotted on the physical model coordinates for the three Reynolds numbers and $h_{zz} = 0.20\ mm$

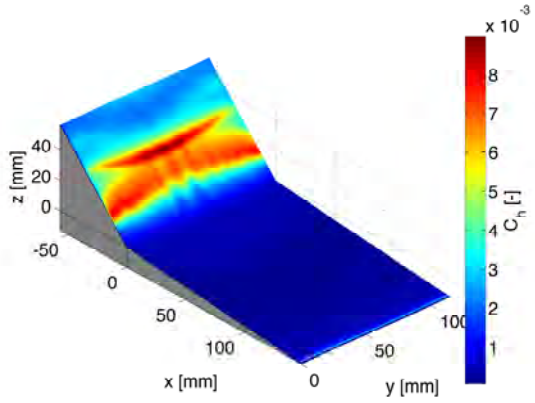

(a) The heat transfer mapped on the surface coordinate system for the case $h = 0.4mm$, $Re = 8.47 \times 10^6\ m^{-1}$

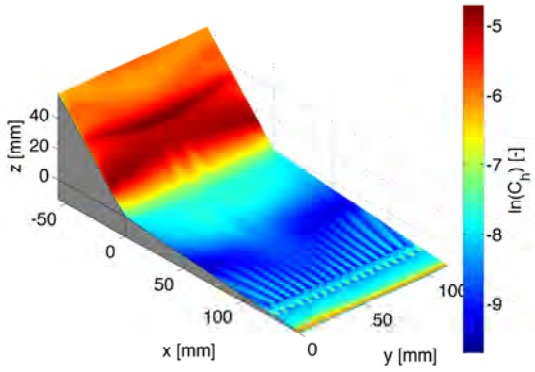

(b) The logarithm of the Stanton number (c_h) mapped on the surface coordinate system for the case $h_{zz} = 0.4mm$, $Re = 8.47 \times 10^6\ m^{-1}$

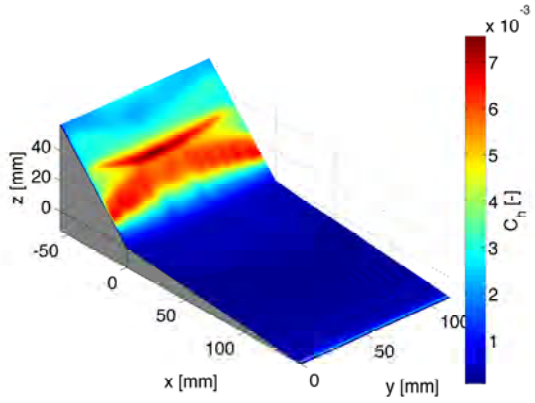

(c) The heat transfer mapped on the surface coordinate system for the case $h = 0.4mm$, $Re = 11.3 \times 10^6\ m^{-1}$

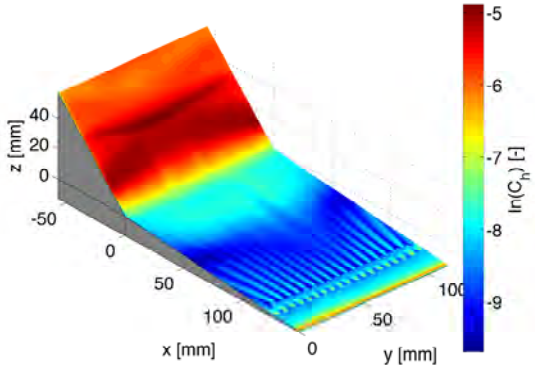

(d) The logarithm of the Stanton number (c_h) mapped on the surface coordinate system for the case $h_{zz} = 0.4mm$, $Re = 11.3 \times 10^6\ m^{-1}$

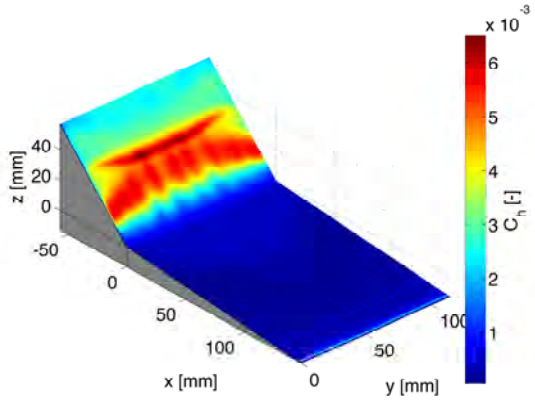

(e) The heat transfer mapped on the surface coordinate system for the case $h = 0.4mm$, $Re = 14.1 \times 10^6\ m^{-1}$

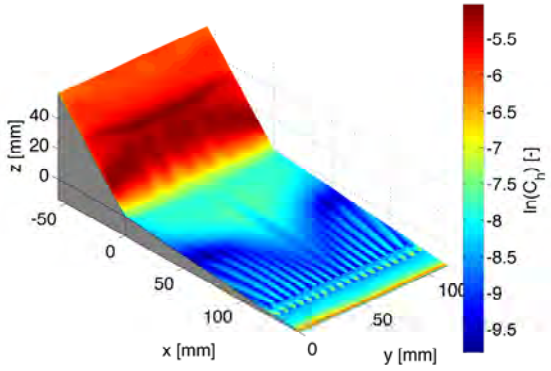

(f) The logarithm of the Stanton number (c_h) mapped on the surface coordinate system for the case $h_{zz} = 0.4mm$, $Re = 14.1 \times 10^6\ m^{-1}$

Figure C.3: The Stanton number (c_h) plotted on the physical model coordinates for the three Reynolds numbers and $h_{zz} = 0.40\ mm$

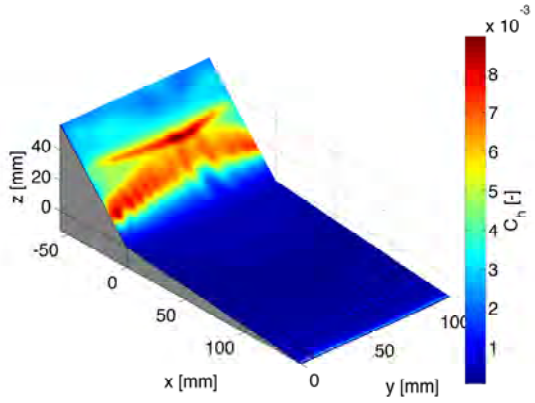

(a) The heat transfer mapped on the surface coordinate system for the case $h = 0.75mm$, $Re = 8.47 \times 10^6\ m^{-1}$

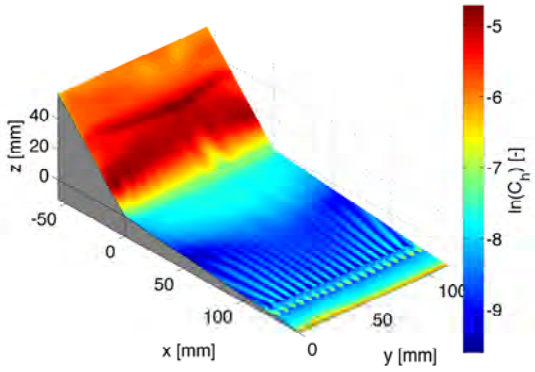

(b) The logarithm of the Stanton number (c_h) mapped on the surface coordinate system for the case $h_{zz} = 0.75mm$, $Re = 8.47 \times 10^6\ m^{-1}$

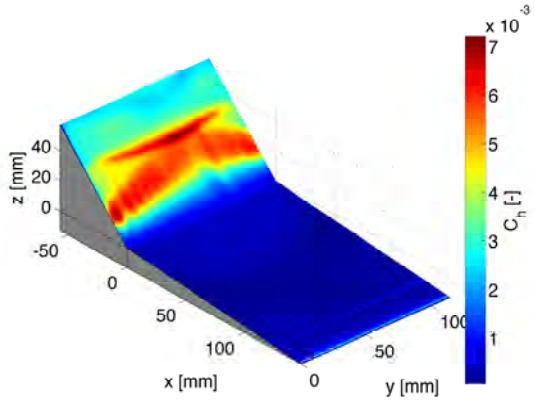

(c) The heat transfer mapped on the surface coordinate system for the case $h_{zz} = 0.75mm$, $Re = 11.3 \times 10^6\ m^{-1}$

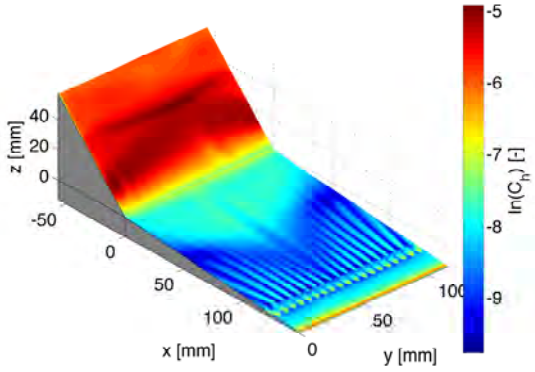

(d) The logarithm of the Stanton number (c_h) mapped on the surface coordinate system for the case $h_{zz} = 0.75mm$, $Re = 11.3 \times 10^6\ m^{-1}$

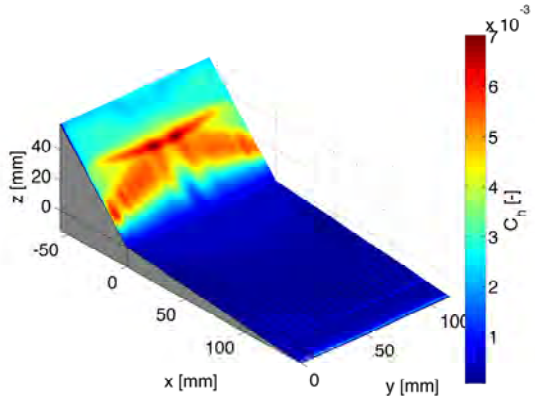

(e) The heat transfer mapped on the surface coordinate system for the case $h = 0.75mm$, $Re = 14.1 \times 10^6\ m^{-1}$

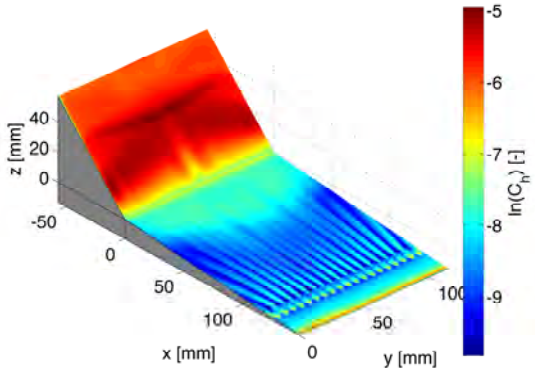

(f) The logarithm of the Stanton number (c_h) mapped on the surface coordinate system for the case $h_{zz} = 0.75mm$, $Re = 14.1 \times 10^6\ m^{-1}$

Figure C.4: The Stanton number (c_h) plotted on the physical model coordinates for the three Reynolds numbers and $h_{zz} = 0.75\ mm$

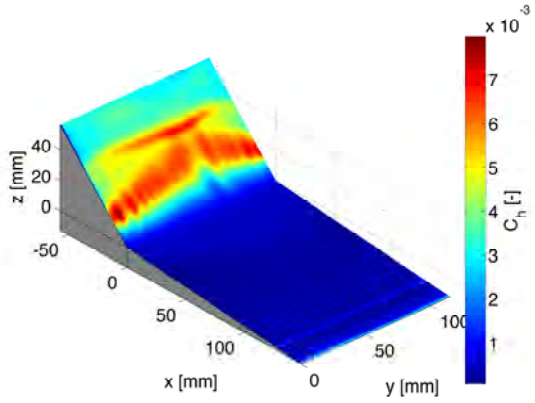

(a) The heat transfer mapped on the surface coordinate system for the case $h = 1.15mm$, $Re = 8.47 \times 10^6\ m^{-1}$

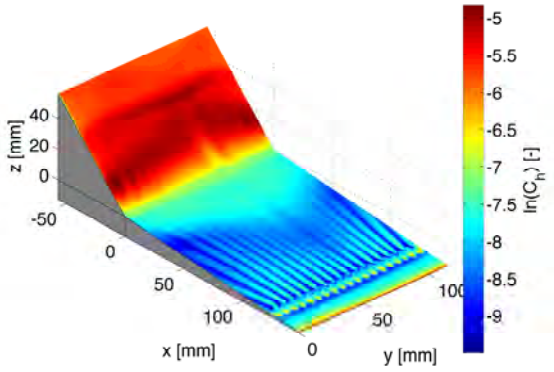

(b) The logarithm of the Stanton number (c_h) mapped on the surface coordinate system for the case $h_{zz} = 1.15mm$, $Re = 8.47 \times 10^6\ m^{-1}$

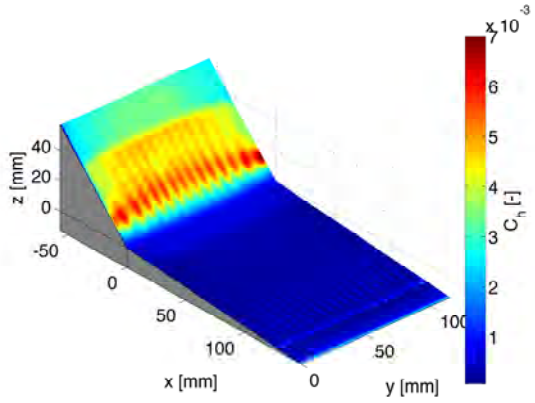

(c) The heat transfer mapped on the surface coordinate system for the case $h_5 = 1.15mm$, $Re = 11.3 \times 10^6\ m^{-1}$

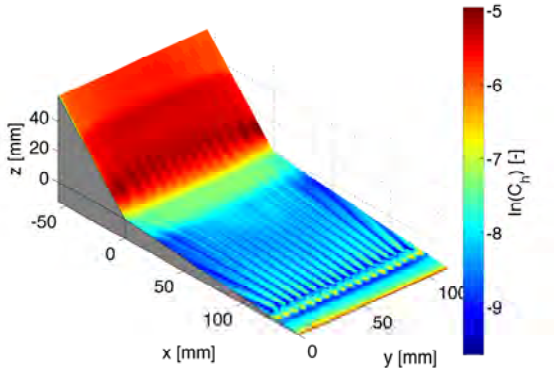

(d) The logarithm of the Stanton number (c_h) mapped on the surface coordinate system for the case $h_{zz} = 1.15mm$, $Re = 11.3 \times 10^6\ m^{-1}$

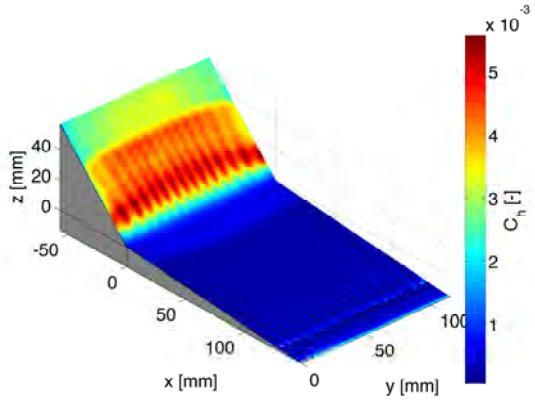

(e) The heat transfer mapped on the surface coordinate system for the case $h = 1.15mm$, $Re = 14.1 \times 10^6\ m^{-1}$

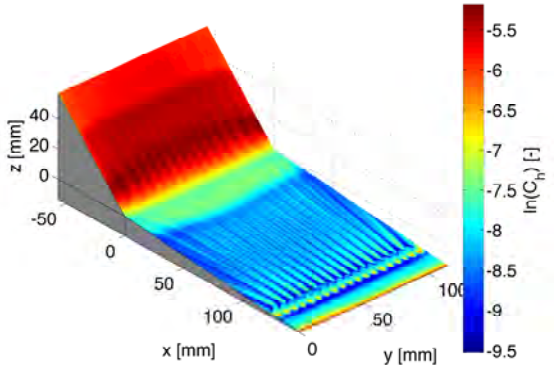

(f) The logarithm of the Stanton number (c_h) mapped on the surface coordinate system for the case $h_{zz} = 1.15mm$, $Re = 14.1 \times 10^6\ m^{-1}$

Figure C.5: The Stanton number (c_h) plotted on the physical model coordinates for the three Reynolds numbers and $h_{zz} = 1.15\ mm$

Appendix D

Disparity map obtained during self calibration for both FOVs

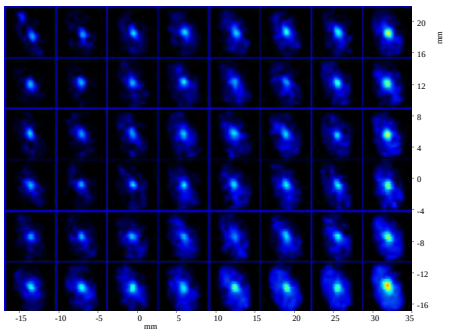

(a) Summed disparity map

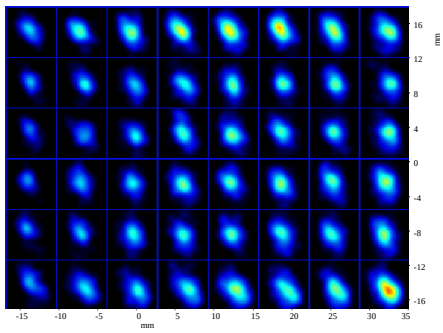

(b) Triangulation peaks for the second calibration update

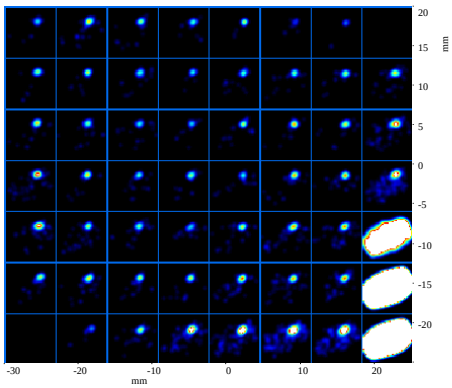

(c) Summed disparity map

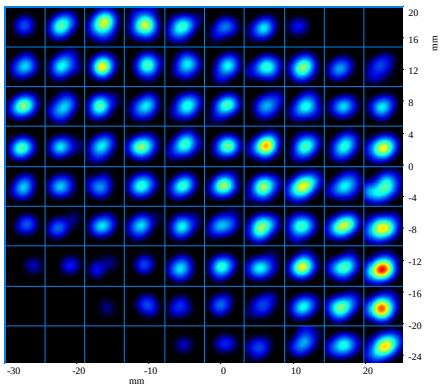

(d) Triangulation peaks for the second calibration update

Figure D.1: Typical disparity map for the three different cameras

Appendix E

Contour plot of the standard deviation in V_x parallel to the 5° ramp

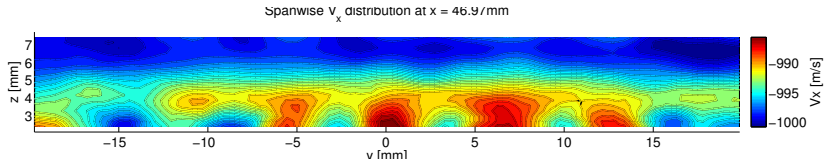

(a) V_x distribution in the (y,z) plane at $x = 47mm$

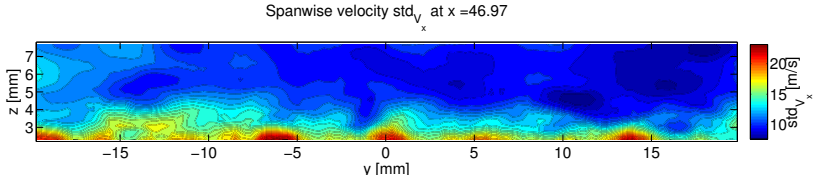

(b) Contour map of std_{V_x} at $x = 47mm$

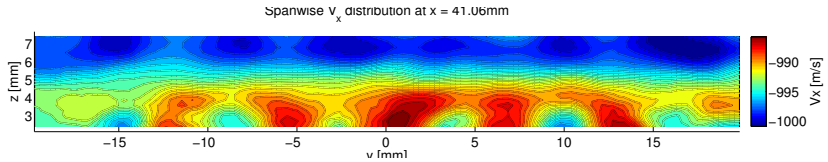

(c) V_x distribution in the (y,z) plane at $x = 41mm$

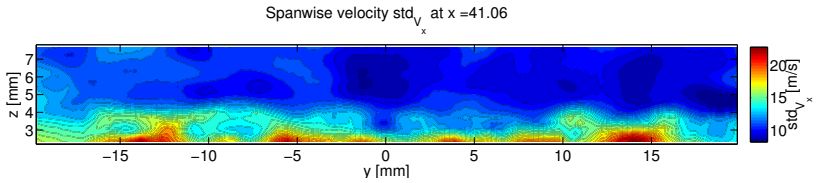

(d) Contour map of std_{V_x} at $x = 41mm$

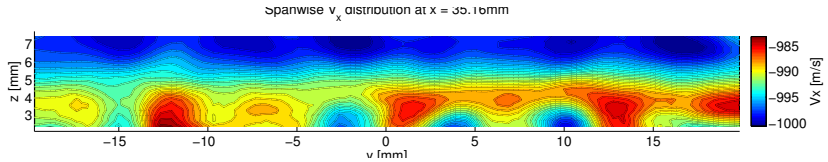

(e) V_x distribution in the (y,z) plane at $x = 35mm$

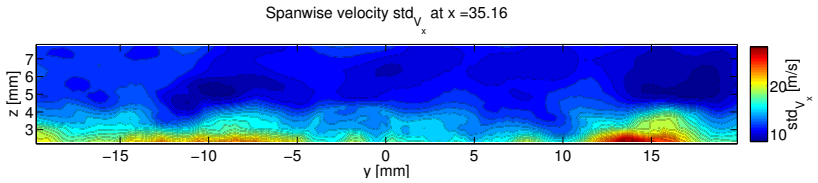

(f) Contour map of std_{V_x} at $x = 35mm$

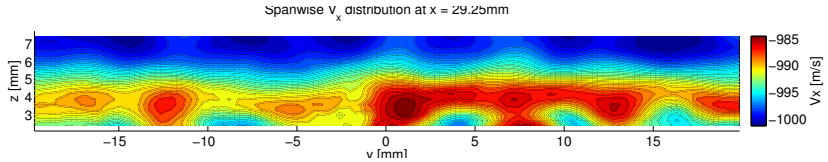

(g) V_x distribution in the (y,z) plane at $x = 29mm$

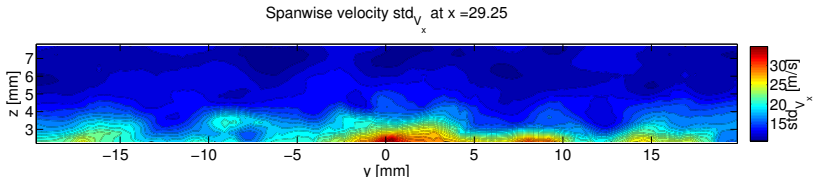

(h) Contour map of std_{V_x} at $x = 29mm$

Figure E.1: Contour map of V_x with its corresponding contour map std_{V_x} for four different fixed streamwise positions on the 5° ramp

Bibliography

J. D. Anderson. *Fundamentals of aerodynamics*. McGraw-Hill, 2005.

J. D. Anderson. *Hypersonic and High-Temperature Gas Dynamics Second Edition*. American Institute of Aeronautics and Astronautics, 2006.

D. Arnal and J. Delery. Laminar-turbulent transition and shock wave/boundary layer interaction. 2004.

C. Atkinson and J. Soria. An efficient simultaneous reconstruction technique for tomographic particle image velocimetry. *Experimental Fluids*, 47:553–568, 2009.

P. Bakker and B. van Leer. *Gas Dynamics Lecture Notes*. TU Delft, 2005.

G. K. Batchelor and J. Miles. *Hydrodynamic stability*. Cambridge University Press, 1981.

A. Bottaro and P. Luchini. Görtler vortices: Are they amenable to local eigenvalue analysis? *European Journal of Mechanics B/Fluids*, 1999.

R. Caljouw. An experimental investigation of a three-dimensional hypersonic flow on a double ramp geometry using stereo-piv. Master's thesis, TU Delft, 2007.

J. Delery. Shock interference in high mach number flows. *La Recherche Aerospatiale*, 3:175–185, 1994.

D. Ekelschot. Literature study: Investigation of görtler vortices in hypersonic flow using tomopiv. Technical report, TU Delft, 2012.

G. Elsinga. Evaluation of aero-optical distortion effects in piv. *Experiments in Fluids*, 39:246–256, 2005.

G. Elsinga. *Tomographic particle image velocimetry and its application to turbulent boundary layers*. PhD thesis, TU Delft, 2008.

G. Elsinga and J. Westerweel. Tomographic-piv measurement of the flow around a zigzag boundary layer trip. *Experimental Fluids*, 52:865–876, 2012.

J. Floryan. On the görtler instability of boundary layers. *Prog. Aerospace Sci*, 28:235–271, 1991.

P. Goulpie, B. G. B. Klingmann, and A. Bottaro. Görtler vortices in boundary layers with streamwise pressure gradient: Linear theory. *American Institute of Physics*, 1996.

F. Li and M. Malik. Fundamental and subharmonic secondary instabilities of gortler vortices. *J. Fluid Mech.*, 297:77–100, 1995.

L. Luca de, G. Cardone, D. d. l. C. Aymer, and A. Fonteneau. Goerlter instability of hypersonic boundary layer. *Experiments in Fluids*, 16, 1993.

A. Melling. Tracer particles and seeding for particle image velocimetry. *Measurement Science and Technology*, 8:1400–1416, 1997.

S. Navarro-Martinez and O. Tutty. Computers and fluids. *Numerical simulation of Görtler vortices in hypersonic compression ramps*, 34:225–247, 2005.

M. Novara, K. Batenburg, and F. Scarano. Motion tracking-enhanced mart for tomographic piv. *Measurement Science and Technology*, 21, 2010.

W. Saric. Görtler vortices. *Annual Review of Fluid Mechanics*, 26:379–409, 1994.

A. Savitzky and M. Golay. Smooting and differentiation of data by simplfied least squares procedures. *Analytical chemistry*, 36(8):1627–1639, 1964.

F. Scarano. Iterative image deformation methods in piv. *Measurement Science and Technology*, 13, 2002.

F. Scarano. *Experimental Aerodynamics*. TU Delft, 2007.

F. Schrijer. *Experimental investigation of re-entry aerodynamic phenomena*. PhD thesis, TU Delft, 2010a.

F. Schrijer. Investigation of görtler vortices in a hypersonic double compression ramp flow by means of infrared thermography. *10th International Conference on Quatitive InfraRed Thermography*, 2010b.

F. Schrijer and W. Bannink. Description and flow assessment of the delft hypersonic ludwieg tube. *AIAA*, 2008.

F. Schrijer, F. Scarano, and B. van Oudheusden. Application of piv in a mach 7 ludwieg tube flow facility. *6th International Symposium on Particle Image Velocimetry*, September 2005.

E. Schülein and V. Trofimov. Steady longitudinal vortices in supersonic turbulent separated flows. *J. Fluid Mech.*, pages 1–26, 2011.

D. Schultz and T. Jones. Heat-transfer measurements in short-duration hypersonic facilities. *AGARD*, 1973.

S. Soloff, R. Adrian, and Z.-C. Liu. Distortion compensation for generalized stereoscopic particle image velocimetry. *Measurement Science and Technology*, 8:1441–1454, 1997.

J. Swearingen and R. Blackwelder. The growth and breakdown of streamwise vortices in the presence of a wall. *J. Fluid Mech.*, 182:255–290, 1987.

B. Wieneke. Volume self-calibration for 3d particle image velocimetry. *Exp Fluids*, 45:549–556, 2008.